

國立交通大學

電信工程學系

博士論文

多重天線技術於超寬頻/車對車/中繼通道  
之分析與設計

Analysis and Design in UWB,  
Mobile-to-Mobile, and Relay Channels With  
MIMO Antenna Techniques

研究生：劉維正

指導教授：王蒞君

中華民國九十七年七月

多重天線技術於超寬頻/車對車/中繼通道之分析  
與設計

Analysis and Design in UWB, Mobile-to-Mobile, and  
Relay Channels With MIMO Antenna Techniques

研究生：劉維正

Student: Wei-Cheng Liu

指導教授：王蒞君 博士

Advisor: Dr. Li-Chun Wang

國立交通大學

電信工程學系

博士論文

A Dissertation

Submitted to Institute of Communication Engineering  
College of Electrical and Computer Engineering

National Chiao Tung University

in Partial Fulfillment of the Requirements  
for the Degree of Doctor of Philosophy

in

Communication Engineering  
Hsinchu, Taiwan

2008 年 7 月

# Analysis and Design in UWB, Mobile-to-Mobile, and Relay Channels With MIMO Antenna Techniques

A Dissertation

Presented to

The Academic Faculty

By

**Wei-Cheng Liu**



In Partial Fulfillment

of the Requirements for the Degree of  
Doctor of Philosophy in Communication Engineering

*Department of Communication Engineering*

*National Chiao Tung University*

July, 2008

Copyright © 2008 by Wei-Cheng Liu

# 多重天線技術於超寬頻/車對車/中繼通道之分析與設計

研究生：劉維正

指導教授：王蒞君 博士

國立交通大學  
電信工程學系

## 摘要

在近年來，多重天線系統在無線通訊領域中是一個很熱門的研究課題。然而，如何有效的使用多重天線技術取決於如何精確的捕捉無線通道的特性。在這篇論文中，我們進行了在超寬頻，車對車，以及中繼通道下，使用多重天線的無線通訊系統的分析與設計。

在第一個部份中，我們分析了在IEEE 802.15.3a和 802.15.4a超寬頻通道模型下，考慮遮蔽效應並使用耙式接收器的位元錯誤率。接著，我們展示了在超寬頻通道中，使用多重傳送與接收天線以及脈衝位置調變的訊號-雜訊比的分析表示式。最後，我們轉向於設計一個在使用多重天線的高度頻率選擇性區塊衰減通道下，使得位元錯誤率為最小的空間-時間-頻率碼。我們的結果定量的指出在IEEE 802.15.3a和 802.15.4a超寬頻通道下，遮蔽效應和耙式接收器的手指數目對於位元錯誤率的影響。再者，傳送天線可以用來降低超寬頻接收器的複雜度，因為在一個超寬頻系統中，耙式接收器的手指數目可以非常的高。因為在超寬頻系統中傳送的功率非常的低，我們建議採用多重接收天線改善涵蓋的範圍。最後，和其他的多頻帶超寬頻多重天線系統的空間-時間-頻率碼比較，我們的編碼在位元錯誤率為  $10^{-4}$  時，分別有 1 和 8 dB 的編碼增益。

在第二個部份中，我們推導了車對車萊式衰減通道的自我相關函數、幅度穿越率、以及平均衰落時間。然後，我們建議了一個弦波加總的多重天線車對車通道模擬方法，可以用來描述空間和時間上通道的相關性和萊氏衰減的效應。我們也考察了多重天線的通道容量經歷衰減的頻繁程度以及和萊氏因子的關係。我們證明了我們所提出的使用弦波加總的雙環加上可目視元件的近似模

型比單環模型更接近理論值，而且只需要稍微增加一些計算量。更進一步的說，我們發現了對於一個具有固定數目的散射體的多重天線系統，增加天線的數目並不能使得容量呈現線性的增加。當萊氏因子增加時，每一根天線的容量會減少。我們也發現了全部的通道容量和散射環境的豐富程度是有關係的。

在第三個部份中，我們考慮了在中繼通道下，使用解碼轉送結合網路編碼的合作式通訊系統。我們推導了合作式網路編碼協定的中斷機率和分集-多工權衡。我們的結果顯示，中繼節點不但能夠提供合作式的分集增益，也可以提供合作式的多工增益。

總而言之，在這篇論文中我們解決了三個重要，具有挑戰性，而且有趣的問題：(1) 使用多重天線的超寬頻系統下的效能分析和空間-時間-頻率碼的設計；(2) 使用多重天線的車對車隨意萊氏通道下的通道模擬模型的建立，自我相關函數、幅度穿越率、平均衰落時間、以及容量的分析；(3) 在中繼通道下，合作式網路編碼的中斷機率分析，以及分集-多工權衡分析。





# Analysis and Design in UWB, Mobile-to-Mobile, and Relay Channels With MIMO Antenna Techniques

A Dissertation

Presented to

The Academic Faculty

By

**Wei-Cheng Liu**



In Partial Fulfillment

of the Requirements for the Degree of  
Doctor of Philosophy in Communication Engineering

*Department of Communication Engineering*

*National Chiao Tung University*

July, 2008

Copyright © 2008 by Wei-Cheng Liu





# Abstract

Multiple-input multiple-output (MIMO) systems are hot research topics recent years. However, how to apply MIMO antenna techniques effectively is related to how to accurately capture the characteristics of wireless channels. In this dissertation, we perform analysis and design for MIMO wireless systems in ultra-wideband (UWB), mobile-to-mobile channels, and relay channels.

In the first part, we analyze the bit error rate (BER) performance in the IEEE 802.15.3a and 802.15.4a UWB channel models with Rake receiver and shadowing effects. Next, we present an analytical expression for the signal-to-noise ratio (SNR) of the pulse position modulated (PPM) signal in an UWB channel with multiple transmit and receive antennas. Finally, we turn to design BER-minimized space-time-frequency (STF) codes for MIMO highly frequency-selective block-fading channels. Our results quantitatively indicate the effect of shadowing and Rake finger numbers on the BER performance in the IEEE 802.15.3a and 802.15.4a UWB channels. Moreover, we suggest to utilize transmit antennas to reduce the UWB receiver's complexity since the number of fingers of a Rake receiver in the UWB system can be very high. Furthermore, due to low transmit power in the UWB system, we suggest to adopt multiple receive antennas to improve the performance from the view point of coverage extension. Finally, compared with other STF codes for

multiband UWB-MIMO communication systems, our code has about 1 and 8 dB coding gain at  $\text{BER} = 10^{-4}$ , respectively.

In the second part, we derive the autocorrelation function (ACF), level crossing rate (LCR), and average fade duration (AFD) of the mobile-to-mobile Rician fading channel. We suggest a sum-of-sinusoid MIMO mobile-to-mobile channel simulation method, which can characterize the spatial/temporal channel correlation and Rician fading effect. We examine how often the MIMO capacity experiences the fades and relate this to the Rician factor. It is proved that the proposed sum-of-sinusoids approximation developed from the double-ring with a LOS component model can approach the theoretical value more closely than the single-ring model at a slightly higher cost of computation loads. Furthermore, we find that for MIMO systems with constant number of scatterers, increasing number of antennas cannot linearly increase the capacity. The capacity per antenna is decreased as Rician factor increases. We also find that the total channel capacity is related to the richness of the scattering environment.

In the third part, we consider a relay channel and explore a decode-and-forward (DF) cooperative communications system combined with the network coding. We derive the outage probability and diversity-multiplexing tradeoff (DMT) for the proposed cooperative network coding (CNC) protocol. Our results show that the relay nodes not only can provide cooperative diversity gain, but also cooperative multiplexing gain.

In summary, we have solved three important, challenging, and interesting problems in this dissertation: (1) performance analysis and STF codes design in MIMO-UWB systems; (2) channel simulation model, ACF, LCR, AFD, and capacity analysis for MIMO mobile-to-mobile ad hoc Rician channels; and (3) analysis of outage probability as well as DMT for cooperative network

coding in relay channels.



# Acknowledgements

First of all, I would like to express my deeply gratitude to my advisor Dr. Li-Chun Wang. Not only the important insights to research problems, encouragement, and support, he also shows me a way of being optimistic to face difficulties. Without his advice, guidance, comments, and all that, this work could not have been done. He indeed opened a door to the future for me. Moreover, Dr. Wang teaches me what is the correct attitude toward the research and my life, including: Think big, different, and simple, and be a confident, humble, and active person. On the other hand, Dr. Wang encourages me to attend international conferences to develop my global view and collect the most recent research results. I would like to thank Dr. Wang for bringing me to attend the IEEE WCNC 2004 in Atlanta, GA, USA. It was my first time to go outside of Taiwan and attend a conference. Dr. Wang also spent much time in revising my papers. Without his helps, I think I could not have any publications.

Special thanks to my mates of Wireless System Lab in NCTU. They gave me kindly help in many aspects in my study years. Dr. Chiung-Jang Chen, Chih-Wen Chang, and Anderson Chen encouraged me every time when I felt frustrated. Dr. Jane-Hwa Huang, Wen-Ching Chung, Hyper Wang, Chu-Jung Yeh, and Samer Talat gave me many valuable suggestions and ideas in my research. I was so lucky to have all these lab mates.

Most importantly, I am deeply indebted to my great parents and sister whose love and understanding have been supporting me without any hesitation through these years. I would like to thank my friends, Path Lin, Yu-Tzu Chen, Chin-Hsiung Chen, Hsun-Yi Huang, Hsiang-Chun Lin, and Jen-Yang Liu. They always warmly back me up from their deeply inside mind.

Finally, I am thankful for valuable comments suggested by Prof. A. Svensson and anonymous reviewers of my journal and conference papers. I also wish to thank Prof. M. Z. Win and A. F. Molisch for their UWB tutorial courses and helpful discussions. Moreover, I would like to thank Prof. Chung-Hsuan Wang and Sau-Hsuan Wu, for their useful comments on my space-time-frequency coding and cooperative communications researches, respectively. I also want to thank Prof. Guu-Chang Yang, Yu-Ted Su, Chi-chao Chao, Li-Chun Wang, John F. An, Chung-Hsuan Wang, and Sau-Hsuan Wu for joining my Ph.D. dissertation oral defense committee in the midst of pressing affairs and give me many valuable comments and suggestions.



# Contents

<b>Abstract</b>	<b>i</b>
<b>Acknowledgements</b>	<b>iv</b>
<b>Contents</b>	<b>vi</b>
<b>List of Tables</b>	<b>xiv</b>
<b>List of Figures</b>	<b>xv</b>
<b>1 Introduction</b>	<b>1</b>
1.1 Problems and Solutions	3
1.1.1 BER Analysis in IEEE 802.15.3a and 802.15.4a UWB Channels	3
1.1.2 Performance of Using Multiple Transmit and Receive Antennas in Pulse-Based Ultrawideband Systems	7
1.1.3 BER-Minimized Space-Time-Frequency Codes for MIMO Highly Frequency-Selective Block-Fading Channels	9
1.1.4 Statistical Analysis of A Mobile-to-Mobile Rician Fad- ing Channel Model	9
1.1.5 Modeling and Capacity Fades Analysis of MIMO Ri- cian Channels in Mobile Ad Hoc Networks	10



1.1.6	Network Coding for Cooperative Multiplexing in Relay Channels . . . . .	11
1.2	Dissertation Outline . . . . .	11
<b>2</b>	<b>Background and Literature Survey</b>	<b>13</b>
2.1	Literature Survey . . . . .	14
2.1.1	Bit Error Rate Analysis in IEEE 802.15.3a and 802.15.4a UWB Channels . . . . .	14
2.1.2	On the Performance of Using Multiple Transmit and Receive Antennas in Pulse-Based Ultrawideband Systems	15
2.1.3	BER-Minimized Space-Time-Frequency Codes for MIMO Highly Frequency-Selective Block-Fading Channels . .	16
2.1.4	Statistical Analysis of A Mobile-to-Mobile Rician Fading Channel Model . . . . .	17
2.1.5	Modeling and Capacity Fades Analysis of MIMO Rician Channels in Mobile Ad Hoc Networks . . . . .	18
2.1.6	Network Coding for Cooperative Multiplexing . . . . .	19
2.2	Background . . . . .	20
2.2.1	IEEE 802.15.3a UWB Channel Model . . . . .	20
2.2.2	Mathematical Background for the IEEE 802.15.4a Channel Model . . . . .	22
2.2.3	Comparisons Between the IEEE 802.15.3a and 802.15.4a Channel . . . . .	24
2.2.4	Gauss-Hermite Formula . . . . .	24
<b>3</b>	<b>Bit Error Rate Analysis in IEEE 802.15.3a and 802.15.4a UWB Channels</b>	<b>27</b>
3.1	Motivation . . . . .	28

3.2	BER Analysis in IEEE 802.15.3a Channel . . . . .	28
3.2.1	Problem Formulation . . . . .	28
3.2.2	PDF of the Received Energy . . . . .	29
3.2.3	Computable Formula . . . . .	34
3.2.4	Discussion . . . . .	36
3.3	BER Analysis in IEEE 802.15.4a Channel . . . . .	38
3.3.1	Receiver Structure . . . . .	38
3.3.2	Characteristic Function of Received Energy . . . . .	38
3.3.3	Discussion . . . . .	42
3.3.4	The Shadowing Effect . . . . .	43
3.4	Numerical Results . . . . .	45
3.4.1	Simulation Method . . . . .	45
3.4.2	Results for BER in IEEE 802.15.3a Channel . . . . .	47
3.4.3	Numerical Results for BER in IEEE 802.15.4a Channel . . . . .	50
3.5	Conclusions . . . . .	53
<b>4</b>	<b>On the Performance of Using Multiple Transmit and Receive Antennas in Pulse-Based Ultrawideband Systems</b>	<b>71</b>
4.1	Motivation . . . . .	72
4.2	Channel Model . . . . .	72
4.2.1	The PDF of the Received Signal Power . . . . .	73
4.2.2	The Number of Simultaneous Arrival Paths . . . . .	74
4.2.3	Average Resolvable Path Power . . . . .	74
4.3	Signal Model and Detection Scheme . . . . .	75
4.3.1	Signal Model . . . . .	75
4.3.2	Signal Detection . . . . .	76
4.4	Analysis of PPM UWB Signals . . . . .	77
4.4.1	The State Probabilities of the Modified Poisson Process . . . . .	77



4.4.2	Mean and Variance of the Processed Data for PPM based UWB Signals . . . . .	78
4.4.3	SNR for PPM signal in the UWB channel . . . . .	82
4.5	Effect of Multiple Transmit and Receive Antennas . . . . .	83
4.5.1	Repetition Codes . . . . .	83
4.5.2	Receive Diversity . . . . .	84
4.5.3	Transmit Diversity . . . . .	85
4.6	Numerical Results . . . . .	86
4.6.1	The UWB Channel Response . . . . .	86
4.6.2	Average SNR and Variance of the Pulse Based UWB Signals . . . . .	87
4.6.3	Comparison for Different Diversity Schemes for the PPM UWB System . . . . .	88
4.6.4	Effect of RAKE Finger Numbers . . . . .	89
4.7	Conclusions . . . . .	90
<b>5</b>	<b>BER-Minimized Space-Time-Frequency Codes for MIMO Highly Frequency-Selective Block-Fading Channels</b>	<b>99</b>
5.1	Motivation . . . . .	100
5.2	System Model . . . . .	101
5.3	BER Performance . . . . .	102
5.4	The Universally Optimal STF Block Codes design . . . . .	103
5.4.1	The Optimum Criterion . . . . .	104
5.4.2	An Efficient Searching Algorithm for the Optimal STF Block Codes . . . . .	105
5.4.3	Optimal STF Block Codes for the Other Cases . . . . .	108
5.5	Properties of the Optimal STF Block Codes . . . . .	115
5.5.1	Coding Gain . . . . .	115

5.5.2	The Linearity . . . . .	115
5.5.3	Diversity Order . . . . .	116
5.6	Numerical Results . . . . .	116
5.6.1	Impact of Number of Transmit Antennas Jointly Encoded ( $N_t$ ) for Two Subcarriers Jointly Encoded ( $M = 2$ )	118
5.6.2	Effect of Number of Receive Antennas . . . . .	118
5.6.3	Effect of Number of Transmit Antennas Jointly Encoded ( $N_t$ ) for Three Subcarriers Jointly Encoded ( $M = 3$ ) . . . . .	119
5.6.4	Effect of Number of Transmit Antennas Jointly Encoded ( $N_t$ ) for Four Subcarriers Jointly Encoded ( $M = 4$ )	120
5.6.5	BER Comparison with STF Codes in [1] and [2] . . . . .	120
5.7	Conclusions . . . . .	120
<b>6</b>	<b>Statistical Analysis of A Mobile-to-Mobile Rician Fading Channel Model</b>	<b>136</b>
6.1	Motivation . . . . .	137
6.2	Scattering Environment . . . . .	137
6.2.1	Traditional Double-Ring Scattering Model . . . . .	137
6.2.2	Double-Ring with a LOS Component Scattering Model	138
6.3	Sum-of-Sinusoids Rician Fading Simulator . . . . .	139
6.3.1	Signal Model for Double-Ring with a LOS component Scattering . . . . .	140
6.3.2	Second-Order Statistics . . . . .	141
6.3.3	Signal Model with Single-Ring Scattering . . . . .	143
6.4	Higher-Order Statistics . . . . .	143
6.4.1	Level Crossing Rate . . . . .	143
6.4.2	Average Fade Duration . . . . .	146

6.5	Numerical Results . . . . .	146
6.5.1	Effects of Rician Factor . . . . .	147
6.5.2	Comparison of Double-Ring with a LOS Component Model and Single-Ring Model . . . . .	147
6.5.3	LCR and AFD . . . . .	148
6.6	Conclusions . . . . .	149

**7 Modeling and Capacity Fades Analysis of MIMO Rician Channels in Mobile Ad Hoc Networks 157**

7.1	Motivation . . . . .	158
7.2	Scattering Model . . . . .	159
7.3	Sum-of-Sinusoids MIMO Rician Fading Simulator . . . . .	160
7.3.1	LOS Component Model . . . . .	160
7.3.2	Sum-of-Sinusoids Simulation Method . . . . .	161
7.4	Capacity Evaluation . . . . .	163
7.4.1	Ergodic Capacity . . . . .	163
7.4.2	Level Crossing Rate and Average Fade Duration . . . . .	164
7.5	Numerical Results . . . . .	166
7.5.1	Channel Correlation . . . . .	166
7.5.2	Impacts of Doppler Frequencies . . . . .	167
7.5.3	Effect of Spatial Correlation . . . . .	168
7.5.4	Impact of Numbers of Antennas . . . . .	168
7.5.5	Impact of Numbers of Scatterers . . . . .	169
7.5.6	Capacity Distribution . . . . .	169
7.5.7	LCR and AFD . . . . .	169
7.6	Conclusions . . . . .	170

<b>8</b>	<b>Network Coding for Cooperative Multiplexing in Relay Channels</b>	<b>181</b>
8.1	Motivation . . . . .	181
8.2	System Model and CNC Protocol . . . . .	183
8.3	Diversity-Multiplexing Tradeoff of CNC Protocol . . . . .	184
8.3.1	Equivalent Signal Models . . . . .	184
8.3.2	Parameterizations . . . . .	185
8.3.3	Diversity-Multiplexing Tradeoff Analysis . . . . .	185
8.4	Numerical Results . . . . .	188
8.5	Conclusions . . . . .	188
<b>9</b>	<b>Conclusions</b>	<b>191</b>
9.1	Bit Error Rate Analysis in IEEE 802.15.3a and 802.15.4a UWB Channels . . . . .	193
9.2	On the Performance of Using Multiple Transmit and Receive Antennas in Pulse-Based Ultrawideband Systems . . . . .	194
9.3	BER-Minimized Space-Time-Frequency Codes for MIMO Highly Frequency-Selective Block-Fading Channels . . . . .	195
9.4	Statistical Analysis of A Mobile-to-Mobile Rician Fading Channel Model . . . . .	196
9.5	Modeling and Capacity Fades Analysis of MIMO Rician Channels in Mobile Ad Hoc Networks . . . . .	197
9.6	Network Coding for Cooperative Multiplexing in Relay Channels	197
9.7	Suggestions for Future Research . . . . .	198
	<b>Bibliography</b>	<b>200</b>
	<b>Appendices</b>	<b>217</b>

A Derivation of the PDF of $\mathcal{E}$	217
B Proof of Theorem 1	219
C Proof of Theorem 2	221
D Proof of Lemma 1	222
E Proof of Theorem 4	224
F Proof of Theorem 5	225
G Proof of Proposition 1	227
H Proof of Proposition 2	229
Vita	232
Publication List	233



# List of Tables

2.1	Comparison between the IEEE 802.15.3a and 802.15.4a channel models. . . . .	25
3.1	The values of the parameters of the IEEE 802.15.4a channel model CM1. . . . .	47
4.1	System Parameters . . . . .	91
5.1	The truth table for discovering the code structure from the optimal codewords. The operator $\sim$ is bitwise NOT, $\&$ is bitwise AND, and $ $ is bitwise OR. . . . .	110
5.2	The coding gain of the optimal codes we have found in Section 5.4. . . . .	115
5.3	The values of $r$ which is the rank of matrix $\mathbf{S} \circ \mathbf{R}_M$ for different kinds of optimal STF block codes. . . . .	117
7.1	The simulation and analytical values of the channel correlation of a $3 \times 3$ MIMO channel. . . . .	167

# List of Figures

3.1	The distributions of $\mathcal{E}$ by simulation and $\tilde{\mathcal{E}}$ by analysis for a RAKE receiver with 10 fingers in the IEEE 802.15.3a UWB channels CM1, where the standard deviations of lognormal fading and shadowing are $\sigma = 4.8$ dB and $\sigma_x = 3$ dB, respectively. (a) PDFs. (b) CDFs. . . . .	56
3.2	The PDF $f_{\tilde{\mathcal{E}}}(x)$ of the received energy $\tilde{\mathcal{E}}$ for a RAKE receiver with 10 fingers in the IEEE 802.15.3a UWB channels CM1, CM2, CM3, and CM4, where the standard deviations of lognormal fading and shadowing are $\sigma = 4.8$ dB and $\sigma_x = 3$ dB, respectively. . . . .	57
3.3	Effect of various shadow standard deviations ( $\sigma_x = 3$ dB and 6 dB) on the BER performance of a 10-finger RAKE receiver in the IEEE 802.15.3a UWB channels CM3. . . . .	58
3.4	BER v.s. $E_b/N_0$ for the 10-finger RAKE receiver in the IEEE 802.15.3a UWB channels CM2, CM3, and CM4 with shadowing standard deviation $\sigma_x = 6$ dB, where the analytical BER is obtained from the characteristic function based approach, i.e. (3.28). . . . .	59

3.5	BER v.s. $E_b/N_0$ for the 10-finger RAKE receiver in the IEEE 802.15.3a UWB channels CM2, CM3, and CM4 with shadowing standard deviation $\sigma_x = 6$ dB, where the analytical BER is obtained from the MGF-based approach, i.e. (3.29). . . . .	60
3.6	The PDF $f_{\tilde{\mathcal{E}}}(x)$ of the received energy $\tilde{\mathcal{E}}$ of a RAKE receiver with number of fingers $L = 10, 20, 30, 40,$ and $50$ in the IEEE 802.15.3a UWB channel CM1. . . . .	61
3.7	BER v.s. the number of fingers of the RAKE receiver ( $L$ ) for CM1, CM2, CM3, and CM4, where $E_b/N_0 = 5$ dB. . . . .	62
3.8	The BER v.s. $E_b/N_0$ for the CM1 model without shadowing and CM1 model with shadowing standard deviation $\sigma_x = 3$ and $6$ dB in the IEEE 802.15.4a standard by simulation and analysis. In CM1, the default value of $\sigma_x$ is $2.22$ dB. . . . .	63
3.9	The BER v.s. $L$ (number of fingers of the RAKE receiver) for the CM1 model in the IEEE 802.15.4a standard by simulation and analysis. The SNR is $E_b/N_0 = 0$ dB. The shadowing standard deviation $\sigma_x$ is $2.22$ dB. . . . .	64
3.10	The BER v.s. $E_b/N_0$ for various inter-cluster arrival rates $\Lambda = 0.01, 0.1, 0.5,$ and $1$ under the CM1 model of the IEEE 802.15.4a UWB channel. In CM1, the default value of $\Lambda$ is $0.047$ . The shadowing standard deviation $\sigma_x$ is $2.22$ dB. . . . .	65
3.11	The effects of different values of ray-arrival parameter $\lambda_1 = 0.01, 0.1, 1,$ and $10$ on the BER v.s. $E_b/N_0$ , where $\lambda_2 = 0.15$ and $\beta = 0.095$ according to the CM1 model of the IEEE 802.15.4a channel. In CM1, the default value of $\lambda_1$ is $1.54$ . The shadowing standard deviation $\sigma_x$ is $2.22$ dB. . . . .	66



3.12	The impacts of various values of $\lambda_2$ on the BER v.s. $E_b/N_0$ for the case $\lambda_1 = 1.54$ and $\beta = 0.095$ in the CM1 model of the IEEE 802.15.4a UWB channel. In CM1, the default value of $\lambda_2$ is 0.15. The shadowing standard deviation $\sigma_x$ is 2.22 dB. . . . .	67
3.13	The effect of various $\beta$ on the BER v.s. $E_b/N_0$ for $\lambda_1 = 1.54$ and $\lambda_2 = 0.15$ in the CM1 model of the IEEE 802.15.4a UWB channel. In CM1, the default value of $\beta$ is 0.095. The shadowing standard deviation $\sigma_x$ is 2.22 dB. . . . .	68
3.14	The effect of the inter-cluster decay constant $\Gamma = 0.1, 1, 10,$ and 100 in the IEEE 802.15.4a UWB channel for various of $E_b/N_0$ , where a 10-finger RAKE receiver is adopted in the CM1 model. In CM1, the default value of $\Gamma$ is 22.61. The shadowing standard deviation $\sigma_x$ is 2.22 dB. . . . .	69
3.15	The effect of intra-cluster decay constant $\gamma_0$ in the IEEE 802.15.4a UWB channel for various values of $E_b/N_0$ , where a 10-finger RAKE receiver is adopted in the CM1 model. The shadowing standard deviation $\sigma_x$ is 2.22 dB. . . . .	70
4.1	The diversity schemes: a) no diversity, b) receive diversity, and c) time-switched transmit diversity. . . . .	92
4.2	An example of the UWB channel response in the time domain.	93
4.3	Analytical and simulation results for the SNR of the PPM signals over the UWB channel with multiple transmit and receive antennas. . . . .	94
4.4	Analytical and simulation results for the variance of the PPM signals over the UWB channel with multiple transmit and receive antennas. . . . .	95

4.5	Effect of spatial correlation of transmit diversity on the variance of the PPM signals over the UWB channel. . . . .	96
4.6	The BER simulation results for the different diversity schemes in the PPM UWB system. Here, Tx and Rx represent the transmit and the receive antenna numbers, respectively, $L$ represents the RAKE finger number, $f$ represents the frame number, and $\delta$ represents the modulation index with PPM. . . . .	97
4.7	The BER simulations of the PPM UWB system with the different RAKE finger numbers, where Tx and Rx represent the transmit and the receive antenna numbers, respectively, $L$ represents the RAKE finger number, $f$ represents the frame number, and $\delta$ represents the modulation index with PPM. . . . .	98
5.1	The system block diagram. . . . .	122
5.2	Illustration of our proposed efficient searching algorithm for the optimal STF block codes for two subcarriers jointly encoded, two transmit antennas jointly encoded, and two input information bits for each codeword. We search complete graphs with four vertices subject to the largest $m$ metrics. (a) $m = 1$ . (b) $m = 2$ . (c) $m = 3$ . . . . .	125
5.3	The effect of different number of transmit antennas jointly encoded ( $N_t$ ) on the BER for CM1, CM2, CM3, and CM4 for the optimal STF block codes for two subcarriers jointly encoded and two input information bits for each codeword. The modulation is BPSK. (a) $N_t = 2$ . (b) $N_t = 3$ . (c) $N_t = 4$ . . . . .	128

5.4	The effect of number of receive antennas ( $N_r$ ) on the BER for CM1, CM2, CM3, and CM4 for the optimal STF block codes for two subcarriers jointly encoded, two input information bits for each codeword, and two transmit antennas jointly encoded. $N_r = 1$ and 2. The modulation is BPSK. . . . .	129
5.5	The effect of number of transmit antennas jointly encoded ( $N_t$ ) on the BER for CM1, CM2, CM3, and CM4 for the optimal STF block codes for three subcarriers jointly encoded and two input information bits for each codeword. The modulation is BPSK. (a) $N_t = 2$ . (b) $N_t = 3$ . (c) $N_t = 4$ . . . . .	132
5.6	The effect of number of transmit antennas jointly encoded ( $N_t$ ) on the BER for CM1, CM2, CM3, and CM4 for the optimal STF block codes for four subcarriers jointly encoded and two input information bits for each codeword. The modulation is BPSK. (a) $N_t = 2$ . (b) $N_t = 3$ . . . . .	134
5.7	The BER comparison of our code versus Zhang's code [1] and Chusing's code [2] for three subcarriers jointly encoded, two input information bits for each codeword, one receive antenna, and three transmit antennas jointly encoded in the IEEE 802.15.3a UWB channel model CM4. The modulation is BPSK. . . . .	135
6.1	Scattering environment in a mobile-to-mobile system with a LOS component. . . . .	150
6.2	Relative velocity $\mathbf{v}_3$ from the TX with velocity $\mathbf{v}_1$ to the RX with velocity $\mathbf{v}_2$ . . . . .	151
6.3	Single-ring scattering environment for a mobile-to-mobile Rician fading channel. . . . .	152

6.4	The real part of the autocorrelation of the complex envelope $Z(t)$ , where $N = M = 8$ for $K = 0, 1, 3$ , and $9$ . . . . .	153
6.5	The real part of the autocorrelation of the fading envelope of double-ring and single-ring scattering models for $K = 1$ . . . . .	154
6.6	Normalized envelope level crossing rate for mobile-to-mobile Rician fading. Solid line denotes the theoretical results and the dashed line denotes the simulation results, where $\rho = \frac{R}{\sqrt{\Omega_p}}$ . . . . .	155
6.7	Normalized average fade duration for a mobile-to-mobile Rician fading channel for $K = 1, 3, 7$ , and $10$ . . . . .	156
7.1	Correlated double-ring scattering model with LOS components. . . . .	171
7.2	Received signals at multiple antennas with an AOA $\theta_{rn}$ and separation distance $d$ under the assumption that the transmission distance is much longer than $d$ . . . . .	172
7.3	LOS component model for moving transmitter TX and receiver RX of which velocity vectors are $\mathbf{v}_1$ and $\mathbf{v}_2$ with a relative angle of $\theta_\beta$ , respectively. . . . .	173
7.4	MIMO Rician capacity with different Doppler frequencies where SNR = 20 dB, $d = \lambda/2$ , $K = 4.77$ dB. . . . .	174
7.5	Effect of antenna separation on the ergodic capacity of a $3 \times 3$ MIMO channel for SNR = 20 dB and various values of $K$ factors. . . . .	175
7.6	The ergodic capacity of MIMO channels against the number of antennas when SNR = 20 dB, $d = \lambda/2$ and $I = N = 8$ . . . . .	176
7.7	The ergodic capacity of MIMO channels against the number of antennas for various number of scatterers ( $I$ and $N$ ) when SNR = 20 dB, $d = \lambda/2$ and $K = -\infty$ dB. . . . .	177
7.8	Probability density functions of MIMO capacity in a mobile-to-mobile Rician fading channel. . . . .	178

7.9 Level crossing rate of the MIMO capacity in a mobile-to-mobile Rician fading channel. . . . . 179

7.10 Average fade duration of the MIMO capacity in a mobile-to-mobile Rician fading channel. . . . . 180

8.1 The system model and proposed CNC protocol, where phase (1):  $A$  sends  $a$  to  $B$  and  $R$ ; phase (2):  $B$  sends  $b$  to  $A$  and  $R$ ; phase (3):  $R$  broadcasts  $a \oplus b$  to  $A$  and  $B$ . . . . . 189

8.2 Diversity-multiplexing tradeoff comparison of the upper bound (UB), cooperative network coding (CNC), selection decode-and-forward (SDF), and decode-and-forward (DF). . . . . 190



# Chapter 1

## Introduction

The Bible says, “Two are better than one because they have a good reward for their labor. For if they fall, one will lift up his companion.” The above words briefly and simply describe the concept of diversity, which is a technique widely used in wireless communications systems of today. There are many forms of diversity. For example, we use multiple-input multiple-output (MIMO) systems to obtain the spatial diversity. Thanks to the help from relays, we can have cooperative diversity. Channel coding gives us time diversity. Multicarrier communication systems provide frequency diversity. Scheduling in the multiuser MIMO systems can benefit from user diversity. Through these diversity techniques, we can improve reliability, capacity, and coverage and suppress the interference in wireless communications systems.

In our dissertation, we focus on two kinds of diversity techniques. They are MIMO and cooperative communications systems. The two subjects are hot research topics on wireless communications in recent years. A MIMO system is a multi-antenna wireless communications system. MIMO systems transmit signals via its multiple transmit antennas and receive and recover the original signals at the receiver using multiple receive antennas. The

MIMO technique is first proposed by Marconi in 1908. He used multiple antennas to restrain channel fading. According to the number of antennas in the transmitter and receiver, the MIMO technique or called the “smart antenna” technique includes the single-input multiple-output (SIMO) and multiple-input single-output (MISO) systems.

Because MIMO can increase data throughput and transmission distance extremely without extra bandwidth or total transmit power expenditure, MIMO technique has attracted much attention in recent years. The core concept of MIMO is to exploit the spatial degree of freedom provided by multiple transmit and receive antennas to improve the spectrum efficiency, transmission data rate, and communications quality of wireless communications systems.

Cooperative communication is another novel communications technique proposed in recent years. Many nodes equipped with single transmit/receive antenna form a wireless network. By the cooperation between the transmitters, relays, and receivers, a virtual antenna array can be established. Thus, cooperative wireless networks can be viewed as another form of MIMO systems. Cooperative communications can increase system capacity and save power. Compared with the single hop transmission which is widely discussed and understood, cooperative communications network consisting of multiple nodes is still an open research issue.

We will investigate several interesting issues about MIMO systems in three different channels, including: (1) ultra-wideband (UWB) channels, (2) mobile-to-mobile channels, and (3) relay channel. In the first part of this dissertation, we analyze the performance and design bit error rate (BER)-minimized space-time-frequency (STF) codes in MIMO-UWB systems. In the second part of this dissertation, we construct the channel model and an-

alyze the autocorrelation function (ACF), level crossing rate (LCR), average fade duration (AFD), and capacity for MIMO mobile-to-mobile ad hoc Rician channels. Last, we propose a cooperative network coding protocol and analyze its outage probability and diversity-multiplexing tradeoff (DMT). In the following, we discuss the problems and the solutions regarding the above issues.

## 1.1 Problems and Solutions

In this section, we will briefly describe our problem formulations and the corresponding solutions, including BER analysis in IEEE 802.15.3a and 802.15.4a UWB channels, performance of using multiple transmit and receive antennas in pulse-based ultrawideband systems, BER-minimized space-time-frequency codes for MIMO highly frequency-selective block-fading channels, statistical analysis of a mobile-to-mobile Rician fading channel model, modeling and capacity fades analysis of MIMO Rician channels in mobile ad hoc networks, and network coding for cooperative multiplexing in relay channels.

### 1.1.1 BER Analysis in IEEE 802.15.3a and 802.15.4a UWB Channels

UWB is a promising wireless communications technique for high data rate transmission. The UWB channel characteristics are very different from conventional narrowband channels. Recently, the IEEE 802.15.3a [3] and 802.15.4a [4] UWB channel models are specified and widely adopted in the industry. However, UWB systems based on the IEEE 802.15.3a and 802.15.4a models are only evaluated by simulations or by analysis with simplified conditions.

Hence, a fundamental question arises: how can a UWB system be ana-



lyzed in the complete IEEE 802.15.3a and 802.15.4a channel models? These UWB channels have two significant properties. First, because the UWB signal bandwidth is much wider than the channel coherence bandwidth, highly frequency selective fading exists. Second, UWB signals usually yield many clusters of non-Rayleigh faded rays because the extremely large bandwidth leads to high-resolution arrival time after being reflected by objects. The challenges of analyzing UWB signals in the IEEE 802.15.3a and 802.15.4a channels can be summarized into four types:

- Instead of fixed-number arrival rays within one cluster for narrowband channel, the UWB signal may arrive in many clusters with a random number of rays. The arrival processes of clusters and rays are modeled by a doubly stochastic Poisson process in the IEEE 802.15.3a model. For the IEEE 802.15.4a UWB signals, the number of clusters is modeled by a Poisson random variable and the inter-arrival time of rays within a cluster is modeled by a hyper-exponential random variable. Due to the unknown number of rays and clusters, it is difficult to compute the total collected signal energy at RAKE receivers.
- The multipath fading in UWB channels is not modeled as a traditional Rayleigh random variable because the central limit theorem is not applicable for insufficient arrival rays in a very narrow time bin. From measurement results [5,6], a lognormal multipath fading as well as shadowing is adopted in the IEEE 802.15.3a UWB channel. Conditioned on the given number of rays as well as clusters, and the average amplitude, a UWB signal amplitude in the IEEE 802.15.3a channel is modeled as a two-dimensional lognormal random variable. Because the mean of signal amplitude is related to the Erlang-distributed inter-arrival time for clusters and rays, such a random signal is difficult to be analyzed.

- The multipath fading signal in the IEEE 802.15.4a UWB channel is characterized by a joint lognormal Nakagami- $m$  random variable. A Nakagami (non-Rayleigh) UWB signal amplitude is adopted because the central limit theorem is no longer applicable for UWB signals due to the limited number of arrival rays in a very narrow time bin (or chip duration). The fading parameter  $m$  is a log-normal random variable and is related to the ray arrival time. Unlike the traditional fading signal amplitude characterized by only one random variable, the fading signal amplitude in the IEEE 802.15.4a channel model is characterized by two random variables and also depends on the ray arrival time. Hence, analyzing the statistical characteristics of fading in the IEEE 802.15.4a channel model is much more complicated than that in the conventional channel model.
- In the IEEE 802.15.4a UWB channel, the shadowing component is turned off for the purpose of comparing different proposals. To evaluate the actual BER, it is necessary to add the shadowing effect back. However, when shadowing is incorporated into the computable formula for BER in the IEEE 802.15.3a UWB channel [7] the simulation results cannot match the analytical results very well. We find that this mismatch is due to the divergence property of the moment generating function (MGF) of the log-normal random variable [8]. Thus, we believe that taking account of shadowing into the BER analysis in the IEEE 802.15.4a channel is very important and not a trivial task.

Characterized by a joint two-dimensional lognormal and doubly stochastic Poisson random variable, the key parameters in the IEEE 802.15.3a UWB channel model include the cluster/ray arrival rates, the cluster/ray decay factors, and the standard deviations of the lognormal multipath fading and

shadowing. To our knowledge, the complete effects with all the key parameters in the IEEE 802.15.3a channel on the BER performance of a UWB system has not been reported as an analytical formula in the literature. The first objective of this part is to develop an analytical method to compute the error performance in the complete IEEE 802.15.3a channel. We will present an explicit BER analytical computation method incorporating the impacts of the number of fingers at the RAKE receiver, the effects of shadowing and all the UWB channel parameters based on the IEEE 802.15.3a model. Comparing with [7], we examine the effect of the number of fingers ( $L$ ) at the RAKE receiver, instead of the window size. However, it is very challenging to obtain the distribution of the *sum* of the collected signal energy from  $L$  fingers at the RAKE receiver in the IEEE 802.15.3a UWB channel because in each time bin of  $L$  fingers both the numbers of clusters and rays are random variables. The distribution of signal energy collected from  $L$  fingers will involve a computationally intractable  $(6L + 4)$ -dimension integration. We develop a fast BER computation approach requiring only an integration of six dimensions instead of  $(6L + 4)$  dimensions for an  $L$ -finger RAKE receiver. Additionally, we suggest using Hermite and Legendre polynomial approach to further simplify the four integrations into weighted summation. Thus, it turns out that only two-dimension integration is required for our approach.

Furthermore, according to the convergence property of MGF in [8], we explain the divergence phenomenon of the MGF-based approach [7] when the shadowing component of the IEEE 802.15.3a channel is included in the BER computation. Thus, we believe that taking account of shadowing into the BER analysis in the IEEE 802.15.3a channel is not a trivial extension. We suggest a characteristic function-based approach to avoid the divergence problem of the MGF-based approach in BER calculation in IEEE 802.15.3a

UWB channel models. With the aforementioned advantages, the proposed computable formula can easily analyze the effects of various UWB channel parameters in the IEEE 802.15.3a channel model without time consuming simulations.

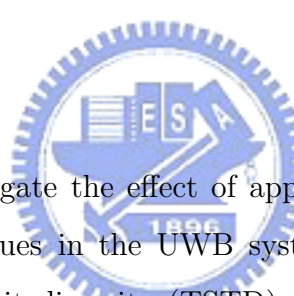
The second objective of this part is to develop a BER computable formula to include the complete effects of the and 802.15.4a UWB channel model, shadowing, as well as RAKE receiver. Mathematically, UWB signals in the IEEE 802.15.4a channel model are characterized by a multi-dimension random variable consisting of Nakagami- $m$  fading amplitude, Poisson distributed number of clusters, and a hyper-exponential inter-ray arrival time. To our knowledge, a BER analytical model to include all the effects of channel parameters specified in the IEEE 802.15.4a model and also shadowing has not seen in the literature. Secondly, by applying the newly developed analytical model we evaluate the impacts of different UWB channel parameters to obtain the insights into the design of UWB systems.

### **1.1.2 Performance of Using Multiple Transmit and Receive Antennas in Pulse-Based Ultrawideband Systems**

To our best knowledge, it has not been seen many reports in the literature to evaluate the performance of the PPM based UWB system using multiple transmit and receive antennas in a frequency selective multipath fading environment. The objective of this part is to investigate to what extent transmit/receive diversity can further improve the performance for the PPM based UWB system.

Toward this end, we first analyze the statistical properties of the PPM

signals in a generalized frequency selective fading model proposed for the UWB system [9]. To accurately evaluate the UWB system performance, choosing an appropriate channel model is very crucial. In the literature, many models have been reported to characterize the UWB channel, such as [10–16]. In particular, according to the measurement results of [11, 14], the authors in [9] proposed a generalized fading channel model for the UWB application, which can possess two major properties of the UWB channel - clustering property and highly frequency selective fading. Through simulations, we demonstrate that the derived analytical model can accurately estimate the first-order and the second-order statistics of the pulse based UWB signals in the considered UWB channel model.



Secondly, we investigate the effect of applying the transmit/receive antenna diversity techniques in the UWB system. Specifically, we consider a time-switched transmit diversity (TSTD) scheme [17] at the transmitter end, and the template-based pulse detection using antenna diversity at the receiver end [18]. Through simulations, we show that using multiple transmit antennas in the UWB channel can improve the system performance in the manner of reducing signal variations. Because of already possessing rich diversity inherently, using multiple transmit antennas does not provide diversity gain in the strict sense (i.e., the slope of BER v.s. SNR), but can reduce the complexity of the Rake receiver. As for the effect of receive diversity, we demonstrate that the multiple receive antennas can improve the performance of the UWB system by providing higher antenna array combining gain even without providing the diversity gain in the strict sense.

### 1.1.3 BER-Minimized Space-Time-Frequency Codes for MIMO Highly Frequency-Selective Block-Fading Channels

The objective of this part is to design the BER-minimized STF block codes for the MIMO systems under four kinds of IEEE 802.15.3a UWB channel models, i.e., CM 1  $\sim$  4. Based on the BER analysis under the aforementioned environment in [19], we provide a BER-minimized design criterion, an efficient searching algorithm for the optimal STF block codes, and optimal BER performance curves.

### 1.1.4 Statistical Analysis of A Mobile-to-Mobile Rician Fading Channel Model

This part develops a sum-of-sinusoids mobile-to-mobile Rician fading simulator. First, the “double-ring with a LOS component” model is proposed to incorporate both the LOS effect and the scattering effect. The double-ring scattering model was originally put forward [20], where the scatterers around the transmitter and the receiver were modeled by two independent rings. Second, the theoretical statistical property of the mobile-to-mobile Rayleigh channel is extended to the Rician fading case. The derived theoretical properties of the mobile-to-mobile Rician fading channel are employed to validate the accuracy of the proposed mobile-to-mobile Rician fading channel simulator involving sum-of-sinusoids. Furthermore, the higher-order statistics of the mobile-to-mobile Rician fading simulator, such as the LCR and AFD, is discussed. Compared with references [21] and [22], this study provides, in addition, the simulation and the theoretical comparisons for the autocorrelation function of the fading envelope, the comparison between the

fading envelope of double-ring and single-ring scattering models for different  $K$  factors, and the difference in the fading envelope of both the double-ring and single-ring scattering models for different  $K$  factors.

### 1.1.5 Modeling and Capacity Fades Analysis of MIMO Rician Channels in Mobile Ad Hoc Networks

The objective of this part is two-fold. First, we aim to develop a simple sum-of-sinusoids MIMO channel simulation method that can characterize the spatial/temporal correlation and Rician fading effect. The sum-of-sinusoids channel simulation method, or ‘Jake’s model’, has been widely used to evaluate the performance of conventional single-input single-output (SISO) mobile systems [23–25]. Jake’s model can capture the time behavior of a mobile-to-base channel. Recently, in [26], a mobile-to-mobile MIMO channel simulator was developed to incorporate the spatial correlation in a Rayleigh fading environment. We will further incorporate the Rician fading effect in the mobile-to-mobile MIMO channel simulator based on a correlated double-ring scattering model (described in Section 7.3). The second objective of this part is to research the capacity of the mobile-to-mobile MIMO Rician fading channel. To this end, we will derive the upper bound of the ergodic capacity of the mobile-to-mobile MIMO Rician channel. The MIMO capacity bound can be used to confirm the accuracy of the proposed sum-of-sinusoids simulation method and explore the impact of spatial correlation. Further, we evaluate the LCR and AFD of the MIMO mobile-to-mobile Rician channel. The LCR and AFD of MIMO capacity was researched in [27, 28], but not in a mobile-to-mobile and not in a Rician fading channel, either. We will relate the LCR and capacity fade of MIMO mobile-to-mobile systems with the Rician  $K$  factor.

### 1.1.6 Network Coding for Cooperative Multiplexing in Relay Channels

In this part, we investigate the diversity-multiplexing tradeoff for the cooperative network coding protocol which integrates the concept of decode-and-forward (DF) relay transmission of cooperative communications with the information mixing of network coding in relay channels. The proposed CNC protocol is suitable for two users which can transmit information to each other. We give a theorem to show our outage probability analytical result with proof and DMT comparison for our CNC protocol with upper bound, selection decode-and-forward (SDF), and DF. We find that the CNC protocol improves both diversity and multiplexing gain compared with the DF protocol.

## 1.2 Dissertation Outline

This dissertation consists of three themes. The first part is to investigate the performance issue and STF codes design for MIMO-UWB systems. The second part aims to investigate the two-ring channel model with a LOS component of MIMO Rician channels in mobile-to-mobile ad hoc networks. We analyze the ACF, LCR, AFD, and capacity of the proposed channel model. The third part contains a cooperative network coding protocol and the analysis of its outage probability and DMT.

The remaining chapters of this dissertation are organized as follows. Chapter 2 reviews some pivotal subjects for UWB, e.g., the IEEE 802.15.3a and 802.15.4a channel models. Then we introduce the Gauss-Hermite formula. Literature surveys of some related works are also provided. In Chapter 3, we analyze the BER performance in the IEEE 802.15.3a and 802.15.4a



UWB channel models with Rake receiver and shadowing effect. In Chapter 4, we present an analytical expression for the SNR of the PPM signal in an UWB channel with multiple transmit and receive antennas. In Chapter 5, we turn to design a BER-minimized STF codes for MIMO highly frequency-selective block-fading channels. In Chapter 6, we derive the ACF, LCR, and AFD of the mobile-to-mobile Rician fading channel and verify the accuracy by simulations. Then, in Chapter 7, we suggest a sum-of-sinusoids MIMO mobile-to-mobile channel simulation method, which can characterize the spatial/temporal channel correlation and Rician fading effect. We examine how often the MIMO capacity experiences the fades and relate this to the Rician factor. In Chapter 8, we consider a relay channel and DF cooperative communications system combined with the network coding. We derive the outage probability and DMT for the proposed CNC protocol. At last, Chapter 9 provides the concluding remarks and some suggestions for future works.



# Chapter 2

## Background and Literature Survey



In this chapter, we survey related works to the performance analysis and STF code design for MIMO-UWB systems, channel modeling and statistical analysis for MIMO Rician channels in mobile ad hoc networks, and the network coding for cooperative multiplexing. We also introduce the background for IEEE 802.15.3a and 802.15.4a UWB channel models. Then, we compare the two channel models. Finally, we review the Gauss-Hermite formula which is used for the BER analysis in IEEE 802.15.3a and 802.15.4a UWB channel models in our dissertation.

## 2.1 Literature Survey

### 2.1.1 Bit Error Rate Analysis in IEEE 802.15.3a and 802.15.4a UWB Channels

In the literature the current research related to the performance analysis of UWB systems can be categorized into two folds. Firstly, the UWB system has been investigated based on simpler channel models [29–32]. In [29], the authors derived the BER formula for the M-ary UWB signals under the AWGN channel and multiple access interference. In [30], the UWB systems was investigated in the presence of the interference from the wideband code division multiple access (WCDMA). [31] derived the BER performance of the UWB system under dispersive Rayleigh fading channels with timing jitter. In [32] a moment-generating function (MGF) approach was proposed to analyze the performance of a transmit-reference (TR) UWB system under a slowly fading channel.

Secondly, [7, 33–37] investigated the performance of UWB systems based on more sophisticated UWB channels, such as the IEEE 802.15.3a model. It is challenging to derive the distribution of the collected signal energy in the IEEE 802.15.3a channel model because the numbers of clusters and rays are random. In [7], the authors applied the techniques of counting integrals and shot noise to derive the computation BER formula in the IEEE 802.15.3a channel assuming the received waveform can be observed over a finite-length window. In [33], the output SNR statistics at the RAKE receiver in the IEEE 802.15.3a channel was presented, but the explicit BER formula for RAKE receivers taking account of shadowing was not presented. [34] analyzed the pairwise error probability (PEP) and outage probability of multiband orthogonal frequency-division multiplexing (OFDM) systems in the IEEE 802.15.3a

channel model, but ignore the effect of the lognormal shadowing. [35] analyzed the effect of multiple antennas on the UWB system under a generalized UWB channel. In [36], the error performance of a multi-antenna RAKE receiver was analyzed over the frequency-selective UWB lognormal fading channels. [37] analyzed the signal-to-interference-plus-noise ratio (SINR) of direct sequence (DS) UWB systems in generalized Saleh–Valenzuela channels based on the theory of renewal process.

### 2.1.2 On the Performance of Using Multiple Transmit and Receive Antennas in Pulse-Based Ultrawide-band Systems

In general, the UWB system can be classified into three kinds: the first one is the multiband orthogonal frequency division multiplexing approach, the second kind is the time hopping ultra-wideband (TH-UWB) system, and the third kind is the DS-UWB [38]. In this part, we focus on the TH-UWB system with pulse position modulation (PPM). Through modulating an information bit over extremely large bandwidth of several gigahertz, the TH-UWB system can possess many nice properties, including: high path resolution in the dense multipath fading environment [39–41], smooth noise-like frequency-domain characteristics [39]; carrierless transmission [40] and low transmission power operation [10, 39, 40].

Besides UWB, space-time processing transmit diversity techniques, such as space-time block codes (STBC) or space-time trellis codes (STTC), is another important research area recently [42–45]. It is noteworthy that these space-time processing transmit diversity schemes are originally designed for signals with information bits modulated by the amplitude or phase of a signal,

rather than the occurrence time of a signal. Since a PPM signal represents its data information bit according to the pulse displacement from a specified time reference. Thus, directly applying STTC or STBC in the PPM based UWB system may not be easy, especially in a highly dense frequency selective fading channel [46].

In spite of numerous advantages for the UWB system, it is crucial to make the best use of the radiation power because of its extremely low transmitted power. Consequently, although fading may not be serious in the pulsed mode UWB system, receive antenna diversity is suggested for the UWB system to improve energy capture [18, 47]. In the literature, fewer papers have been reported to address the issue of employing transmit diversity for the pulsed-UWB system, except [48] and [49]. In [48], the authors evaluated the performance of the pulse-amplitude modulation (PAM) signals in the UWB MIMO channel. In [49], the authors proposed a space-time block code scheme for the PPM based UWB system in the flat fading real channel, where the received pulses through the radio channel are assumed to be orthogonal with each other.

### **2.1.3 BER-Minimized Space-Time-Frequency Codes for MIMO Highly Frequency-Selective Block-Fading Channels**

Here, we introduce some related works about space-time-frequency codes (STFC) for the MIMO-OFDM systems. In [50], the authors investigated STFC for MIMO-OFDM and found an equivalence between antennas and subcarriers. The authors then suggested a complexity-reduced scheme with coding across subcarriers only. In [51], the authors proposed an adaptive

STFC scheme according to the space-frequency water-filling procedure for MIMO-OFDM systems. In [52], the authors considered STFC over MIMO-OFDM block-fading channels and derived a sphere packing lower bound on the average word error probability and an upper bound for pairwise word error probability, but they did not show how to design the optimal codes to achieve these bounds. In [1], authors proposed a systematic design method for high-rate full-diversity STF codes for broadband MIMO block-fading channels. In [2], authors presented rate-two STF block codes for multiband UWB-MIMO communication systems using rotated multidimensional modulation. We will show by simulation that our proposed STF codes have better BER performance than the codes in [1] and [2] do.

#### **2.1.4 Statistical Analysis of A Mobile-to-Mobile Rayleigh Fading Channel Model**

In the literature, most channel models for wireless communications were mainly developed for the conventional base-to-mobile cellular radio systems [23, 53–55]. Whether these mobile-to-base channel models are applicable to the mobile-to-mobile communication systems remains unclear. Some, but not many, channel models had been previously studied. In [56], the theoretical performance of the mobile-to-mobile channel was developed. The authors in [57] introduced the discrete line spectrum method for modeling the mobile-to-mobile channel. However, the accuracy of this method was assured only for short-duration waveforms as discussed in [58]. A simple but accurate sum-of-sinusoids method was proposed for modeling the mobile-to-mobile Rayleigh fading channel in [58]. The inverse fast Fourier transform (IFFT)-based mobile-to-mobile channel model was also proposed in [59]. Although most accurate compared with the discrete line spectrum and the

sum-of-sinusoids methods, the IFFT-based method requires a complex elliptic integration. In [60], the authors presented an analysis of measured radio channel statistics and their possible influence on the system performances in outdoor-to-indoor mobile-to-mobile communication channels. However, in [20, 56–60], the effects of the line-of-sight (LOS) are all ignored.

To evaluate the performance of the physical layer, a simple channel simulator, such as Jake’s method in conventional cellular systems, is necessary. Related works on the mobile-to-mobile Rician fading channel include the following. In [21], a statistical model for a mobile-to-mobile Rician fading channel with Doppler shifts is presented. In [22], the model in [21] is employed to obtain the probability density function (PDF) of the received signal envelope, the time-correlation function and radio frequency (RF) spectrum of the received signal, LCR, and AFD.

### **2.1.5 Modeling and Capacity Fades Analysis of MIMO Rician Channels in Mobile Ad Hoc Networks**

In the literatures, some MIMO channel models have been reported. In [61], the authors described the capacity behavior of outdoor MIMO channels as a function of scattering radii, antenna beamwidths, antenna spacing, and the distance between the transmit and receive arrays. We only consider the antenna spacing for simplicity, but we consider Rician fading, LCR, AFD, and the impact of the number of scatterers. In [62], the author derived a general model for the MIMO wireless channel which considered the interdependency of directions-of-arrival and directions-of-departure, angle dispersion by far clusters, and rank reduction of the transfer function matrix. This MIMO wireless channel model based on several physical phenomena such as scattering by far clusters, diffraction, waveguiding effects, and the interde-

pendency of the directions-of-arrival and the directions-of-departure. Our proposed MIMO channel is an extension of Jake’s model, which can help channel simulation by only considering the channel correlation in both the spatial and time domain. In [63], the authors derived the MIMO capacity, LCR, and AFD considering the impact of spatial/temporal channel correlation. However, the model in [63] considered the one-ring model which is more suitable for the mobile to base station scenario. In this chapter, the two-ring scattering model is adopted to capture the channel characteristics of the mobile-to-mobile communication. Further, we consider the impact of the Rician  $K$  factor and the number of scatterers on the total channel capacity, both of which are not considered in [63]. In [64], the authors proposed a single-bounce two-ring statistical model for the time-varying MIMO flat Rayleigh fading channels and derived the spatial-temporal correlations, LCR, AFD, and the instantaneous mutual information (IMI). However, they did not consider the impact of Rician  $K$  factor, number of scatterers, and the antenna separation. In [65], the authors investigated the effects of fading correlations in MIMO systems using the one-ring model. We consider the general two-ring model and derive the LCR, AFD, and an upper bound for the average channel capacity. In [66], the author presented the narrowband one-ring and two-ring models but did not consider the LOS component. In our channel model, we include the LOS component and consider the impact of Rician  $K$  factor on channel capacity, LCR, and AFD.

### 2.1.6 Network Coding for Cooperative Multiplexing

Many cooperative communication protocols were proposed to improve diversity gain, such as orthogonal amplify and forward (OAF) [67], nonorthogonal amplify and forward (NAF) [68], space-time coded (STC) cooperative



diversity protocols [69–71], dynamic decode-and-forward (DDF) [68], enhanced static decode-and-forward (ESDF), and enhanced dynamic decode-and-forward (EDDF) [72]. However, how to provide multiplexing gain by taking advantage of relays has not received much attention so far. Combining the network coding with the cooperative communications, or called the cooperative network coding (CNC) [73–84], have a potential to exploit the multiplexing gain in many relay nodes (virtual antennas). The diversity-multiplexing tradeoff (DMT) analysis of CNC has not been seen in the literature.

## 2.2 Background

### 2.2.1 IEEE 802.15.3a UWB Channel Model

We first discuss the key attributes of the IEEE 802.15.3a UWB channel [3]. The impulse response in this UWB channel is expressed as

$$h(t) = X \sum_{l=0}^{N_c-1} \sum_{k=0}^{N_r-1} \alpha_{k,l} \delta(t - T_l - \tau_{k,l}) , \quad (2.1)$$

where  $X$  represents the lognormal shadowing (or  $20 \log X$  is normally distributed),  $\{\alpha_{k,l}\}$  are the multipath gain coefficients,  $T_l$  is the arrival time of the  $l$ -th cluster,  $\tau_{k,l}$  is the arrival time of the  $k$ -th multipath component relative to the  $l$ -th cluster arrival time ( $T_l$ ). Note that the number of clusters  $N_c$  and the number of rays in a cluster  $N_r$  are both random variables. By definition, we set  $\tau_{0,l} = 0$ .

The cluster inter-arrival time and the ray inter-arrival time are characterized by exponentially distributed random variables. That is, given the  $(l-1)$ -th cluster's arrival time  $T_{l-1}$ , the PDF of the  $l$ -th cluster's arrival

time  $T_l$  is expressed as

$$p(T_l|T_{l-1}) = \begin{cases} \Lambda \exp[-\Lambda(T_l - T_{l-1})], & T_l > T_{l-1}, \\ 0, & \text{otherwise,} \end{cases} \quad (2.2)$$

where  $\Lambda$  is the cluster arrival rate and  $l \geq 1$ . Similarly, given the ray arrival rate  $\lambda$  and the arrival time of the  $(k-1)$ -th ray in the  $l$ -th cluster  $\tau_{(k-1),l}$ , the PDF of the arrival time of the  $k$ -th ray in the  $l$ -th cluster  $\tau_{k,l}$  is

$$p(\tau_{k,l}|\tau_{(k-1),l}) = \begin{cases} \lambda \exp[-\lambda(\tau_{k,l} - \tau_{(k-1),l})], & \tau_{k,l} > \tau_{(k-1),l}, \quad k \geq 1, \\ 0, & \text{otherwise.} \end{cases} \quad (2.3)$$

Note that  $T_0 = 0$  for the LOS channel, whereas  $T_0$  for an exponential random variable for the non-line-of-sight (NLOS) channel. That is,

$$p(T_0) = \begin{cases} \Lambda \exp(-\Lambda T_0), & T_0 > 0, \\ 0, & \text{otherwise.} \end{cases} \quad (2.4)$$

The channel coefficients  $\alpha_{k,l}$  are defined as follows:

$$\alpha_{k,l} = p_{k,l} \xi_l \beta_{k,l}, \quad (2.5)$$

where  $p_{k,l}$  is equiprobable  $\pm 1$  to account for signal inversion due to reflections,  $\xi_l$  reflects the fading associated with the  $l$ -th cluster, and  $\beta_{k,l}$  corresponds to the fading associated with the  $k$ -th ray of the  $l$ -th cluster. The total energy contained in the terms  $\{\alpha_{k,l}\}$  is normalized to unity in each realization. The distribution of  $\xi_l \beta_{k,l}$  is expressed as

$$20 \log(\xi_l \beta_{k,l}) \propto \text{Normal}(\mu_{k,l}, \sigma_1^2 + \sigma_2^2), \quad (2.6)$$

or equivalently

$$|\xi_l \beta_{k,l}| = 10^{(\mu_{k,l} + n_1 + n_2)/20}, \quad (2.7)$$

where the two independent normal random variables  $n_1$  and  $n_2$  with variance of  $\sigma_1^2$  and  $\sigma_2^2$  represent the fading on each cluster and ray in the dB domain, respectively. Note that

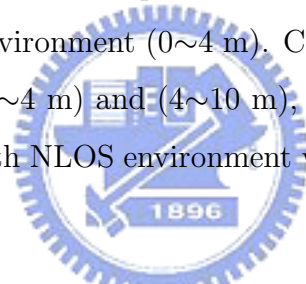
$$\mu_{k,l} = \frac{10 \ln(\Omega_0) - 10T_l/\Gamma - 10\tau_{k,l}/\gamma}{\ln(10)} - \frac{(\sigma_1^2 + \sigma_2^2) \ln(10)}{20} \quad (2.8)$$

and

$$\mathbb{E}[|\xi_l \beta_{k,l}|^2] = \Omega_0 e^{-T_l/\Gamma} e^{-\tau_{k,l}/\gamma}, \quad (2.9)$$

where  $\Omega_0$  is the mean energy in the first path of the first cluster,  $\Gamma$  is the cluster decay factor, and  $\gamma$  is the ray decay factor.

The four sets of channel parameters (CM1~4) in the IEEE 802.15.3a standardized channel model are specified for different environments. CM 1 is suitable for a LOS environment (0~4 m). CM 2 and CM 3 are suitable for NLOS environments (0~4 m) and (4~10 m), respectively. CM 4 is suitable for an extreme multipath NLOS environment with 25 nsec rms delay spread.



## 2.2.2 Mathematical Background for the IEEE 802.15.4a Channel Model

The IEEE 802.15.4a channel model can be viewed as a joint random process associated with time-of-arrivals and multipath amplitudes. First, the time-domain random variables contain the arrival time of clusters and rays, i.e.,  $\{T_l\}$  and  $\{\tau_{k,l}\}$ . Second, the amplitude-domain random variables contain the amplitudes  $a_{k,l}$  and phases  $\phi_{k,l}$  of the channel impulses where  $k$  and  $l$  are the indexes for the ray and cluster, respectively. Due to the infinite numbers of clusters and rays, analyzing the above UWB signal may also involve infinite-dimension integrations. To make this problem tractable, the channel impulse

response  $h(t)$  is represented as

$$h(t) = \sum_n G_n \delta(t - t_n), \quad (2.10)$$

where  $G_n$  is the gain of the  $n$ -th multipath component and  $t_n$  is the arrival time of the  $n$ -th multipath component, regardless of whether it is a cluster or a ray. Note that  $\{t_n\}$  is arranged to be a nondecreasing sequence. Define  $\Phi$  as the sum of the squared path gains arriving in the time window  $[a, b]$ , and the indicator function  $I_{[a,b]}(t_n)$  as

$$I_{[a,b]}(t_n) = \begin{cases} 1, & \text{if } t_n \in [a, b], \\ 0, & \text{if } t_n \notin [a, b]. \end{cases} \quad (2.11)$$

Then, we can represent  $\Phi$  as

$$\Phi = \sum_n |G_n|^2 I_{[a,b]}(t_n). \quad (2.12)$$

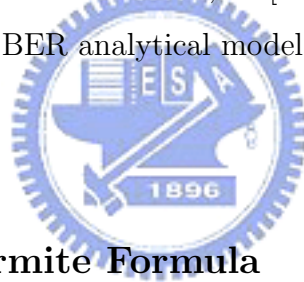
By applying the counting integral technique, the issue of analyzing a UWB signal with randomly arriving clusters and rays can be transformed from an infinite-dimension integration into a two-dimension integration. The counting integral is the Lebesgue integral based on the counting measure [85]. Specifically, we can express  $\Phi$  as

$$\Phi = \sum_n \varphi(t_n, G_n) = \int_0^\infty \int_0^\infty \varphi(s, g) N(ds \times dp), \quad (2.13)$$

where  $\varphi(s, g) = |g|^2 I_{[a,b]}(s) = p I_{[a,b]}(s)$  and  $N(ds \times dp)$  is the counting measure within a small interval  $ds$  and a small power interval  $dp$ . Integrating  $\varphi(s, g)$  over all the possible values of  $s \in [0, \infty)$  and  $p \in [0, \infty)$  is equivalent to summing up the value of the function  $\varphi(t_n, G_n)$  for all  $n$  as shown in (2.13). In the IEEE 802.15.3a channel, the characteristic function of  $\Phi$  was derived in [86]. Now in this part we derive the characteristic function of  $\Phi$  in the IEEE 802.15.4a channel and obtain the BER performance of the UWB system.

### 2.2.3 Comparisons Between the IEEE 802.15.3a and 802.15.4a Channel

Table 2.1 compares the IEEE 802.15.3a and 802.15.4a channel models. As shown in the table, these two channel models are different in amplitude fading, number of clusters, ray inter-arrival time, ray decay factor, and power delay profile. Furthermore, the IEEE 802.15.4a model specifies the path loss model which depends on distance and frequency, but the path loss model of the IEEE 802.15.3a model only depends on distance. Recently, the statistical property of the IEEE 802.15.4a UWB channel is reported in [87]. However, the BER computable formula for the IEEE 802.15.4a UWB channel is still unavailable. Thus, although having developed a BER analytical method for the IEEE 802.15.3a channel model, in [88], we feel that it is still quite important to develop a BER analytical model for the IEEE 802.15.4a UWB channel.



### 2.2.4 Gauss-Hermite Formula

We briefly introduce the Gauss-Hermite formula [89, 90], which will be used later in the BER analysis of the IEEE 802.15.3a UWB channel. The Gauss-Hermite formula can effectively calculate the improper integration of a function  $f(x)$  by a weighted sum as follows:

$$\int_{-\infty}^{\infty} f(x) dx = \sum_{k=1}^{N^{(H)}} w_k^{(H)} \left[ e^{(x_k^{(H)})^2} f(x_k^{(H)}) \right] + R_{N^{(H)}}(\xi), \quad (2.14)$$

where  $x_k^{(H)}$  is the  $k$ -th root of the Hermite polynomial  $H_{N^{(H)}}(x)$ . The Hermite polynomial  $H_{N^{(H)}}(x)$  satisfies the differential equation  $y'' - 2xy' + 2N^{(H)}y = 0$ .

Table 2.1: Comparison between the IEEE 802.15.3a and 802.15.4a channel models.

Properties	3a	4a
Amplitude fading	Lognormal	Nakagami- $m$ , $m$ : lognormal
Number of Clusters	Infinity	Poisson RV
Cluster interarrival time	Exponential RV	Exponential RV
Number of Rays	Infinity	Infinity
Ray interarrival time	Exponential RV	Hyperexponential RV
Cluster decay factor	Constant	Constant
Ray decay factor	Constant	Depends on ray arrival time
PDP	Exponential	Exponential and rise exponential
Pathloss	Distance dependent	Distance and frequency dependent

The weight  $w_k^{(H)}$  corresponding to the root  $x_k^{(H)}$  is given by

$$w_k^{(H)} = \frac{2^{N^{(H)}-1} N^{(H)}! \sqrt{\pi}}{(N^{(H)})^2 \left[ H_{N^{(H)}-1}(x_k^{(H)}) \right]^2}. \quad (2.15)$$

The remaining term  $R_{N^{(H)}}(\xi)$  is equal to

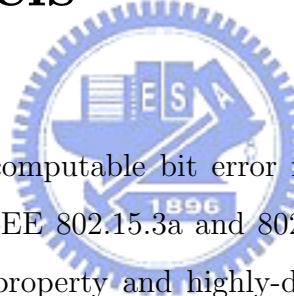
$$R_{N^{(H)}}(\xi) = \frac{N^{(H)}! \sqrt{\pi}}{2^{N^{(H)}} (2N^{(H)})!} f^{(2N^{(H)})}(\xi), \quad (2.16)$$

where  $\xi$  is an unknown real number. The values of  $x_k^{(H)}$  and  $w_k^{(H)}$  of the Gauss-Hermite formula with  $N^{(H)} = 20$  are already pre-calculated in [89]. Consequently, an improper integration of a function  $f(x)$  can be accurately approximated by a simple summation.



# Chapter 3

## Bit Error Rate Analysis in IEEE 802.15.3a and 802.15.4a UWB Channels



In this chapter, we present a computable bit error rate (BER) expression for the binary signals in the IEEE 802.15.3a and 802.15.4a ultra-wideband (UWB) channel. The cluster property and highly-dense multipath effects make performance analysis in such a UWB channel challenging but interesting. Mathematically, the IEEE 802.15.3a UWB signal is characterized by a joint two-dimension lognormal and doubly stochastic Poisson random signal. The lognormal random variable models the fading as well as shadowing amplitude, while Poisson random variable models the clustering effects. BER analysis under the IEEE 802.15.4a UWB channel model is also challenging because both the numbers and the arrival time of rays and clusters are random, and the signal fading amplitude is a joint lognormal-Nakagami random variable. In the literature, the performances of UWB systems in the IEEE 802.15.3a and 802.15.4a channels are either evaluated by simulations



or analyzed only with incomplete factors. In particular, the impacts of the RAKE receiver's finger numbers and lognormal shadowing on the BER performance have not been reported yet. Simulation results demonstrate that the presented BER computation formula can accurately estimate the complete effects of the cluster and ray arrival processes, the lognormal fading as well as shadowing, and the finger numbers at RAKE receivers.

### 3.1 Motivation

Ultra-wideband (UWB) is a promising wireless communications technique for high data rate transmission. The UWB channel characteristics are very different from conventional narrowband channels. Recently, the IEEE 802.15.3a [3] and 802.15.4a [4] UWB channel model are specified and widely adopted in the industry. However, UWB systems based on the IEEE 802.15.3a and 802.15.4a model are only evaluated by simulations or by analysis with simplified conditions. Thus, it motivates us to do the complete BER analysis in IEEE 802.15.3a and 802.15.4a channels.

## 3.2 BER Analysis in IEEE 802.15.3a Channel

### 3.2.1 Problem Formulation

For a coherent RAKE receiver with  $L$  fingers, the received SNR  $\gamma_b$  is

$$\gamma_b = \frac{E_b}{N_0} \sum_{m=1}^L a_m^2, \quad (3.1)$$

where  $E_b/N_0$  is the bit SNR and  $a_m$  is the channel amplitude at the  $m$ -th finger of the RAKE receiver normalized to the total energy. Based on the IEEE 802.15.3a channel model,  $a_m$  is the sum of lognormal fading  $\alpha_{k,l}$  and

shadowing amplitudes  $X$  of rays in many clusters which arrive in the duration of the  $m$ -th finger. That is,

$$a_m = X \cdot \sum_{(k,l):(m-1)T_c \leq T_l + \tau_{k,l} < mT_c} \alpha_{k,l} , \quad (3.2)$$

where  $T_c$  is the chip duration between two fingers. Define  $\mathcal{E} \triangleq \sum_{m=1}^L a_m^2$  as the normalized received energy in the UWB channel. From (3.2), it follows that

$$\mathcal{E} = X^2 \cdot \sum_{m=1}^L \left( \sum_{(k,l):(m-1)T_c \leq T_l + \tau_{k,l} < mT_c} \alpha_{k,l} \right)^2 . \quad (3.3)$$

From [91] we know that the error probability of binary signals with the coherent RAKE receiver is

$$P_2(\gamma_b) = Q \left( \sqrt{\gamma_b(1 - \rho_r)} \right) , \quad (3.4)$$

where  $\rho_r = -1$  and  $\rho_r = 0$  for antipodal signals and orthogonal signals, respectively.

Substituting (3.1), (3.2), and (3.3) into (3.4), we can express the BER of the RAKE receiver with  $L$  fingers as follows:

$$\begin{aligned} P_2 &= \mathbb{E}_{\mathcal{E}} \left[ Q \left( \sqrt{(1 - \rho_r) \frac{E_b}{N_0} \mathcal{E}} \right) \right] \\ &= \int_0^{\infty} Q \left( \sqrt{(1 - \rho_r) \frac{E_b}{N_0} x} \right) f_{\mathcal{E}}(x) dx, \end{aligned} \quad (3.5)$$

where  $f_{\mathcal{E}}(x)$  is the PDF of the received energy  $\mathcal{E}$ . The next step is to find the  $f_{\mathcal{E}}(x)$  in the IEEE 802.15.3a UWB channel.

### 3.2.2 PDF of the Received Energy

In this subsection, we discuss two methods to obtain  $f_{\mathcal{E}}(x)$ . The first method is to derive the exact form of  $f_{\mathcal{E}}(x)$ . However, the derived expression may be

too complicated to be implemented. In the second method, we suggest an approximation technique for  $f_{\mathcal{E}}(x)$ , which can facilitate the derivation of a computable BER formula taking account of all the UWB channel effects of the IEEE 802.15.3a model and the number of fingers of the RAKE receiver ( $L$ ).

### Method 1

Let  $A_m$  be the sum of fading amplitudes of rays in many clusters arriving in the duration of the  $m$ -th finger:

$$\begin{aligned} A_m &= \sum_{(k,l):(m-1)T_c \leq T_l + \tau_{k,l} < mT_c} \alpha_{k,l} \\ &= \alpha_{0,0} + \Phi_{r0} + \Phi_{\otimes} , \end{aligned} \quad (3.6)$$

where  $\alpha_{0,0}$  is the amplitude of the first ray in the first cluster,  $\Phi_{r0}$  and  $\Phi_{\otimes}$  are the sum of the amplitudes of the rays in the first cluster excluding  $\alpha_{0,0}$ , and that in the remaining clusters, respectively. Note that  $\alpha_{0,0}$ ,  $\Phi_{r0}$ , and  $\Phi_{\otimes}$  are statistically independent. Thus, the characteristic function of  $A_m$  is equal to

$$\Psi_{A_m}(\nu) = \begin{cases} \mathcal{L}_{0,0}(\nu)R_m(\nu)S_m(\nu), & \text{for } m = 1, \\ R_m(\nu)S_m(\nu), & \text{for } m = 2, \dots, L, \end{cases} \quad (3.7)$$

where  $\mathcal{L}_{0,0}(\nu)$ ,  $R_m(\nu)$ , and  $S_m(\nu)$  are the characteristic functions of  $\alpha_{0,0}$ ,  $\Phi_{r0}$ , and  $\Phi_{\otimes}$ , respectively. Modifying (12) and (16) in Theorem 1 of [86] by setting  $a = (m-1)T_c$  and  $b = mT_c$  to be the left and right boundaries of the time window, respectively, we can obtain  $R_m(\nu)$ ,  $S_m(\nu)$ , and  $\Psi_{A_m}(\nu)$  for (3.7).

Let  $B = \sum_{m=1}^L A_m^2$ . Thus, (3.3) becomes  $\mathcal{E} = X^2 \cdot B$ . Denote  $f_B(x)$  and  $f_{X^2}(x)$  as the PDFs of  $B$  and the squared lognormal shadowing random variable  $X^2$ , respectively. The PDF of  $\mathcal{E}$  can be shown in Appendix A as

$$f_{\mathcal{E}}(z) = \int_{-\infty}^{\infty} \frac{1}{|y|} f_{X^2}\left(\frac{z}{y}\right) f_B(y) dy, \quad (3.8)$$

where

$$f_{X^2}(x) = \begin{cases} \frac{5\sqrt{\frac{2}{\pi}} \exp\left[-50\left(\frac{\log_{10} x}{\sigma_x}\right)^2\right]}{x\sigma_x \ln 10}, & x > 0, \\ 0, & x \leq 0, \end{cases} \quad (3.9)$$

and

$$f_B(x) = \frac{1}{(2\pi)^{L+1}} \int_{-\infty}^{\infty} e^{-j\nu x} \prod_{m=1}^L \left[ \int_{-\infty}^{\infty} \frac{e^{j\nu y}}{\sqrt{y}} \int_{-\infty}^{\infty} \Psi_{A_m}(u) \cos(u\sqrt{y}) du dy \right] d\nu. \quad (3.10)$$

Note  $\Psi_{A_m}(\cdot)$  in (3.10) requires multiple-dimension integrals. Specifically, computing  $P_2$  of (3.5) based on (3.8) requires  $(6L + 4)$ -dimension integrals if method 1 is adopted. Note that  $A_1, A_2, \dots, A_L$  are not independent. (3.10) is obtained under the assumption that  $A_1, A_2, \dots, A_L$  are independent. Even if we make this assumption to simplify the derivation of  $f_B(x)$ , it still seems to be intractable to calculate  $f_B(x)$  via (3.8)–(3.10).

## Method 2

To ease the computation, we suggest a BER approximation method as follows. First, we conjecture that the characteristic function of the sum of squared *combined* signal amplitudes at each of  $L$  fingers is close to that of the sum of squared signal amplitudes at each *individual ray* within a time window  $[0, LT_c]$ . Because each cross term  $\alpha_{k,l}\alpha_{j,n}$  for  $k \neq j$  and  $l \neq n$  in (3.3) is equiprobably positive or negative due to  $p_{k,l}$  in (2.5), all the odd-order moments will vanish. In other words, given an odd number  $q$ , we have

$$\begin{aligned} & \mathbb{E}[(\alpha_{k,l}\alpha_{j,n})^q] \\ &= \frac{1}{4}(\xi_l\beta_{k,l})^q(\xi_n\beta_{j,n})^q + \frac{1}{4}(\xi_l\beta_{k,l})^q(-\xi_n\beta_{j,n})^q \\ & \quad + \frac{1}{4}(-\xi_l\beta_{k,l})^q(\xi_n\beta_{j,n})^q + \frac{1}{4}(-\xi_l\beta_{k,l})^q(-\xi_n\beta_{j,n})^q \\ &= 0. \end{aligned} \quad (3.11)$$

Define  $\tilde{\mathcal{E}}$  as the sum of squared path gains of the clusters and rays which arrive within the time window  $[0, LT_c]$ . Then  $\tilde{\mathcal{E}}$  can represent the signal energy collected by the  $L$  fingers of the RAKE receiver. That is,

$$\begin{aligned}\tilde{\mathcal{E}} &= X^2 \sum_{(k,l):0 \leq T_l + \tau_k, l \leq LT_c} \alpha_{k,l}^2 \\ &= X^2(\alpha_{0,0}^2 + \tilde{\Phi}_{r0} + \tilde{\Phi}_{\otimes}) ,\end{aligned}\quad (3.12)$$

where  $X$  is the lognormal shadowing random variable,  $\alpha_{0,0}$  is the amplitude of the first ray in the first cluster as defined in (2.5),  $\tilde{\Phi}_{r0}$  is the sum of *squared* path gains of the first cluster excluding  $\alpha_{0,0}^2$ ,  $\tilde{\Phi}_{\otimes}$  is the sum of *squared* path gains of rays in the remaining clusters. Note that  $X^2$ ,  $\alpha_{0,0}^2$ ,  $\tilde{\Phi}_{r0}$ , and  $\tilde{\Phi}_{\otimes}$  are statistically independent. Denote the received energy without shadowing by  $\tilde{\mathcal{E}}_{X0} \triangleq \alpha_{0,0}^2 + \tilde{\Phi}_{r0} + \tilde{\Phi}_{\otimes}$ . Similar to the reason obtaining (3.7), the characteristic function  $\Psi_{\tilde{\mathcal{E}}_{X0}}(\nu)$  of  $\tilde{\mathcal{E}}_{X0}$  in the IEEE 802.15.3a UWB channel can be written as

$$\Psi_{\tilde{\mathcal{E}}_{X0}}(\nu) = \tilde{\mathcal{L}}_{0,0}(\nu) \tilde{R}(\nu, L) \tilde{S}(\nu, L), \quad (3.13)$$

where  $\tilde{\mathcal{L}}_{T,t}(\nu)$ ,  $\tilde{R}(\nu, L)$ , and  $\tilde{S}(\nu, L)$  are the characteristic functions of  $\alpha_{T,t}^2$ ,  $\tilde{\Phi}_{r0}$ , and  $\tilde{\Phi}_{\otimes}$ , respectively. Compared with [86], we further consider the effects of  $X$ ,  $L$ , and  $T_c$ . The following theorem gives the computation formula of  $\tilde{\mathcal{L}}_{T,t}(\nu)$ .

**Theorem 1** *For the squared signal amplitude at a path arriving at time  $t$  in a cluster arriving at time  $T$  in the IEEE 802.15.3a UWB channel, its characteristic function  $\tilde{\mathcal{L}}_{T,t}(\nu)$  can be computed by*

$$\tilde{\mathcal{L}}_{T,t}(\nu) = \int_0^\infty e^{j\nu x} \frac{10 \exp\left[-\frac{1}{2\sigma^2} (10 \log_{10} x - \mu_{T,t})^2\right]}{\sqrt{2\pi\sigma x \ln 10}} dx \quad (3.14)$$

where

$$\mu_{T,t} = \frac{10}{\ln 10} \left[ \ln \Omega_0 - \frac{T}{\Gamma} - \frac{t-T}{\gamma} - \left(\frac{\ln 10}{10}\right)^2 \frac{\sigma^2}{2} \right]. \quad (3.15)$$

and

$$\sigma = \sqrt{\sigma_1^2 + \sigma_2^2}. \quad (3.16)$$

The parameters  $\Omega_0$ ,  $\Gamma$ , and  $\gamma$  are defined in (2.9).

*Proof:* See Appendix B.

**Theorem 2** For the RAKE receiver with  $L$  fingers, the function  $\tilde{R}(\nu, L)$  in (3.13) can be written as

$$\tilde{R}(\nu, L) = \exp[-\lambda\tilde{\psi}_\nu(0, L)] , \quad (3.17)$$

and function  $\tilde{\psi}_\nu(T, L)$  can be computed by

$$\tilde{\psi}_\nu(T, L) = \begin{cases} \int_T^{LT_c} [1 - \tilde{\mathcal{L}}_{T,t}(\nu)] dt, & T \leq LT_c , \\ 0, & T > LT_c . \end{cases} \quad (3.18)$$

Similarly,  $\tilde{S}(\nu, L)$  can be computed by

$$\tilde{S}(\nu, L) = \exp[-\Lambda\tilde{J}(\nu, L)] , \quad (3.19)$$

where

$$\tilde{J}(\nu, L) = \int_0^{LT_c} [1 - \tilde{\mathcal{L}}_{T,T}(\nu)e^{-\lambda\tilde{\psi}_\nu(T,L)}] dT. \quad (3.20)$$

*Proof:* See Appendix C.

Substituting (3.14) into (3.18) and (3.20), we can obtain  $\tilde{R}(\nu, L)$  and  $\tilde{S}(\nu, L)$ , respectively. The characteristic function  $\Psi_{\tilde{\mathcal{E}}_{X_0}}(\nu)$  of the received energy  $\tilde{\mathcal{E}}_{X_0}$  without shadowing at the RAKE receiver with  $L$  fingers in the IEEE 802.15.3a channel model can be easily obtained by using (3.13). The PDF of  $\tilde{\mathcal{E}}_{X_0}$  can be computed as follows:

$$f_{\tilde{\mathcal{E}}_{X_0}}(x) = \frac{1}{2\pi} \int_{-\infty}^{\infty} \Psi_{\tilde{\mathcal{E}}_{X_0}}(\nu) e^{-jx\nu} d\nu. \quad (3.21)$$

Finally, with shadowing the PDF of  $\tilde{\mathcal{E}}$  can be computed as follows:

$$f_{\tilde{\mathcal{E}}}(x) = \int_{-\infty}^{\infty} \frac{1}{|y|} f_{X^2} \left( \frac{x}{y} \right) f_{\tilde{\mathcal{E}}_{x_0}}(y) dy. \quad (3.22)$$

### 3.2.3 Computable Formula

We apply the Gauss-Hermite formula to calculate the characteristic function  $\tilde{\mathcal{L}}_{T,t}(\nu)$  of the squared signal amplitude at a path with cluster arrival time  $T$  and ray arrival time  $t$ . Let  $y = \frac{1}{\sqrt{2\sigma}}(10 \log_{10} x - \mu_{T,t})$  in (3.14). It follows that  $x = 10^{(\sqrt{2}\sigma y + \mu_{T,t})/10}$  and  $\frac{dy}{dx} = \frac{5\sqrt{2}}{(\ln 10)\sigma x}$ . Then, we can obtain the Hermite computation form for  $\tilde{\mathcal{L}}_{T,t}(\nu)$  as

$$\begin{aligned} \tilde{\mathcal{L}}_{T,t}(\nu) &= \frac{1}{\sqrt{\pi}} \int_{-\infty}^{\infty} e^{-y^2} e^{j\nu 10^{(\sqrt{2}\sigma y + \mu_{T,t})/10}} dy \\ &\approx \frac{1}{\sqrt{\pi}} \sum_{k=1}^{N^{(H)}} w_k^{(H)} e^{j\nu 10^{(\sqrt{2}\sigma x_k^{(H)} + \mu_{T,t})/10}} \\ &= \sum_{k=1}^{N^{(H)}} w_k^{(H)} e^{(x_k^{(H)})^2} f(x_k^{(H)}), \end{aligned} \quad (3.23)$$

where  $x_k^{(H)}$  is the  $k$ -th root of the Hermite polynomial of the  $N^{(H)}$ -th order, and  $w_k^{(H)}$  is the corresponding weight of the root  $x_k^{(H)}$  and

$$f(x) = \frac{1}{\sqrt{\pi}} \exp \left( j\nu 10^{(\sqrt{2}\sigma y + \mu_{T,t})/10} - y^2 \right). \quad (3.24)$$

The error due to using the Gauss-Hermite formula (denoted by  $\epsilon$ ) can be quantified by an upper bound

$$|\epsilon| \leq \max_{\xi \in \mathbb{R}} \left| \frac{N^{(H)}! \sqrt{\pi}}{2^{N^{(H)}} (2N^{(H)})!} f^{(2N^{(H)})}(\xi) \right|. \quad (3.25)$$

This upper bound is a function of  $\nu, T$  and  $t$ . It also depends on the type of the selected channel models and the number of points  $N^{(H)}$  used in the Gauss-Hermite formula. For CM1 with  $\nu = T = t = 0$  and  $N^{(H)} = 100$ , we

find that  $|\epsilon| \leq 1.56631 \times 10^{-17}$ . Equation (3.25) can be used to compute the error bound for different UWB channels with other values of  $\nu, T, t, N^{(H)}$ .

Next, we apply the Gauss-Legendre formula [89, 90] to obtain the characteristic functions  $\tilde{R}(\nu, L)$  and  $\tilde{S}(\nu, L)$ . Thus, the function  $\tilde{\psi}_\nu(T, L)$  in the exponent of  $\tilde{R}(\nu, L)$  can be computed by

$$\tilde{\psi}_\nu(T, L) \approx \begin{cases} \frac{LT_c - T}{2} \sum_{p=1}^{N^{(L)}} w_p^{(L)} \left[ 1 - \tilde{\mathcal{L}}_{T,t}(\nu) \right] \Big|_{t=\frac{LT_c - T}{2} x_p^{(L)} + \frac{LT_c + T}{2}} & T \leq LT_c, \\ 0 & T > LT_c, \end{cases} \quad (3.26)$$

where  $\{w_p^{(L)}\}$  and  $\{x_p^{(L)}\}$  are the weights and abscissas of the Gauss-Legendre formula, respectively;  $N^{(L)}$  is the number of points of the Gauss-Legendre integration. Similarly, the function  $\tilde{J}(\nu, L)$  in the exponent of  $\tilde{S}(\nu, L)$  can be computed by

$$\tilde{J}(\nu, L) \approx \frac{LT_c}{2} \sum_{i=1}^{N^{(L)}} w_i^{(L)} \left[ 1 - \tilde{\mathcal{L}}_{T,T}(\nu) e^{-\lambda \tilde{\psi}_\nu(T, L)} \right] \Big|_{T=\frac{LT_c}{2} x_i^{(L)} + \frac{LT_c}{2}}. \quad (3.27)$$

Combining (3.22), (3.23), (3.26), and (3.27), the BER of the RAKE re-



ceiver in the IEEE 802.15.3a UWB channel can be computed by

$$\begin{aligned}
\tilde{P}_2 &= \mathbb{E}_{\tilde{\mathcal{E}}} \left[ Q \left( \sqrt{(1 - \rho_r) \frac{E_b}{N_0}} \tilde{\mathcal{E}} \right) \right] \\
&= \int_0^\infty Q \left( \sqrt{(1 - \rho_r) \frac{E_b}{N_0}} x \right) f_{\tilde{\mathcal{E}}}(x) dx \\
&= \frac{1}{2\pi^{3/2}} \sum_{k=1}^{N^{(H)}} \sum_{l=1}^{N^{(H)}} \sum_{m=1}^{N^{(H)}} w_k^{(H)} w_l^{(H)} w_m^{(H)} \frac{1}{|y|} \exp \left( j\nu 10^{\frac{\sqrt{2}\sigma x_l^{(H)} + \mu_{0,0}}{10}} \right) \\
&\quad \exp \left( -\frac{1}{2} \lambda L T_c \sum_{p=1}^{N^{(L)}} w_p^{(L)} \left[ 1 - \tilde{\mathcal{L}}_{0,t}(\nu) \right] \Big|_{t=\frac{1}{2} L T_c (x_p^{(L)} + 1)} \right) \\
&\quad \exp \left( -\frac{1}{2} \lambda L T_c \sum_{i=1}^{N^{(L)}} w_i^{(L)} \left[ 1 - \tilde{\mathcal{L}}_{T,T}(\nu) e^{-\lambda \tilde{\psi}_\nu(T,L)} \right] \Big|_{T=\frac{1}{2} L T_c (x_i^{(L)} + 1)} - j\nu y + \nu^2 + y^2 \right) \\
&\quad \int_0^\infty Q \left( \sqrt{(1 - \rho_r) \frac{E_b}{N_0}} x \right) f_{X^2} \left( \frac{x}{y} \right) dx \Big|_{\nu=x_k^{(H)}, y=x_m^{(H)}}. \tag{3.28}
\end{aligned}$$

Importantly, one can see that (3.28) requires only two integrals in the last line including the integral for evaluating the  $Q$  function. Other integrals are replaced by the summations based on the Hermite and the Legendre polynomial methods with the  $N^{(H)}$ -th and  $N^{(L)}$ -th orders.

### 3.2.4 Discussion

Comparing to [7], we further consider the effects of the RAKE receiver and shadowing into the BER formula. This extension is nontrivial because of the following two reasons. First, the calculation of the energy collected by the RAKE receiver is very complicated. The complexity is proportional to the number of fingers of the RAKE receiver. More specifically, we have to find the energy on each finger and find the total energy. It is much more difficult than just find the energy during a certain time window. We find an approximation method that can evaluate the BER with a very small error

as we will show in the numerical results. Second, adding shadowing involves an additional lognormal random variable in our problem. This implies we need one more integral in the  $\tilde{P}'_2$ . We have tried to use the Craig's formula as in [7] to include the shadowing term  $X$  into the BER formula as follows

$$\begin{aligned}\tilde{P}'_2 &= \mathbb{E} \left[ \frac{1}{2\pi} \int_{-1}^1 \frac{\exp[-\eta X^2 \Phi(0, LT_c)/2y^2]}{\sqrt{1-y^2}} dy \right] \\ &= \frac{1}{2\pi} \int_{-1}^1 \frac{\mathbb{E}[M_{\Phi(0, LT_c)}(-\eta X^2/2y^2)]}{\sqrt{1-y^2}} dy,\end{aligned}\quad (3.29)$$

where

$$\Phi(0, LT_c) = \sum_{(k,l): 0 \leq T_i + \tau_{k,l} \leq LT_c} \alpha_{k,l}^2 \quad (3.30)$$

and  $M_{\Phi(0, LT_c)}(\cdot)$  is the MGF of  $\Phi(0, LT_c)$ . However, as it will be shown in the next section, we find that the analytical BER obtained from (3.29) has a large error compared with simulation results. The reason is described as follows: The BER formula (3.29) can be rewritten as

$$\tilde{P}'_2 = \frac{1}{2\pi} \int_{-1}^1 \frac{\mathbb{E}[M_{X^2}(-\eta \Phi(0, LT_c)/2y^2)]}{\sqrt{1-y^2}} dy, \quad (3.31)$$

where  $M_{X^2}(\cdot)$  is the MGF of  $X^2$ , which is also a lognormal random variable. Since the MGF of a lognormal random variable is infinite [92], the expectation in (3.31) diverges and the value of  $\tilde{P}'_2$  in (3.31) can not be calculated accurately. Hence, we develop the characteristic function based BER formula with shadowing in the IEEE 802.15.3a model. Therefore, we believe that adding the shadowing effect into the BER calculation under the IEEE 802.15.3a UWB channel model is not a straightforward extension from the existing work.

### 3.3 BER Analysis in IEEE 802.15.4a Channel

#### 3.3.1 Receiver Structure

For a coherent  $L$ -finger RAKE receiver, the instantaneous received SNR is expressed as

$$\text{SNR} = \frac{E_b}{N_0} \sum_{i=1}^L |c_i|^2, \quad (3.32)$$

where  $E_b/N_0$  is the SNR per bit,  $c_i$  is the channel amplitude appearing at the  $i$ -th finger of the RAKE receiver. From [91], the conditional error probability of binary signals with a given SNR at the coherent RAKE receiver can be computed by

$$P_2(\text{SNR}) = Q\left(\sqrt{\text{SNR}(1 - \rho_r)}\right), \quad (3.33)$$

where  $\rho_r = -1$  and  $0$  for antipodal signals and orthogonal signals, respectively. To obtain SNR, we derive the characteristic function of the received energy  $\mathcal{E} \triangleq \sum_{i=1}^L |c_i|^2$ , where

$$c_i = \sum_{(k,l):(i-1)T_c \leq T_l + \tau_{k,l} < iT_c} a_{k,l} \exp(j\phi_{k,l}), \quad i = 1, \dots, L, \quad (3.34)$$

$$\mathcal{E} = \sum_{i=1}^L \left| \sum_{(k,l):(i-1)T_c \leq T_l + \tau_{k,l} < iT_c} a_{k,l} \exp(j\phi_{k,l}) \right|^2, \quad (3.35)$$

and  $T_c$  is the chip duration between two fingers.

#### 3.3.2 Characteristic Function of Received Energy

Similar to the case for the IEEE 802.15.3a channel model, the calculation of the characteristic function of  $\mathcal{E}$  in (3.35) requires many integrals and much computation time [93]. Thus, we turn to find the characteristic function of the sum of the squared path gain for the impulses arriving in the time interval

$[0, LT_c]$  (denoted by  $\tilde{\mathcal{E}}$ ), i.e.,

$$\tilde{\mathcal{E}} = \sum_{(k,l): 0 \leq T_l + \tau_{k,l} \leq LT_c} a_{k,l}^2, \quad (3.36)$$

where  $a_{k,l}$  is the amplitude of the  $k$ -th ray in the  $l$ -th cluster. Although  $\tilde{\mathcal{E}}$  is only an approximation of  $\mathcal{E}$ , it will be seen in Section 3.4 that the analytical BER based on  $\tilde{\mathcal{E}}$  is quite close to the simulated BER based on  $\mathcal{E}$ . Importantly, the calculation time for the characteristic function of  $\tilde{\mathcal{E}}$  is much shorter than that of  $\mathcal{E}$ .

Denote  $\Phi_{r0}$  as the sum of the squared amplitudes of the rays in the zeroth cluster excluding  $a_{0,0}^2$  in the time interval  $[0, LT_c]$ , i.e.,

$$\Phi_{r0} = \sum_{k>0, 0 \leq \tau_{k,0} \leq LT_c} a_{k,0}^2. \quad (3.37)$$

Also, let  $\Phi_{\otimes}$  be the sum of the squared amplitudes except for the first cluster, i.e.,

$$\Phi_{\otimes} = \sum_{l>0, 0 \leq \tau_{k,l} \leq LT_c} a_{k,l}^2. \quad (3.38)$$

Then we can express the approximated received energy  $\tilde{\mathcal{E}}$  as

$$\tilde{\mathcal{E}} = a_{0,0}^2 + \Phi_{r0} + \Phi_{\otimes}. \quad (3.39)$$

According to [86], the three random variables  $a_{0,0}$ ,  $\Phi_{r0}$ , and  $\Phi_{\otimes}$  are independent. Thus, characteristic function of  $\tilde{\mathcal{E}}$  in the IEEE 802.15.4a UWB channel can be computed by

$$\Psi(\nu) = \mathcal{L}_{0,0}(\nu)R(\nu, L)S(\nu, L), \quad (3.40)$$

where  $\mathcal{L}_{0,0}(\nu)$ ,  $R(\nu, L)$ , and  $S(\nu, L)$  are the characteristic functions of  $a_{0,0}^2$ ,  $\Phi_{r0}$ , and  $\Phi_{\otimes}$ , respectively.

In the following theorem, we present a formula to compute  $\mathcal{L}_{T,t}(\nu)$ , the characteristic function of the squared amplitude of the ray arriving at time

$t$  and belongs to the cluster which arrives at time  $T$  in the IEEE 802.15.4a channel model.

**Theorem 3** *The characteristic function  $\mathcal{L}_{T,t}(\nu)$  in the IEEE 802.15.4a channel model can be computed by*

$$\mathcal{L}_{T,t}(\nu) = (1 - j\nu\Omega/\widehat{m})^{-\widehat{m}}, \quad (3.41)$$

where  $\Omega$  is the mean-squared value of the signal amplitude

$$\Omega = \frac{1}{\gamma_l} \exp\left(-\frac{T}{\Gamma} - \frac{t-T}{\gamma_l}\right), \quad (3.42)$$

and  $\gamma_l$  has already been defined in [4, (20)].  $\widehat{m}$  in (3.41) is an approximation of the Nakagami- $m$  fading parameter  $m$ :

$$\widehat{m} = \exp\left(m_0 + \widehat{m}_0^2/2\right), \quad (3.43)$$

where  $m_0$  and  $\widehat{m}_0$  are given in (27) and (28) in [4], respectively.

*Proof:* It is quite straightforward since the square of a Nakagami- $m$  random variable is a Gamma random variable. The mean fading power  $\Omega$  and the  $m$  parameter are actually replaced by their means. These simplifications make the derivation tractable.

Second, to calculate the function  $R(\nu, L)$ , we derive the closed form expression for the ray arrival rate  $\lambda(\tau)$  in the IEEE 802.15.4a channel. According to the IEEE 802.15.4a channel model, the ray inter-arrival time is modeled by a hyper-exponential random variable with two different rates,  $\lambda_1$  and  $\lambda_2$ , as shown in [4, (18)]. The effective ray arrival rate  $\lambda$  of the whole time-of-arrival process can be computed by the following lemma.

**Lemma 1** *The effective ray arrival rate  $\lambda$  of the time-of-arrival process in the IEEE 802.15.4a channel model can be expressed as*

$$\lambda(\tau) = \begin{cases} \frac{\beta\lambda_1 e^{-\lambda_1\tau} + (1-\beta)\lambda_2 e^{-\lambda_2\tau}}{\beta e^{-\lambda_1\tau} + (1-\beta)e^{-\lambda_2\tau}}, & \tau \geq 0, \\ 0, & \tau < 0, \end{cases} \quad (3.44)$$

where  $\tau = t - T$  is the ray arrival time with respect to the cluster arrival time.

*Proof:* See Appendix D.

Now we give the formulas of the characteristic functions  $R(\nu, L)$  and  $S(\nu, L)$ .

**Theorem 4** *For the  $L$ -finger RAKE receiver in the IEEE 802.15.4a channel, the characteristic function  $R(\nu, L)$  of the sum of the squared amplitude of the rays in the first cluster except for  $a_{0,0}$  can be written as*

$$R(\nu, L) = \exp[-\psi_\nu(0, L)], \quad (3.45)$$

where the function  $\psi_\nu(T, L)$  is computed by

$$\psi_\nu(T, L) = \begin{cases} \int_T^{LT_c} [1 - \mathcal{L}_{T,t}(\nu)] \lambda(t - T) dt, & T \leq LT_c, \\ 0, & T > LT_c. \end{cases} \quad (3.46)$$

The characteristic function  $S(\nu, L)$  of the squared amplitude of the rays in the other clusters except for the first cluster can be written as

$$S(\nu, L) = \exp[-\Lambda J(\nu, L)], \quad (3.47)$$

where

$$J(\nu, L) = \int_0^{LT_c} [1 - \mathcal{L}_{T,T}(\nu) e^{-\psi_\nu(T, L)}] dT. \quad (3.48)$$

*Proof:* See Appendix E.

Substituting (3.41), (3.45), and (3.47) into (3.40), one can obtain the characteristic function of  $\tilde{\mathcal{E}}$  (denoted by  $\Psi(\nu)$ ). Next we suggest computing the PDF of  $\tilde{\mathcal{E}}$  by the Gauss-Hermite formula as follows:

$$\begin{aligned} f_{\tilde{\mathcal{E}}}(x) &= \frac{1}{2\pi} \int_{-\infty}^{\infty} \Psi(\nu) e^{-jx\nu} d\nu \\ &\approx \frac{1}{2\pi} \sum_{k=1}^{N^{(H)}} w_k^{(H)} \Psi(\nu) e^{-jx\nu} e^{\nu^2} \Big|_{\nu=x_k^{(H)}}. \end{aligned} \quad (3.49)$$

Combining (3.41), (3.49), and (16) and (17) in [88], the BER of the RAKE receiver in the IEEE 802.15.4a UWB channel can be computed as

$$\begin{aligned} P_2 &\approx \mathbb{E}_{\tilde{\mathcal{E}}} \left[ Q \left( \sqrt{(1-\rho_r) \frac{E_b}{N_0}} \tilde{\mathcal{E}} \right) \right] \\ &= \int_0^{\infty} Q \left( \sqrt{(1-\rho_r) \frac{E_b}{N_0}} x \right) f_{\tilde{\mathcal{E}}}(x) dx \\ &\approx \frac{1}{2\pi} \sum_{k=1}^{N^{(H)}} w_k^{(H)} \left( 1 - j \frac{\nu}{\gamma_0 \exp(m_0 + \hat{m}_0^2/2)} \right)^{-\exp(m_0 + \hat{m}_0^2/2)} \\ &\quad \exp \left( -\frac{1}{2} \lambda L T_c \sum_{p=1}^{N^{(L)}} w_p^{(L)} [1 - \mathcal{L}_{0,t}(\nu)] \Big|_{t=\frac{1}{2} L T_c (x_p^{(L)} + 1)} \right) \\ &\quad \exp \left( -\frac{1}{2} \Lambda L T_c \sum_{i=1}^{N^{(L)}} w_i^{(L)} [1 - \mathcal{L}_{T,T}(\nu) e^{-\lambda \tilde{\psi}_\nu(T,L)}] \Big|_{T=\frac{1}{2} L T_c (x_i^{(L)} + 1)} \right) \\ &\quad \int_0^{\infty} Q \left( \sqrt{(1-\rho_r) \frac{E_b}{N_0}} x \right) \exp(-jx\nu) dx \exp(\nu^2) \Big|_{\nu=x_k^{(H)}}. \end{aligned} \quad (3.50)$$

Note that  $P_2$  in (3.50) is an approximated BER formula.

### 3.3.3 Discussion

The above analytical method can be applied to a generalized UWB frequency selective fading channel with other fading distributions, PDP, as well as different cluster and ray inter-arrival processes. For a given PDP, we only need

to express it as a function of the cluster and ray arrival time  $T$  and  $t$ , and replace them in (3.42). For a given PDF of the fading amplitude, we can first find the PDF of the squared amplitude and use the Fourier transform to find  $\mathcal{L}_{T,t}(\nu)$ . For a given PDF of ray inter-arrival time, we can use the same method as in Appendix D to find the intensity function  $\lambda(\tau)$  referring to (3.40). Given the PDF of other types of cluster inter-arrival time, the associated intensity function  $\Lambda(T)$  can be obtained by the procedures shown in Lemma 1. Unlike  $J(\nu, L)$  in (3.48) where  $\Lambda$  is a fixed value, in a general case  $\Lambda(T)$  is a function of  $T$ . Thus,  $J(\nu, L)$  is redefined as

$$J(\nu, L) = \int_0^{LT_c} \Lambda(T) [1 - \mathcal{L}_{T,T}(\nu) e^{-\tilde{\psi}_\nu(T,L)}] dT . \quad (3.51)$$

Similarly, the characteristic function  $\Psi(\nu)$  of the received energy is rewritten as

$$\Psi(\nu) = \mathcal{L}_{0,0}(\nu) \exp[-\psi_\nu(0, L)] \exp[-J(\nu, L)] . \quad (3.52)$$

Note that  $\exp[-\psi_\nu(0, L)]$  is the same as  $R(\nu, L)$  in (3.45), but  $\exp[-J(\nu, L)]$  is slightly different from  $S(\nu, L)$  in (3.47).

### 3.3.4 The Shadowing Effect

The IEEE 802.15.4a group decided to not consider shadowing for the evaluation of the different proposals. The reason was that the shadowing would have drowned out more subtle effects of the delay dispersion, and it was anticipated that shadowing would affect all proposed transceiver structures in the same form anyway. Since the goal in the IEEE 802.15.4a group was only a relative comparison of the different proposals, shadowing was turned off. For any reasonable evaluations for absolute performance predictions, the shadowing has to be activated again.



In order to calculate the BER formula that takes the shadowing effect into consider, let us define the channel impulse response with shadowing as

$$h_X(t) = X \sum_n G_n \delta(t - t_n), \quad (3.53)$$

where  $X$  is a lognormal random variable which reflects the shadowing fading. As in the IEEE 802.15.3a channel model, the random variable  $X$  satisfies  $20 \log_{10} X \propto \text{Normal}(0, \sigma_x^2)$  and is independent of all the other random variables. Hence, the approximated received energy including the shadowing is

$$\tilde{\mathcal{E}}_X = X^2 \tilde{\mathcal{E}}. \quad (3.54)$$

The following theorem gives an approximation for the PDF of  $\tilde{\mathcal{E}}_X$ :



**Theorem 5** *The PDF of  $\tilde{\mathcal{E}}_X$ , which is the received energy including the shadowing effect, can be approximated as*

$$f_{\tilde{\mathcal{E}}_X}(x) \approx \frac{1}{2\pi\sqrt{\pi}} \sum_{k=1}^{N^{(H)}} w_k^{(H)} \Psi(x_k^{(H)}) e^{[x_k^{(H)}]^2} \sum_{l=1}^{N^{(H)}} w_l^{(H)} \exp\left(-jxx_k^{(H)} 10^{-\frac{\sigma_x x_l^{(H)}}{\sqrt{50}}}\right) 10^{-\frac{\sigma_x x_l^{(H)}}{\sqrt{50}}}. \quad (3.55)$$

*Proof:* See Appendix F.

Combining the results in Theorem 3 ~ 5, the BER of the RAKE receiver

in the IEEE 802.15.4a UWB channel with shadowing can be computed as

$$\begin{aligned}
P_{2X} &\approx \mathbb{E}_{\tilde{\mathcal{E}}_X} \left[ Q \left( \sqrt{(1 - \rho_r) \frac{E_b}{N_0} \tilde{\mathcal{E}}_X} \right) \right] \\
&= \int_0^\infty Q \left( \sqrt{(1 - \rho_r) \frac{E_b}{N_0} x} \right) f_{\tilde{\mathcal{E}}_X}(x) dx \\
&\approx \frac{1}{2\pi\sqrt{\pi}} \sum_{k=1}^{N^{(H)}} w_k^{(H)} e^{[x_k^{(H)}]^2} \left( 1 - j \frac{x_k^{(H)}}{\gamma_0 \exp(m_0 + \hat{m}_0^2/2)} \right)^{-\exp(m_0 + \hat{m}_0^2/2)} \\
&\quad \exp \left( -\frac{1}{2} \lambda L T_c \sum_{p=1}^{N^{(L)}} w_p^{(L)} \left[ 1 - \mathcal{L}_{0,t}(x_k^{(H)}) \right] \Big|_{t=\frac{1}{2} L T_c (x_p^{(L)} + 1)} \right) \\
&\quad \exp \left( -\frac{1}{2} \Lambda L T_c \sum_{i=1}^{N^{(L)}} w_i^{(L)} \left[ 1 - \mathcal{L}_{T,T}(x_k^{(H)}) e^{-\lambda \psi_{x_k^{(H)}}(T)} \right] \Big|_{T=\frac{1}{2} L T_c (x_i^{(L)} + 1)} \right) \\
&\quad \sum_{l=1}^{N^{(H)}} w_l^{(H)} 10^{-\frac{\sigma_x x_l^{(H)}}{\sqrt{50}}} \int_0^\infty Q \left( \sqrt{(1 - \rho_r) \frac{E_b}{N_0} x} \right) \exp \left( -j x x_k^{(H)} 10^{-\frac{\sigma_x x_l^{(H)}}{\sqrt{50}}} \right) dx. \tag{3.56}
\end{aligned}$$

## 3.4 Numerical Results

### 3.4.1 Simulation Method

In order to verify the derivation of the BER formula presented in the last section, we perform simulations based on MATLAB. For pulse position modulation (PPM) signals, the transmitted signal of the information bit 0 is

$$s_0(t) = \begin{cases} 1, & 0 \leq t < T_c, \\ 0, & \text{otherwise.} \end{cases} \tag{3.57}$$

Here we set  $T_c = 1$  nsec. When the information bit is 1, the signal waveform  $s_1(t) = s_0(t - \delta T_c)$  for a positive integer  $\delta$ . From the `uwb_sv_model_ct` function in [3], we can get the output vectors  $\mathbf{h}$  and  $\mathbf{t}$ . The vector  $\mathbf{t}$  stores the arrival time of every channel impulse response with increasing chronological order, while the vector  $\mathbf{h}$  stores the corresponding amplitudes.

Let  $\mathbf{p}_0$  be a template vector with size  $1 \times (L + \delta)$ , and  $\mathbf{p}_0[m]$  the  $m$ -th element of  $\mathbf{p}_0$ . Then, we can represent  $\mathbf{p}_0[m]$  as

$$\mathbf{p}_0[m] = \begin{cases} \sum_{n:(m-1)T_c \leq t[n] < mT_c} \mathbf{h}[n], & 1 \leq m \leq L, \\ 0, & L < m \leq L + \delta. \end{cases} \quad (3.58)$$

The physical meaning of vector  $\mathbf{p}_0$  is the received signal for the information bit 0 with the sampling rate  $1/T_c$ , excluding the noise. For the information bit 1, the template vector can be expressed as

$$\mathbf{p}_1 = [\mathbf{0}_{1 \times \delta}, \mathbf{p}_0[1], \dots, \mathbf{p}_0[L]]. \quad (3.59)$$

After adding noise  $\mathbf{n}$ , the sampled received signals for the information bits 0 and 1 are

$$\mathbf{r} = \mathbf{p}_0 + [\mathbf{n}, \mathbf{0}_{1 \times \delta}], \quad (3.60)$$

and

$$\mathbf{r} = \mathbf{p}_1 + [\mathbf{0}_{1 \times \delta}, \mathbf{n}], \quad (3.61)$$

respectively. Note that the noise vector  $\mathbf{n}$  contains  $L$  independent identically distributed normal random variables, each of which has zero mean and  $N_0/2$  variance.

When the coherent RAKE receiver is applied to detect the IEEE 802.15.3a UWB signal. Let the decision variable  $U_0 = \mathbf{r} \cdot \mathbf{p}_0$  and  $U_1 = \mathbf{r} \cdot \mathbf{p}_1$ , where the operator “ $\cdot$ ” is the inner product of two vectors. If  $U_0 \geq U_1$ , then the information bit is 0; otherwise, the information bit is 1.

For the IEEE 802.15.4a channel, we evaluate the effect of different UWB channel parameters, including the cluster arrival rate  $\Lambda$ , inter-cluster decay constant  $\Gamma$ , intra-cluster decay constant  $\gamma_0$ , ray arrival parameters ( $\lambda_1$ ,  $\lambda_2$ , and  $\beta$ ), and the mean of the Nakagami- $m$  factor ( $m_0$ ). The values of the parameters of the IEEE 802.15.4a channel model CM1 is listed in Table 3.1.

Table 3.1: The values of the parameters of the IEEE 802.15.4a channel model CM1.

cluster arrival rate	$\Lambda$ [1/ns]	0.047
inter-cluster decay constant	$\Gamma$ [ns]	22.61
intra-cluster decay constant	$\gamma_0$ [ns]	12.53
ray arrival parameter	$\lambda_1$ [1/ns]	1.54
ray arrival parameter	$\lambda_2$ [1/ns]	0.15
ray arrival parameter	$\beta$	0.095
mean of the Nakagami- $m$ factor	$m_0$ [dB]	0.67

### 3.4.2 Results for BER in IEEE 802.15.3a Channel

Figures 3.1(a) and 3.1(b) compare the simulative PDF/CDF and the analytical results according to (3.22) for the collected signal energy  $\mathcal{E}$  at a 10-finger RAKE receiver. We can see that the analytical and simulative PDF/CDF are close to each other. It is implied that our proposed random variable  $\tilde{\mathcal{E}}$  can approximate the random variable  $\mathcal{E}$  quite well.

Figure 3.2 shows the PDF  $f_{\tilde{\mathcal{E}}}(x)$  of a 10-finger RAKE receiver in the IEEE 802.15.3a CM1  $\sim$  CM4 channels according to (3.22). In the high energy range, CM1 has the most probability mass; CM2 ranks second; CM3 ranks third; and CM4 has the least probability mass. This phenomenon can explain why CM1 has the better BER performance than CM2, CM3, and CM4.

Figure 3.3 shows the shadowing effect with the standard deviation  $\sigma_x = 3$  and 6 dB on the BER performance of a 10-finger RAKE receiver in the IEEE 802.15.3a UWB channel CM3 based on (3.28). At BER = 0.02, the

required  $E_b/N_0$  for  $\sigma_x = 6$  dB is 3 dB higher than that for  $\sigma_x = 3$  dB. Hence, the shadowing effect in the IEEE 802.15.3a channel is quite significant and should not be ignored when evaluating the UWB system performance.

In Fig. 3.4, the proposed characteristic function based analytical BER formula (3.28) is verified by simulations. We consider a 10-finger RAKE receiver in the IEEE 802.15.3a channel models CM2~4, where shadowing standard deviation  $\sigma_x = 6$  dB, the modulation index of PPM  $\delta = 1$ , and  $T_c = 1$  nsec. As seen from the figure, the analytical results according to (3.28) match the simulation results quite well in general. However, there are discrepancies between the simulation and the analytical curves at some points. This is because the usage of Gauss-Hermite and Gauss-Legendre formulas may cause some integration errors. Nevertheless, it is generally true that using  $f_{\tilde{\mathcal{E}}}(x)$  can save a lot of calculation time compared with using  $f_{\mathcal{E}}(x)$ , and provide very good approximation to the simulative BER in the IEEE 802.15.3a UWB channel.

In Fig. 3.5, the MGF-based analytical BER formula (3.29) is examined by simulations for a 10-finger RAKE receiver in the IEEE 802.15.3a CM2~4 channels with shadowing standard deviation  $\sigma_x = 6$  dB. Surprisingly, one can see large errors between the analytical and simulation BER curves. Thus, the MGF-based BER formula (3.29) and the Craig's formula may not be adequate for BER analysis in the IEEE 802.15.3a UWB channel when shadowing is included.

Figure 3.6 shows the PDF  $f_{\tilde{\mathcal{E}}}(x)$  in the channel model CM1 for RAKE finger numbers  $L = 10 \sim 50$ . In the low energy range, the curve of  $L = 10$  has the most probability mass; the curve of  $L = 20$  ranks second; the curve of  $L = 30$  ranks third; the curve of  $L = 40$  ranks fourth; and the curve of  $L = 50$  has the least probability mass. This phenomenon can explain why the

case of  $L = 10$  has the worst BER performance compared to  $L = 20, 30, 40$ , and 50.

Figure 3.7 shows the effect of various RAKE finger numbers on the BER performance of orthogonal binary signals (i.e.,  $\rho_r = 0$ ) in the IEEE 802.15.3a CM1~4 channel models. We set  $E_b/N_0 = 5$  dB and adopt the same parameters in Fig. 3.4. For a given  $E_b/N_0$ , we simulate 100,000 bits. In general, the BER decreases as  $L$  increases because more signal energy is collected at the RAKE receiver. For a large value of  $L$ , the BER curves become flat when  $E_b/N_0$  increases. This is because the RAKE receiver already captures most signal energy. The figure shows that the four channels actually give almost the same BER result (about  $6 \times 10^{-2}$ ) when the number of fingers is increased up to 80.

Furthermore, it would be interesting to compute the confidence interval of simulative BER result. From the central limit theorem, an  $100(1 - \alpha)$  confidence interval can be expressed as

$$(\bar{x} - Z_{1-\alpha/2}s/\sqrt{M}, \bar{x} + Z_{1-\alpha/2}s/\sqrt{M}), \quad (3.62)$$

where  $\bar{x}$  is the sample mean,  $s$  is the sample standard deviation,  $M$  is the sample size, and  $Z_{1-\alpha/2}$  is the  $(1-\alpha/2)$ -quantile of a standard normal random variable. For example, if the goal is to find the 95% confidence interval of the BER for CM2 at  $E_b/N_0 = 1$  dB, the  $\tilde{P}_2 = 0.19259$  at  $E_b/N_0 = 1$  dB from Fig. 3.4. Thus the sample mean is  $\bar{x} = 0.19259$ . In each simulation, an output bit is either the same as or different from the information bit. Thus, it is the same as a Bernoulli process with parameter  $p$  and the sample standard deviation  $s = \sqrt{p(1-p)}$ . Note that  $p$  can be estimated by  $\bar{x}$ . For  $\alpha = 0.05$ , one can obtain  $Z_{1-\alpha/2} = 1.95996$  by either table lookup or integration. This

leads to

$$Z_{1-\alpha/2}s/\sqrt{M} = 1.95996\sqrt{0.17131(1 - 0.17131)/100,000} = 2.44406 \times 10^{-3}. \quad (3.63)$$

The 95% confidence interval for the BER at  $E_b/N_0 = 1$  dB is

$$(0.17131 - 2.33526 \times 10^{-3}, 0.17131 + 2.33526 \times 10^{-3}) = (0.190146, 0.195034). \quad (3.64)$$

That is, with 0.95 probability the real BER value will lie in this range. Using the same method, we can find the confidence intervals of any simulation points.

### 3.4.3 Numerical Results for BER in IEEE 802.15.4a Channel

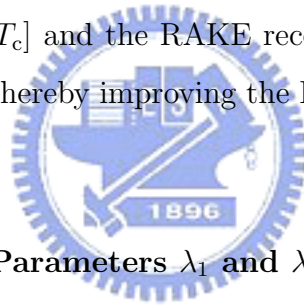
#### Comparison of Simulation and Analytical BER

Figure 3.8 shows the BER v.s.  $E_b/N_0$  for the CM1 model in the IEEE 802.15.4a standard with/without the shadowing by simulation and analysis. CM1 represents the residential line-of-sight (LOS) environment. The related channel parameters for CM1 can be found in Table 3.1. For the analytical curves, the orthogonal binary signal, i.e.,  $\rho_r = 0$ , is considered and  $\delta = 1$  for the PPM signal. For each  $E_b/N_0$ , we simulate 100,000 bits to obtain the BER. As seen from the figure, the analytical results match the simulation results quite well. Also, the BERs for CM1 with shadowing standard deviation  $\sigma_x = 3$  and 6 dB are worse than the BER for CM1 without shadowing. Moreover, the BER for  $\sigma_x = 6$  dB is worse than the BER for  $\sigma_x = 3$  dB. This result agrees with our common sense that more severe shadowing fading causes worse BER performance.

Figure 3.9 shows the BER v.s.  $L$ , the number of fingers of the RAKE receiver, for the CM1 model in the IEEE 802.15.4a standard by simulation and analysis. The simulation parameters are the same as that of the last figure. From the figure we see that the simulation and analytical BER are very close. Hence we can conclude that the approximation of  $\tilde{\mathcal{E}}$  in (3.36) is good for a large range of  $L$ .

### Impact of the Inter-Cluster Arrival Rate $\Lambda$

Figure 3.10 shows the BER v.s.  $E_b/N_0$  for various inter-cluster arrival rates  $\Lambda = 0.01, 0.1, 0.5, \text{ and } 1$ . When the cluster arrival rate increases, we find that the BER decreases and the slope of BER v.s.  $E_b/N_0$  becomes steeper. This is because when the inter-cluster arrival rate increases, more clusters arrive in the time interval  $[0, LT_c]$  and the RAKE receiver can collect more energy of the channel impulse, thereby improving the BER performance and increasing the diversity order.



### Impact of the Ray Arrival Parameters $\lambda_1$ and $\lambda_2$

Figure 3.11 shows the effects of different values of ray-arrival parameter  $\lambda_1$  on the BER v.s.  $E_b/N_0$ , when  $\lambda_2 = 0.15$  and  $\beta = 0.095$  according to the IEEE 802.15.4a model. The figure shows that in the considered case, a larger  $\lambda_1$  results in lower BER. When  $\lambda_1$  increases, the RAKE receiver can obtain higher energy from more rays. Compared with the impact of the cluster arrival rate, changing  $\lambda_1$  yields smaller variations on the BER performance. This is because the cluster arrival rate is a macroscopic parameter that influences all the clusters and  $\lambda_1$  is a microscopic parameter that influences only rays within each cluster.

Figure 3.12 shows the impacts of various values of  $\lambda_2$  on the BER for



the case  $\lambda_1 = 1.54$  and  $\beta = 0.095$ . As shown in the figure, a larger value of  $\lambda_2$  leads to a lower BER. Compared to Fig. 3.11,  $\lambda_2$  affects the BER more significantly than  $\lambda_1$ . Referring to [4, (18)], the condition of  $\beta = 0.095$  implies that ray interarrival time is decided by the parameter  $\lambda_1$  with a probability of 0.095 and is decided by the parameter  $\lambda_2$  with a probability of 0.905. This explains why  $\lambda_2$  becomes a more dominant parameter than  $\lambda_1$  in the case of  $\beta = 0.095$ .

### **Impact of the Ray Arrival Parameter $\beta$**

Figure 3.13 shows the effect of various values of  $\beta$  on the  $E_b/N_0$  in the case  $\lambda_1 = 1.54$  and  $\lambda_2 = 0.15$ . From [4, (18)], we expect that when  $\beta$  increases, the ray process is more likely to choose the arrival rate  $\lambda_1$  than  $\lambda_2$ . According to CM1 model of the IEEE 802.15.4a channel,  $\lambda_1 = 1.54$  and  $\lambda_2 = 0.15$ . Thus, a larger value of  $\beta$  indicates a higher ray arrival rate. Thus, the BER is improved for a larger  $\beta$  in the considered case.

### **Impact of the Inter-Cluster Decay Constant $\Gamma$**

Figure 3.14 shows the effect of various inter-cluster decay constants  $\Gamma$ . One can see that a larger value of  $\Gamma$  yields a better BER performance. From [4, (21)] one can see that the total energy  $\Omega_l$  is proportional to  $\exp(-T_l/\Gamma)$ . Thus, when  $\Gamma$  increases, the total energy  $\Omega_l$  of the  $l$ -th cluster also increases. With more signal energy captured by the RAKE receiver, the BER performance is therefore improved.

### **Impact of the Intra-Cluster Decay Constant $\gamma_0$**

Figure 3.15 illustrates the effect of the intra-cluster decay constant  $\gamma_0$  of [4, (20)]. As  $\gamma_0$  increases, the BER first increases and then remains the

same or even decreases. This phenomenon can be explained by (19) and (20) in [4]. From [4, (20)],  $\gamma_0$  is proportional to  $\gamma_l$ . According to [4, (19)],  $E[|a_{k,l}|^2] = \frac{\Omega_l}{\gamma_l} \exp(-\tau_{k,l}/\gamma_l)$ . For a small value of  $\gamma_l$ , the term  $1/\gamma_l$  dominates the value of  $E[|a_{k,l}|^2]$ . Thus, as  $\gamma_0$  increases, a smaller  $E[|a_{k,l}|^2]$  will yield higher BER. On the other hand, for a larger  $\gamma_l$ ,  $\exp(-\tau_{k,l}/\gamma_l)$  will affect  $E[|a_{k,l}|^2]$  more significantly. Thus, a larger  $\gamma_0$  leads to a larger  $E[|a_{k,l}|^2]$ , and lower BER. The maximal BER occurs at  $\gamma_0 = 30, 40,$  and  $90$  for  $E_b/N_0 = 5, 10,$  and  $15$  dB, respectively.

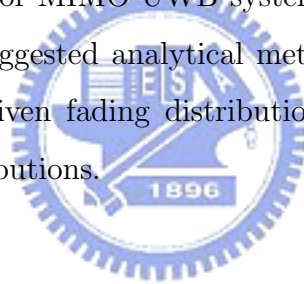
### 3.5 Conclusions

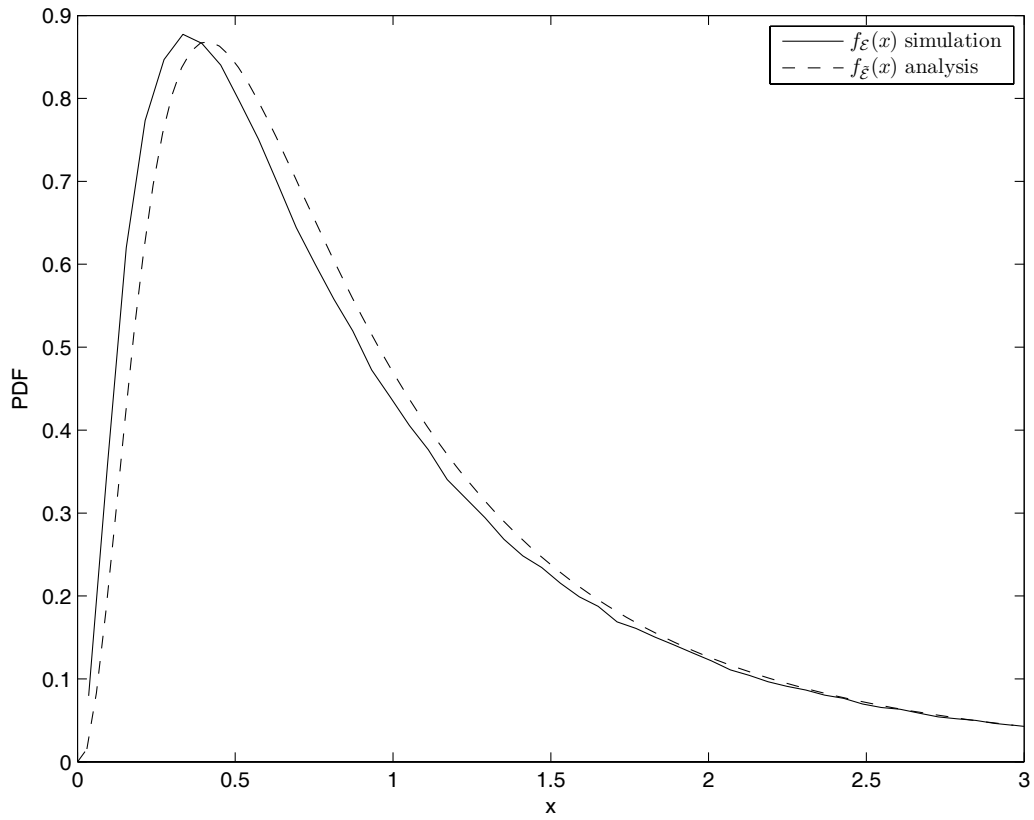
First, we have derived the computable BER formula for a RAKE receiver in the complete IEEE 802.15.3a UWB channel models. In particular, we find that deriving a BER formula taking account of RAKE finger numbers and shadowing is quite challenging for the IEEE 802.15.3a UWB channel. This is mainly because the jointly two-dimension lognormal and doubly-stochastic Poisson random variables yield infinite number of rays. We propose an approximation technique for the collected energy at an  $L$ -finger RAKE receiver. We find that the proposed BER computation method can save a significant amount of computer simulation time. Furthermore, we propose a characteristic function based BER formula to overcome the convergence problem of MGF-based BER formula when shadowing is included. The accuracy of the proposed technique is verified by simulations. Our results quantitatively indicate the effect of shadowing and RAKE finger numbers on BER performance in the IEEE 802.15.3a UWB channel.

Second, we have derived the BER analytical formula for a coherent RAKE receiver under the IEEE 802.15.4a UWB channel model. Our proposed an-

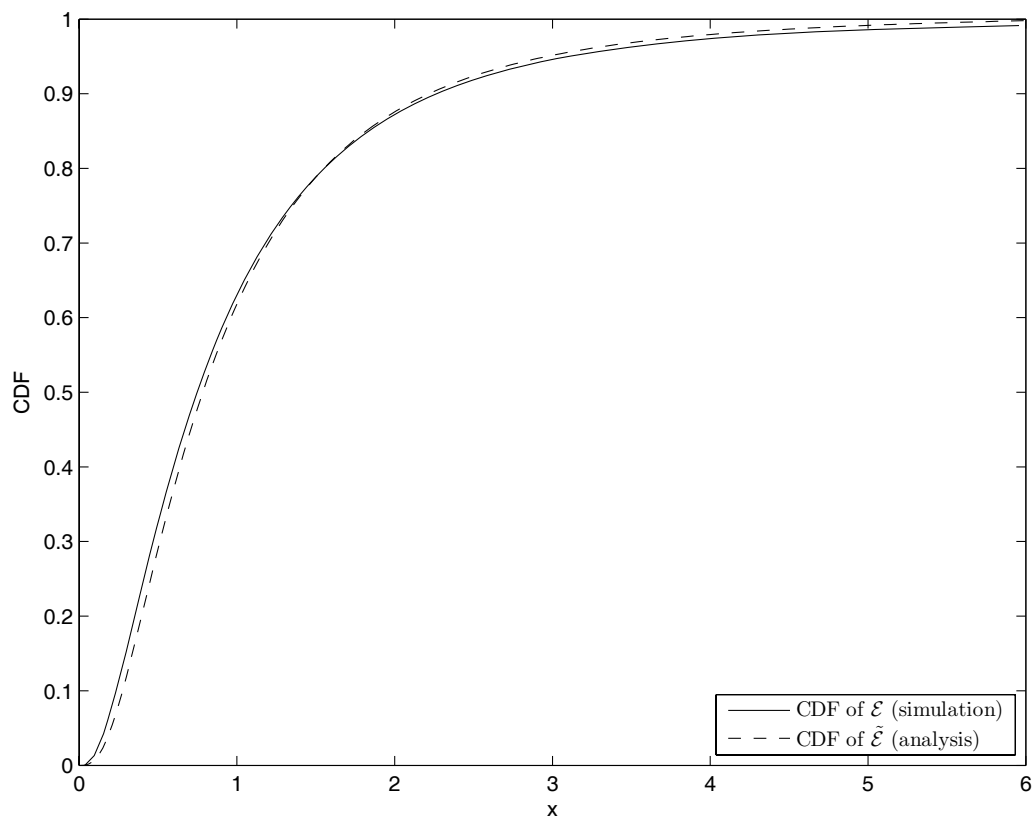
analytical method can accurately and quickly compute the BER values for the sophisticated IEEE 802.15.4a UWB channel, and evaluate the impact of various channel parameters. We find that of all the parameters in the IEEE 802.15.4a channel, the inter-cluster arrival rate  $\Lambda$  has the most significant impact on the BER performance. We also observe that the BER can be lowered due to the increase on the inter-cluster arrival rate  $\Lambda$ , the inter-cluster decay constant  $\Gamma$ , the ray arrival parameters  $\lambda_1$ ,  $\lambda_2$ , and  $\beta$ . We also find that increasing the intra-cluster decay constant  $\gamma_0$  causes the BER to first increase and then remain the same or even decrease.

In general, the time-domain parameters in the IEEE 802.15.4a UWB channel affect BER performance quite significantly. This reflects the comment in [94], that time-of-arrival characteristics are more important than amplitude characteristics for MIMO-UWB systems. In the future, it would be worth extending the suggested analytical method to other multipath channel models with any given fading distribution, PDP, and cluster and ray inter-arrival time distributions.





(a)



(b)

Figure 3.1: The distributions of  $\mathcal{E}$  by simulation and  $\tilde{\mathcal{E}}$  by analysis for a RAKE receiver with 10 fingers in the IEEE 802.15.3a UWB channels CM1, where the standard deviations of lognormal fading and shadowing are  $\sigma = 4.8$  dB and  $\sigma_x = 3$  dB, respectively. (a) PDFs. (b) CDFs.

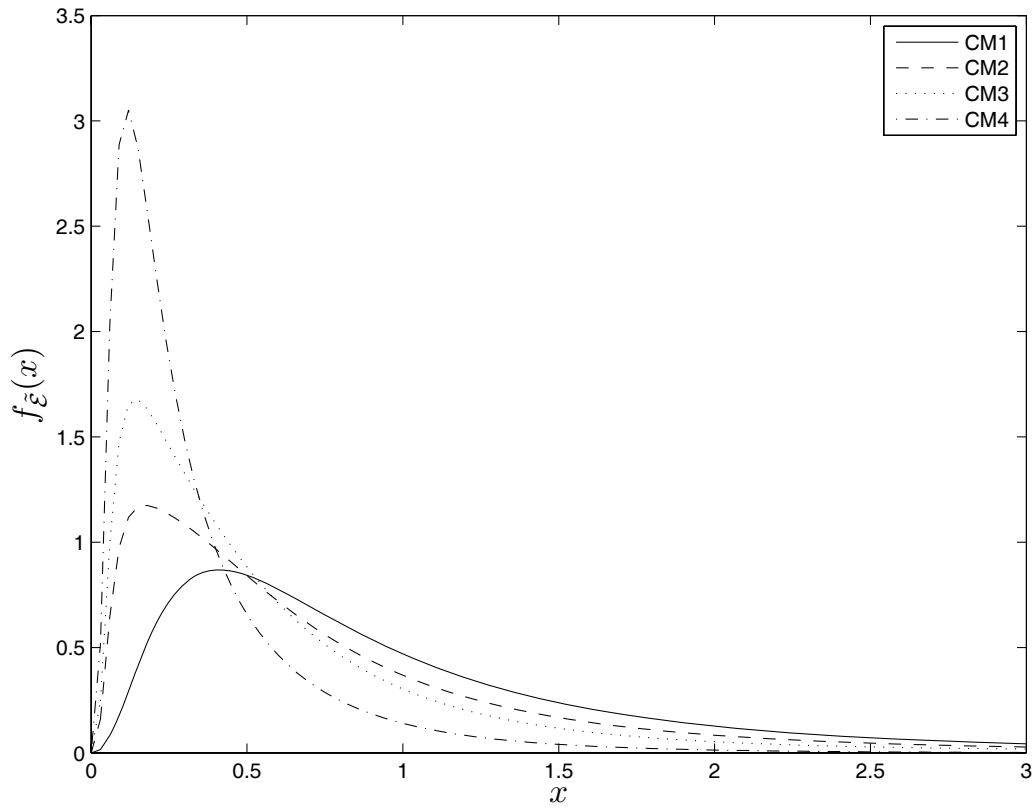


Figure 3.2: The PDF  $f_{\tilde{\mathcal{E}}}(x)$  of the received energy  $\tilde{\mathcal{E}}$  for a RAKE receiver with 10 fingers in the IEEE 802.15.3a UWB channels CM1, CM2, CM3, and CM4, where the standard deviations of lognormal fading and shadowing are  $\sigma = 4.8$  dB and  $\sigma_x = 3$  dB, respectively.

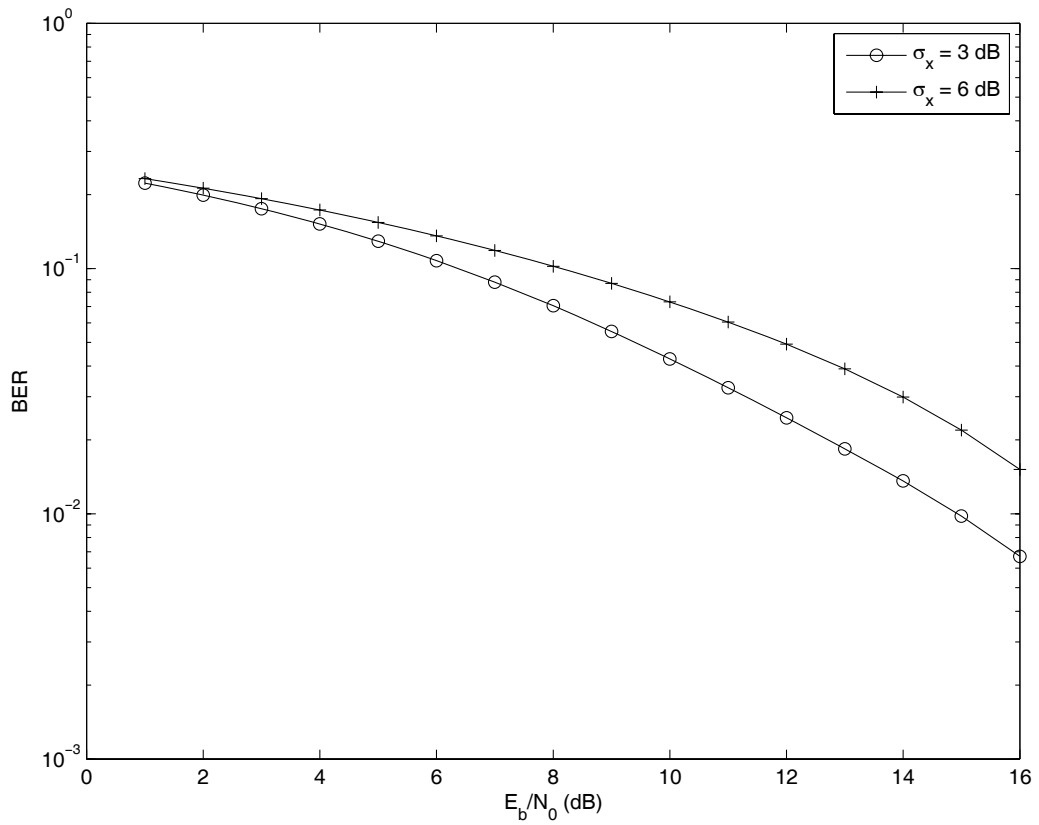


Figure 3.3: Effect of various shadow standard deviations ( $\sigma_x = 3$  dB and 6 dB) on the BER performance of a 10-finger RAKE receiver in the IEEE 802.15.3a UWB channels CM3.

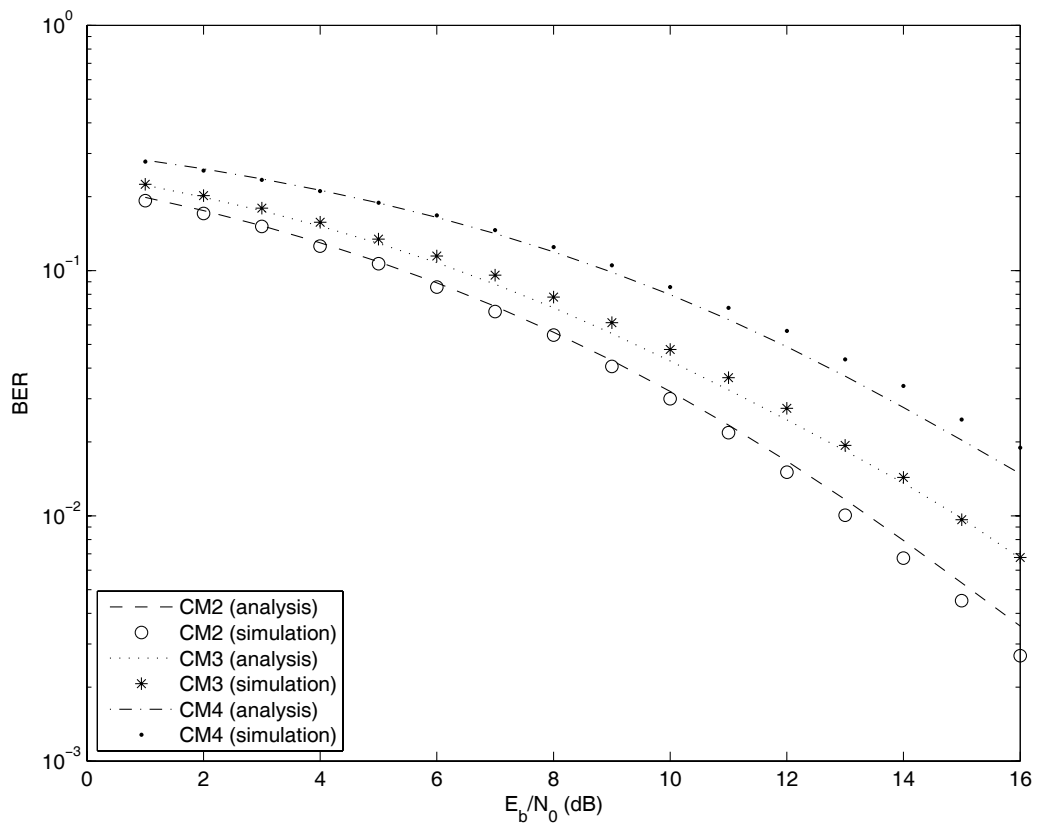


Figure 3.4: BER v.s.  $E_b/N_0$  for the 10-finger RAKE receiver in the IEEE 802.15.3a UWB channels CM2, CM3, and CM4 with shadowing standard deviation  $\sigma_x = 6$  dB, where the analytical BER is obtained from the characteristic function based approach, i.e. (3.28).



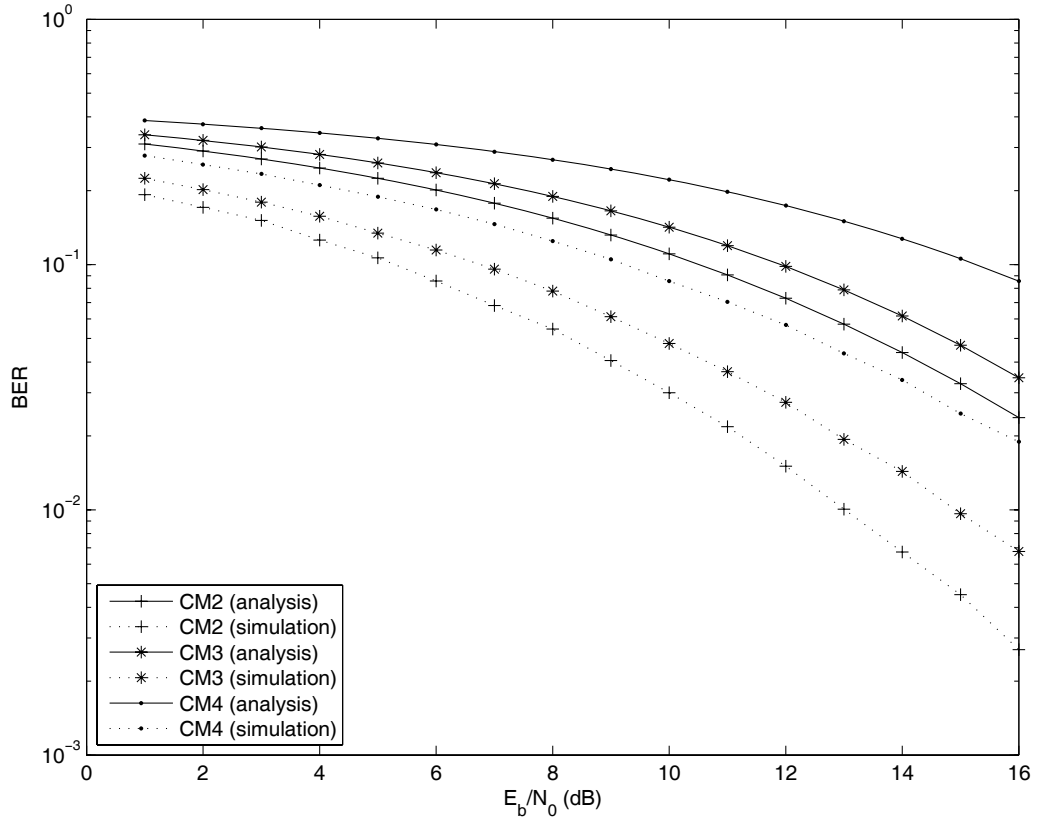


Figure 3.5: BER v.s.  $E_b/N_0$  for the 10-finger RAKE receiver in the IEEE 802.15.3a UWB channels CM2, CM3, and CM4 with shadowing standard deviation  $\sigma_x = 6$  dB, where the analytical BER is obtained from the MGF-based approach, i.e. (3.29).

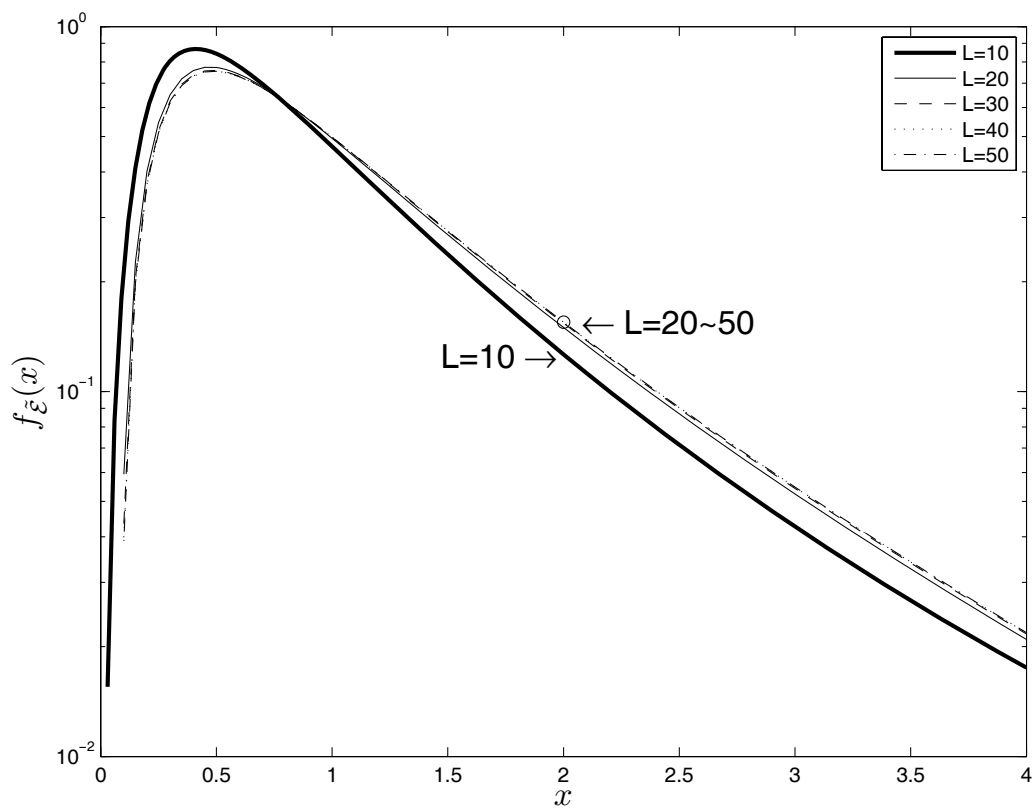


Figure 3.6: The PDF  $f_{\tilde{\mathcal{E}}}(x)$  of the received energy  $\tilde{\mathcal{E}}$  of a RAKE receiver with number of fingers  $L = 10, 20, 30, 40$ , and  $50$  in the IEEE 802.15.3a UWB channel CM1.

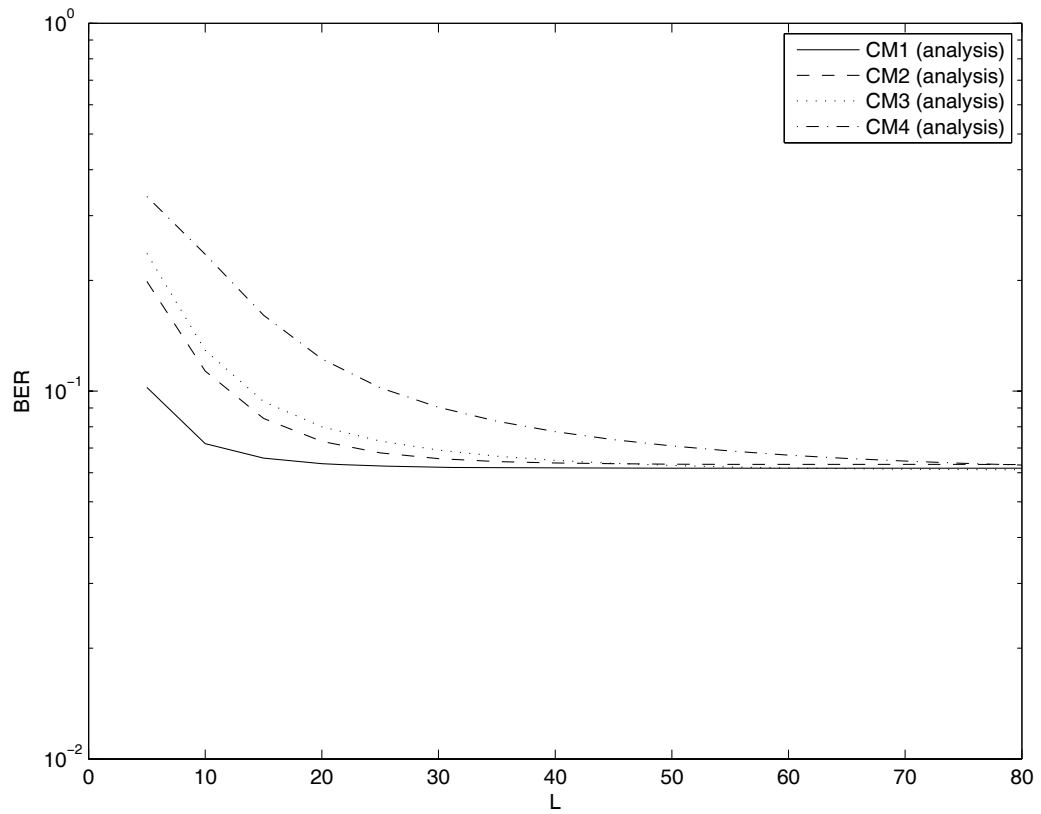


Figure 3.7: BER v.s. the number of fingers of the RAKE receiver ( $L$ ) for CM1, CM2, CM3, and CM4, where  $E_b/N_0 = 5$  dB.

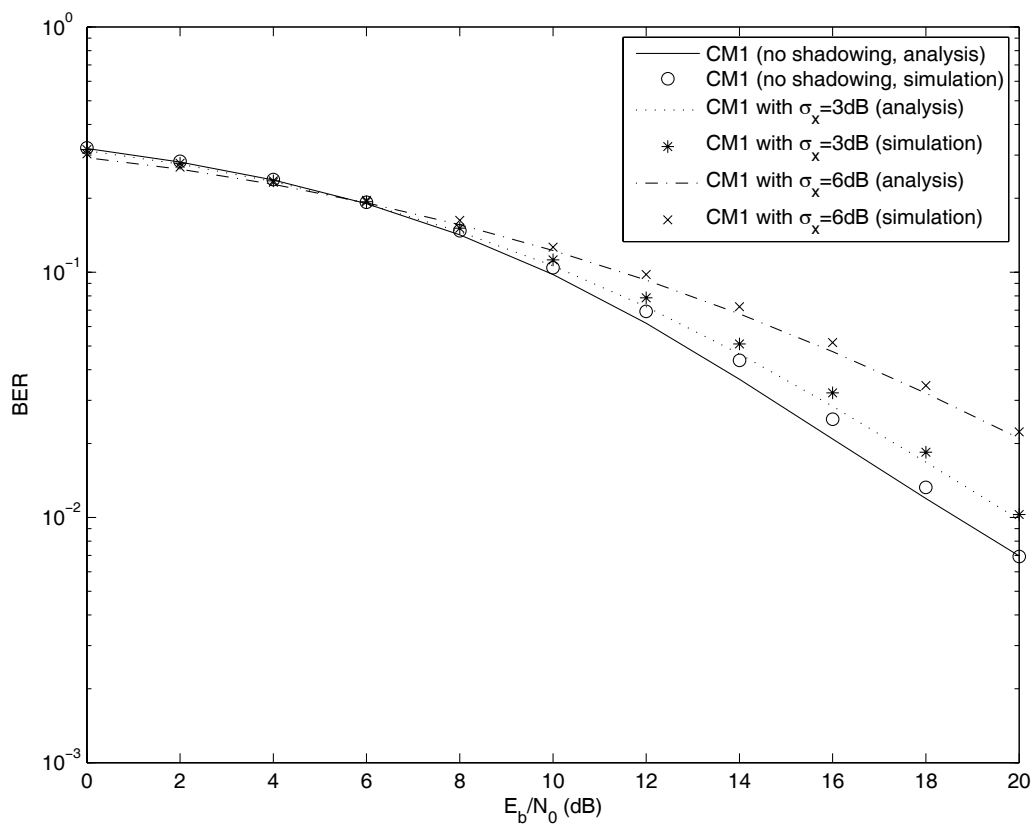


Figure 3.8: The BER v.s.  $E_b/N_0$  for the CM1 model without shadowing and CM1 model with shadowing standard deviation  $\sigma_x = 3$  and 6 dB in the IEEE 802.15.4a standard by simulation and analysis. In CM1, the default value of  $\sigma_x$  is 2.22 dB.

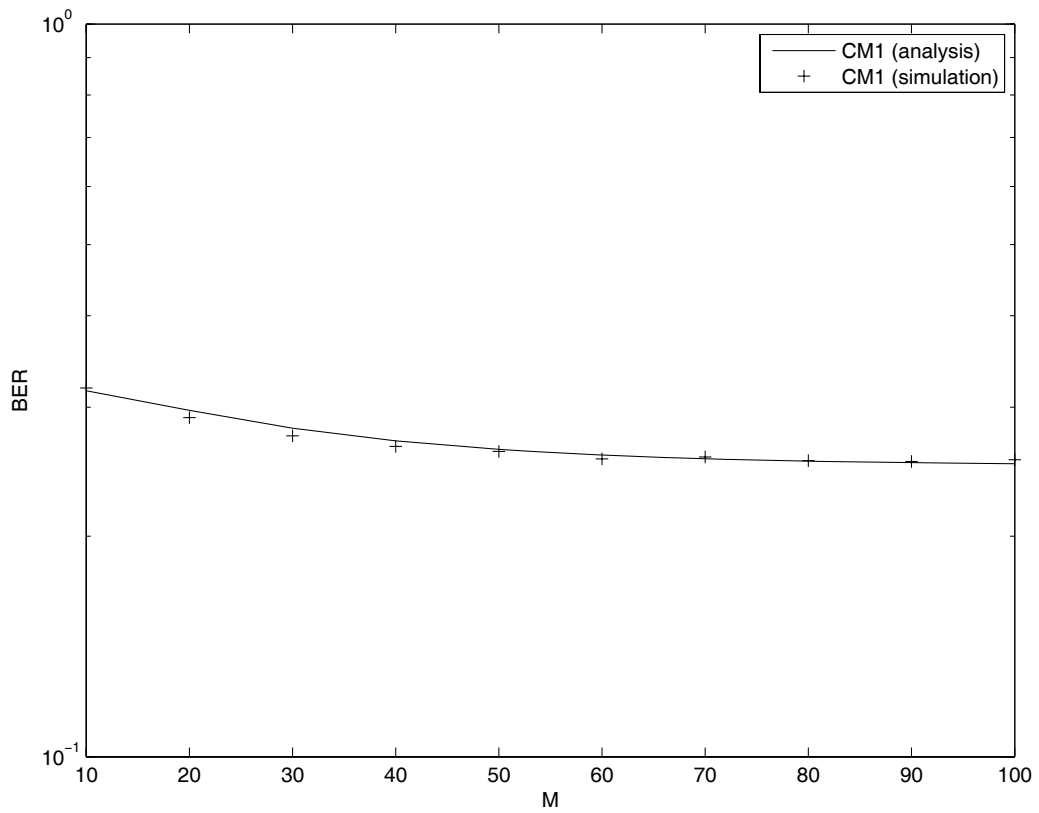


Figure 3.9: The BER v.s.  $L$  (number of fingers of the RAKE receiver) for the CM1 model in the IEEE 802.15.4a standard by simulation and analysis. The SNR is  $E_b/N_0 = 0$  dB. The shadowing standard deviation  $\sigma_x$  is 2.22 dB.

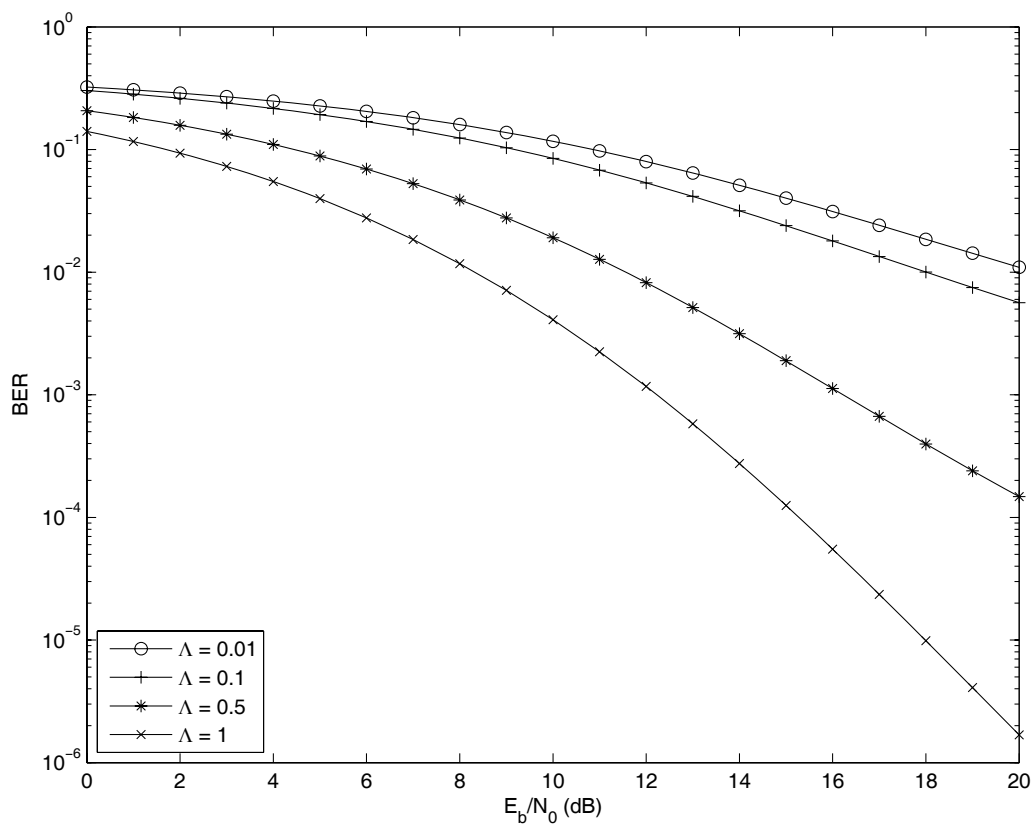


Figure 3.10: The BER v.s.  $E_b/N_0$  for various inter-cluster arrival rates  $\Lambda = 0.01, 0.1, 0.5,$  and  $1$  under the CM1 model of the IEEE 802.15.4a UWB channel. In CM1, the default value of  $\Lambda$  is 0.047. The shadowing standard deviation  $\sigma_x$  is 2.22 dB.

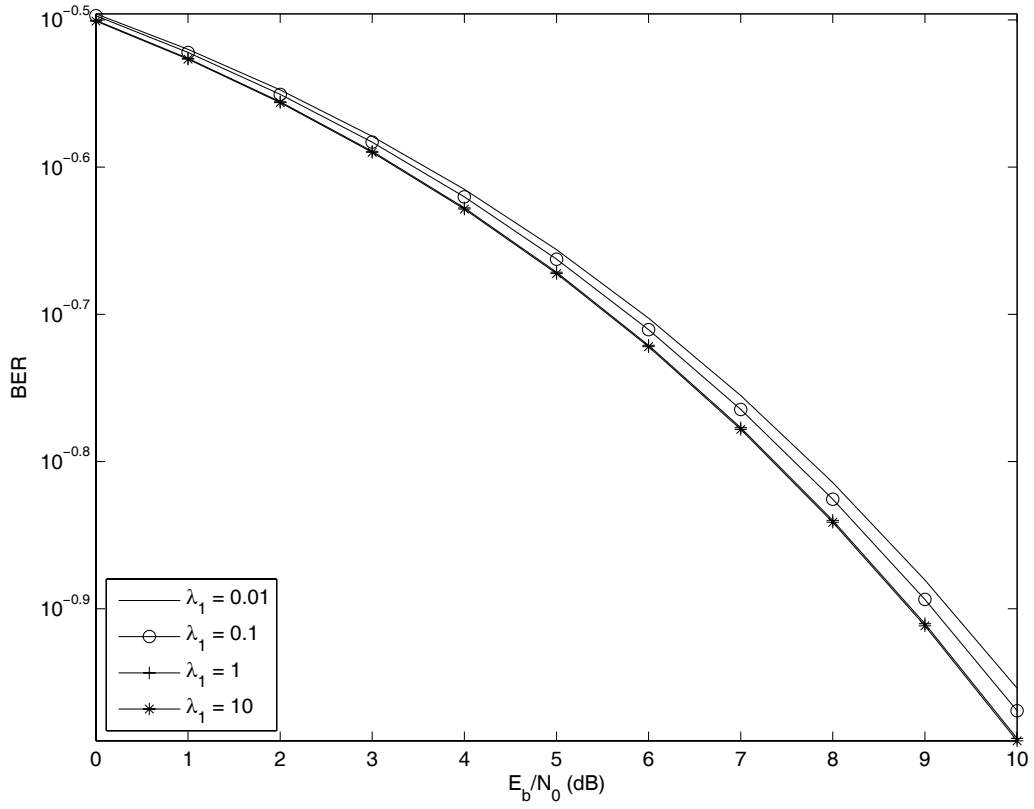


Figure 3.11: The effects of different values of ray-arrival parameter  $\lambda_1 = 0.01, 0.1, 1,$  and  $10$  on the BER v.s.  $E_b/N_0$ , where  $\lambda_2 = 0.15$  and  $\beta = 0.095$  according to the CM1 model of the IEEE 802.15.4a channel. In CM1, the default value of  $\lambda_1$  is  $1.54$ . The shadowing standard deviation  $\sigma_x$  is  $2.22$  dB.

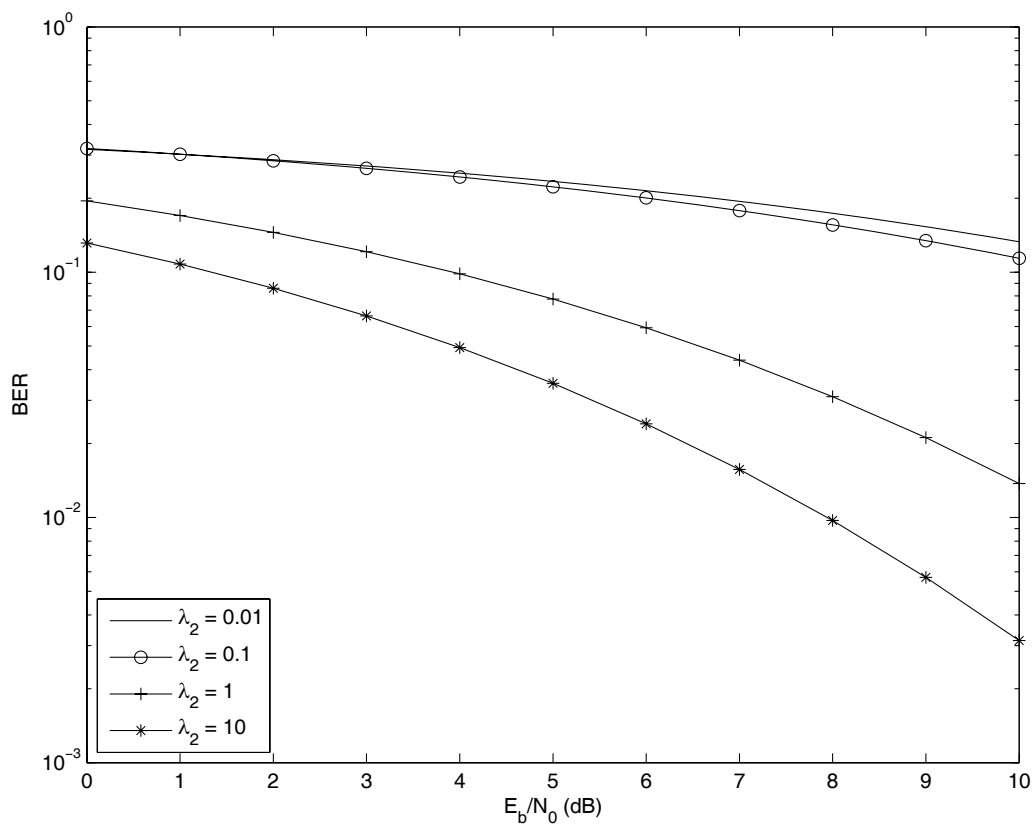


Figure 3.12: The impacts of various values of  $\lambda_2$  on the BER v.s.  $E_b/N_0$  for the case  $\lambda_1 = 1.54$  and  $\beta = 0.095$  in the CM1 model of the IEEE 802.15.4a UWB channel. In CM1, the default value of  $\lambda_2$  is 0.15. The shadowing standard deviation  $\sigma_x$  is 2.22 dB.



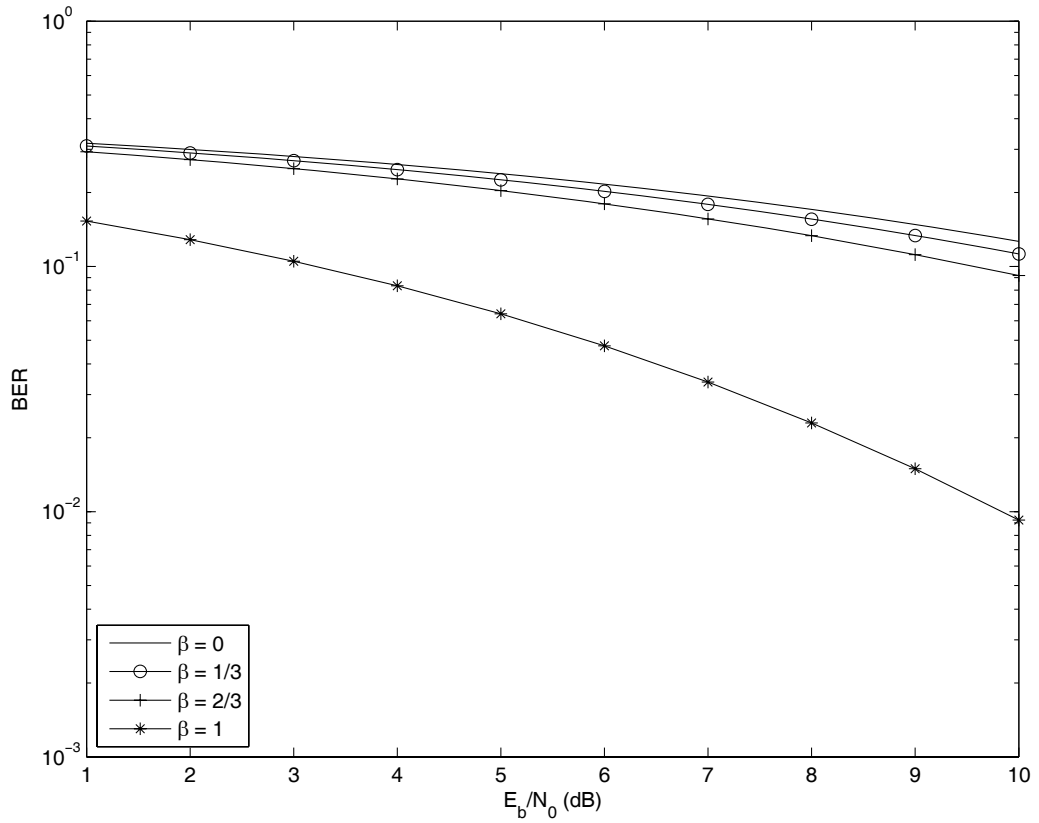


Figure 3.13: The effect of various  $\beta$  on the BER v.s.  $E_b/N_0$  for  $\lambda_1 = 1.54$  and  $\lambda_2 = 0.15$  in the CM1 model of the IEEE 802.15.4a UWB channel. In CM1, the default value of  $\beta$  is 0.095. The shadowing standard deviation  $\sigma_x$  is 2.22 dB.

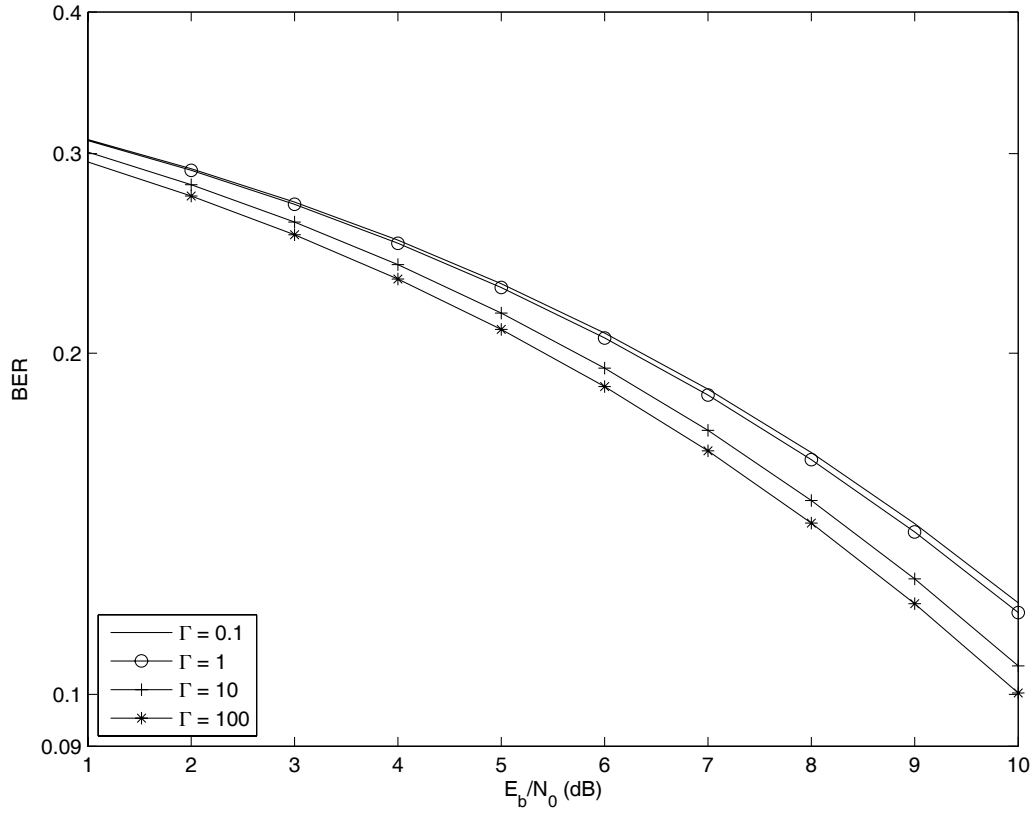


Figure 3.14: The effect of the inter-cluster decay constant  $\Gamma = 0.1, 1, 10,$  and  $100$  in the IEEE 802.15.4a UWB channel for various of  $E_b/N_0$ , where a 10-finger RAKE receiver is adopted in the CM1 model. In CM1, the default value of  $\Gamma$  is 22.61. The shadowing standard deviation  $\sigma_x$  is 2.22 dB.

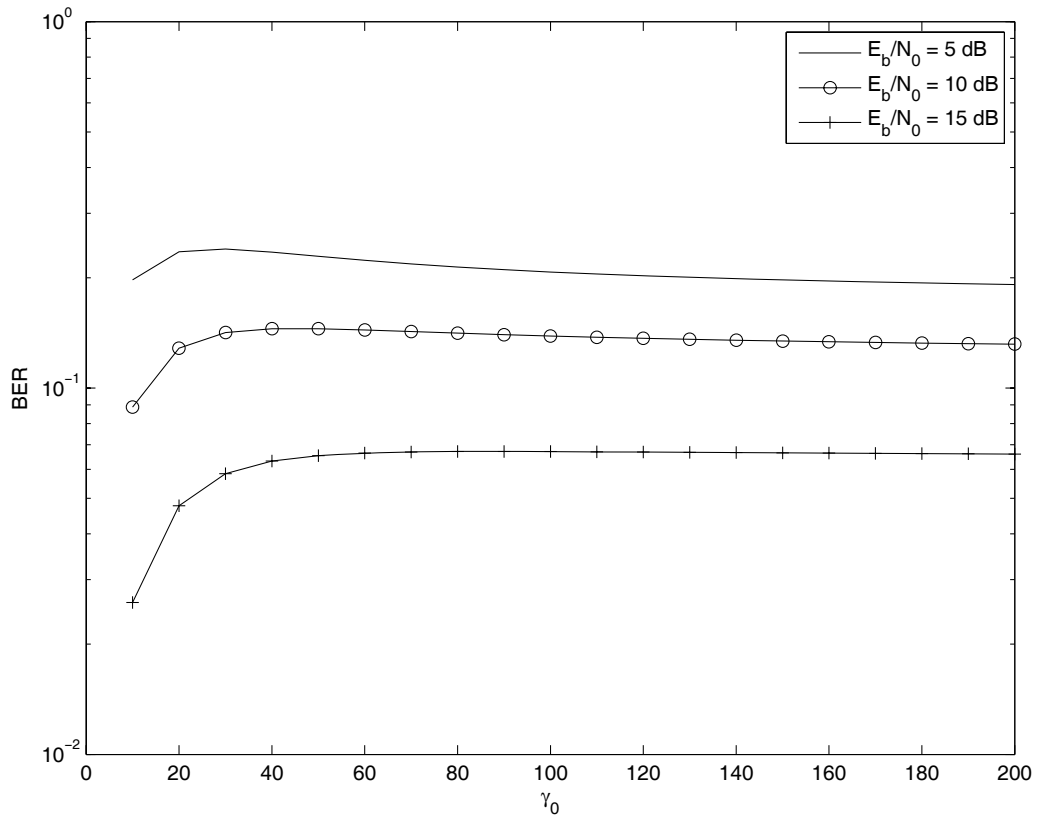


Figure 3.15: The effect of intra-cluster decay constant  $\gamma_0$  in the IEEE 802.15.4a UWB channel for various values of  $E_b/N_0$ , where a 10-finger RAKE receiver is adopted in the CM1 model. The shadowing standard deviation  $\sigma_x$  is 2.22 dB.

# Chapter 4

## On the Performance of Using Multiple Transmit and Receive Antennas in Pulse-Based Ultrawideband Systems



This chapter presents an analytical expression for the signal-to-noise ratio (SNR) of the pulse position modulated (PPM) signal in an ultra-wideband (UWB) channel with multiple transmit and receive antennas. We consider a generalized fading channel model that can capture the cluster property and the highly dense multipath effect of the UWB channel. Through simulations, we demonstrate that the derived analytical model can accurately estimate the mean and variance properties of the pulse based UWB signals in a frequency selective fading channel. Furthermore, we investigate to what extent the performance of the PPM based UWB system can be further enhanced by exploiting the advantage of multiple transmit antennas or receive antennas. Our numerical results show that using multiple transmit antennas

in the UWB channel can improve the system performance in the manner of reducing signal variations. However, because of already possessing rich diversity inherently in the UWB channel, using multiple transmit antennas does not provide diversity gain in the strict sense (i.e., improving the slope of bit error rate (BER) v.s. SNR), but can possibly reduce the required fingers of the Rake receiver for the UWB channel. Furthermore, because multiple receive antennas can provide higher antenna array combining gain, multiple receive antennas technique can be used to improve the coverage performance for the UWB system, which is crucial for a UWB system due to the low transmission power operation.

## 4.1 Motivation

Wireless systems continue to pursue even higher data rates and better quality. The ultra-wideband (UWB) technique and space time processing techniques are two promising techniques to achieve this objective. However, how to merge these two techniques together to further increase the data rates is not an easy task. This chapter investigates how multiple transmit/receive antennas and the UWB system can function together to exploit the synergy of marrying these two advanced techniques.

## 4.2 Channel Model

To evaluate the performance of a UWB system with multipath fading, the following discrete impulse response of the channel is considered:

$$h(t) = \sum_{l=0}^{L_c-1} \xi_l \Delta(t - lT_c), \quad (4.1)$$

where  $L_c$  is the number of resolvable multipath components,  $T_c$  is the chip duration or the length of the time bin,  $\Delta(t)$  is the Dirac delta function. In (4.1), the amplitude fading factor on path  $l$  (denoted as  $\xi_l$ ) can be expressed as

$$\xi_l = b_l a_l, \quad (4.2)$$

where  $b_l$  is equiprobable to take on the value  $+/- 1$ , and  $a_l$  is the Nakagami fading term. The term  $b_l$  is used to account for the random pulse inversion that can occur due to reflections, as observed in the measurements [16].

In this chapter, we consider a UWB channel characterized by the following three major properties [9]:

- Gamma distribution to describe each resolvable path power;
- A modified Poisson process to characterize the clustering property of the UWB channel and the number of the simultaneous arrival paths;
- Exponential decay to model the average resolvable path power in the time domain.

### 4.2.1 The PDF of the Received Signal Power

For the  $l$ -th path with path gain  $\xi_l$  and  $n_l$  simultaneous arrival paths, the probability density function (PDF) of the received signal power  $y = \xi_l^2 = a_l^2$  can be characterized by a Gamma distributed random variable as [14]:

$$f_Y(y) = \frac{1}{\sigma_l^{n_l} 2^{n_l/2} \Gamma(\frac{1}{2}n_l)} y^{n_l/2-1} e^{-y/2\sigma_l^2}, \quad (4.3)$$

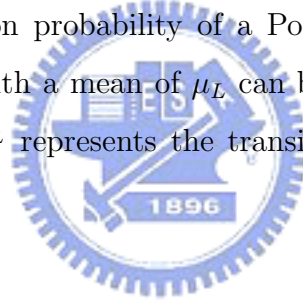
where  $\Gamma(\alpha) = \int_0^\infty t^{\alpha-1} \exp(-t) dt$ , and  $\sigma_l^2 = \frac{1}{n_l} \mathbb{E}[a_l^2]$ . In the following, we discuss the way to calculate the terms  $n_l$  and  $\mathbb{E}[a_l^2]$ .

### 4.2.2 The Number of Simultaneous Arrival Paths

The clustering property in the UWB channel can be characterized by a modified Poisson process driven through a two-state Markov chain [11]. If a resolvable path appears in the previous time bin, a Poisson arrival process will be in the high state with  $\mu_H$  average simultaneous arrival paths; otherwise, it will be in the low state with  $\mu_L$  average simultaneous arrival paths, where  $\mu_H > \mu_L$ . Let  $n_l$  denote the simultaneous arrival paths in the  $l$ -th time bin. Then,

$$\text{Prob}[n_l = k] = \begin{cases} \frac{\mu_H^k}{k!} e^{-\mu_H}, & \text{when } n_{l-1} \neq 0; \\ \frac{\mu_L^k}{k!} e^{-\mu_L}, & \text{when } n_{l-1} = 0. \end{cases} \quad (4.4)$$

Note that the transition probability of a Poisson process with a mean of  $\mu_H$  changing to that with a mean of  $\mu_L$  can be calculated by  $\alpha = e^{-\mu_H}$ ; or similarly,  $\beta = 1 - e^{-\mu_L}$  represents the transition probability from the low state to the high state.



### 4.2.3 Average Resolvable Path Power

We apply the exponential decay model to characterize the received signal power  $a_l^2$  in the time domain [14]. Obviously, if  $n_l = 0$ ,  $\mathbb{E}[a_l] = 0$ . When  $n_l \neq 0$ ,

$$\mathbb{E}[a_l^2] = \begin{cases} 1, & \text{when } l = 0; \\ \gamma \cdot e^{-\eta(l-2)}, & \text{when } l \geq 1, \end{cases} \quad (4.5)$$

where  $\eta$  is the decay constant, and  $\gamma$  is the power adjustment factor except the first path.

## 4.3 Signal Model and Detection Scheme

### 4.3.1 Signal Model

Consider a single user employing binary PPM in the UWB channel. Let  $T_f$  and  $T_c$  be the frame time and the chip time of the PPM signal, respectively. With the transmitted pulse waveform  $w_{tr}(t)$ , the transmitted signal for the  $i$ -th message bit  $d^{(i)}$  is written as [40]:

$$s_{tr}^{(i)} = \sum_{j=0}^{N_p-1} w_{tr}(t - jT_f - c_j^{(i)}T_c - d^{(i)}\delta T_c), \quad (4.6)$$

where  $N_p$  is the repetition number for one information bit,  $\{c_j^{(i)}\}$  is a time-hopping sequence, and  $\delta$  is the modulation index associated with the message bit which is an integer multiple of the chip time  $T_c$ . The frame time  $T_f$  is assumed to be much larger than  $T_c$ . In this chapter, we assume that the transmitted pulse waveform  $w_{tr}(t)$  is

$$w_{tr}(t) = \begin{cases} 1, & 0 \leq t < T_c \\ 0, & \text{otherwise} \end{cases}. \quad (4.7)$$

With the channel response  $h(t)$  and the noise  $n(t)$ , the received PPM data for the  $i$ -th information bit is written as

$$\begin{aligned} & s_{rec}^{(i)}(t) \\ &= s_{tr}^{(i)} * h(t) + n(t) \\ &= \sum_{j=0}^{N_p-1} x(t - jT_f - c_j^{(i)}T_c - d^{(i)}\delta T_c) + n(t), \end{aligned} \quad (4.8)$$

where the received pulse waveform  $x(t) = w_{tr}(t) * h(t)$ . Since the goal of this work is focused on the impact of the UWB channel on the PPM signal



detection in the single user case, we ignore the time hopping code. When  $x(t)$  is sampled at  $t = lT_c$ , denote  $x_l = x(lT_c)$ . Then, we can have

$$x_l = \sum_{k=0}^{L_c-1} \sum_{j=0}^{N_p-1} \xi_l w_{tr}((l-k)T_c - jT_f - d^{(i)}\delta T_c) \quad (4.9)$$

where  $\xi_l$  and  $w_{tr}$  are defined in (4.1) and (4.6).

For the message bit  $d^{(i)} = 0$  in the channel response with a length of  $L_c$ , the received data  $\mathbf{r}_0$  can be expressed as

$$\mathbf{r}_0 = \mathbf{x}_0 + \mathbf{n} \quad (4.10)$$

where  $\mathbf{x}_0 = [x_0, x_1, \dots, x_{L_c-1}, \overbrace{0 \dots 0}^{\delta's0}]^T$  and  $\mathbf{n} = [n_0, n_1, \dots, n_{L_c-1}, n_{L_c}, \dots, n_{L_c+\delta-1}]^T$ . Similarly, for the message bit  $d^{(i)} = 1$ ,

$$\mathbf{r}_1 = \mathbf{x}_1 + \mathbf{n}, \quad (4.11)$$

where  $\mathbf{x}_1 = [\overbrace{0 \dots 0}^{\delta's0}, x_0, x_1, \dots, x_{L_c-1}]^T$ .

### 4.3.2 Signal Detection

Similar to [18, 40, 95], we consider a template-based detection scheme for the PPM signals. It is assumed that perfect channel knowledge is available at the receiver. Having two possible output waveforms  $\mathbf{x}_0$  and  $\mathbf{x}_1$  for message bit  $d^{(i)} = 0$  and  $d^{(i)} = 1$  defined in (4.10) and (4.11), respectively, we can choose  $\mathbf{p}_0 = \mathbf{x}_0$  and  $\mathbf{p}_1 = \mathbf{x}_1$  and represent a template signal  $\mathbf{p}$  for the binary PPM case as

$$\mathbf{p} = -\mathbf{p}_0 + \mathbf{p}_1. \quad (4.12)$$

Now we take  $\mathbf{r}_1$  as an example. Consider a Rake receiver with  $L$  fingers and denote the processed data  $z_{p1}$  as the inner product of the received data  $\mathbf{r}_1$  of

(4.11) and the template  $\mathbf{p}$  of (4.12). Then we have

$$\begin{aligned}
z_{p1} &= \mathbf{p}^T \mathbf{r}_1 = (-\mathbf{p}_0^T + \mathbf{p}_1^T) \mathbf{r}_1 \\
&= \sum_{i=0}^{L-1} x_i x_i - \sum_{i=0}^{L-\delta-1} x_i x_{i+\delta} + \sum_{i=0}^{L-1} n_{i+\delta} x_i - \sum_{i=0}^{L-1} n_i x_i \\
&= s_{p1} + r_{p1} + n_{p1} + n_{p0},
\end{aligned} \tag{4.13}$$

where  $s_{p1} = \sum_{i=0}^{L-1} x_i x_i$  is the signal part,  $r_{p1} = -\sum_{i=0}^{L-\delta-1} x_i x_{i+\delta}$  is the redundancy part,  $n_{p1} = \sum_{i=0}^{L-1} n_{i+\delta} x_i$  is the noise part of the processed data  $z_{p1}$  from  $\mathbf{p}_1$ , and  $n_{p0} = -\sum_{i=0}^{L-1} n_i x_i$  is the noise part of the processed data  $z_{p1}$  from  $\mathbf{p}_0$ . From (4.13), we can use the sum of the pulse correlator outputs as the test statistics to detect the transmitted symbol. Specifically, if the processed data  $z_{p1}$  is larger than zero, the transmitted message bit  $d^{(i)} = 0$ ; otherwise, we take the transmitted message bit  $d^{(i)} = 1$ .

## 4.4 Analysis of PPM UWB Signals

### 4.4.1 The State Probabilities of the Modified Poisson Process

Consider a two-state Markov chain of (4.4) with the probability  $\alpha = e^{-\mu H}$  changing from the high state to the low state, and the probability  $\beta = 1 - e^{-\mu L}$  changing from the low state to the high state. Then, the transition probability matrix  $\mathbf{P}$  is represented as

$$\mathbf{P} = \begin{bmatrix} 1 - \alpha & \alpha \\ \beta & 1 - \beta \end{bmatrix}. \tag{4.14}$$

According to [96], the  $i$ -step transition probability matrix  $\mathbf{P}^i$  can be expressed as

$$\mathbf{P}^i = \frac{1}{\alpha + \beta} \begin{bmatrix} \beta & \alpha \\ \beta & \alpha \end{bmatrix} + \frac{(1 - \alpha - \beta)^i}{\alpha + \beta} \begin{bmatrix} \alpha & -\alpha \\ -\beta & \beta \end{bmatrix}. \quad (4.15)$$

Denote  $\pi_H(l)$  and  $\pi_L(l) = 1 - \pi_H(l)$  as the probability of the  $l$ -th time bin in the high state of the Markov chain and that in the low state of the Markov chain, respectively. Clearly,  $\pi_H(l)$  can be expressed as

$$\pi_H(l) = \begin{cases} 1 & \text{if } l = 0 \\ 1 - \alpha & \text{if } l = 1 \\ (1 - \alpha)^2 + \alpha\beta & \text{if } l = 2 \\ (1 - \alpha)^3 + 2\alpha\beta(1 - \alpha) + \alpha\beta(1 - \beta) & \text{if } l = 3 \\ \frac{\beta}{\alpha + \beta} & \text{if } l \geq 4 \end{cases} \quad (4.16)$$

Note that the steady state probabilities  $\pi_H(l)$  and  $\pi_L(l)$  are  $\pi_H(4) = \frac{\beta}{\alpha + \beta}$  and  $\pi_L(4) = \frac{\alpha}{\alpha + \beta}$ .

#### 4.4.2 Mean and Variance of the Processed Data for PPM based UWB Signals

In the following, we describe the mean and the variance of the processed data  $z$  (defined in (4.13)) for the PPM signal under the UWB channel model described in Section II. Without loss of generality, we take the processed data  $z_{p1}$  as an example.

**Proposition 1** *The average energy of the processed data  $z_{p1}$  can be calculated as*

$$\mathbb{E}[z_{p1}] = \left( \frac{\beta}{\alpha + \beta} \right) \frac{\gamma e^{-3\eta} - \gamma e^{-(L-1)\eta}}{1 - e^{-\eta}} + A, \quad (4.17)$$

where

$$\begin{aligned}
A &= 1 + (1 - \alpha)\gamma + [(1 - \alpha)^2 + \alpha\beta]\gamma e^{-\eta} \\
&\quad + [(1 - \alpha)^3 + 2\alpha\beta(1 - \alpha) + \alpha\beta(1 - \beta)]\gamma e^{-2\eta}. \tag{4.18}
\end{aligned}$$

*Proof:* See Appendix G.

**Proposition 2** *The variance of the processed data  $z_{p1}$  can be calculated as*

$$\begin{aligned}
&\text{var}[z_{p1}] \\
&= 2 \sum_{l=0}^{L-1} \sum_{k=1}^{\infty} \frac{1}{k} (\mathbb{E}[a_l^2])^2 \left( \frac{\beta}{\alpha + \beta} \cdot \frac{\mu_H^k}{k!} e^{-\mu_H} \right. \\
&\quad \left. + \frac{\alpha}{\alpha + \beta} \cdot \frac{\mu_L^k}{k!} e^{-\mu_L} \right) \\
&\quad + 2 \sum_{l=0}^{L-2} (\pi_H(4)\pi_H(1) - \pi_H(l)\pi_H(l+1)) \mathbb{E}[a_l^2] \mathbb{E}[a_{l+1}^2] \\
&\quad + \sum_{l=0}^{L-3} (\pi_H(4)\pi_H(2) - \pi_H(l)\pi_H(l+2)) \mathbb{E}[a_l^2] \mathbb{E}[a_{l+2}^2] \\
&\quad + 2 \sum_{l=0}^{L-4} (\pi_H(4)\pi_H(3) - \pi_H(l)\pi_H(l+3)) \mathbb{E}[a_l^2] \mathbb{E}[a_{l+3}^2] \\
&\quad + \sum_{l=0}^{L-\delta-1} \pi_H(l)\pi_H(\delta+1) \mathbb{E}[a_l^2] \mathbb{E}[a_{l+\delta}^2] \\
&\quad + \sum_{l=0}^{L-1} \pi_H(l) \sigma_n^2 \mathbb{E}[a_l^2], \tag{4.19}
\end{aligned}$$

where  $\pi_H(\cdot)$  is defined in (4.16),  $\mathbb{E}[a_l^2]$  is described in (4.5),  $L$  is the number of fingers in the Rake receiver,  $\delta$  is the modulation index associated with binary PPM, and  $\sigma_n$  is the standard deviation of the Gaussian noise.

*Proof:* From (4.13), we can express the variance of the processed data  $z_{p1}$  as follows:

$$\begin{aligned}
& \text{var}[z_{p1}] \\
&= \text{var}[s_{p1}] + \text{var}[r_{p1}] + \text{var}[n_{p1}] + \text{var}[n_{p0}] + \\
& \quad 2\text{cov}[s_{p1}, r_{p1}] + 2\text{cov}[s_{p1}, n_{p1}] + 2\text{cov}[s_{p1}, n_{p0}] + \\
& \quad 2\text{cov}[r_{p1}, n_{p1}] + 2\text{cov}[r_{p1}, n_{p0}] + 2\text{cov}[n_{p1}, n_{p0}]. \tag{4.20}
\end{aligned}$$

First, we can calculate the signal part  $\text{var}[s_{p1}]$  as follows:

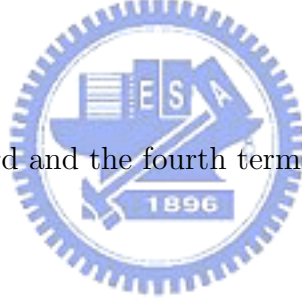
$$\begin{aligned}
& \text{var}[s_{p1}] \\
&= \text{var} \sum_{l=0}^{L-1} x_l x_l \\
&= \sum_{l=0}^{L-1} \text{var}[a_l^2] + 2 \sum_{m=0}^{L-2} \sum_{n=m+1}^{L-1} \text{cov}[a_m^2, a_n^2] \\
&= \sum_{l=0}^{L-1} \sum_{k=1}^{\infty} \text{var}[a_l^2 | n_l = k] (\pi_H(l) \text{Prob}[n_l = k, n_{l-1} \neq 0] \\
& \quad + \pi_L(l) \text{Prob}[n_l = k, n_{l-1} = 0]) \\
& \quad + 2 \sum_{l=0}^{L-2} \text{cov}[a_l^2, a_{l+1}^2] + 2 \sum_{l=0}^{L-3} \text{cov}[a_l^2, a_{l+2}^2] \\
& \quad + 2 \sum_{l=0}^{L-4} \text{cov}[a_l^2, a_{l+3}^2]. \tag{4.21}
\end{aligned}$$

Applying the method of [97] to (4.16) and (4.4), the first term of (4.21) can be computed as

$$\begin{aligned}
\sum_{l=0}^{L-1} \text{var}[a_l^2] &= 2 \sum_{l=0}^{L-1} \sum_{k=1}^{\infty} \frac{1}{k} (\mathbb{E}[a_l^2])^2 \left( \pi_H(l) \frac{\mu_H^k}{k!} e^{-\mu_H} \right. \\
& \quad \left. + \pi_L(l) \frac{\mu_L^k}{k!} e^{-\mu_L} \right). \tag{4.22}
\end{aligned}$$

From (4.27), the second term of (4.21) can be obtained as

$$\begin{aligned}
& 2 \sum_{l=0}^{L-2} \text{cov}[a_l^2, a_{l+1}^2] \\
&= 2 \sum_{l=0}^{L-2} (\mathbb{E}[a_l^2 a_{l+1}^2] - \mathbb{E}[a_l^2] \mathbb{E}[a_{l+1}^2]) \\
&= 2 \sum_{l=0}^{L-2} ([\pi_H(4)(1-\alpha)^2 + \pi_L(4)\beta(1-\alpha)] \mathbb{E}[a_l^2] \mathbb{E}[a_{l+1}^2] \\
&\quad - \pi_H(l) \mathbb{E}[a_l^2] \pi_H(l+1) \mathbb{E}[a_{l+1}^2]) \\
&= 2 \sum_{l=0}^{L-2} (\pi_H(4)\pi_H(1) - \pi_H(l)\pi_H(l+1)) \mathbb{E}[a_l^2] \mathbb{E}[a_{l+1}^2]. \tag{4.23}
\end{aligned}$$



Similarly, we can derive the third and the fourth terms of (4.21) as follows:

$$\begin{aligned}
& 2 \sum_{l=0}^{L-3} \text{cov}[a_l^2, a_{l+2}^2] \\
&= 2 \sum_{l=0}^{L-3} (\mathbb{E}[a_l^2 a_{l+2}^2] - \mathbb{E}[a_l^2] \mathbb{E}[a_{l+2}^2]) \\
&= 2 \sum_{l=0}^{L-3} ([\pi_H(4)(1-\alpha)^3 + \pi_H(4)(1-\alpha)\alpha\beta \\
&\quad + \pi_L(4)\beta(1-\alpha)^2 + \pi_L(4)\alpha\beta^2] \mathbb{E}[a_l^2] \mathbb{E}[a_{l+2}^2] \\
&\quad - \pi_H(l) \mathbb{E}[a_l^2] \pi_H(l+2) \mathbb{E}[a_{l+2}^2]) \\
&= 2 \sum_{l=0}^{L-3} (\pi_H(4)\pi_H(2) - \pi_H(l)\pi_H(l+2)) \mathbb{E}[a_l^2] \mathbb{E}[a_{l+2}^2] \tag{4.24}
\end{aligned}$$

and

$$\begin{aligned}
& 2 \sum_{l=0}^{L-4} \text{cov}[a_l^2, a_{l+3}^2] \\
&= 2 \sum_{l=0}^{L-4} \mathbb{E}[a_l^2] \mathbb{E}[a_{l+3}^2] \{ \pi_H(4)[(1-\alpha)^4 + (1-\alpha)^2\alpha\beta \\
&\quad + (1-\alpha)\alpha\beta(1-\alpha) + (1-\alpha)\alpha(1-\beta)\beta] \\
&\quad + \pi_L(4) [\beta(1-\alpha)^3 + \beta(1-\alpha)\alpha\beta \\
&\quad + \beta\alpha(1-\beta)\beta + \beta\alpha\beta(1-\alpha)] \} \\
&\quad - \pi_H(l)\mathbb{E}[a_l^2]\pi_H(l+3)\mathbb{E}[a_{l+3}^2] \\
&= 2 \sum_{l=0}^{L-4} (\pi_H(4)\pi_H(3) - \pi_H(l)\pi_H(l+3))\mathbb{E}[a_l^2]\mathbb{E}[a_{l+3}^2]. \tag{4.25}
\end{aligned}$$

From (4.22) to (4.25), we can compute  $\text{var}[s_{p1}]$  of (4.19). The remaining terms of (4.19) will be derived in Appendix H.

### 4.4.3 SNR for PPM signal in the UWB channel

With the mean and the variance of the processed data  $z$ , we can compute the energy of a PPM signal in the UWB channel as

$$S_{p1} = \mathbb{E}[s_{p1}^2] = \mathbb{E}[s_{p1}]^2 + \text{var}[s_{p1}], \tag{4.26}$$

where

$$\mathbb{E}[s_{p1}] = \sum_{l=1}^L \pi_H(l)\mathbb{E}[a_l^2], \tag{4.27}$$

$\mathbb{E}[a_l^2]$  is given in (4.5), and  $\text{var}[s_{p1}]$  can be obtained from (4.21). As for the noise energy  $N_{p1}$ , it can be calculated by

$$\begin{aligned}
N_{p1} &= \text{var}[r_{p1}] + \text{var}[n_{p1}] + \text{var}[n_{p0}] \\
&\quad + \mathbb{E}[r_{p1}]^2 + \mathbb{E}[n_{p1}]^2 + \mathbb{E}[n_{p0}]^2, \tag{4.28}
\end{aligned}$$

where  $\mathbb{E}[r_{p1}]$ ,  $\mathbb{E}[n_{p1}]$ ,  $\mathbb{E}[n_{p0}]$ ,  $\text{var}[r_{p1}]$ ,  $\text{var}[n_{p1}]$ , and  $\text{var}[n_{p0}]$  are given in (G.5), (G.6), (G.7), (H.1), (H.3), and (H.4), respectively. According to the results obtained (4.26) and (4.28), we can estimate the  $\text{SNR}_{p1}$  of the processed data  $z_{p1}$  by

$$\text{SNR}_{p1} = \frac{S_{p1}}{N_{p1}}. \quad (4.29)$$

We will perform simulations to validate the accuracy of the proposed analytical method in Section 4.6.

## 4.5 Effect of Multiple Transmit and Receive Antennas

### 4.5.1 Repetition Codes

Figure 4.1 (a) shows the scenario of using repetition code with no diversity (Tx1-Rx1) in the case  $N_p = 2$ . First, we define the processed data  $z_{p1,T1}^{(f1)}$  and  $z_{p1,T1}^{(f2)}$  in frames 1 and 2 as:

$$z_{p1,T1}^{(f1)} = s_{p1,T1} + r_{p1,T1} + n_{p1}^{(f1)} + n_{p0}^{(f1)} \quad (4.30)$$

and

$$z_{p1,T1}^{(f2)} = s_{p1,T1} + r_{p1,T1} + n_{p1}^{(f2)} + n_{p0}^{(f2)}, \quad (4.31)$$

where  $s$ ,  $r$ , and  $n$  represent the signal part, the redundancy part, and the noise part of the processed data  $z$ , the superscript  $(fi)$  means the  $i$ -th frame, the subscript  $p1$  means the message bit  $d^{(i)} = 1$ , and the subscript  $Ti$  means the  $i$ -th transmit antenna. Denote the processed data for the no diversity scheme as  $z_{p1}^{\text{ND}}$ . Then, we have

$$\begin{aligned} z_{p1}^{\text{ND}} &= z_{p1,T1}^{(f1)} + z_{p1,T1}^{(f2)} \\ &= 2s_{p1,T1} + 2r_{p1,T1} + n_{p1}^{(f1)} + n_{p0}^{(f1)} + n_{p1}^{(f2)} + n_{p0}^{(f2)}. \end{aligned} \quad (4.32)$$



From (4.17), (4.19), and (4.32), the mean and variance of the processed data  $z_{p1}^{\text{ND}}$  can be computed respectively by

$$\begin{aligned}\mathbb{E}[z_{p1}^{\text{ND}}] &= 2\mathbb{E}[s_{p1,T1}] + 2\mathbb{E}[r_{p1,T1}] \\ &\quad + \mathbb{E}[n_{p1}^{(f1)}] + \mathbb{E}[n_{p0}^{(f1)}] + \mathbb{E}[n_{p1}^{(f2)}] + \mathbb{E}[n_{p0}^{(f2)}].\end{aligned}\quad (4.33)$$

and

$$\begin{aligned}\text{var}[z_{p1}^{\text{ND}}] &= \text{var}[2 \cdot s_{p1,T1}] + \text{var}[2 \cdot r_{p1,T1}] + \text{var}[n_{p1}^{(f1)}] \\ &\quad + \text{var}[n_{p0}^{(f1)}] + \text{var}[n_{p1}^{(f2)}] + \text{var}[n_{p0}^{(f2)}].\end{aligned}\quad (4.34)$$

Represent  $S_{p1}^{\text{ND}}$  and  $N_{p1}^{\text{ND}}$  as the signal energy and the noise energy of the processed data  $z_{p1}^{\text{ND}}$ , respectively. Then, we have

$$S_{p1}^{\text{ND}} = 4\mathbb{E}[s_{p1}]^2 + 4\text{var}[s_{p1}],\quad (4.35)$$

where  $\text{var}[s_{p1}]$  and  $\mathbb{E}[s_{p1}]$  can be obtained from (4.21) and (4.27), respectively.

Furthermore, the noise energy  $N_{p1}^{\text{ND}}$  can be derived as

$$\begin{aligned}N_{p1}^{\text{ND}} &= 2\sigma_n^2 \sum_{l=0}^{L-1} \pi_H(l) \mathbb{E}[a_l^2] \\ &\quad + 2 \sum_{l=0}^{L-\delta-1} \pi_H(l) \pi_H(1+\delta) \mathbb{E}[a_l^2] \mathbb{E}[a_{l+\delta}^2].\end{aligned}\quad (4.36)$$

Thus, by substituting related channel information of  $a_l$  and  $\pi_H(l)$  into (4.36),  $N_{p1}^{\text{ND}}$  can be also obtained analytically. From (4.35) and (4.36), we show how to calculate  $\text{SNR}_{p1}^{\text{ND}}$  analytically.

## 4.5.2 Receive Diversity

Consider the receive diversity scheme (Tx1-Rx2) having repetition codes with  $N_p = 2$  as shown in Fig. 4.1 (b). We express the processed data  $z_{p1}^{\text{RD}}$  for the receive diversity scheme as follows:

$$z_{p1}^{\text{RD}} = z_{p1,T1}^{\text{ND}} + z_{p1,T2}^{\text{ND}},\quad (4.37)$$

where the superscript RD means receive diversity. Clearly, we can use the same method of obtaining  $\mathbb{E}[z_{p1}^{\text{ND}}]$  in (4.33) to compute the mean of the processed data  $z_{p1}^{\text{RD}}$ , which is defined as

$$\mathbb{E}[z_{p1}^{\text{RD}}] = \mathbb{E}[z_{p1,T1}^{\text{ND}}] + \mathbb{E}[z_{p1,T2}^{\text{ND}}]. \quad (4.38)$$

Likewise, the variance of the processed data  $z_{p1}^{\text{RD}}$  can be calculated by

$$\text{var}[z_{p1}^{\text{RD}}] = \text{var}[z_{p1,T1}^{\text{ND}}] + \text{var}[z_{p1,T2}^{\text{ND}}]. \quad (4.39)$$

Denote  $S_{p1}^{\text{RD}}$  and  $N_{p1}^{\text{RD}}$  as the signal energy and the noise energy of the processed data  $z_{p1}^{\text{RD}}$ , respectively and recall that the (Tx1-Rx2) receive diversity scheme and repetition length  $N_p = 2$  is considered. Then we have

$$S_{p1}^{\text{RD}} = 16\mathbb{E}[s_{p1}]^2 + 8\text{var}[s_{p1}] \quad (4.40)$$

and

$$N_{p1}^{\text{RD}} = 2N_{p1}^{\text{ND}}. \quad (4.41)$$

### 4.5.3 Transmit Diversity

Now we consider a time-switched transmit diversity (TSTD) (Tx2-Rx1) scheme as shown in Fig. 4.1 (c). For the case with repetition length  $N_p = 2$ , one can express the processed data  $z_{p1}^{\text{TD}}$  for the transmit diversity scheme as follows:

$$z_{p1}^{\text{TD}} = z_{p1,T1}^{(f1)} + z_{p1,T2}^{(f2)}. \quad (4.42)$$

Since

$$\mathbb{E}[z_{p1}^{\text{TD}}] = \mathbb{E}[z_{p1,T1}] + \mathbb{E}[z_{p1,T2}] = 2\mathbb{E}[z_{p1}], \quad (4.43)$$

we can calculate  $\mathbb{E}[z_{p1}^{\text{TD}}]$  by following the procedures of evaluating  $\mathbb{E}[z_{p1}]$  in (4.17). Define  $\rho$  as the correlation coefficient between the two transmit antennas. Then the variance of the processed data  $z_{p1}^{\text{TD}}$  is

$$\begin{aligned} \text{var}[z_{p1}^{\text{TD}}] &= \text{var}[z_{p1,T1}] + \text{var}[z_{p1,T2}] + 2\text{cov}[z_{p1,T1}, z_{p1,T2}] \\ &= 2\text{var}[z_{p1}] + 2\rho \left( \sqrt{\text{var}[s_{p1,T1}]\text{var}[s_{p1,T2}]} \right. \\ &\quad \left. + \sqrt{\text{var}[r_{p1,T1}]\text{var}[r_{p1,T2}]} \right) \end{aligned} \quad (4.44)$$

where  $\text{var}[z_{p1}]$  is defined in (4.19) of Proposition 2. Thus, we can compute  $\text{SNR}^{\text{TD}}$  from

$$S_{p1}^{\text{TD}} = 4\mathbb{E}[s_{p1}]^2 + 2(1 + \rho)\text{var}[s_{p1}] \quad (4.45)$$

and

$$N_{p1}^{\text{TD}} = 2N_{p1}^{\text{ND}}, \quad (4.46)$$

where  $\mathbb{E}[s_{p1}]$ ,  $\text{var}[s_{p1}]$  and  $N_{p1}^{\text{ND}}$  are given in (4.27), (4.21), and (4.36), respectively.



## 4.6 Numerical Results

### 4.6.1 The UWB Channel Response

Figure 4.2 shows an example of the UWB channel response using the channel model described in Section 4.2 with parameters listed in Table 4.1. In the considered model, the channel response time is set to 225 nanoseconds as in [9], the average number of the resolvable paths is 80.72. Let  $N$  be the total time bin number during the channel response time,  $T_A$  the first path arrival time, and  $t_i$  is the arrival time of each resolvable path. Then, in our simulations, the mean excess delay  $T_m = \frac{\sum_{i=1}^N (t_i - T_A) a_i^2}{\sum_{i=1}^N a_i^2} = 34.61$  nanoseconds,

and the root mean square delay spread  $T_{RMS} = \sqrt{\frac{\sum_{i=1}^N (t_i - T_m - T_A)^2 a_i^2}{\sum_{i=1}^N a_i^2}} = 37.98$  nanoseconds.

## 4.6.2 Average SNR and Variance of the Pulse Based UWB Signals

Figure 4.3 compares the SNR of PPM signals for no diversity, receive diversity, and transmit diversity schemes. Through simulations, we validate the analytical results obtained by (4.35), (4.36), (4.40), (4.41), (4.45), and (4.46) in Section 4.4. From Fig. 4.3, one can find that the SNR of the receive diversity is the highest, while the no diversity scheme and the transmit diversity have the similar SNR.

Figure 4.4 shows the variance of PPM signals with no diversity, receive diversity, and transmit diversity schemes in the UWB channel by analysis and simulations. From the viewpoint of the signal variance, transmit diversity is the best, no diversity ranks second, and receive diversity is the worst. Here, we assume that the antennas of both receive diversity and transmit diversity are mutually independent.

Figure 4.5 shows the effect of spatial correlation  $\rho$  of transmit diversity on the variance of the PPM signals over the UWB channel. As shown in the figure, the variance of the PPM signals increases as the correlation of transmit diversity increases. From the results, it is implied that the diversity gain of transmit diversity may not be significant in the UWB channel. In the following, we will quantify the performance difference between no diversity and having antenna diversity in terms of BER performance.

### 4.6.3 Comparison for Different Diversity Schemes for the PPM UWB System

Figure 4.6 shows the BER performances of different diversity schemes for the binary PPM signals in the UWB channel. In the figure, the numbers adjacent to Tx and Rx represent the numbers of the transmit and receive antennas;  $L$  represents the finger number in the RAKE receiver;  $f$  represents the frame number; and  $\delta$  represents the modulation index associated with the message bit which is an integer multiple of the chip time  $T_c$ . From Fig. 4.6, we have the following observations:

- Comparing the no diversity (Tx1-Rx1) scheme to the time switched transmit diversity (Tx2-Rx1) scheme, one can find that the TSTD scheme can improve BER performance by about 2 dB at  $\text{BER} = 10^{-4}$ . As shown in Fig. 4.4, the signal of the transmit diversity scheme is more stable than that of the no diversity scheme, which can explain the BER performance improvement of the transmit diversity scheme over the no diversity scheme even though the SNRs of these two diversity schemes are about the same in Fig. 4.3.
- Recall that the diversity order can be roughly viewed as the slope of BER v.s. SNR in the region with high SNRs where the slope does not increase any more. The higher the diversity order, the steeper will be the slope of the performance curve for BER v.s. SNR. As shown in the figure, the (Tx2-Rx1) TSTD scheme indeed achieves the same diversity order as the (Tx1-Rx2) receive diversity scheme. Furthermore, comparing the Tx2-Rx2 and the Tx1-Rx4 schemes, we find that the Tx2-Rx2 scheme can achieve about the same diversity order as the Tx1-Rx4 scheme but at the cost of about 3 dB  $E_b/N_0$  loss. In this figure, it is demonstrated

that employing multiple time switched transmit diversity or multiple receive antennas can improve the UWB performance even though the UWB channel possesses inherently rich diversity.

Note that because the UWB MIMO channel may perform differently from the narrowband MIMO channel. For example, severe correlation between channel paths may exist in a UWB channel. Thus, the above results should be used cautiously as an upper bound that quantifies the extent to which transmit or receive antenna combining techniques can improve the performance for the PPM based UWB system. In the following, we will examine how to exploit transmit diversity in the UWB channel from a different perspective – reducing the complexity of Rake receiver.

#### 4.6.4 Effect of RAKE Finger Numbers

Figure 4.7 shows the BER performance of the PPM UWB system with different RAKE finger numbers. Two major remarks are given below:

- The transmit diversity scheme (Tx2-Rx1) with  $L = 30$  (with the squared legend) has the similar performance to the scheme (Tx1-Rx1) with  $L = 50$  (with the triangle legend). It is implied that the complexity of Rake receiver can be alleviated at the cost of increasing the transmit antennas by using time-switched transmit diversity.
- Because of inherit large path diversity, adding more transmit antennas in the UWB system cannot increase the diversity order significantly. In the figure, the slope of BER v.s. SNR for the cases of  $L > 50$  with single antenna (with the triangle legend) and that of  $L > 30$  with two transmit antennas (with the squared legend) are about the same. Nevertheless, transmit diversity can slightly improve the BER performance for the

PPM UWB system from the signal variance perspective as explained in Fig. 4.4.

## 4.7 Conclusions

In this chapter, we have derived an analytical expression for the PPM signal in an UWB channel characterized by the cluster effect and highly dense frequency selective fading. Furthermore, we have demonstrated that the time-switched transmit diversity combined with the template-based pulse detection can improve the performance of the PPM based UWB system.

Through analysis and simulations, we have the following two major remarks:

- Although multiple transmit or receive antennas cannot deliver diversity gain for the UWB system in the strict sense (i.e., improving the slope of BER v.s. SNR), multiple transmit antennas can improve the system performance in the manner of reducing signal variations. Thus, transmit antennas can be used to reduce receiver complexity since the number of fingers of a Rake receiver in the UWB system can be very high.
- Multiple receive antennas can provide higher antenna array combining gain. Because the transmitted power in the UWB system is extremely low, multiple receive antennas techniques can be an effective approach to improve the performance from the view point of coverage extension.

Table 4.1: System Parameters

The UWB pulse width	1 ns
The sampling time (time bin)	1 ns
Simultaneous arrival path number $n$	A modified Poisson process.
$\mu_H$	2/3
$\mu_L$	1/3
Average resolvable path power	Exponential decay.
$\gamma$	-5 dB
$\beta$	0.025
The PDF of the received signal power	Gamma distribution.
The diversity schemes	1) no diversity, Tx1-Rx1, 2) receive diversity, Tx1-Rx2, 3) transmit diversity, Tx2-Rx1, 4) transmit diversity, Tx1-Rx4, 5) MIMO, Tx2-Rx2.
The modulation schemes	PPM
The frame number $f$	2
The RAKE finger number $L$	10, 30, 50, 100, or 200
The delay time $\delta$ associated with PPM	1 ns



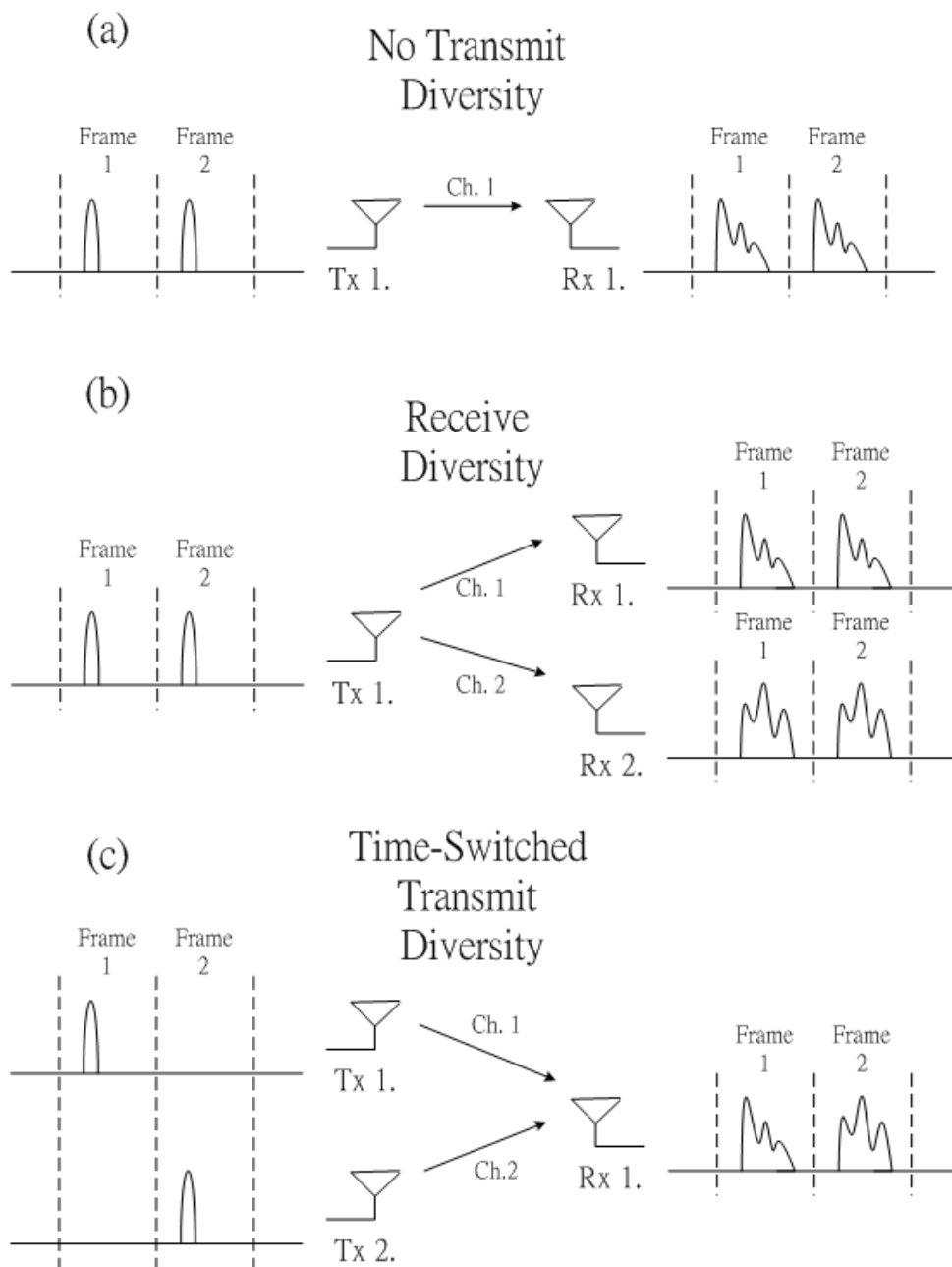


Figure 4.1: The diversity schemes: a) no diversity, b) receive diversity, and c) time-switched transmit diversity.

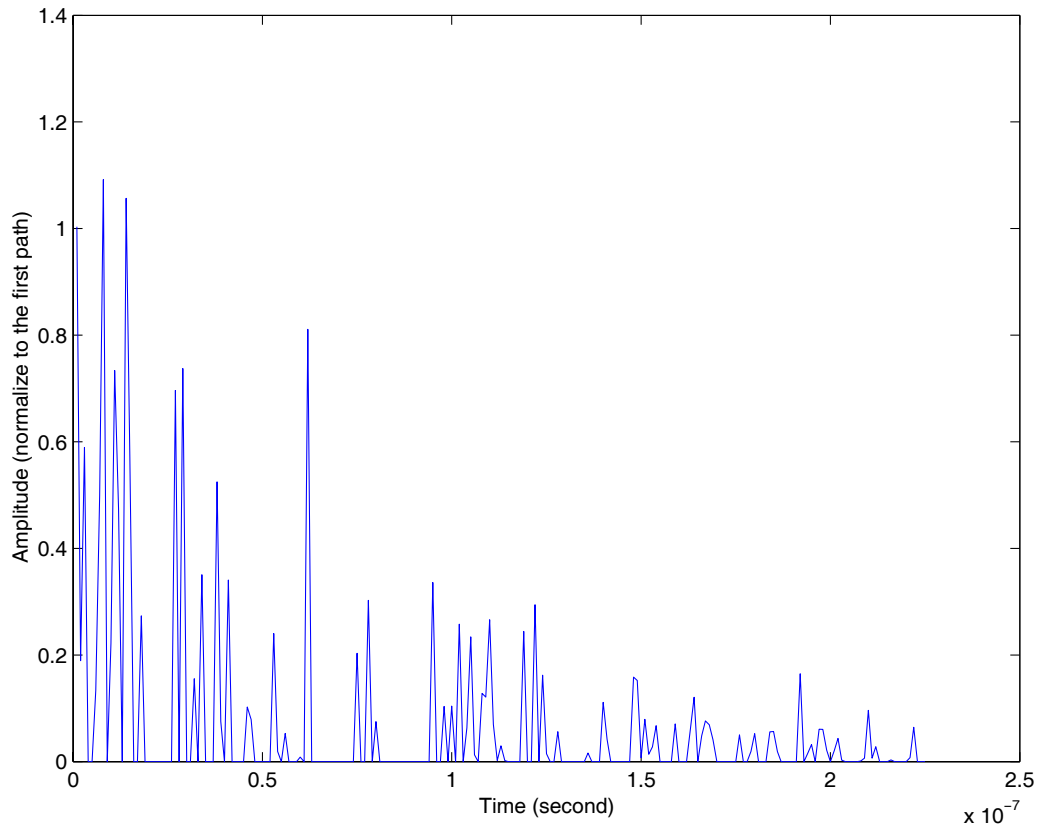


Figure 4.2: An example of the UWB channel response in the time domain.

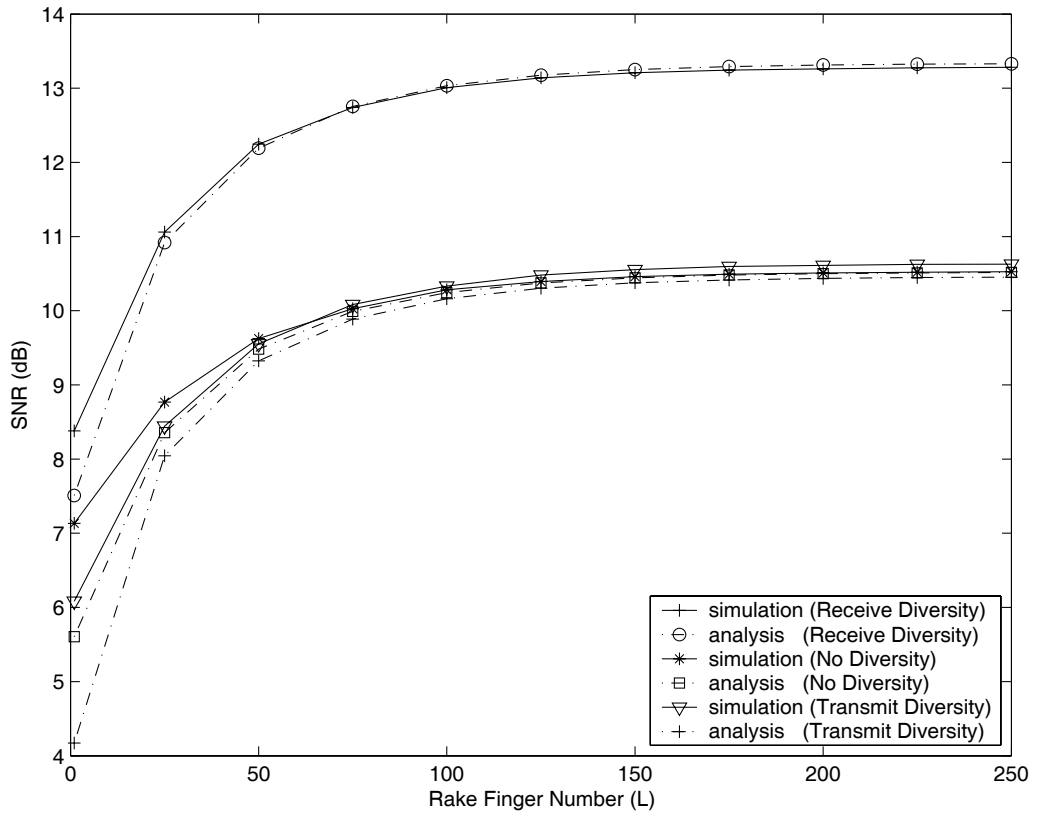


Figure 4.3: Analytical and simulation results for the SNR of the PPM signals over the UWB channel with multiple transmit and receive antennas.

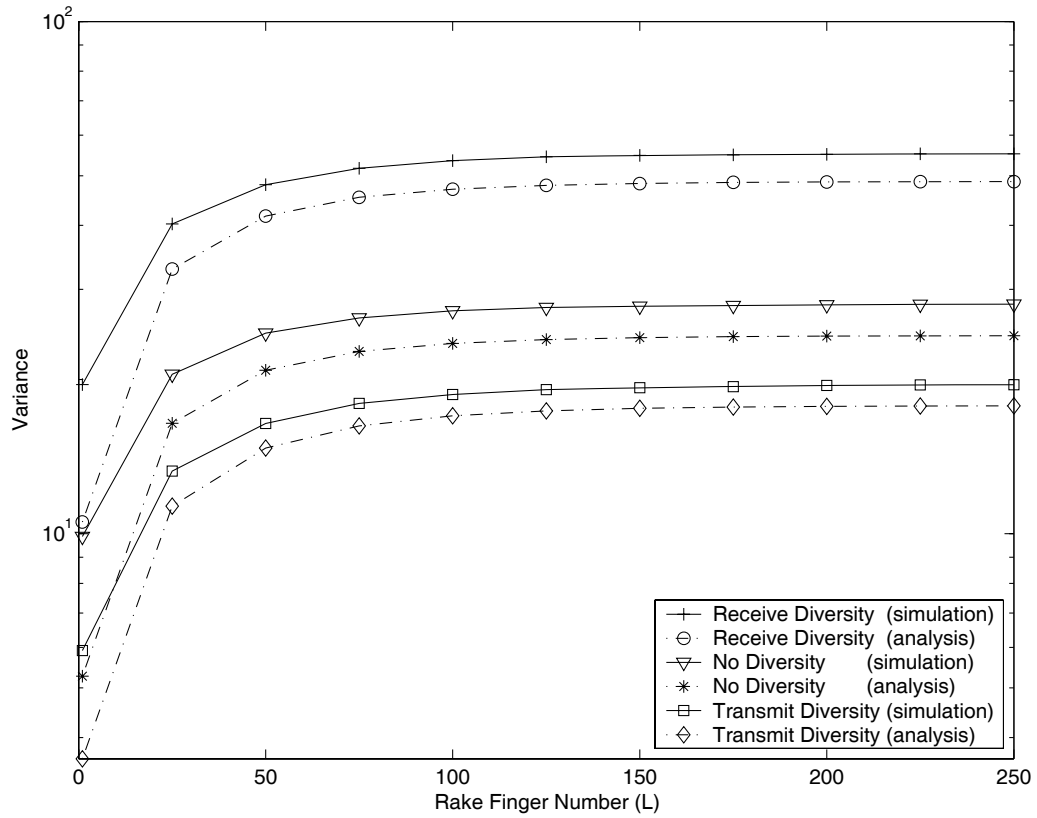


Figure 4.4: Analytical and simulation results for the variance of the PPM signals over the UWB channel with multiple transmit and receive antennas.

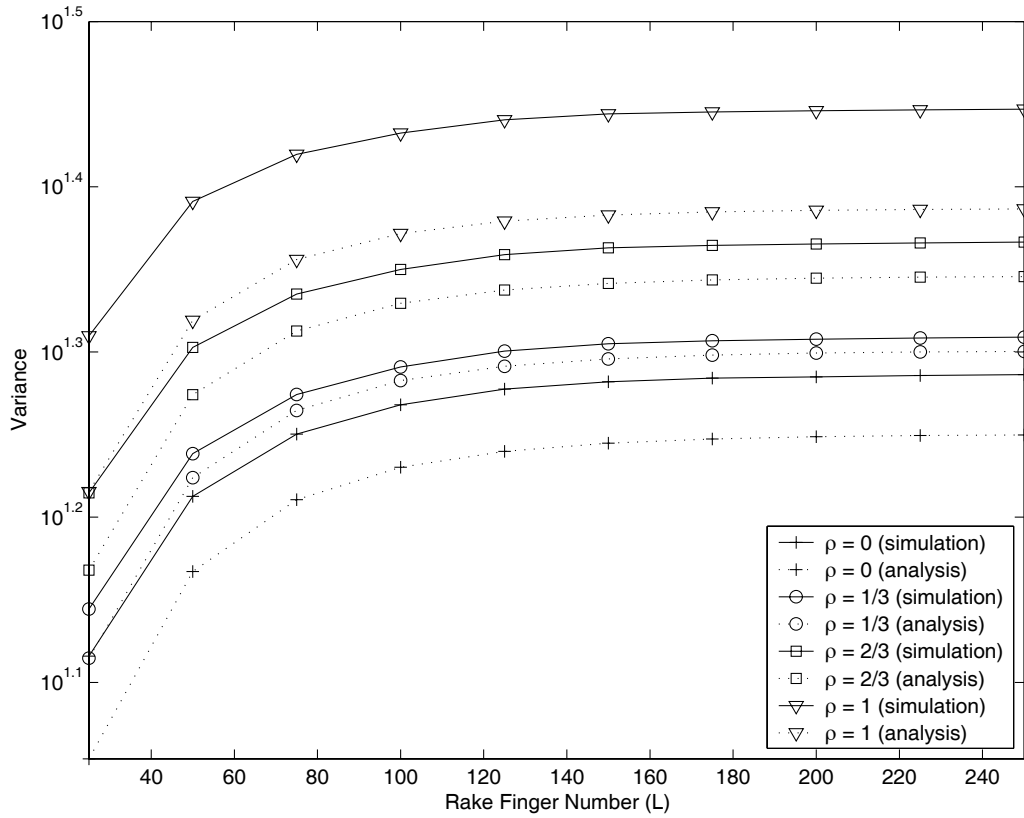


Figure 4.5: Effect of spatial correlation of transmit diversity on the variance of the PPM signals over the UWB channel.

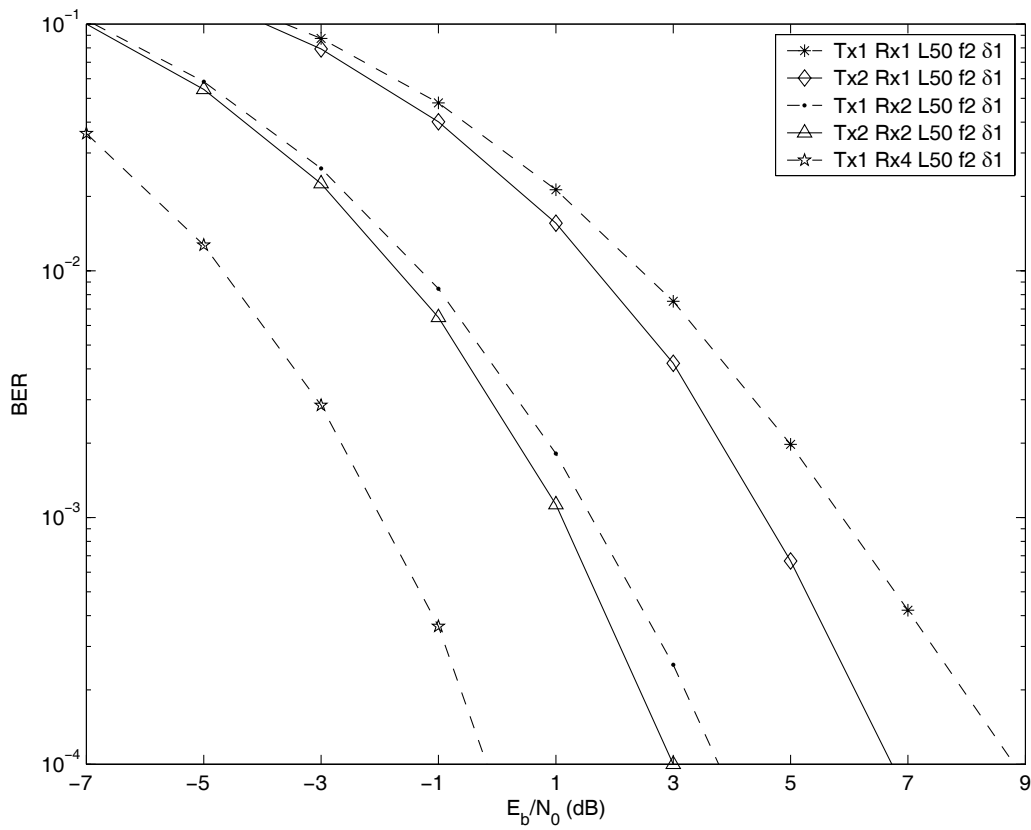


Figure 4.6: The BER simulation results for the different diversity schemes in the PPM UWB system. Here, Tx and Rx represent the transmit and the receive antenna numbers, respectively,  $L$  represents the RAKE finger number,  $f$  represents the frame number, and  $\delta$  represents the modulation index with PPM.

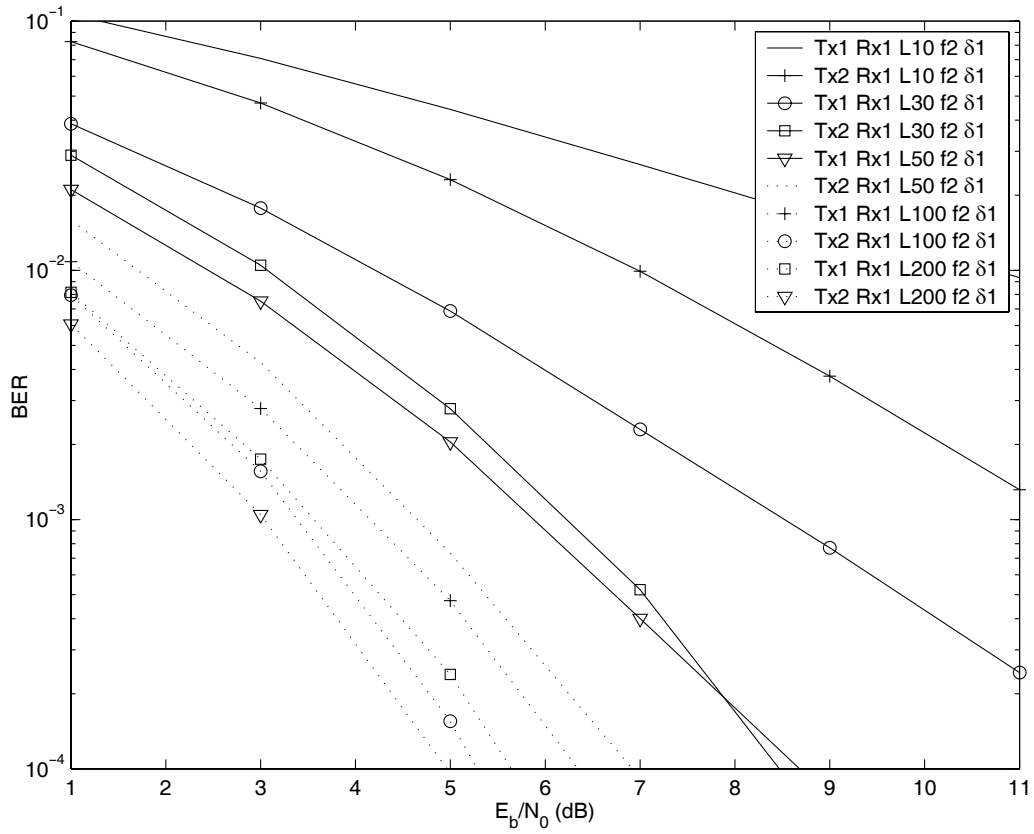


Figure 4.7: The BER simulations of the PPM UWB system with the different RAKE finger numbers, where Tx and Rx represent the transmit and the receive antenna numbers, respectively,  $L$  represents the RAKE finger number,  $f$  represents the frame number, and  $\delta$  represents the modulation index with PPM.

# Chapter 5

## BER-Minimized Space-Time-Frequency Codes for MIMO Highly Frequency-Selective Block-Fading Channels



In this chapter, we present bit error rate (BER)-minimized space-time-frequency (STF) block codes for multi-input multi-output (MIMO) highly frequency-selective block-fading channels. We consider the IEEE 802.15.3a ultra-wide band (UWB) channel models (CM) 1–4. Based on a new STF block codes design criterion with the objective of minimizing BER, we develop an efficient searching algorithm for the design of the optimal STF block codes which maximize the coding gain. For 128 subcarriers with two subcarriers jointly encoding with 2–4 transmitting antennas, we find that the optimal STF block codes for all the IEEE 802.15.3a UWB channel models CM 1–



4 can be found. Furthermore, the designed STF block codes outperform the recently published high-rate full-diversity STF codes [1] by 1 dB. Last, the proposed STF codes can be decoded by maximum likelihood decoding approach, which is simpler than the sphere decoding principle used in [1].

## 5.1 Motivation

The space-time-frequency (STF) coding is a technique which provides error control ability in multi-input multi-output (MIMO) systems, which are usually combined with the orthogonal frequency-division multiplexing (OFDM) technology. The main purpose of using the STF coding is to achieve the full diversity gain. For example, in [1], the authors proposed STF codes which achieve the diversity gain of  $N_t N_r K L$ , where  $N_t$  is the number of transmit antennas,  $N_r$  is the number of receive antennas,  $K$  is the number of independent fading blocks in one codeword, and  $L$  is the number of taps of channel impulse response (CIR) between any pair of transmit and receive antennas. The space diversity, time diversity, and frequency diversity are  $N_t N_r$ ,  $K$ , and  $L$ , respectively.

However, in a highly frequency-selective fading channel, the number of taps of CIR could be very large. For example, in the IEEE 802.15.3a UWB channel model [98], the number of taps of CIR is infinity theoretically and about 1000 to 2000 practically. Thus, it is difficult to achieve the full frequency diversity under the highly frequency-selective fading channel. Thus, it motivates us to turn to a more fundamental problem: How to design BER-minimized STF codes for MIMO highly frequency-selective block-fading channels? Here the block-fading channel is defined as follows: The channel remains the same within one fading block and is independent from one block

to another one [1].

The difficulties of design BER-minimized STF block codes for the MIMO highly frequency-selective block-fading channels can be discussed in three aspects. Note that we take the IEEE 802.15.3a UWB channel model as an example in this chapter.

1. First, the IEEE 802.15.3a channel model has four different sets of parameters, named CM1, CM2, CM3, and CM4. For different channels, we have to design different codes to reflect the channel characteristics. One challenging issue arises: Is there a universal code which is optimal for all the four channel models CM 1  $\sim$  4 for given numbers of subcarriers and transmit antennas?
2. As the numbers of subcarriers and transmit antennas increase, the number of all possible codes becomes astronomical. Thus, the second challenge is to search the optimal codes efficiently.
3. Because traditional STF coding methods focus on linear codes, it will be challenging to examine if there exist nonlinear optimal STF block codes.

To our best knowledge, the design of STF block codes for the MIMO-OFDM systems under the IEEE 802.15.3a channel models considering all the three aforementioned challenges has not been seen in the literature.

## 5.2 System Model

Figure 5.1 shows our system block diagram. First, we divide the information bits into groups. Each group has two bits. Then we pass the bits to our STF block encoder. For example, if we want to encode across two transmit

antennas and two subcarriers, then the codeword can be expressed as a matrix. Then we use an OFDM modulator to allocate every elements in the codeword to corresponding subcarriers and transmit antennas. That is,  $d_{ij}$  is allocated on the  $i$ -th subcarrier and  $j$ -th antenna, for  $i = 1, 2$  and  $j = 1, 2$ . The transmitted signals pass the IEEE 802.15.3a UWB channel. The receiver recovers the original information bits via inverse operations as in the transmitter: We first use an OFDM demodulator to find the codewords. Then we use a maximum likelihood (ML) STF block decoder to find the original information bits.

### 5.3 BER Performance

In [19], the authors approximated the average pairwise error probability (PEP) of MIMO-OFDM system under the IEEE 802.15.3a UWB channel model as

$$P_e \approx \frac{1}{\pi} \int_0^{\pi/2} \prod_{n=1}^M \left( 1 + \frac{\rho \text{eig}_n(\mathbf{S} \circ \mathbf{R}_M)}{4N_t \sin^2 \theta} \right)^{-KN_r} d\theta, \quad (5.1)$$

where  $M$  is the number of OFDM subcarriers jointly encoded,  $\rho = E_s/N_0$  is the average signal-to-noise ratio (SNR),  $E_s$  is the average transmitted energy per symbol,  $\text{eig}_n(\mathbf{A})$  is the  $n$ -th largest eigenvalues of the matrix  $\mathbf{A}$ ,

$$\mathbf{S} = (\mathbf{D} - \hat{\mathbf{D}})(\mathbf{D} - \hat{\mathbf{D}})^{\mathcal{H}}, \quad (5.2)$$

where  $\mathbf{D}$  and  $\hat{\mathbf{D}}$  are two distinct STF block codes codewords.  $\circ$  denotes the Hadamard product [99],  $\mathbf{R}_M$  is the auto-covariance matrix of the channel:

$$\mathbf{R}_M = \begin{bmatrix} 1 & R(1)^* & \dots & R(M-1)^* \\ R(1) & 1 & \dots & R(M-2)^* \\ \vdots & \vdots & \ddots & \vdots \\ R(M-1)R(M-2)\dots & & & 1 \end{bmatrix} \quad (5.3)$$

where

$$R(m) = \Omega_0 \frac{\Lambda + g(\frac{1}{\Gamma}, m)}{g(\frac{1}{\Gamma}, m)} \frac{\lambda + g(\frac{1}{\gamma}, m)}{g(\frac{1}{\gamma}, m)} \quad (5.4)$$

and

$$g(a, m) = a + j2\pi m\Delta f. \quad (5.5)$$

$\Delta f$  is the frequency separation between two adjacent subcarriers,  $N_t$  is the number of transmit antennas jointly encoded,  $K$  is the number of OFDM blocks jointly encoded, and  $N_r$  is the number of receive antennas.

At high SNR, the PEP in (5.1) can be upper bounded as

$$P_e \lesssim \prod_{n=1}^r \left( \frac{\rho}{4N_t} \text{eig}_n(\mathbf{S} \circ \mathbf{R}_M) \right)^{-KN_r}, \quad (5.6)$$

where  $r$  denotes the rank of matrix  $\mathbf{S} \circ \mathbf{R}_M$ . (5.6) implies a diversity order of  $rKN_r$  and the coding gain is

$$\text{CG} = \frac{1}{4N_t} \left[ \prod_{n=1}^r \text{eig}_n(\mathbf{S} \circ \mathbf{R}_M) \right]^{1/r}. \quad (5.7)$$

From the numerical results in [19] we observe that although (5.6) is an approximated upper bound of PEP, it is close to the simulated symbol error rate (SER).

## 5.4 The Universally Optimal STF Block Codes design

In this section, we describe a criterion and a efficient searching algorithm of the BER-minimized STF block codes.

### 5.4.1 The Optimum Criterion

Our goal is to design the STF block codes to minimize  $P_e$  in (5.6). For given  $\rho$ ,  $N_t$ ,  $N_r$ ,  $K$ , and  $M$ , it is equivalent to maximize the term

$$q = \prod_{n=1}^r \text{eig}_n(\mathbf{S} \circ \mathbf{R}_M) \quad (5.8)$$

by designing the matrix  $\mathbf{S}$ . Similar to the rank and determinant criteria of the space-time block coding (STBC) [100], we have to maximize the minimal  $q$  along the pairs of distinct codewords.

We first consider the simplest case. Let  $N_i$  be the number of input information bits for each codeword  $\mathbf{D}$ . Let  $M = N_t = N_i = 2$ . Let  $b_1, b_2 \in \{0, 1\}$  be the two input bits. We use the binary phase shift keying (BPSK) modulation. Let  $s_1$  and  $s_2$  be the two corresponding symbols, then  $s_i = \text{mod}(b_i)$  for  $i = 1, 2$ , where

$$\text{mod}(x) = \begin{cases} 1, & \text{if } x = 1, \\ -1, & \text{if } x = 0. \end{cases} \quad (5.9)$$

The codeword  $\mathbf{D}$  is a  $2 \times 2$  matrix with each element being 1 or  $-1$ , i.e.,  $\mathbf{D} \in \{1, -1\}^{2 \times 2}$ . Then there are  $2^{2 \times 2} = 16$  different codewords. Since there are two input bits, there are  $2^2 = 4$  possible inputs, i.e.,  $b_1 b_2 \in \{00, 01, 10, 11\}$ . Hence, we have to choose four distinct codewords for these four different inputs.

For the convenience of expression, let us define the demodulation function  $\text{dem}(x) \triangleq \text{mod}^{-1}(x)$  and the multiple digits version of  $\text{dem}(\cdot)$  is defined as

$$\text{dem}(\mathbf{x}) \triangleq [\text{dem}(x_1), \text{dem}(x_2), \dots, \text{dem}(x_m)], \quad (5.10)$$

where the vector  $\mathbf{x}$  stands for an  $m$ -digit number and the  $i$ -th digit is  $x_i$  for  $1 \leq i \leq m$ .

The following equation gives each codeword  $\mathbf{D}$  a unique positive integer  $n$  as its subscript:

$$\mathbf{D}_n = \left\{ \begin{bmatrix} d_{11}d_{12} \\ d_{21}d_{22} \end{bmatrix} : \text{bd}(\text{dem}(\mathbf{d}) + 1) = n \right\}, \quad (5.11)$$

where the function  $\text{bd}(x)$  is to transform a binary number  $x$  into its decimal form and  $\mathbf{d} = [d_{11}, d_{12}, d_{21}, d_{22}]$ . Now, the set that contains all the codewords is  $C = \{\mathbf{D}_1, \mathbf{D}_2, \dots, \mathbf{D}_{16}\}$ . Let  $B$  be a subset of  $C$  and  $B$  contains four codewords. Now, our problem can be mathematically described as finding a set  $B^*$  such that

$$B^* = \arg \max_{B \subset C, |B|=4} \min_{\mathbf{D}, \hat{\mathbf{D}} \in B, \mathbf{D} \neq \hat{\mathbf{D}}} \prod_{n=1}^r \text{eig}_n(((\mathbf{D} - \hat{\mathbf{D}})(\mathbf{D} - \hat{\mathbf{D}})^T) \circ \mathbf{R}_M), \quad (5.12)$$

where  $|B|$  is the number of elements of  $B$ .

### 5.4.2 An Efficient Searching Algorithm for the Optimal STF Block Codes

In order to simplify the representation of our problem and provide more insight, we introduce a graph representation to our code space. We represent each codeword as a vertex with number  $n$ , and between any two distinct vertices there is an undirected edge with metric  $q$ . Then, for the  $M = N_t = N_i = 2$  case, we can use a complete graph [101] with 16 vertices which is denoted by  $K_{16}$  to represent our code space. Then our problem becomes to find the optimal  $K_4^*$  in  $K_{16}$  such that the minimal metric in  $K_4^*$  is the largest one among that of all  $K_4$  in  $K_{16}$ . There are  $\binom{16}{4} = 1820$  distinct  $K_4$  in  $K_{16}$ . To find the minimal metric within each  $K_4$  we need to search for  $\binom{4}{2} = 6$  metrics. Thus, we need to do  $1820 \cdot 6 = 10920$  times of searching to find  $K_4^*$ .

For general  $M$ ,  $N_t$ , and  $N_i$ , there are  $2^{MN_t}$  vertices for the BPSK case. The complexity of the complete search becomes

$$O\left(\binom{2^{MN_t}}{2^{N_i}}\binom{2^{N_i}}{2}\right). \quad (5.13)$$

The complexity grows rapidly as  $M$ ,  $N_t$ , and  $N_i$  increase. Thus, it is necessary to find a more efficient algorithm to search for the optimal STF block codes.

For the case  $M = N_t = N_i = 2$  and CM1, we find that the metric  $q$  takes only on eight different values. Sorting these values in the decreasing order, we then have  $q \in \{64, 16.3314, 16, 8, 4, 1.32562, 0.331406, 0\}$ . We find that it will save many searching steps if we search  $K_4$  *subject to the largest  $m$  metrics* for  $m = 1, 2, \dots$ , until we find all  $K_4^*$  for a certain value of  $m$ . Let us take the  $M = N_t = N_i = 2$  case as an example. Please see Fig. 5.2. In this figure, we show the graph representation of the code space. In Fig. 5.2(a), we only consider the edges with the largest metric 64. Obviously, it does not contain any  $K_4$ . In Fig. 5.2(b), we consider the edges with the largest two metrics: 64 and 16.3314. After searching, we also find that there is no  $K_4$  in this graph. In Fig. 5.2(c), we consider the edges with the largest three metrics: 64, 16.3314, and 16. We find that there are totally eight  $K_4$  in this graph, they are:  $\{1, 7, 12, 14\}$ ,  $\{1, 8, 10, 15\}$ ,  $\{2, 8, 9, 15\}$ ,  $\{2, 8, 11, 13\}$ ,  $\{3, 5, 12, 14\}$ ,  $\{3, 6, 12, 13\}$ ,  $\{4, 5, 11, 14\}$ , and  $\{4, 6, 9, 15\}$ . Note that we do not need to search for the case  $m > 3$ , because we already find that the max-min value of  $q$  is 16.

We use the same method to search the optimal STF block codes for CM2, CM3, and CM4. CM2 and CM3 both have the same optimal STF block codes as CM1 does, but there are nine optimal STF block codes for CM4. These nine codes contains the eight optimal codes which are the same as that of CM1 and an additional codes  $\{4, 6, 11, 13\}$ . This is an interesting discovery that for different channel model, the optimal codes may be different. Thus,

in order to design the optimal codes, we have to take the channel model into account.

In order to design the codes that are optimal for all channel model, we choose the eight optimal STF block codes for CM1 out of  $\binom{2^{2-2}}{4} = 1820$  candidates. The next step is to transform these codes to a code structure. Take the code  $\{3, 5, 12, 14\}$  as an example, which corresponds to the  $K_4$  with bold edges in Fig. 5.2(c). According to the matrix-indexing procedure we defined in Section 5.4.1, we find these four integers correspond to the following codewords:

$$\begin{aligned} \mathbf{D}_3 &= \begin{bmatrix} -1 & -1 \\ 1 & -1 \end{bmatrix}, \mathbf{D}_5 = \begin{bmatrix} -1 & 1 \\ -1 & -1 \end{bmatrix}, \\ \mathbf{D}_{12} &= \begin{bmatrix} 1 & -1 \\ 1 & 1 \end{bmatrix}, \mathbf{D}_{14} = \begin{bmatrix} 1 & 1 \\ -1 & -1 \end{bmatrix}. \end{aligned} \quad (5.14)$$

We assign these four codewords to the information bits 00, 01, 10, and 11, respectively. Note that we can choose another assignment and the maximum value of  $q$  will not change. To discover the code structure from these codewords, we first consider the element in the first row and first column of them. They are  $\mathbf{D}_i[1, 1] = \{-1, -1, 1, 1\}$ , where  $i \in \{3, 5, 12, 14\}$ . Since each position can take values on  $-1$  or  $1$ , there are totally  $2^4 = 16$  possibilities. We establish a truth table of these 16 values, as a function of  $s_1$  and  $s_2$ . For some cases, we find it is more convenient to express the function in terms of  $b_1$  and  $b_2$ . The truth table is listed in Table 5.1. Use this table to check the function  $f(s, b)$  for all the elements of  $\mathbf{D}_i$ , we finally find the code structure is

$$\begin{bmatrix} s_1 & s_2 \\ -s_2 & s_1 \end{bmatrix}. \quad (5.15)$$

It is the Alamouti coding scheme [102]. The other seven optimal code struc-



tures are

$$\begin{aligned} & \begin{bmatrix} s_1 & s_2 \\ -s_1 s_2 s_1 \end{bmatrix}, \begin{bmatrix} s_1 & s_2 \\ s_2 - s_1 s_2 \end{bmatrix}, \begin{bmatrix} s_1 & s_2 \\ s_2 - s_1 \end{bmatrix}, \begin{bmatrix} s_1 & s_2 \\ -s_1 s_2 - s_1 \end{bmatrix}, \\ & \begin{bmatrix} s_1 & s_2 \\ -s_2 - s_1 s_2 \end{bmatrix}, \begin{bmatrix} s_1 & s_2 \\ -s_2 s_1 s_2 \end{bmatrix}, \text{ and } \begin{bmatrix} s_1 & s_2 \\ s_1 s_2 - s_1 \end{bmatrix}. \end{aligned} \quad (5.16)$$

The pseudo code of our proposed searching algorithm for the optimal STF block codes can be found in Algorithm 1. Note that in the ninth line we only consider the vertices with degree being at least three because any vertex in a  $K_4$  must satisfy this condition.

### 5.4.3 Optimal STF Block Codes for the Other Cases

We use the algorithm described in Section 5.4.2 to find the optimal STF block codes for the case  $M = N_i = 2$  and  $N_t = 3$ . We find that there are 54 different optimal STF block codes for all the four CM out of  $\binom{2^{3-2}}{4} = 635376$  candidates. In order to simplify the expression of the code matrix, we define  $s_3 \triangleq s_1 s_2$ ,  $s_{i'} \triangleq -s_i$  for  $i = 1, 2, 3$ , and  $\mathbf{s}_{ijk} \triangleq [s_i \ s_j \ s_k]$ . Then, among these 54 optimal STF block codes, 28 of them have the form of

$$\begin{bmatrix} \mathbf{s}_{123'} \\ \mathbf{s}_a \end{bmatrix} \quad (5.17)$$

and the other 26 codes have the form of

$$\begin{bmatrix} \mathbf{s}_{123} \\ \mathbf{s}_b \end{bmatrix}, \quad (5.18)$$

where  $a \in \{3'12, 23'1, 13'2', 3'12', 23'1', 3'21', 132, 231, 21'3', 3'1'2, 231', 3'2'1', 21'3, 3'1'2', 312, 2'13', 321, 2'3'1, 312', 2'13, 2'3'1', 1'3'2', 32'1, 2'31, 31'2, 1'32, 2'31', 31'2'\}$  and  $b \in \{13'2, 3'12, 23'1, 3'21, 3'12', 23'1', 3'2'1,$

---

**Algorithm 1:** The searching algorithm for the optimal STF block codes.

---

**input** :  $M, N_t, N_i$ , and CM.  
**output:**  $B^*$ .

- 1  $B^* \leftarrow \emptyset$
- 2  $G \leftarrow K_{2^{MN_t}}$
- 3 found  $\leftarrow$  False
- 4 **foreach**  $1 \leq i, j \leq 2^{MN_t}$  **do**
- 5      $\mathbf{S} \leftarrow (\mathbf{D}_i - \mathbf{D}_j)(\mathbf{D}_i - \mathbf{D}_j)^{\mathcal{H}}$
- 6      $E(G)_{i,j} \leftarrow \prod_{n=1}^r \text{eig}_n(\mathbf{S} \circ \mathbf{R}_M(\text{CM}))$
- 7 metric  $\leftarrow$  list of distinct values of  $E(G)$  in decreasing order
- 8 **for**  $m \leftarrow 1$  **to** Length(metric) **do**
- 9      $F \leftarrow (\{e : e \in E(G), e \geq \text{metric}[m]\}, \{v : v \in V(G), \text{deg}(v) \geq 3\})$
- 10    **foreach**  $B, \{B \subset F, |V(B)| = 2^{N_i}\}$  **do**
- 11        **if**  $B$  is  $K_{2^{N_i}}$  **then**
- 12            found  $\leftarrow$  True
- 13             $B^* \leftarrow B^* \cup \{B\}$
- 14        **if** found **then**
- 15            **return**  $B^*$

---

Table 5.1: The truth table for discovering the code structure from the optimal codewords. The operator  $\sim$  is bitwise NOT,  $\&$  is bitwise AND, and  $|$  is bitwise OR.

$\mathbf{D}_i[1, 1]$	$f(s, b)$
$\{-1, -1, -1, -1\}$	$-1$
$\{-1, -1, -1, 1\}$	$(-1)^{\sim(b_1 \& b_2)}$
$\{-1, -1, 1, -1\}$	$(-1)^{(\sim b_1)   b_2}$
$\{-1, -1, 1, 1\}$	$s_1$
$\{-1, 1, -1, -1\}$	$(-1)^{b_1   (\sim b_2)}$
$\{-1, 1, -1, 1\}$	$s_2$
$\{-1, 1, 1, -1\}$	$-s_1 s_2$
$\{-1, 1, 1, 1\}$	$(-1)^{\sim(b_1   b_2)}$
$\{1, -1, -1, -1\}$	$(-1)^{b_1   b_2}$
$\{1, -1, -1, 1\}$	$s_1 s_2$
$\{1, -1, 1, -1\}$	$-s_2$
$\{1, -1, 1, 1\}$	$(-1)^{(\sim b_1) \& b_2}$
$\{1, 1, -1, -1\}$	$-s_1$
$\{1, 1, -1, 1\}$	$(-1)^{b_1 \& (\sim b_2)}$
$\{1, 1, 1, -1\}$	$(-1)^{b_1 \& b_2}$
$\{1, 1, 1, 1\}$	$1$

21'3', 3'1'2, 132', 231', 21'3, 3'1'2', 2'13', 2'3'1, 1'3'2, 312', 2'13, 321', 2'3'1', 2'31, 31'2, 32'1', 2'31', 31'2', 1'32'}. For the case  $M = N_i = 2$  and  $N_t = 4$ , we find 5148 different optimal STF block codes for all the four CM out of  $\binom{2^{4-2}}{4} = 174792640$  candidates. Due to the space limit, we do not list all codes here. One of the optimal STF block codes is

$$\begin{bmatrix} s_1 & s_1 & s_2 - s_1 s_2 \\ s_2 - s_1 s_2 s_1 & s_2 & \end{bmatrix}. \quad (5.19)$$

For the case  $M = 3$  and  $N_i = N_t = 2$ , there is an interesting fact. We find that there does not exist any optimal STF block codes for all the four CM out of  $\binom{2^{2 \cdot 3}}{4} = 635376$  candidates. For CM1, there are 0 linear code and 80 nonlinear codes. One of the nonlinear codes is

$$\begin{bmatrix} s_1 & s_1 \\ -1 & s_2 \\ -s_1 s_2 s_1 s_2 \end{bmatrix}. \quad (5.20)$$

For CM2, there are 48 linear codes and 144 nonlinear codes. One of the linear codes and one of the nonlinear codes are

$$\begin{bmatrix} s_1 & s_1 \\ s_1 & s_2 \\ s_2 - s_2 \end{bmatrix} \quad \text{and} \quad \begin{bmatrix} s_1 & s_1 \\ -1 & s_2 \\ -s_1 s_2 s_1 s_2 \end{bmatrix}, \quad (5.21)$$

respectively. For CM3, there are 0 linear code and 16 nonlinear codes. One of the nonlinear codes is

$$\begin{bmatrix} s_1 & s_1 \\ s_2 & -s_1 s_2 \\ -s_1 s_2 & -s_2 \end{bmatrix}. \quad (5.22)$$

For CM4, there are 0 linear code and 16 nonlinear codes. One of the nonlinear

codes is

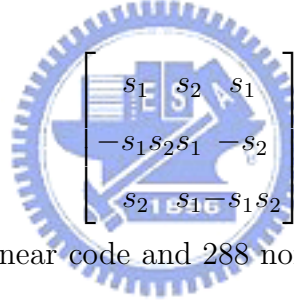
$$\begin{bmatrix} s_1 & s_1 \\ s_2 & -s_1s_2 \\ -s_1s_2 & -s_2 \end{bmatrix}. \quad (5.23)$$

Due to the space limit, we do not list all optimal codes here.

For the case  $M = N_t = 3$  and  $N_i = 2$ , we find that there does not exist any optimal STF block codes for all the four CM out of  $\binom{2^{3-3}}{4} = 2829877120$  candidates. For CM1, there are 0 linear code and 96 nonlinear codes. One of the nonlinear codes is

$$\begin{bmatrix} s_1 & s_2 & s_1 \\ -s_1s_2 & -1 & s_1s_2 \\ s_2 & -s_1 & s_2 \end{bmatrix}. \quad (5.24)$$

For CM2, there are 0 linear code and 192 nonlinear codes. One of the nonlinear codes is



$$\begin{bmatrix} s_1 & s_2 & s_1 \\ -s_1s_2s_1 & -s_2 & \\ s_2 & s_1 & s_1s_2 \end{bmatrix}. \quad (5.25)$$

For CM3, there are 0 linear code and 288 nonlinear codes. One of the nonlinear codes is

$$\begin{bmatrix} s_1 & s_2 & s_1 \\ -s_1s_2s_1 & -s_2 & \\ s_2 & s_1 & -s_1s_2 \end{bmatrix}. \quad (5.26)$$

For CM4, there are 0 linear code and 48 nonlinear codes. One of the nonlinear codes is

$$\begin{bmatrix} s_1 & s_2 & -s_1s_2 \\ -s_1s_2 & s_2 & -s_1 \\ s_1 & -s_2 & -s_1s_2 \end{bmatrix}. \quad (5.27)$$

For the case  $M = 3, N_t = 4$ , and  $N_i = 2$ , we find that the set of optimal STF block codes for all the four CM are the same. There are totally 1464

optimal codes out of  $\binom{2^{4-3}}{4} = 11710951848960$  candidates and they are all nonlinear. One of the optimal codes is

$$\begin{bmatrix} s_1 & s_2 & s_1 & s_2 \\ s_2 & -s_1s_2 - s_1s_2 & -s_1 & \\ -s_1s_2 & s_1 & -s_2 & -s_1s_2 \end{bmatrix}. \quad (5.28)$$

For the case  $M = 4$  and  $N_i = N_t = 2$ , we find that there does not exist any optimal STF block codes for all the four CM out of  $\binom{2^{2-4}}{4} = 174792640$  candidates. For CM1, there are 0 linear code and 18 nonlinear codes. One of the nonlinear codes is

$$\begin{bmatrix} s_1 & s_1 \\ -s_1 & s_1 \\ s_2 & s_2 \\ -s_1s_2s_1s_2 \end{bmatrix}. \quad (5.29)$$

For CM2, there are 10 linear codes and 18 nonlinear codes. One of the linear codes and one of the nonlinear codes are

$$\begin{bmatrix} s_1 & s_1 \\ -s_1 & s_1 \\ s_2 & s_2 \\ s_2 & -s_2 \end{bmatrix} \text{ and } \begin{bmatrix} s_1 & s_1 \\ -s_1 & s_1 \\ s_2 & s_2 \\ -s_1s_2s_1s_2 \end{bmatrix}, \quad (5.30)$$

respectively. For CM3, there are 32 linear codes and 64 nonlinear codes. One of the linear codes and one of the nonlinear codes are

$$\begin{bmatrix} s_1 & s_1 \\ s_1 - s_1 \\ s_2 & s_2 \\ s_2 - s_2 \end{bmatrix} \text{ and } \begin{bmatrix} s_1 & s_1 \\ s_1 & -s_1 \\ s_2 & s_2 \\ -s_1s_2s_1s_2 \end{bmatrix}, \quad (5.31)$$

respectively. For CM4, there are 0 linear codes and 160 nonlinear codes. One

of the nonlinear codes is

$$\begin{bmatrix} s_1 & s_1 \\ s_2 & -s_1s_2 \\ -s_1s_2 & s_2 \\ s_2 & s_1s_2 \end{bmatrix}. \quad (5.32)$$

For the case  $M = 4, N_i = 2$ , and  $N_t = 3$ , we find that there does not exist any optimal STF block codes for all the four CM out of  $\binom{2^{3 \cdot 4}}{4} = 11710951848960$  candidates. For CM1, there are 0 linear code and 2112 nonlinear codes. One of the nonlinear codes is

$$\begin{bmatrix} s_1 & s_1 & s_1 \\ s_2 & s_2 & -s_2 \\ -1 - s_1s_2 - s_1s_2 \\ s_1 - s_1s_2 & s_1s_2 \end{bmatrix}. \quad (5.33)$$

For CM2, there are 0 linear code and 4608 nonlinear codes. One of the nonlinear codes is

$$\begin{bmatrix} s_1 & s_2 & -s_1s_2 \\ -s_1s_2 & s_1 & s_2 \\ s_2 & -1 & s_1s_2 \\ -s_1s_2 - s_1 & s_2 \end{bmatrix}. \quad (5.34)$$

For CM3, there are 0 linear code and 384 nonlinear codes. One of the nonlinear codes is

$$\begin{bmatrix} s_1 & s_2 & -s_1s_2 \\ s_2 & -s_1s_2 & -s_2 \\ s_1 & s_2 & s_1s_2 \\ -s_1s_2 & -s_2 & s_1 \end{bmatrix}. \quad (5.35)$$

For CM4, there are 0 linear code and 96 nonlinear codes. One of the nonlinear

Table 5.2: The coding gain of the optimal codes we have found in Section 5.4.

Coding Gain (dB)	CM1	CM2	CM3	CM4
$N_t = 2$	0	0	0	0
$N_t = 3$	0.64	0.66	0.71	0.84
$N_t = 4$	0.49	0.50	0.54	0.61

codes is

$$\begin{bmatrix} s_1 & s_2 & -s_1 s_2 \\ -s_1 s_2 & s_2 & -s_1 \\ s_1 & -s_2 - s_1 s_2 \\ -s_1 s_2 - s_2 & -s_1 & \end{bmatrix}. \quad (5.36)$$

## 5.5 Properties of the Optimal STF Block Codes

### 5.5.1 Coding Gain

The coding gain of a code can be computed via (5.7). In Table 5.2 we list the coding gain of the optimal codes we have found in Section 5.4. For the  $N_t = 2$  case, the optimal STF block code is Alamouti code. Its coding gain is one [100]. For the  $N_t = 3$  and  $N_t = 4$  cases, we find that the coding gain is greater than 0 dB by a little amount. Thus, we can predict that the BER performance of these three codes will be very close.

### 5.5.2 The Linearity

In Table 5.1, we observe that some elements only associate with linear operations, they are  $-1, s_1, s_2, -s_2, -s_1$ , and 1. The other ten elements use



nonlinear operations. In the STBC cases, we usually consider the code structure that only use the linear operations for the simplicity. Some examples are given in [100, Chapter 3]. Using the complete search, we find that almost all optimal STF block codes in Section 5.4 use nonlinear operations. Thus, our searching algorithm can find the codes use linear operations as well as nonlinear operations. The story also tell us that it is necessary to consider the codes which use nonlinear operations and is much different from the traditional STBC which only use linear operations.

### 5.5.3 Diversity Order

The diversity order of a code is  $rKN_r$ . The optimal codes we found above all have the same value of  $r$  for the same values of  $M$ ,  $N_i$ ,  $N_t$ , and CM and the same modulation. Thus, for the same values of  $K$  and  $N_r$ , the optimal codes achieves the same diversity order under the same condition. The values of  $r$  for different kinds of optimal codes are listed in Table 5.3. From this table, we find a interesting fact. Sometimes the optimal codes achieve different diversity order for different values of CM. For example, when  $M = 3$ ,  $N_i = 2$ ,  $N_t = 2$ , and the modulation is BPSK, the diversity order is two for CM1 and CM2 and three for CM3 and CM4.

## 5.6 Numerical Results

Our simulation environment is a multiband UWB MIMO system. The number of total subcarriers is 128 and the sub-band bandwidth is 528 MHz. We apply the IEEE 802.15.3a UWB channel model CM 1  $\sim$  4 [98].

Table 5.3: The values of  $r$  which is the rank of matrix  $\mathbf{S} \circ \mathbf{R}_M$  for different kinds of optimal STF block codes.

$M$	$N_i$	$N_t$	CM	modulation	$r$
2	2	2	1-4	BPSK	2
2	2	2	1-4	QPSK	2
2	2	3	1-4	BPSK	2
2	2	4	1-4	BPSK	2
3	2	2	1,2	BPSK	2
3	2	2	3,4	BPSK	3
3	2	3	1	BPSK	2
3	2	3	2-4	BPSK	3
3	2	4	1-4	BPSK	3
4	2	2	1	BPSK	3
4	2	2	2,3	BPSK	2
4	2	2	4	BPSK	4
4	2	3	1	BPSK	3
4	2	3	2-4	BPSK	4

### 5.6.1 Impact of Number of Transmit Antennas Jointly Encoded ( $N_t$ ) for Two Subcarriers Jointly Encoded ( $M = 2$ )

Figure 5.3 shows the impact of number of transmit antennas jointly encoded on the BER for CM1, CM2, CM3, and CM4 for the optimal STF block codes for the  $M = N_i = 2$  case. Figs. 5.3(a), 5.3(b), and 5.3(c) are for the cases  $N_t = 2, 3, 4$ , respectively. For each sub-figure, the BER decreases as CM increases. This phenomenon can be explained by the coding gain. In Table 5.2, the coding gain increases as CM increases for the cases  $N_t = 34$ , thus the BER decreases.

Moreover, we find a surprising fact. The BER in Figs. 5.3(a), 5.3(b), and 5.3(c) are almost the same for the same CM. In other words, the BER for a certain CM does not change as the number of transmit antennas increases. This result is quite different from the STBC case. In STBC, increasing the number of transmit antennas will decrease the BER performance [100]. Thus, we may conclude that in the MIMO-UWB systems, using multiple transmit antennas does not provide significant improvement to the BER performance, because the UWB channels already possess rich diversity inherently. In the uncoded UWB systems using multiple antennas, there exists the same phenomenon [103].

### 5.6.2 Effect of Number of Receive Antennas

Figure 5.4 shows the effect of number of receive antennas on the BER for CM1, CM2, CM3, and CM4 for the optimal STF block codes for the  $M = N_i = N_t = 2$ ,  $N_r = 12$  cases. We find that the BER decreases as CM increases. Thus we can conclude that our optimal STF block codes can

exploit the channel fading to improve the performance. On the other hand, increasing the number of receive antennas can significantly decrease the BER because  $N_r$  is proportional to the diversity order. In the uncoded UWB systems using multiple antennas, there exists the same phenomenon again [103].

### 5.6.3 Effect of Number of Transmit Antennas Jointly Encoded ( $N_t$ ) for Three Subcarriers Jointly Encoded ( $M = 3$ )

Figure 5.5 shows the effect of number of transmit antennas jointly encoded on the BER for CM1, CM2, CM3, and CM4 for the optimal STF block codes for the  $M = 3$  and  $N_i = 2$  case. The modulation is BPSK. The sub-figures (a), (b), and (c) correspond to the cases  $N_t = 2, 3$ , and 4, respectively. As the same in the  $M = 2$  case, when the number of channel model increases, the BER decreases. However, unlike the  $M = 2$  case which has diversity order of 2, the  $M = 3$  case has diversity order of 2 for the  $N_t = 2$  and CM = 1, 2,  $N_t = 3$  and CM = 1 cases. The diversity order equals to 3 for other cases. This can be seen both from Fig. 5.5 and Table 5.3. Moreover, as the number of transmit antennas  $N_t$  increase, the BER decreases. Thus, the optimal STF block codes in the  $M = 3$  case improve the BER performance when  $N_t$  increases. In the  $M = 2$  case, this phenomenon does not occur. On the other hand, compared with the  $M = 2$  case, the  $M = 3$  case has better BER performance. Hence, increasing the number of subcarriers which are jointly encoded also improves the BER performance.

#### 5.6.4 Effect of Number of Transmit Antennas Jointly Encoded ( $N_t$ ) for Four Subcarriers Jointly Encoded ( $M = 4$ )

Figure 5.6 shows the effect of number of transmit antennas jointly encoded on the BER for CM 1 ~ 4 for the optimal STF block codes for  $M = 4$  and  $N_i = 2$ . Figs. 5.6(a) and 5.6(b) show the BER for  $N_t = 23$ , respectively. Like the  $M = 3$  case, the BER decreases as CM or  $N_t$  increase. Different CM have different diversity orders. The  $M = 4$  case also has better BER performance than the  $M = 3$  case does.

#### 5.6.5 BER Comparison with STF Codes in [1] and [2]

Figure 5.7 shows the BER comparison of our code with Chusing's code [2] and Zhang's code [1] for the  $M = 4, N_i = 2, N_r = 1, N_t = 2$  case in the IEEE 802.15.3a UWB channel model CM4. We can see that the diversity gains of the three codes are the same, but our code has better BER performance than Chusing's and Zhang's codes do. At  $\text{BER} = 10^{-4}$ , the coding gain between our code and Chusing's code is about 8 dB and the coding gain between our code and Zhang's code is about 1 dB.

### 5.7 Conclusions

In this chapter, we study the BER-minimized STF block codes design for the MIMO highly frequency-selective block fading channels. We consider the IEEE 802.15.3a UWB channel model. Based on the BER analysis under the aforementioned environment in [19], we provide a BER-minimized design criterion, an efficient searching algorithm for the optimal STF block codes,

and optimal BER performance curves. Among our proposed optimal STF block codes, we find that almost all of them need nonlinear operations in the encoder. Thus it is necessary to consider nonlinear codes when we design the optimal STF block codes for the MIMO-OFDM systems under the IEEE 802.15.3a UWB channel model. When the number of subcarriers  $M$  which are jointly encoded is equal to two and the number of transmit antennas  $N_t$  is  $2 \sim 4$  or  $M = 3, N_t = 4$ , the optimal STF block codes for all the IEEE 802.15.3a UWB channel models CM 1  $\sim$  4 can be found according to the proposed code search algorithm in the above considered cases. When 1)  $M = 3, N_t = 2 \sim 3$ , and 2)  $M = 4, N_t = 2 \sim 3$ , there does not exist optimal STF block codes for all the four UWB channel models. We also find that the BER decreases as CM increases, i.e., our optimal STF block codes provide better BER performance when the channel fading is more severe. On the other hand, increasing the number of transmit antennas does NOT improve the BER performance for the MIMO-UWB systems when  $M = 2$ . This is similar to the case of the uncoded MIMO-UWB systems but opposite to the STBC case. However, increasing the number of received antennas improves the BER performance for the MIMO-UWB systems. This is similar to the STBC case. We also find that the diversity order is different for different CM in the  $M = 3 \sim 4, N_t = 2 \sim 3$  cases. Compared with other STF codes [1, 2] for multiband UWB-MIMO communication systems, our code has about 1 and 8 dB coding gain at  $\text{BER} = 10^{-4}$ , respectively.

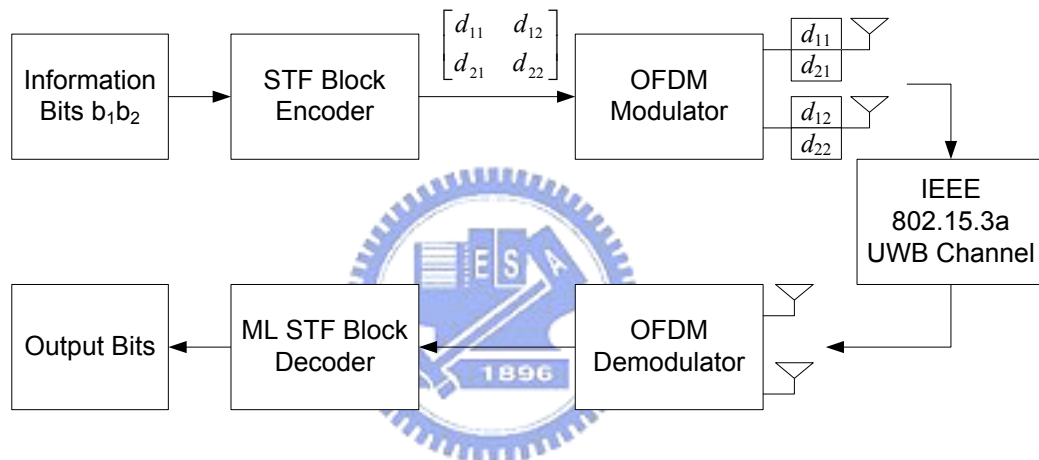
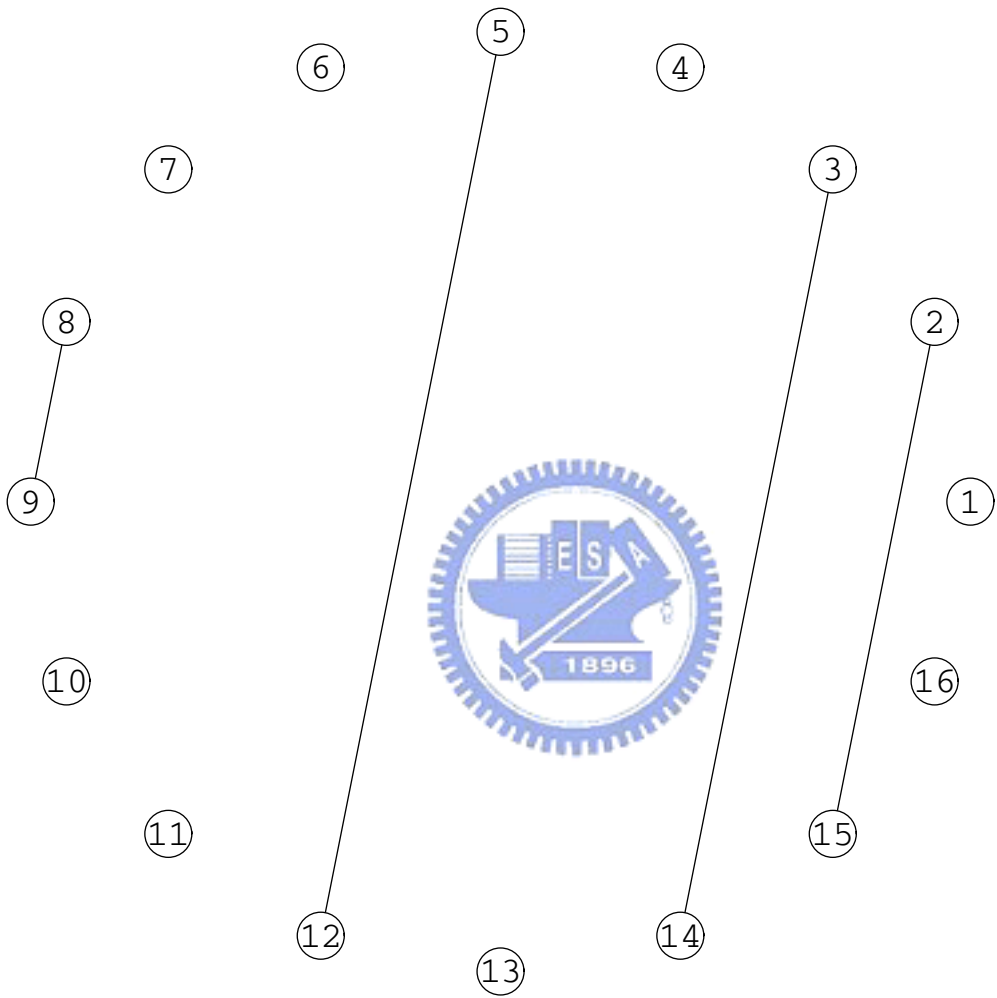
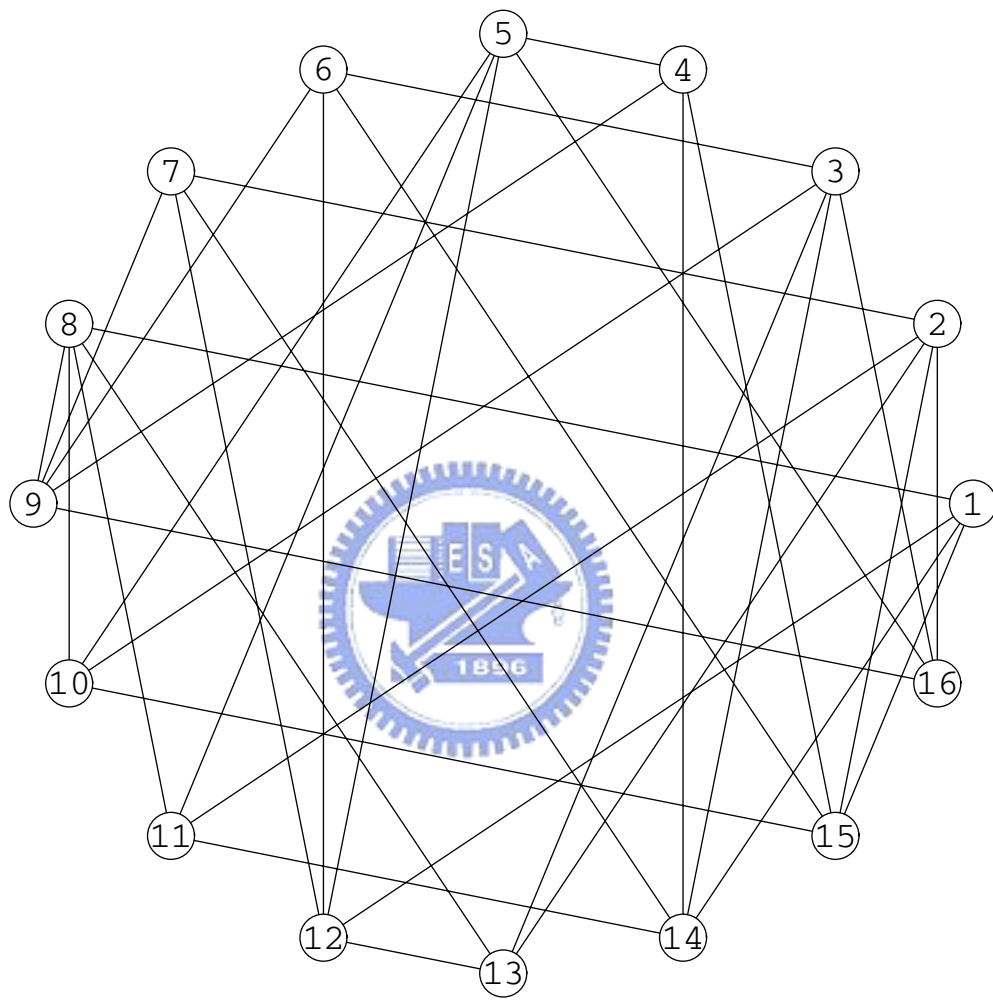


Figure 5.1: The system block diagram.

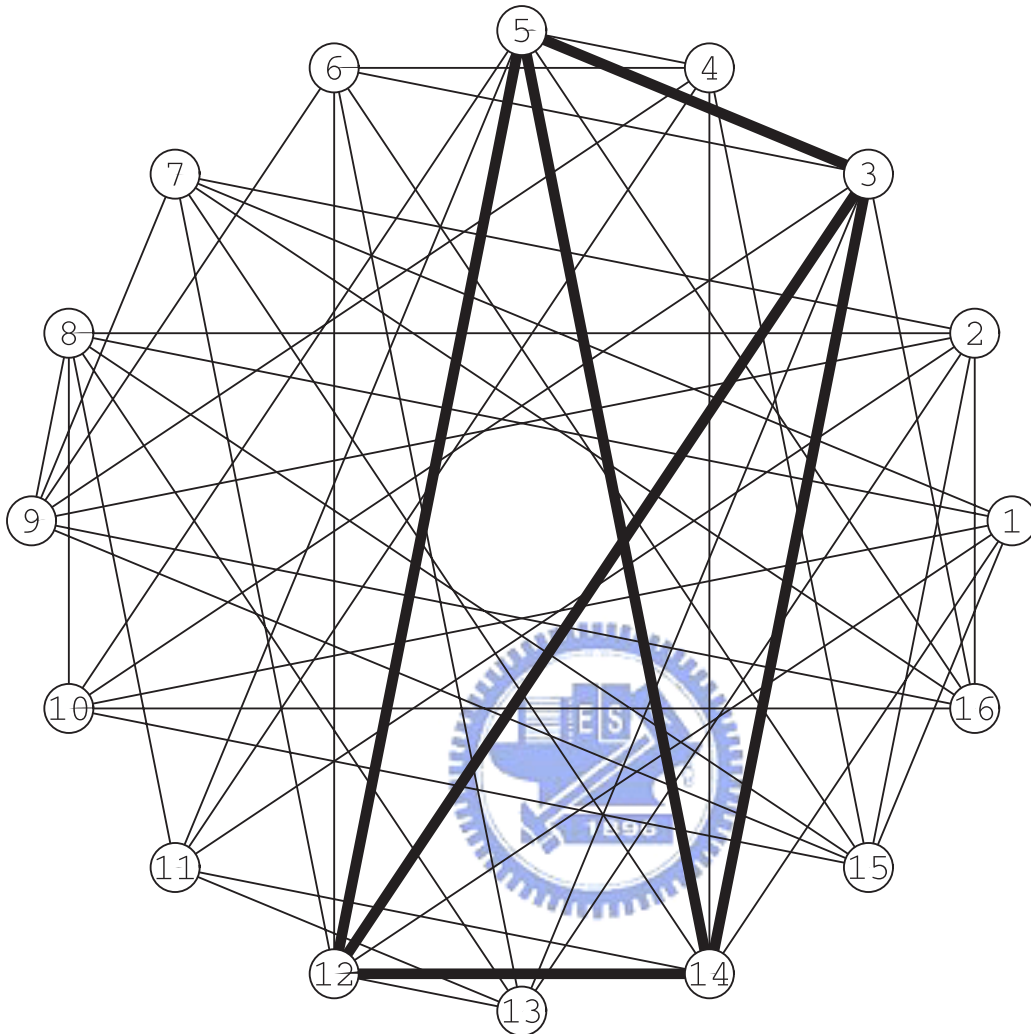


(a)



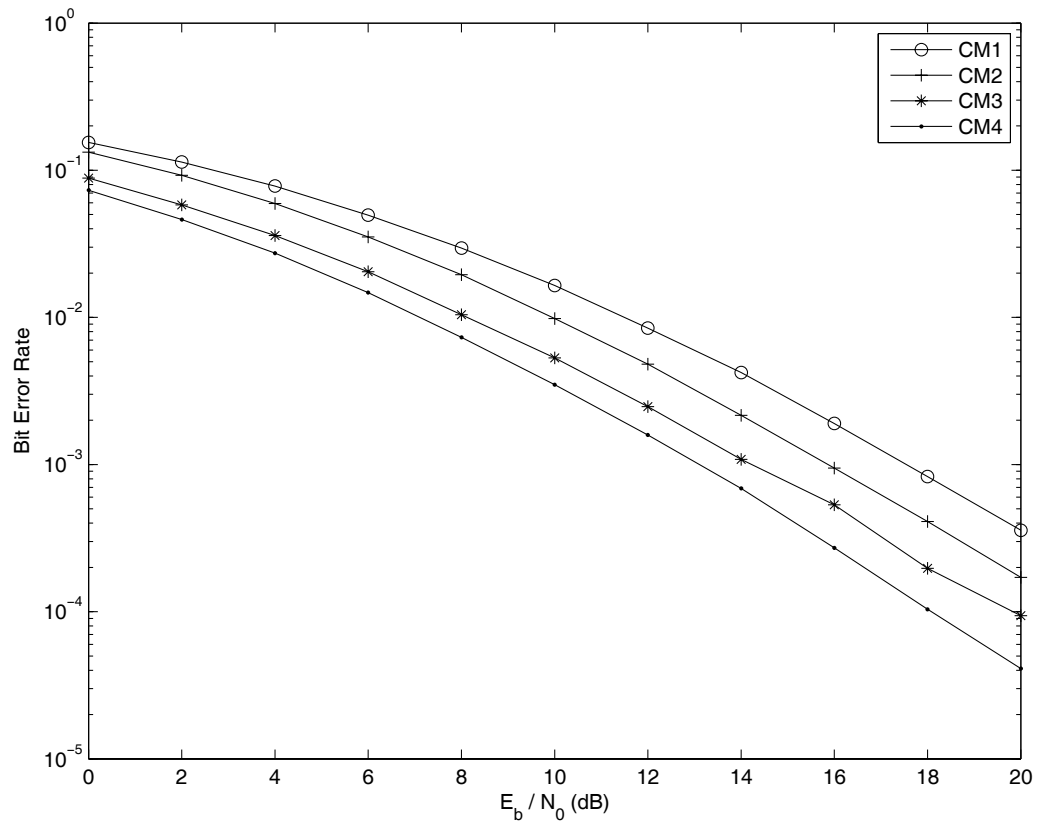


(b)

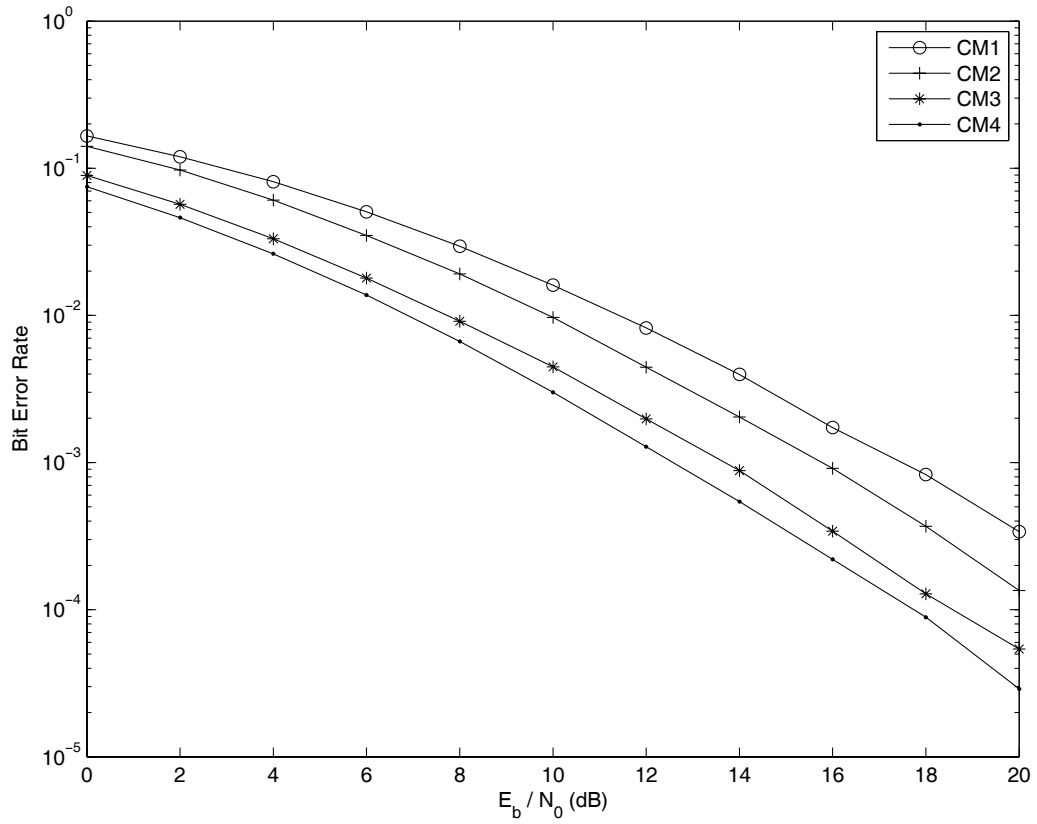


(c)

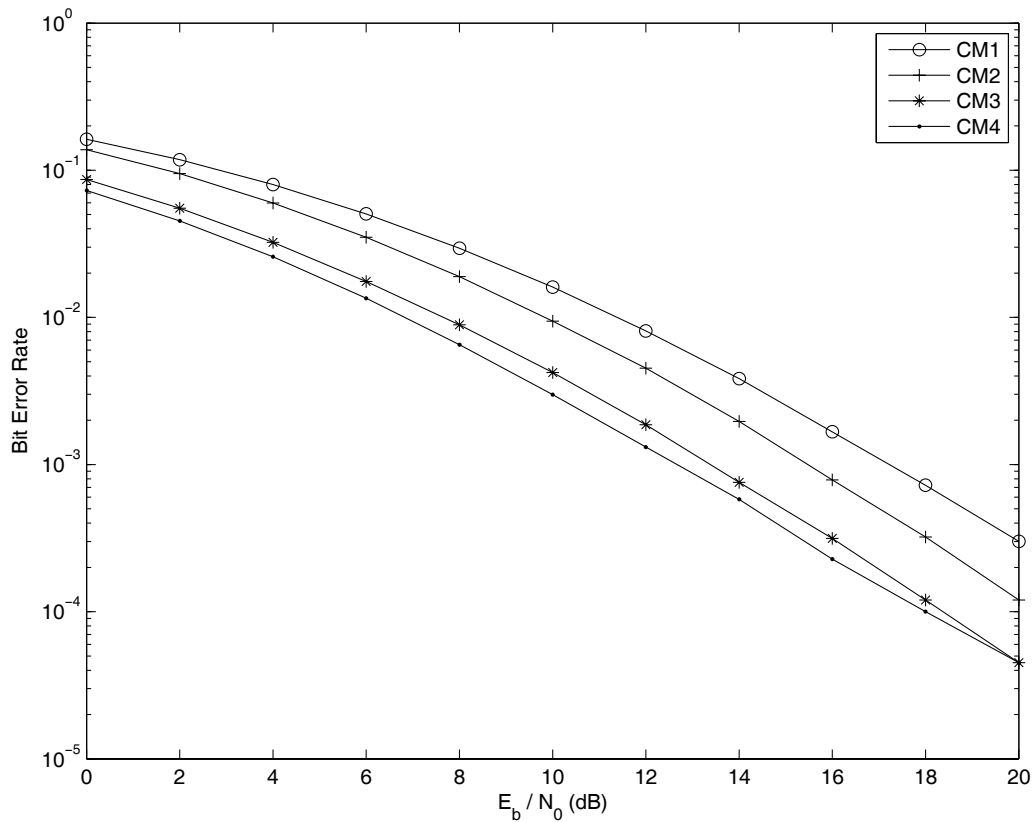
Figure 5.2: Illustration of our proposed efficient searching algorithm for the optimal STF block codes for two subcarriers jointly encoded, two transmit antennas jointly encoded, and two input information bits for each codeword. We search complete graphs with four vertices subject to the largest  $m$  metrics. (a)  $m = 1$ . (b)  $m = 2$ . (c)  $m = 3$ .



(a)



(b)



(c)

Figure 5.3: The effect of different number of transmit antennas jointly encoded ( $N_t$ ) on the BER for CM1, CM2, CM3, and CM4 for the optimal STF block codes for two subcarriers jointly encoded and two input information bits for each codeword. The modulation is BPSK. (a)  $N_t = 2$ . (b)  $N_t = 3$ . (c)  $N_t = 4$ .

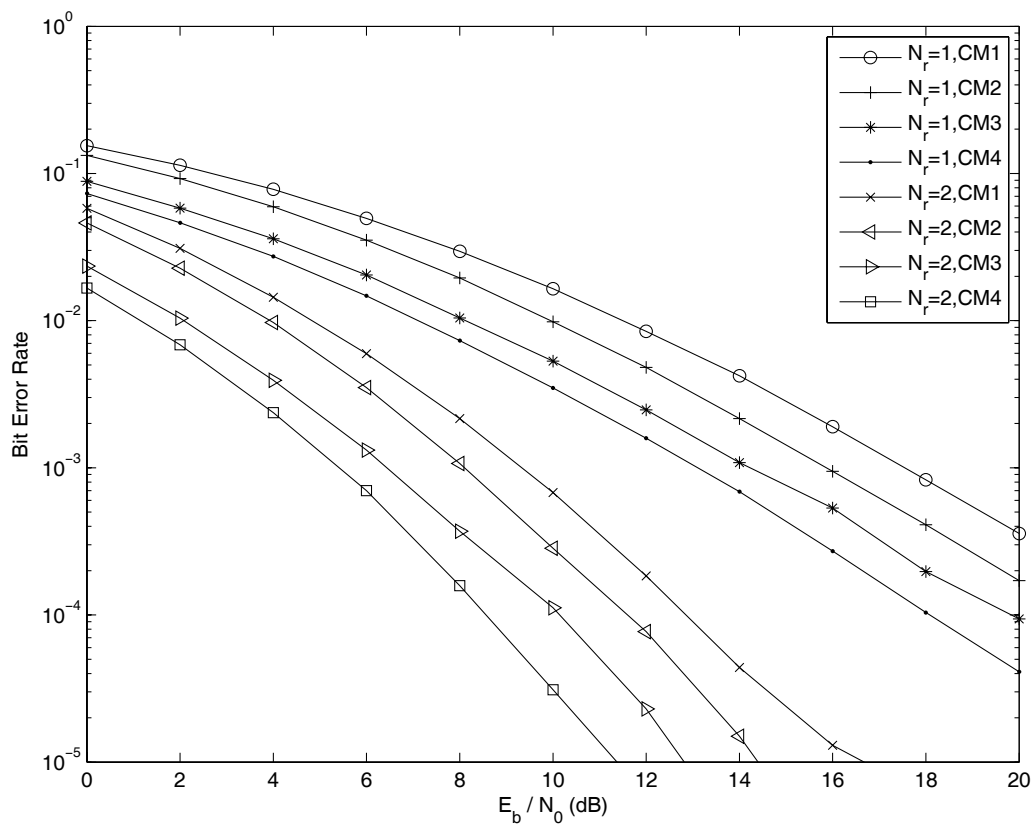
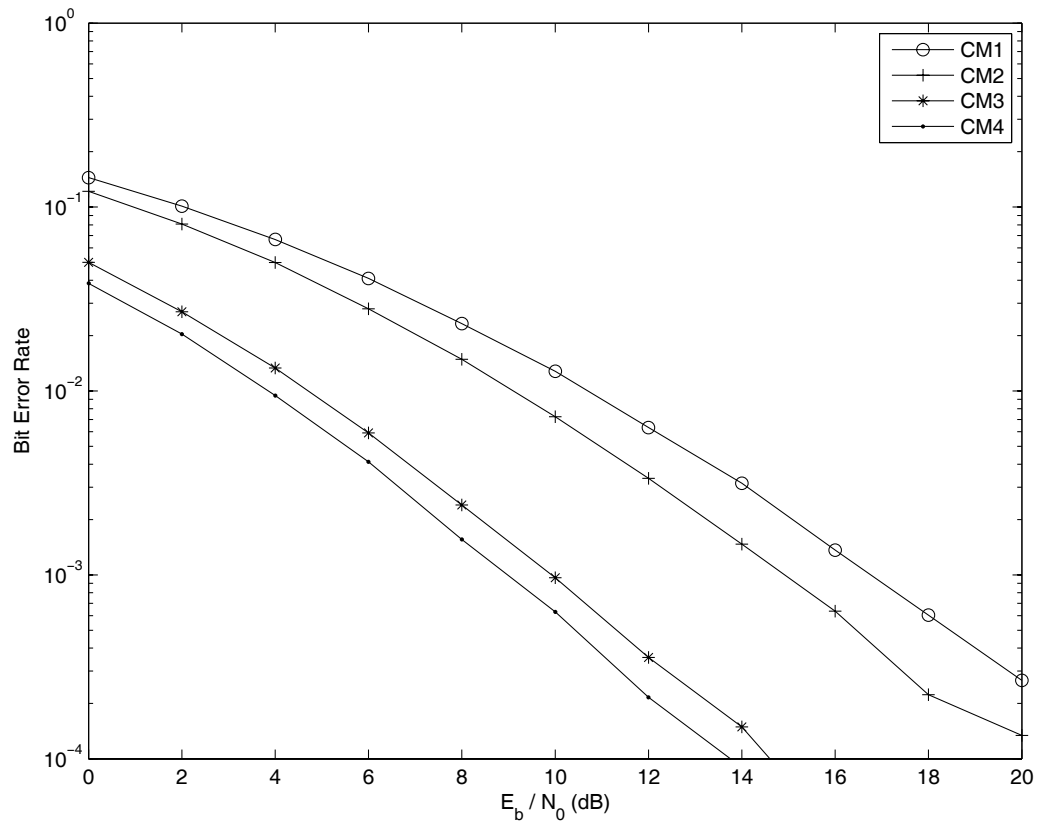
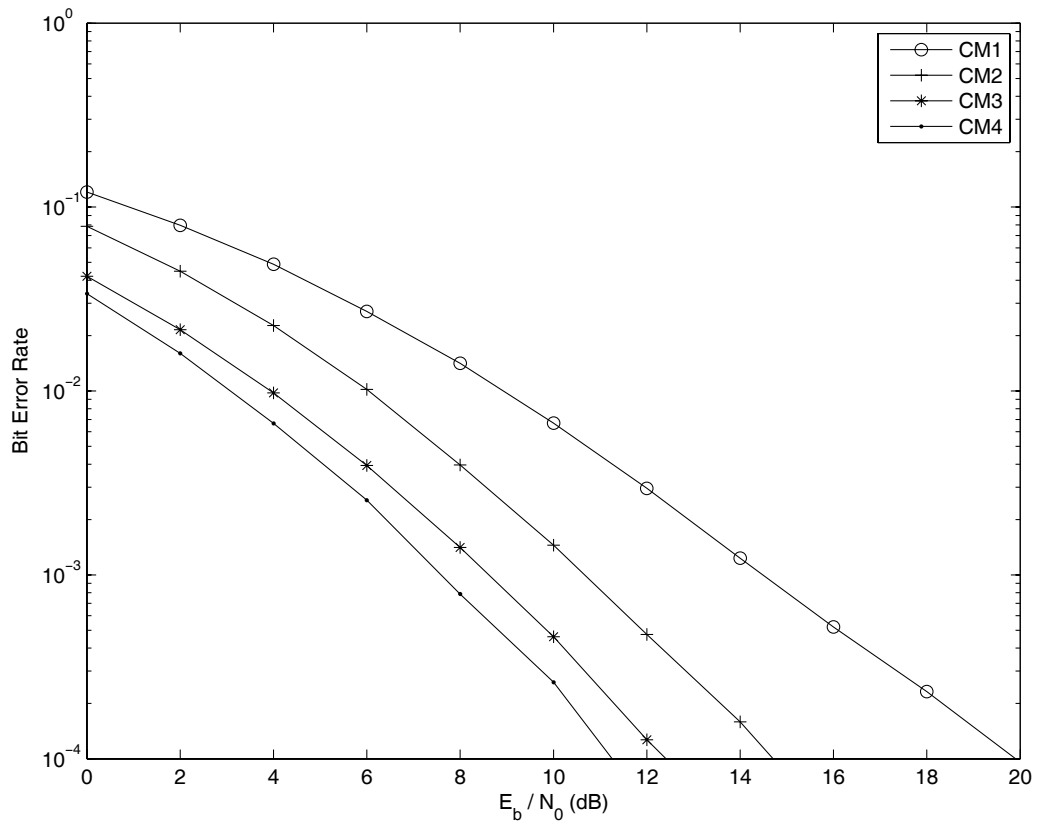


Figure 5.4: The effect of number of receive antennas ( $N_r$ ) on the BER for CM1, CM2, CM3, and CM4 for the optimal STF block codes for two sub-carriers jointly encoded, two input information bits for each codeword, and two transmit antennas jointly encoded.  $N_r = 1$  and 2. The modulation is BPSK.

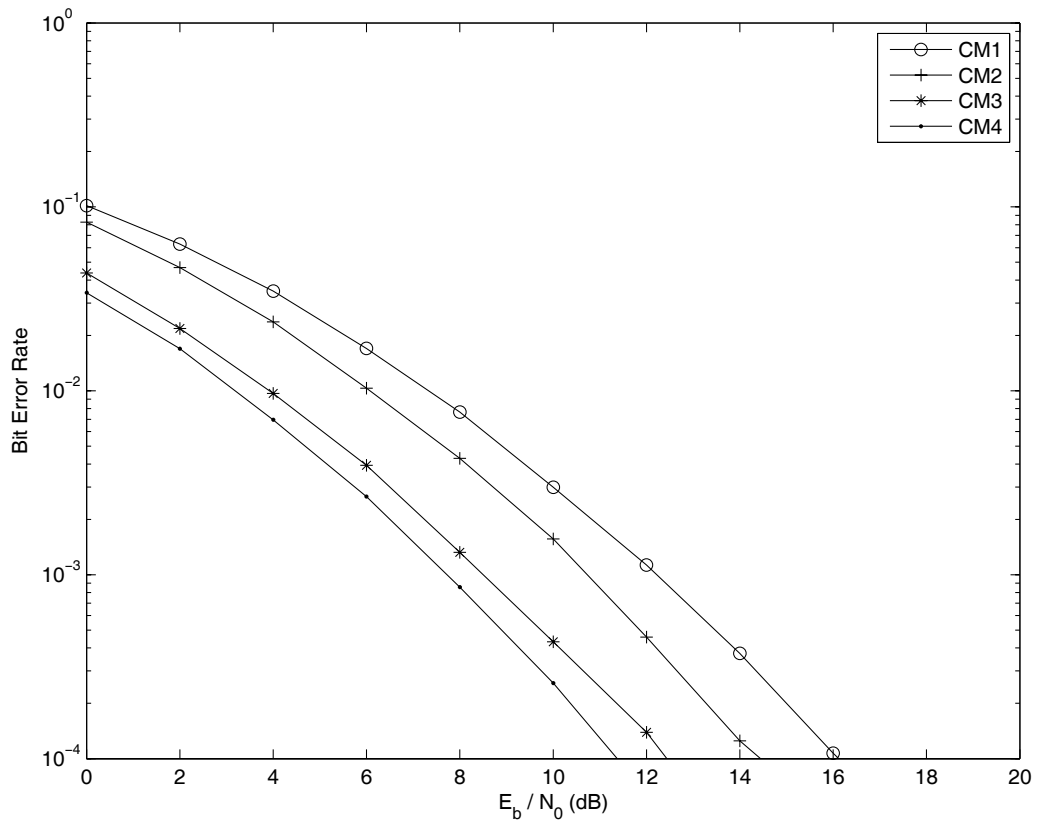


(a)



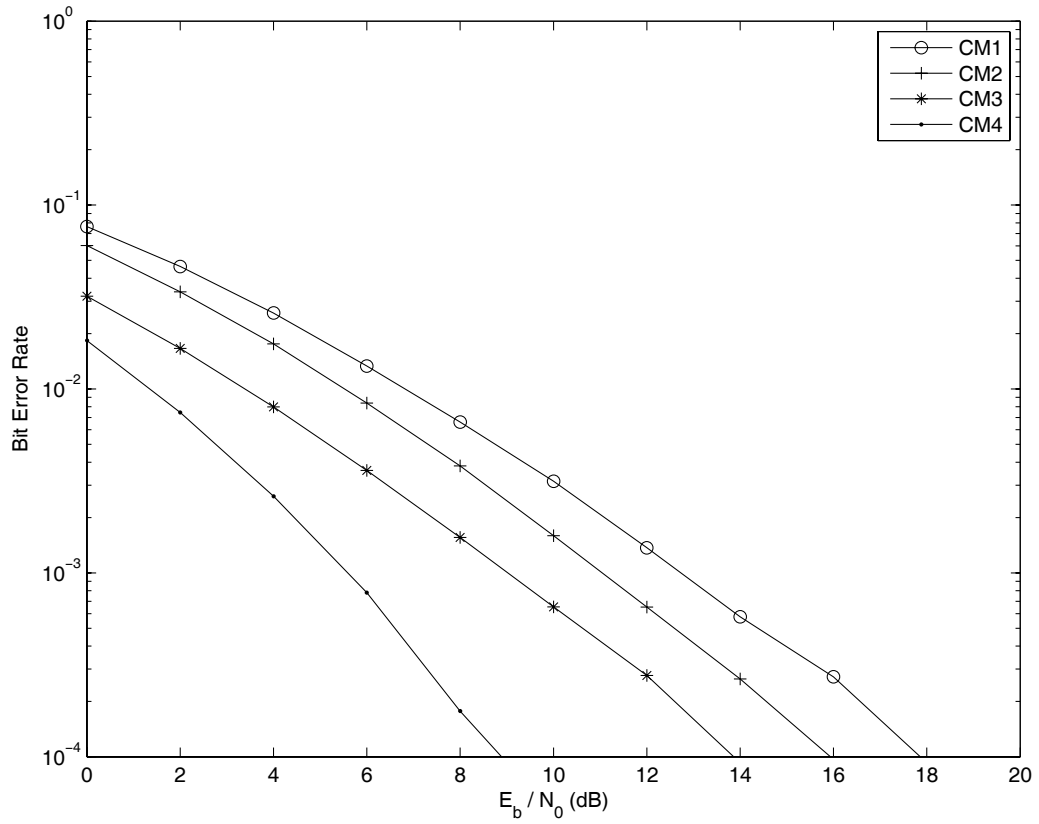
(b)



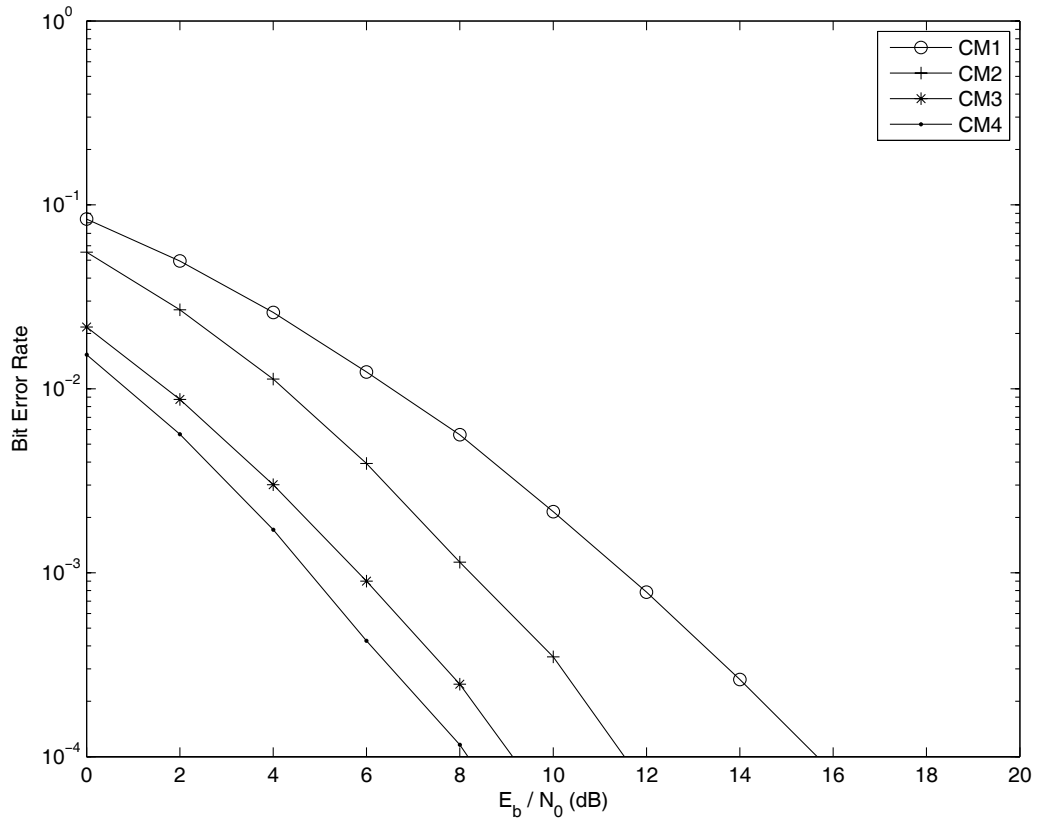


(c)

Figure 5.5: The effect of number of transmit antennas jointly encoded ( $N_t$ ) on the BER for CM1, CM2, CM3, and CM4 for the optimal STF block codes for three subcarriers jointly encoded and two input information bits for each codeword. The modulation is BPSK. (a)  $N_t = 2$ . (b)  $N_t = 3$ . (c)  $N_t = 4$ .



(a)



(b)

Figure 5.6: The effect of number of transmit antennas jointly encoded ( $N_t$ ) on the BER for CM1, CM2, CM3, and CM4 for the optimal STF block codes for four subcarriers jointly encoded and two input information bits for each codeword. The modulation is BPSK. (a)  $N_t = 2$ . (b)  $N_t = 3$ .

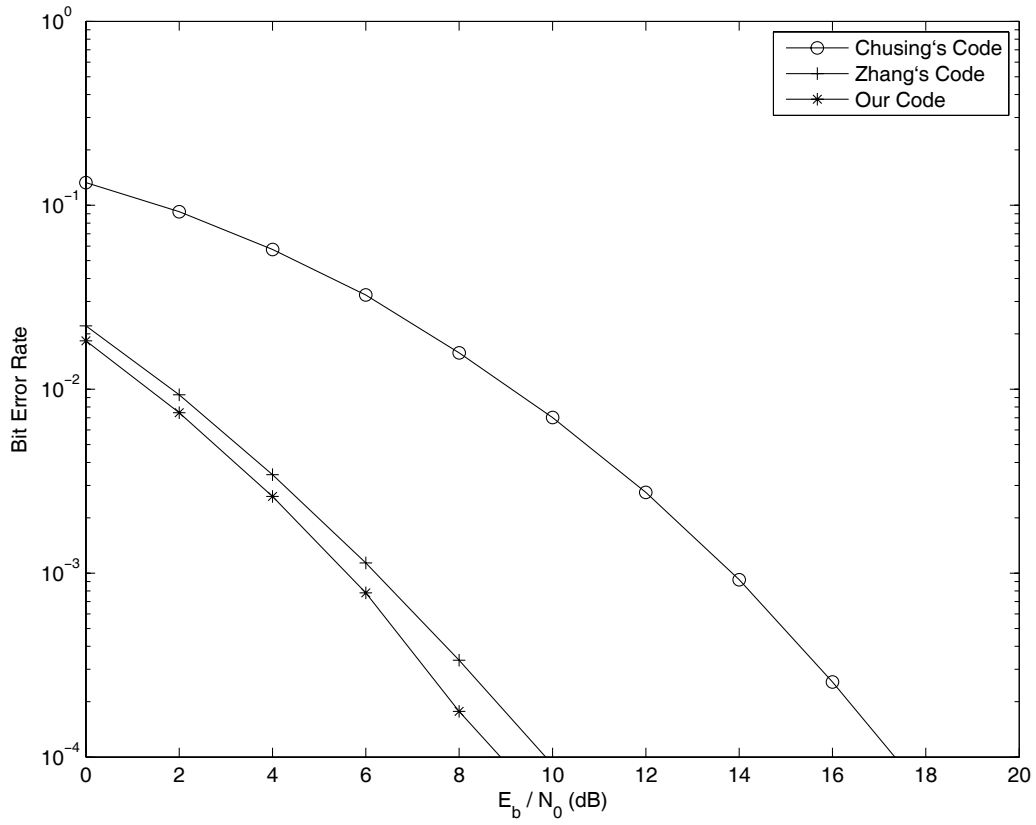
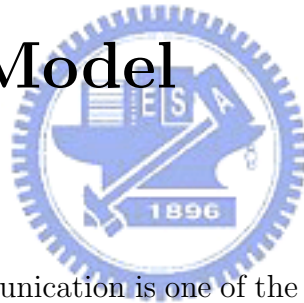


Figure 5.7: The BER comparison of our code versus Zhang's code [1] and Chusing's code [2] for three subcarriers jointly encoded, two input information bits for each codeword, one receive antenna, and three transmit antennas jointly encoded in the IEEE 802.15.3a UWB channel model CM4. The modulation is BPSK.

# Chapter 6

## Statistical Analysis of A Mobile-to-Mobile Rician Fading Channel Model



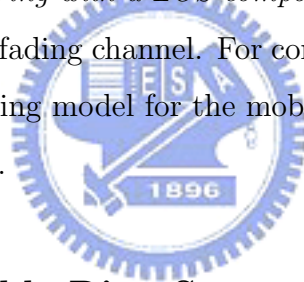
Mobile-to-mobile communication is one of the important applications for the intelligent transport systems and mobile ad hoc networks. In these systems, both the transmitter and receiver are in motion, subjecting to the signals to Rician fading and different scattering effects. In this chapter, we present a double-ring with a LOS component scattering model and a sum-of-sinusoids simulation method to characterize the mobile-to-mobile Rician fading channel. The developed model can facilitate the physical layer simulation for a mobile ad hoc communication systems. We also derive the autocorrelation function, level crossing rate (LCR), and average fade duration (AFD) of the mobile-to-mobile Rician fading channel and verify the accuracy by simulations.

## 6.1 Motivation

Mobility affects wireless networks significantly. In traditional cellular systems, the base station is stationary and only mobile terminals are in motion. However, in many new wireless systems, such as intelligent transport systems (ITS) and mobile ad hoc networks, a mobile connects directly to another mobile without the help of fixed base stations. Thus, how mobility affects a system of which both the transmitter and the receiver move simultaneously becomes an interesting problem.

## 6.2 Scattering Environment

This section describes a *double-ring with a LOS component scattering* model for the mobile-to-mobile Rician fading channel. For comparison purpose, the independent double-ring scattering model for the mobile-to-mobile Rayleigh fading channel is also presented.



### 6.2.1 Traditional Double-Ring Scattering Model

In a mobile-to-mobile communication channel, the antenna heights of both the transmitter and the receiver are below the surrounding objects, it is thus likely that both the transmitter and the receiver experience rich scattering effect in the propagation paths. [20] showed an independent two-ring scattering environment for characterizing the mobile-to-mobile Rayleigh fading channel. According to this scattering model, a sum-of-sinusoids method was suggested to approximate the mobile-to-mobile Rayleigh fading channel. The scatterers are assumed to be uniformly distributed. Let the transmitter and receiver move at the speeds of  $\mathbf{v}_1$  and  $\mathbf{v}_2$ , respectively. For all  $MN$  indepen-

dent paths, the amplitude of the normalized complex signal received in the mobile-to-mobile Rayleigh fading channel can be expressed as

$$Y(t) = \sqrt{\frac{1}{MN}} \sum_{m=1}^M \sum_{n=1}^N \exp[j(2\pi f_1 t \cos \alpha_n + 2\pi f_2 t \cos \beta_m + \phi_{nm})] , \quad (6.1)$$

where  $f_1 = \frac{|\mathbf{v}_1|}{\lambda}$  and  $f_2 = \frac{|\mathbf{v}_2|}{\lambda}$  are the maximum Doppler frequencies resulted from the motion of TX and RX, respectively.  $|\mathbf{v}|$  denotes the length of a vector  $\mathbf{v}$  while  $\lambda$  is the carrier wavelength. In (6.1),

$$\alpha_n = \frac{2n\pi - \pi + \theta_n}{4N} \quad (6.2)$$

and

$$\beta_m = \frac{2(2m\pi - \pi + \psi_m)}{4M} , \quad (6.3)$$

where the angles of departure in each scattering path ( $\theta_n$ ) and the angle of arrival ( $\psi_m$ ) and  $\phi_{nm}$  in  $Y(t)$  are all independent uniform random variables over  $[-\pi, \pi)$ . It was proved in [54] and [20] that the autocorrelation function of the complex envelope  $Y(t)$  is equal to

$$R_{YY}(\tau) = \frac{J_0(2\pi f_1 \tau) J_0(2\pi f_2 \tau)}{2} , \quad (6.4)$$

where  $J_0(\cdot)$  is the zeroth-order Bessel function of the first kind.

### 6.2.2 Double-Ring with a LOS Component Scattering Model

In some situations, certain LOS components exist between the transmitter and the receiver. Figure 6.1 shows the proposed “double-ring with a LOS component” scattering model. In addition to the two scattering rings, a LOS component is added between the transmitter and the receiver. It is complex

to present the LOS component by a mathematical formula, especially when both the transmitter and the receiver are in motion. Therefore, we use the concept of relative motion to simplify the problem. Figure 6.2 shows the relative velocity ( $\mathbf{v}_3$ ) of the transmitter to the receiver if the velocity of the receiver is set to be zero. In the figure,  $\theta_3$  is the angle between  $\mathbf{v}_3$  and the LOS component. The relative velocity of the transmitter  $\mathbf{v}_3$  can be derived as follows:

$$|\mathbf{v}_3| = \sqrt{(|\mathbf{v}_1| \cos \theta_{12} - |\mathbf{v}_2|)^2 + (|\mathbf{v}_1| \sin \theta_{12})^2} , \quad (6.5)$$

$$\theta_3 = \theta_1 + \theta_{13} , \quad (6.6)$$

where  $\theta_{12}$  is the angle between vectors  $\mathbf{v}_1$  and  $\mathbf{v}_2$ ;  $\theta_1$  is the angle between vector  $\mathbf{v}_1$  and LOS component and the angle between vectors  $\mathbf{v}_1$  and  $\mathbf{v}_3$  is

$$\theta_{13} = \cos^{-1} \left( \frac{|\mathbf{v}_1|^2 + |\mathbf{v}_3|^2 - |\mathbf{v}_2|^2}{2|\mathbf{v}_1||\mathbf{v}_3|} \right) . \quad (6.7)$$

Thus, the LOS component of the mobile-to-base station case can be expressed as

$$\text{LOS} = \sqrt{K} \exp[j(2\pi f_3 t \cos \theta_3 + \phi_0)] , \quad (6.8)$$

where  $K$  is the ratio of the specular power to the scattering power,  $f_3$  is the Doppler frequency caused by  $\mathbf{v}_3$  and the initial phase  $\phi_0$  is uniformly distributed over  $[-\pi, \pi)$ .

### 6.3 Sum-of-Sinusoids Rician Fading Simulator

According to the “double-ring with a LOS component” scattering model shown in Fig. 6.1, a new sum-of-sinusoids Rician fading simulator for the mobile-to-mobile communication is developed.



### 6.3.1 Signal Model for Double-Ring with a LOS component Scattering

Because Rayleigh fading is a special case of Rician fading without the specular component, the received complex signal of the mobile-to-mobile Rician fading channel is equivalent to the sum of the scattering signal and a LOS component. Therefore, with reference to (6.1) and (6.8) the received complex envelope of the mobile-to-mobile Rician fading channel can be written as

$$Z(t) = \frac{Y(t) + \sqrt{K} \exp[j(2\pi f_3 t \cos \theta_3 + \phi_0)]}{\sqrt{1 + K}} . \quad (6.9)$$

The complex signal  $Z(t)$  is decomposed into the in-phase component  $Z_c(t)$  and the quadrature component  $Z_s(t)$ . Then it follows that

$$Z(t) = Z_c(t) + jZ_s(t) , \quad (6.10)$$

where

$$Z_c(t) = \frac{Y_c(t) + \sqrt{K} \cos(2\pi f_3 t \cos \theta_3 + \phi_0)}{\sqrt{1 + K}} , \quad (6.11)$$

$$Z_s(t) = \frac{Y_s(t) + \sqrt{K} \sin(2\pi f_3 t \cos \theta_3 + \phi_0)}{\sqrt{1 + K}} , \quad (6.12)$$

$$Y_c(t) = \Re\{Y(t)\} , \quad (6.13)$$

and

$$Y_s(t) = \Im\{Y(t)\} . \quad (6.14)$$

### 6.3.2 Second-Order Statistics

The second-order statistical properties of  $Z(t)$  are then derived. The auto-correlation function of  $Z_c(t)$  can be calculated as

$$\begin{aligned}
 & R_{Z_c Z_c}(\tau) \\
 &= \mathbb{E} [Z_c(t)Z_c(t + \tau)] \\
 &= \frac{1}{1 + K} \left\{ \frac{1}{MN} \right. \\
 & \quad \mathbb{E} \left[ \sum_{m=1}^M \sum_{n=1}^N \cos(2\pi(f_1 \cos \alpha_n + f_2 \cos \beta_m)t + \phi_{nm}) \right. \\
 & \quad \left. \sum_{p=1}^N \sum_{q=1}^M \cos(2\pi(f_1 \cos \alpha_p + f_2 \cos \beta_q)(t + \tau) + \phi_{pq}) \right] \\
 & \quad + K \mathbb{E} [\cos(2\pi f_3 t \cos \theta_3 + \phi_0) \cos(2\pi f_3 (t + \tau) \cos \theta_3 \\
 & \quad + \phi_0)] + \left. \sqrt{\frac{K}{MN}} A + \sqrt{\frac{K}{MN}} B \right\}, \tag{6.15}
 \end{aligned}$$

where  $\mathbb{E}$  is the statistical expectation operator,

$$\begin{aligned}
 A = \mathbb{E} \left[ \sum_{m=1}^M \sum_{n=1}^N \cos(2\pi(f_1 \cos \alpha_n + f_2 \cos \beta_m)t + \phi_{nm}) \right. \\
 \left. \cos(2\pi f_3 (t + \tau) \cos \theta_3 + \phi_0) \right] = 0 \tag{6.16}
 \end{aligned}$$

and

$$\begin{aligned}
 B = \mathbb{E} \left[ \cos(2\pi f_3 t \cos \theta_3 + \phi_0) \sum_{m=1}^M \sum_{n=1}^N \cos(2\pi(f_1 \cos \alpha_n \right. \\
 \left. + f_2 \cos \beta_m)(t + \tau) + \phi_{nm}) \right] = 0 . \tag{6.17}
 \end{aligned}$$

Because  $\phi_{nm}$ ,  $\theta_n$ ,  $\psi_m$ , and  $\phi_0$  are mutually independent random variables,  $R_{Z_c Z_c}(\tau)$  can be further simplified as

$$\begin{aligned}
& R_{Z_c Z_c}(\tau) \\
&= \frac{1}{1+K} \left\{ \frac{1}{2NM} \right. \\
& \quad \mathbb{E} \left[ \sum_{n=1}^N \cos(2\pi f_1 \tau \cos \alpha_n) \sum_{m=1}^M \cos(2\pi f_2 \tau \cos \beta_m) \right. \\
& \quad \left. - \sum_{n=1}^N \sin(2\pi f_1 \tau \cos \alpha_n) \sum_{m=1}^M \sin(2\pi f_2 \tau \cos \beta_m) \right] \\
& \quad \left. + K \mathbb{E} [\cos(2\pi f_3 t \cos \theta_3 + \phi_0) \right. \\
& \quad \left. \cos(2\pi f_3 (t + \tau) \cos \theta_3 + \phi_0)] \right\} \\
&= \frac{1}{1+K} \left[ \frac{2}{\pi} \int_0^{\frac{\pi}{2}} \cos(2\pi f_1 \tau \cos \alpha) d\alpha \right. \\
& \quad \frac{1}{\pi} \int_0^{\pi} \cos(2\pi f_2 \tau \cos \beta) d\beta \\
& \quad \left. - \frac{2}{\pi} \int_0^{\frac{\pi}{2}} \sin(2\pi f_1 \tau \cos \alpha) d\alpha - \frac{1}{\pi} \int_0^{\pi} \sin(2\pi f_2 \tau \cos \beta) d\beta \right] \\
& \quad + \frac{K}{2(1+K)} \cos(2\pi f_3 \tau \cos \theta_3) . \tag{6.18}
\end{aligned}$$

Consequently,

$$R_{Z_c Z_c}(\tau) = \frac{J_0(2\pi f_1 \tau) J_0(2\pi f_2 \tau) + K \cos(2\pi f_3 \tau \cos \theta_3)}{2(1+K)} \tag{6.19}$$

is obtained. Similarly, other time-correlation functions of  $Z(t)$  can be obtained as follows:

$$R_{Z_s Z_s}(\tau) = \frac{J_0(2\pi f_1 \tau) J_0(2\pi f_2 \tau) + K \cos(2\pi f_3 \tau \cos \theta_3)}{2(1+K)} ; \tag{6.20}$$

$$R_{Z_c Z_s}(\tau) = \frac{K \sin(2\pi f_3 \tau \cos \theta_3)}{2(1+K)} ; \tag{6.21}$$

$$R_{Z_s Z_c}(\tau) = -\frac{K \sin(2\pi f_3 \tau \cos \theta_3)}{2(1+K)} ; \tag{6.22}$$

and

$$R_{ZZ}(\tau) = \frac{J_0(2\pi f_1\tau)J_0(2\pi f_2\tau) + K \exp(j2\pi f_3\tau \cos \theta_3)}{1 + K} . \quad (6.23)$$

Similar derivation and results for mobile-to-base Rician fading channels can be found in [25, 104, 105].

### 6.3.3 Signal Model with Single-Ring Scattering

For comparison purpose, the Rician fading channel model developed from the single-ring scattering model is shown [56]. Note that the single-ring model developed for mobile-to-base channels may not be directly used for mobile-to-mobile channels. In Fig. 6.3, scatterers are distributed around the mobile terminal and there exists a LOS component between the TX and the RX.

In this model, the received signal is the sum of signals from each scattering path with a LOS component. It was shown in [105] that the theoretical autocorrelation function of the complex envelope of fading signal  $Z(t)$  for the single-ring model is

$$R_{ZZ}(\tau) = \frac{J_0(2\pi f_1\tau) + K \exp(j2\pi f_3\tau \cos \theta_3)}{1 + K} . \quad (6.24)$$

We will see later in the numerical results that the new double-ring with a LOS component scattering model is more accurate than the single-ring model through the simulation.

## 6.4 Higher-Order Statistics

### 6.4.1 Level Crossing Rate

The fading envelope is denoted as  $a(t)$ , the derivative of the fading envelope as  $\dot{a}(t)$ , the PDF of the fading envelope as  $p_a(a)$ , and the PDF of the slope of

the fading envelope as  $p_{\dot{a}}(\dot{a})$ . Then the level crossing rate ( $L_R$ ) of the fading envelope  $|Z(t)|$  with respect to a specified level  $R$  can be calculated by [106]

$$L_R = \int_0^{\infty} \dot{a} p_{a,\dot{a}}(R, \dot{a}) d\dot{a} \quad (6.25)$$

where  $p_{a,\dot{a}}(a, \dot{a})$  is the joint distribution function of  $a$  and  $\dot{a}$ . Now, the key issue is to find the joint distribution  $p_{a,\dot{a}}(a, \dot{a})$ .

From [107] and [108], we know that the joint distribution of the fading envelope and envelope slope of a Rician fading signal can be expressed as [109]

$$p_{a,\dot{a}}(a, \dot{a}) = \sqrt{\frac{1}{2\pi b_2}} \exp\left(-\frac{\dot{a}^2}{2b_2}\right) \cdot \frac{a}{b_0} \exp\left(-\frac{a^2 + s^2}{2b_0}\right) I_0\left(\frac{as}{b_0}\right) \quad (6.26)$$

where

$$\begin{aligned} s^2 &= \mathbb{E}[Z_c(t)]^2 + \mathbb{E}[Z_s(t)]^2 ; \\ \Omega_p &= \mathbb{E}[a^2] = s^2 + 2b_0 ; \\ s^2 &= \frac{K\Omega_p}{K+1} ; \quad 2b_0 = \frac{\Omega_p}{K+1} ; \end{aligned} \quad (6.27)$$

where  $I_n(\cdot)$  is the modified  $n$ th-order Bessel function of the first kind.  $\Omega_p$  is the square mean of the fading envelope;  $s^2$  is the power of the specular component and  $2b_0$  is the scattered power. Note that (6.26) holds only when the frequency of the specular component ( $f_s$ ) equals the carrier frequency ( $f_c$ ). This means that the Doppler shift of the specular component is zero. This situation occurs only when the impinging angle  $\theta_3$  is fixed at 90 or 270 degrees.

From (6.26), it is implied that  $a$  and  $\dot{a}$  are mutually independent. Thus, we have

$$p_{\dot{a}}(\dot{a}) = \sqrt{\frac{1}{2\pi b_2}} \exp\left(-\frac{\dot{a}^2}{2b_2}\right) \quad (6.28)$$

and

$$p_a(a) = \frac{a}{b_0} \exp\left(-\frac{a^2 + s^2}{2b_0}\right) I_0\left(\frac{as}{b_0}\right). \quad (6.29)$$

Then  $L_R$  can be simplified as

$$\begin{aligned} L_R &= p_a(R) \int_0^\infty \dot{a} p_{\dot{a}}(\dot{a}) d\dot{a} \\ &= p_a(R) \sqrt{\frac{b_2}{2\pi}}, \end{aligned} \quad (6.30)$$

where  $b_2 = -d^2 R_{ZZ}(\tau)/d\tau^2|_{\tau=0}$  [108]. Recall that the auto-correlation function  $R_{ZZ}(\tau)$  of the faded signal  $Z(t)$  is derived in (6.23). After derivation,  $b_2$  can be expressed as

$$b_2 = \frac{2\pi^2 (f_1^2 + f_2^2 + 2K \cos^2 \theta_3 f_3^2)}{K + 1}. \quad (6.31)$$

Note that  $b_2$  here is different from that in [105], which is  $b_2 = 2\pi^2 b_0 f_3^2 (1 + 2 \cos^2 \theta_3)$ . Because we consider the mobile-to-mobile double-ring model here,  $b_2$  here is a function of  $f_1$ ,  $f_2$ , and  $f_3$ , but  $b_2$  in [105] only associates with a single Doppler frequency  $f_3$ .

When  $\theta_3$  is 90 or 270 degrees, substituting (6.27) and (6.31) into (6.30) yields

$$\begin{aligned} L_R &= \frac{2(K + 1)R}{\Omega_p} \sqrt{\frac{b_2}{2\pi}} \exp\left(-K - \frac{(K + 1)R^2}{\Omega_p}\right) \\ &\cdot I_0\left(2R \sqrt{\frac{K(K + 1)}{\Omega_p}}\right). \end{aligned} \quad (6.32)$$

For the general case where  $\theta_3$  can take a random value, the LCR has no closed form solution. In [105], the LCR with uniform impinging angles was shown for the mobile-to-base Rician channels. For the special case of the single-ring model (that is,  $f_1 = f_3$ ,  $f_2 = 0$ ) with  $\theta_3$  being 90 or 270 degrees,  $b_2$  can be simplified as that in [105] and (6.32) can be simplified to (16) in [105].

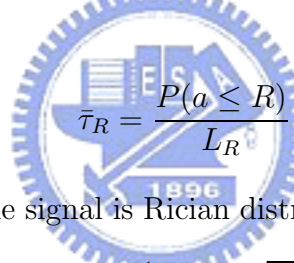
From (15a) in [105] with an assumption that  $\theta_3$  is uniform distributed on  $[0, 2\pi)$ , we can also have

$$\begin{aligned}
L_R = & \sqrt{\frac{2(1+K)}{\pi\Omega_p}} R f_3 \cdot \exp \left[ -K - \frac{(1+K)R^2}{\Omega_p} \right] \\
& \cdot \int_0^\pi \left[ 1 + \frac{2}{R} \sqrt{\frac{\Omega_p K}{1+K}} \cos^2 \theta_3 \cdot \cos \alpha \right] \\
& \cdot \exp \left[ 2R \sqrt{\frac{K(1+K)}{\Omega_p}} \cos \alpha - 2K \cos^2 \theta_3 \cdot \sin \alpha \right] d\alpha. \quad (6.33)
\end{aligned}$$

When  $\theta_3$  is 90 or 270 degrees, (6.33) can be simplified to (6.32).

## 6.4.2 Average Fade Duration

According to the definition in [106], the average fade duration ( $\bar{\tau}_R$ ) for a specified level  $R$  is



$$\bar{\tau}_R = \frac{P(a \leq R)}{L_R}. \quad (6.34)$$

Since the envelope of the signal is Rician distributed,  $\bar{\tau}_R$  can be expressed as

$$\bar{\tau}_R = \frac{1 - Q \left( \sqrt{2K}, \sqrt{\frac{2(K+1)}{\Omega_p}} R \right)}{L_R}, \quad (6.35)$$

where the Marcum's  $Q$  function is defined as

$$Q(a, b) = \int_b^\infty x \exp \left( -\frac{x^2 + a^2}{2} \right) I_0(ax) dx. \quad (6.36)$$

## 6.5 Numerical Results

This section first validates the proposed sum-of-sinusoids mobile-to-mobile Rician fading simulator, and then compare the correlation functions, PDF and the LCR and AFD of the proposed model with the theoretical values.

Consider that the maximum Doppler frequency for TX and RX is 100Hz and 20Hz, respectively, and  $\theta_1 = \pi/3$ ,  $\theta_{12} = \pi/5$ . From these values we can find that  $\theta_3 = 1.1865$ .

### 6.5.1 Effects of Rician Factor

Figure 6.4 shows the correlation properties of the proposed sum-of-sinusoids mobile-to-mobile simulator. The solid line in the figure represents the theoretical value and the dashed line represents the simulation results of the proposed channel model. Clearly, the two values match quite well for different Rician factors. Furthermore, for the same delay time  $\tau$ , the magnitude of the channel correlation ( $R_{ZZ}(\tau)$ ) is proportional to the magnitude of the Rician factor ( $K$ ). With reference to (6.23), it can be seen that for a large enough delay time  $\tau$ ,  $J_0(2\pi f_1\tau)J_0(2\pi f_2\tau) \approx 0$  and  $J_0(2\pi f_1\tau)J_0(2\pi f_2\tau) \ll K \exp(2\pi f_3\tau \cos \theta_3)$ . Thus, it follows that

$$\begin{aligned} \Re\{R_{ZZ}(\tau)\} &\simeq \Re\left\{\frac{K}{1+K}\exp(j2\pi f_3\tau \cos \theta_3)\right\} \\ &= \frac{K}{1+K} \cos(2\pi f_3\tau \cos \theta_3) . \end{aligned} \quad (6.37)$$

Therefore, the maximum amplitude of the autocorrelation function  $R_{ZZ}(\tau)$  is proportional to  $\frac{K}{1+K}$  because  $-1 \leq \cos(2\pi f_3\tau \cos \theta_3) \leq 1$ . As  $K$  increases, the peaks of  $R_{ZZ}(\tau)$  are close to one.

### 6.5.2 Comparison of Double-Ring with a LOS Component Model and Single-Ring Model

This part compares the proposed mobile-to-mobile Rician channel model developed from the double-ring with a LOS component scattering model with that developed from the single-ring scattering model [25] for different



Rician factors and different numbers of scatterers. The main purpose of the comparison is to demonstrate that it is more suitable to employ the double-ring scattering model to characterize the mobile-to-mobile communication channel, i.e., the single-ring model developed for mobile-to-base channels may not be directly used for mobile-to-mobile channels. Figure 6.5 show the correlation of the double-ring model with eight scatterers, the single-ring model with eight scatterers, the single-ring model with 64 scatterers and the theoretical correlation functions for  $K = 1$ . Obviously, the double-ring model matches the ideal curve for  $\Re[R_{ZZ}(\tau)]$  perfectly and yields better performance than the single-ring model even when 64 scatterers are used in the single-ring model. The difference between the two scattering models is significant.

### 6.5.3 LCR and AFD

Figure 6.6 shows the LCR of a mobile-to-mobile Rician channel fading envelope obtained using the sum-of-sinusoids method and that from theoretical analysis. As can be seen, LCR decreases with increase in the Rician factor. This phenomenon can be explained by the fact that channel fading has greater correlation with larger amount of LOS components. Once the correlation arises, the change in channel fading decreases.

Figure 6.7 shows the analytical and simulated values of the normalized AFD for different Rician factors. As shown in the figure, the larger the Rician factor, the larger the AFD is. This property is caused by higher correlation of fading envelope for a larger Rician factor. Thus, if the signal envelope fades below a specified level, it is less likely that it will exceed the level.

The numerical results for LCR and AFD show some deviation of the simulation from the theoretical values, especially for small  $K$  (1 and 3). The

simulation curves consistently fall below the analytical curves, which do not occur for the larger values of  $K$ . This is because when  $K$  is small, the scatterers term will dominate the double-ring model. The simulation can only produce finite scatterers which cannot approach the ideal case enough, thus the deviation occurs. When  $K$  is large, the LOS term dominates the double-ring model, hence the problem of finite number of scatterers is not so significant compared to the cases of small values of  $K$ .

## 6.6 Conclusions

In this chapter, a sum-of-sinusoids-based mobile-to-mobile Rician fading simulator is developed. The double-ring scattering model is proposed for characterizing the mobile-to-mobile communication environment with LOS components. Furthermore, the theoretical correlation functions of the mobile-to-mobile Rician channel are derived and its accuracy is verified by simulations. The LCR and AFD of the mobile-to-mobile Rician fading channel are derived. Finally, it is proved that the proposed sum-of-sinusoids approximation developed from the double-ring with a LOS component model can approach the theoretical value more closely than the single-ring model at a slightly higher cost of computation loads.

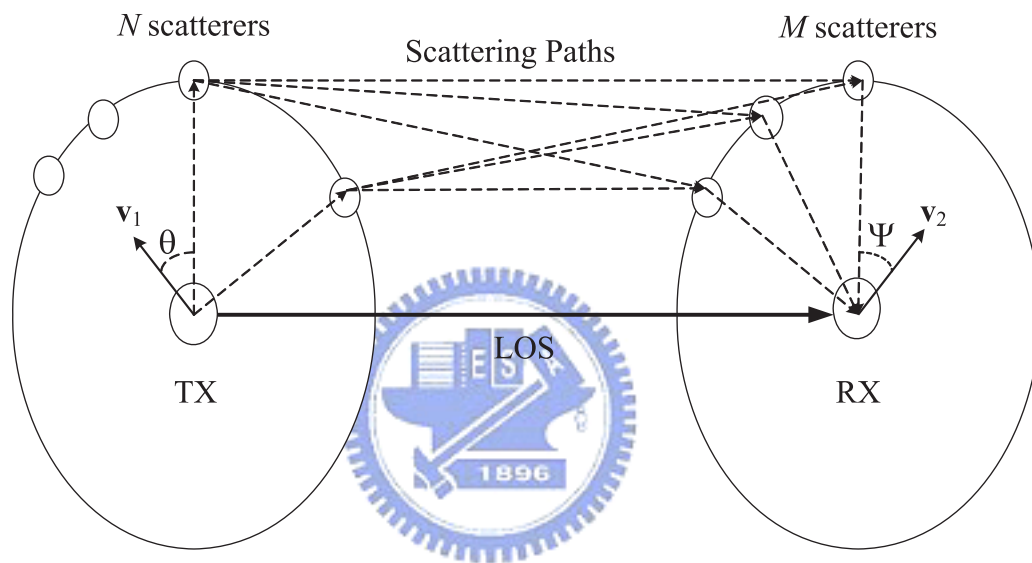


Figure 6.1: Scattering environment in a mobile-to-mobile system with a LOS component.

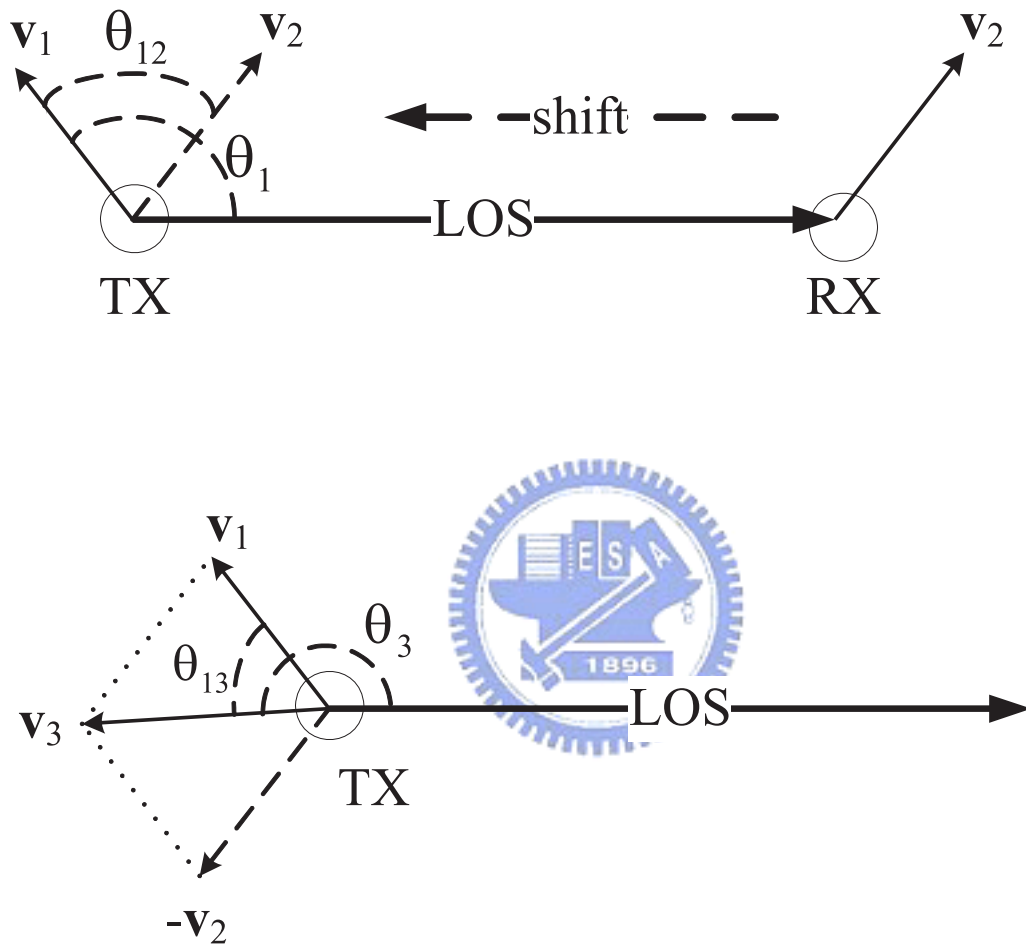


Figure 6.2: Relative velocity  $\mathbf{v}_3$  from the TX with velocity  $\mathbf{v}_1$  to the RX with velocity  $\mathbf{v}_2$ .

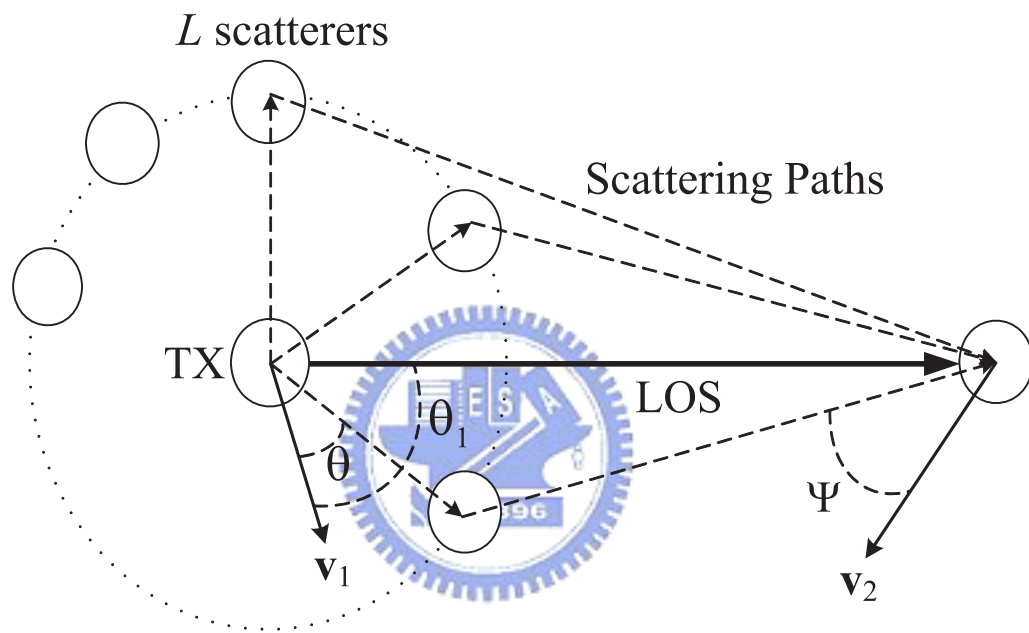


Figure 6.3: Single-ring scattering environment for a mobile-to-mobile Rician fading channel.

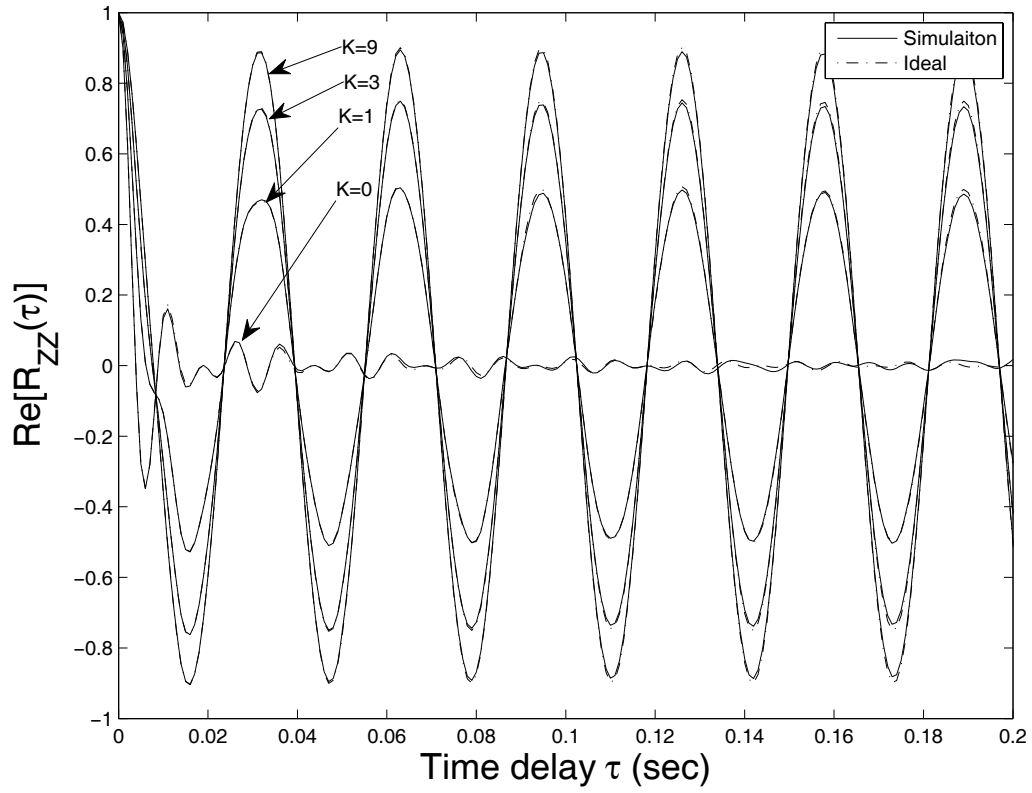


Figure 6.4: The real part of the autocorrelation of the complex envelope  $Z(t)$ , where  $N = M = 8$  for  $K = 0, 1, 3$ , and  $9$ .

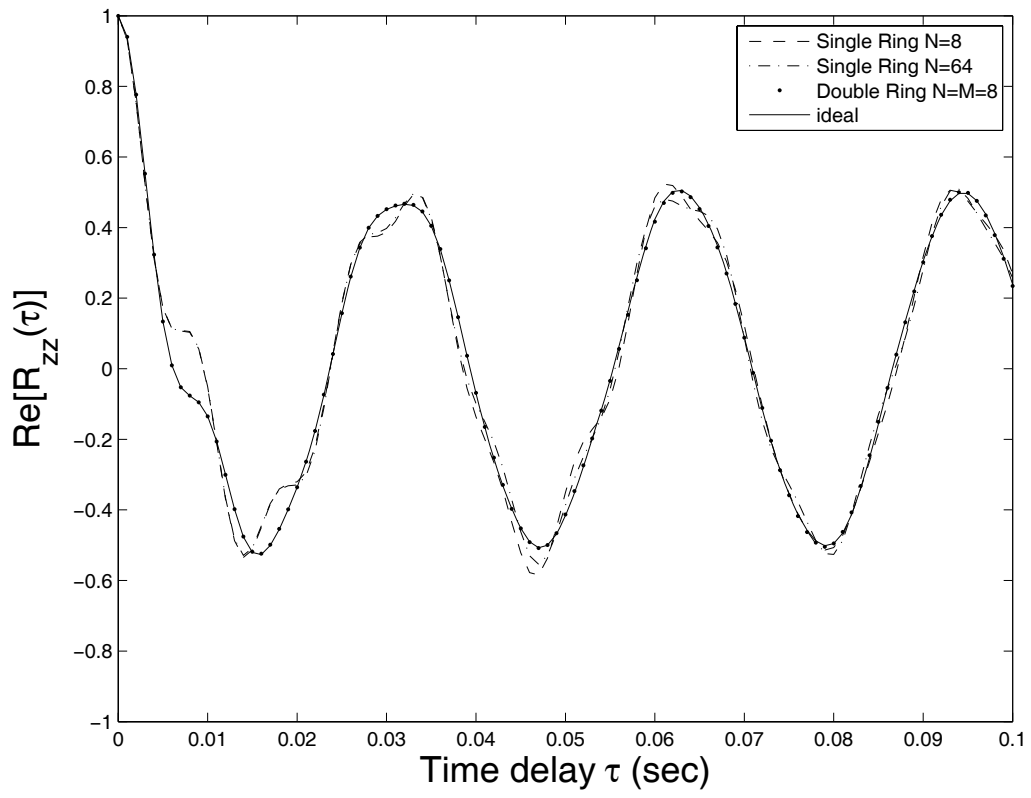


Figure 6.5: The real part of the autocorrelation of the fading envelope of double-ring and single-ring scattering models for  $K = 1$ .

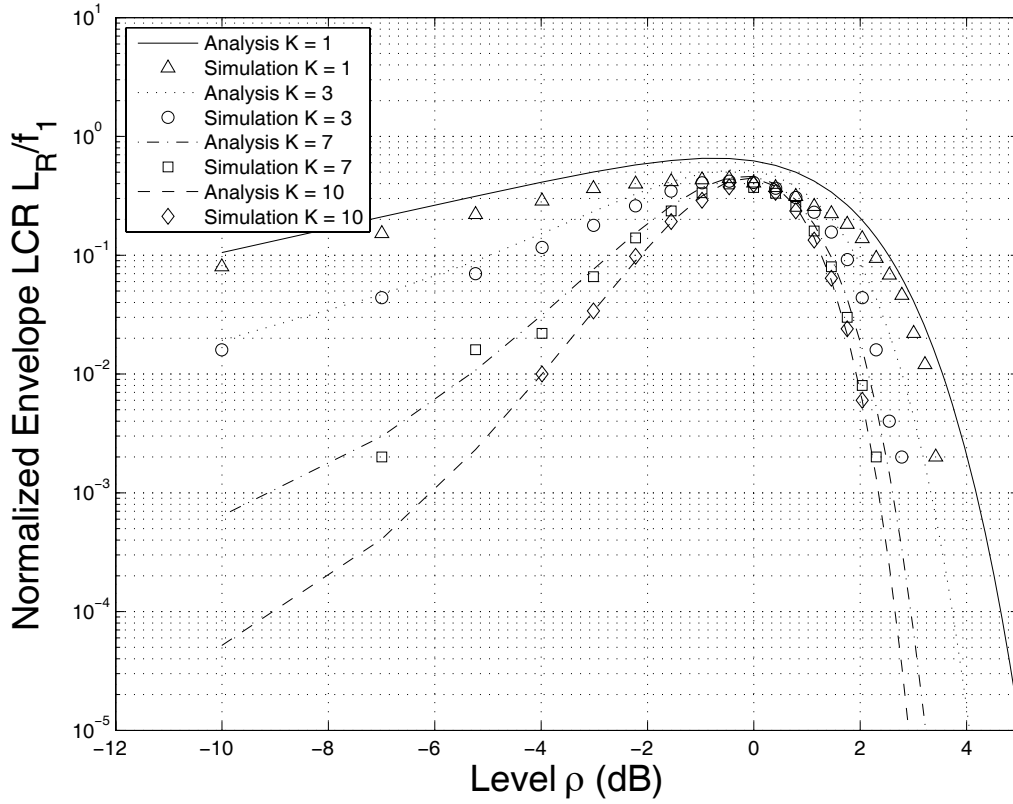


Figure 6.6: Normalized envelope level crossing rate for mobile-to-mobile Rician fading. Solid line denotes the theoretical results and the dashed line denotes the simulation results, where  $\rho = \frac{R}{\sqrt{\Omega_p}}$ .



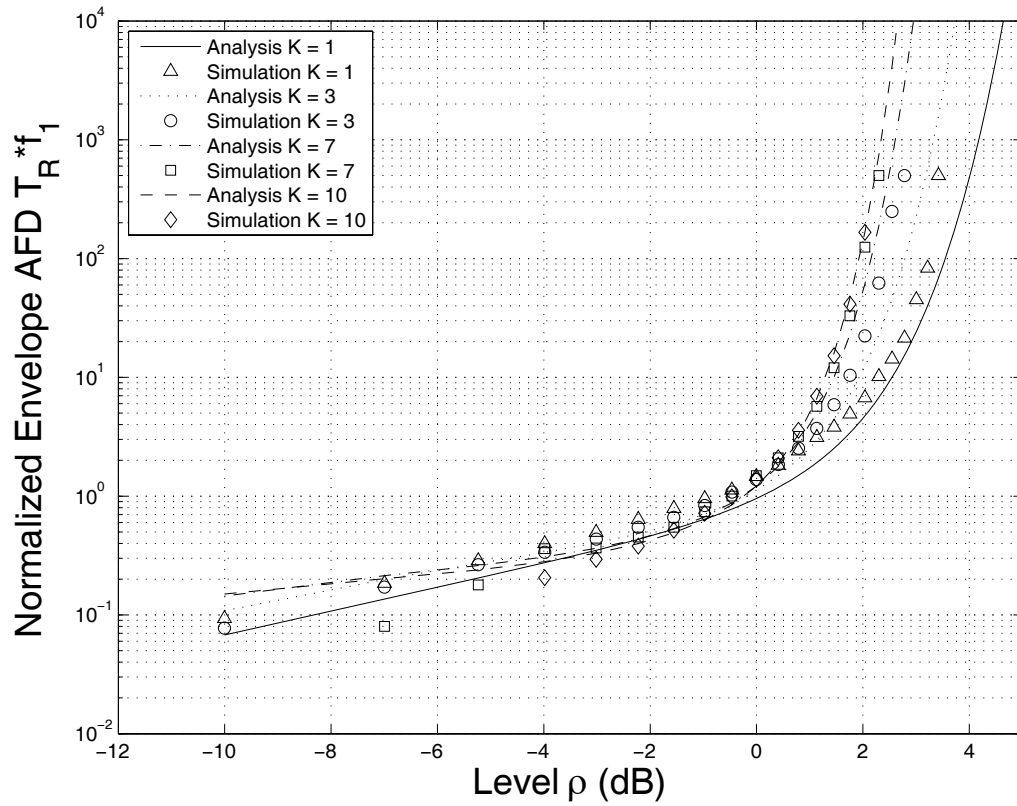


Figure 6.7: Normalized average fade duration for a mobile-to-mobile Rician fading channel for  $K = 1, 3, 7,$  and  $10$ .

# Chapter 7

## Modeling and Capacity Fades

### Analysis of MIMO Rician

### Channels in Mobile Ad Hoc

### Networks



Multiple-input multiple-output (MIMO) mobile ad hoc networks have been receiving increasing attention in both commercial and military applications. Just as in cellular networks, MIMO technologies can benefit ad hoc networks by providing the diversity and capacity advantages as well as the spatial degree of freedom in designing the media access control (MAC) protocol. However, one fundamental issue of MIMO mobile ad hoc networks is how to accurately model the impact of spatial/temporal channel correlation in the mobile-to-mobile communication environment. In such a channel, a line-of-sight (LOS) component and different scattering environments will affect both ergodic capacity and average capacity fade duration of the MIMO system. In this chapter, based on the correlated double-ring scattering model we sug-

gest a sum-of-sinusoids MIMO mobile-to-mobile channel simulation method, which can characterize the spatial/temporal channel correlation and Rician fading effect. We examine how often the MIMO capacity experiences the fades and relate this to the Rician factor.

## 7.1 Motivation

Multiple-input multiple-output (MIMO) antenna technique has recently emerged as one of the most significant breakthroughs in communications. The fourth generation (4G) cellular system [110] and the next generation high-speed IEEE 802.11n [111] wireless local area network (WLAN) all adopt the MIMO technique to deliver capacity and diversity gains.

Meanwhile, another communication paradigm – ad hoc networks – has become an important alternative for next generation wireless systems. In contrast to conventional cellular systems with a master-slave relation between the base station and mobile users, nodes in ad hoc networks adopt peer-to-peer communications. Specifically, this communication is supported by direct connection or multiple hop relays without fixed wireless infrastructure. Ad hoc networks have been enabled in many standards such as Bluetooth and IEEE 802.11 WLAN. Ad hoc networking is considered the key enabling technique of many future wireless systems, such as wireless mesh networks [112] and cognitive radio [113].

Unlike conventional mobile-to-fixed base station systems that have been benefited from the MIMO technique, how and to what extent the ad hoc networks can benefit from the MIMO technique is still an open research area. One fundamental issue is how to accurately model the impact of spatial/temporal correlation on MIMO capacity from the viewpoint of the

mobile-to-mobile communication. Scattering model and the line-of-sight (LOS) component are two important factors that need to be considered. First, in a mobile-to-mobile environment, the antenna heights of both the transmitter and the receiver are lower than the surrounding objects. Thus, the signal in a mobile-to-mobile environment will experience a richer scattering effect than in a mobile-to-base environment [20, 26, 114]. Second, an LOS component may more likely exist in a short distance mobile-to-mobile application than in a long-distance mobile-to-base environment. In [115], the distribution of the Rician  $K$  factor was modeled as lognormal, with the median as a function of distance:  $K \propto (\text{distance})^{-0.5}$ . Implicitly, the  $K$  factor increases as the distance decreases. Thus, the Rician fading effect cannot be neglected in a short-distance mobile-to-mobile communication environment.

## 7.2 Scattering Model

In this section, we introduce the correlated double-ring scattering model [114]. This model can be used to capture the scattering effect and the LOS effect in a mobile-to-mobile environment as shown in Fig. 7.1. In the figure, the transmitter and the receiver moving at a speed of  $\mathbf{v}_1$  and  $\mathbf{v}_2$  m/sec, are surrounded by  $I$  and  $N$  scatterers, respectively. The angles of departure (AOD) between vector  $\mathbf{v}_1$  and scattering paths, denoted by  $\theta_{ti}$  ( $i = 1, 2, \dots, I$ ) and  $\theta_{rn}$  ( $n = 1, 2, \dots, N$ ), are the angles of arrival between vector  $\mathbf{v}_2$  and the scattering paths. We assume that  $\theta_{ti}$  and  $\theta_{rn}$  are independent and uniformly distributed over  $[-\pi, \pi)$ . Note that there exist LOS components between the transmitter TX and the receiver RX, where both TX and RX are equipped with multiple antennas.

Consider that the multiple antennas are separated by a distance  $d$ . In the

case where transmission distance from the scatterers to the receive antenna is much longer than  $d$ , then the angle of arrival (AOA) from the  $n$ -th scatterer to each receive antenna will be about the same. Thus, as shown in Fig. 7.2, for the case with two receive antennas, the transmission distance from the  $n$ -th scatterer to the second receive antenna is  $d \cos \theta_{rn}$  longer than that to the first receive antenna.

## 7.3 Sum-of-Sinusoids MIMO Rician Fading Simulator

### 7.3.1 LOS Component Model

To begin with, we discuss the approach to model the LOS component between each pair of moving transmit and receive antennas. For simplicity, we first consider the single antenna case. Referring to Fig. 7.3(a), let the transmitter TX move at a speed of  $\mathbf{v}_1$  toward the direction of the angle  $\theta_\beta$  relative to the direction of velocity  $\mathbf{v}_2$  of receiver RX, where  $\theta_\alpha$  is the angle between  $\mathbf{v}_1$  and the transmission direction of the LOS component. Using the concept of relative motion [116], let the velocity of RX be zero and denote  $\mathbf{v}_3$  the relative velocity from TX to RX, as shown in Fig. 7.3(b). In the figure,  $\theta'$  is the angle between  $\mathbf{v}_3$  and LOS component. The relative velocity  $\mathbf{v}_3$  can be derived as follows:

$$|\mathbf{v}_3| = \sqrt{(|\mathbf{v}_1| \cos \theta_\beta - |\mathbf{v}_2|)^2 + (|\mathbf{v}_1| \sin \theta_\beta)^2} , \quad (7.1)$$

$$\theta' = 2\pi - \theta_\alpha - \theta_\gamma , \quad (7.2)$$

and

$$\theta_\gamma = \cos^{-1} \left( \frac{|\mathbf{v}_1|^2 + |\mathbf{v}_3|^2 - |\mathbf{v}_2|^2}{2|\mathbf{v}_1||\mathbf{v}_3|} \right) , \quad (7.3)$$

where  $|\mathbf{v}|$  is the length of a vector  $\mathbf{v}$ ,  $\theta_\gamma$  is the angle between velocity vectors  $\mathbf{v}_3$  and  $\mathbf{v}_1$ . Thus the LOS component can be expressed as

$$\text{LOS} = \sqrt{K} \exp[j(2\pi f_c t - 2\pi f_3 t \cos \theta')] , \quad (7.4)$$

where the Rician  $K$  factor is defined as the ratio of the specular power to scattering power [25],  $f_c$  is the carrier frequency,  $f_3 = |\mathbf{v}_3|/\lambda$  is the relative maximum Doppler frequency between TX and RX, and  $\lambda$  is the wavelength.

Now, we consider the scenario with multiple antennas. Define  $H_{ml}$  as the complex channel gain between the  $l$ -th transmit antenna and  $m$ -th receive antenna. From Fig. 7.3(c), the LOS components for  $H_{11}$  and  $H_{21}$  can be respectively expressed as

$$\text{LOS}_{11} = \sqrt{K_{11}} \exp[j(2\pi f_c t - 2\pi f_3 t \cos \theta'_{11})] \quad (7.5)$$

and

$$\text{LOS}_{21} = \sqrt{K_{21}} \exp[j(2\pi f_c t - 2\pi f_3 t \cos \theta'_{21})] , \quad (7.6)$$

where  $K_{ml}$  is the Rician factor defined as the ratio of specular power to the scattering power of the channel  $H_{ml}$  [117];  $\theta'_{11}$  and  $\theta'_{21}$  are the angles between the LOS components  $\text{LOS}_{11}$  and  $\text{LOS}_{21}$  to the velocity vector  $\mathbf{v}_3$ , respectively. Assume that the transmission distance between the two mobiles is much longer than the antenna separation  $d$ . Then, the angles  $\theta'_{11}$  and  $\theta'_{21}$  are about the same. Likewise,  $\theta'_{21} = \theta'_{22} = \theta'_{11} = \theta'_{12}$ . To ease notation for all  $m$  and  $l$ , let

$$\rho = 2\pi f_c t - 2\pi f_3 t \cos \theta'_{ml} . \quad (7.7)$$

### 7.3.2 Sum-of-Sinusoids Simulation Method

Based on the correlated double-ring scattering model and the LOS component model which was proposed in [118], we suggest the sum-of-sinusoids

simulation method for a mobile-to-mobile MIMO channel model with LOS components. Consider narrowband signals in a flat Rician fading channel. The MIMO channel is expressed as an  $M \times L$  matrix  $\mathbf{H}$ , where  $M$  and  $L$  are the numbers of antennas at the receiver and transmitter, respectively.  $H_{ml}$  is the element of the  $m$ -th row and  $l$ -th column. With this notation, we have

$$H_{11} = \frac{1}{\sqrt{1 + K_{11}}} \left[ \frac{1}{\sqrt{IN}} \sum_{n=1}^N \sum_{i=1}^I A_{in} \exp(j\phi_{in}) + \sqrt{K_{11}} \exp(j\rho) \right], \quad (7.8)$$

where

$$\phi_{in} = 2\pi f_c(t - \tau_{in}) - 2\pi f_2(t - \tau_{in}) \cos \theta_{rn} - 2\pi f_1(t - \tau_{in}) \cos \theta_{ti}, \quad (7.9)$$

$A_{in}$  and  $\phi_{in}$  are the amplitude and phase of the  $in$ -th scattering path, respectively,  $f_1 = |\mathbf{v}_1|/\lambda$  and  $f_2 = |\mathbf{v}_2|/\lambda$  are the maximum Doppler frequencies resulted from the motion of TX and RX, respectively,  $I$  and  $N$  are the numbers of the scatterers around TX and RX, respectively.  $\tau_{in}$  is the transmission delay of the  $in$ -th scattering path.

For  $H_{21}$ , we further consider the added transmission delay because of the antenna separation  $d$ . Thus, it follows that

$$H_{21} = \frac{1}{\sqrt{1 + K_{21}}} \left[ \frac{1}{\sqrt{IN}} \sum_{n=1}^N \sum_{i=1}^I A_{in} \exp(j\phi_{in} + j\beta d(2 - 1) \cos \theta_{rn}) + \sqrt{K_{21}} \exp(j\rho) \right], \quad (7.10)$$

where  $\beta = 2\pi/\lambda$  is the wave number. Thus, the general form of the channel  $H_{ml}$  can be computed by

$$H_{ml} = \frac{1}{\sqrt{1 + K_{ml}}} \left[ \frac{1}{\sqrt{IN}} \sum_{n=1}^N \sum_{i=1}^I A_{in} \exp(j\phi_{in} + j\beta d(m - 1) \cos \theta_{rn} + j\beta d(l - 1) \cos \theta_{ti}) + \sqrt{K_{ml}} \exp(j\rho) \right], \quad (7.11)$$

for every  $m = 1, 2, \dots, M$  and  $l = 1, 2, \dots, L$ .

## 7.4 Capacity Evaluation

Consider an  $M \times L$  MIMO channel matrix, and assume that the knowledge of a frequency flat faded signal can be known perfectly at the receiver. Let  $\mathbf{n}$  be an  $M \times 1$  zero mean complex AWGN vector, of which the covariance matrix is equal to  $\sigma^2 \mathbf{I}_M$ , where  $\mathbf{I}_M$  stands for an  $M \times M$  identity matrix. The  $M \times 1$  received signal vector  $\mathbf{y}$  can be expressed as [119]

$$\mathbf{y} = \mathbf{H}\mathbf{x} + \mathbf{n} \quad , \quad (7.12)$$

where  $\mathbf{x}$  is an  $L \times 1$  transmitted signal vector.

### 7.4.1 Ergodic Capacity

The instantaneous capacity of an MIMO channel can be written as [120–122]

$$c(t) = \begin{cases} \log_2 \left[ \det \left( \mathbf{I}_M + \frac{\text{SNR}}{L} \cdot \mathbf{H}\mathbf{H}^\dagger \right) \right] & \text{if } M < L, \\ \log_2 \left[ \det \left( \mathbf{I}_L + \frac{\text{SNR}}{L} \cdot \mathbf{H}^\dagger \mathbf{H} \right) \right] & \text{if } M \geq L, \end{cases} \quad (7.13)$$

where SNR is the signal-to-noise ratio and  $\dagger$  denotes transpose conjugate.

In this part, we derive the channel correlation and find its channel capacity. The channel correlation between  $H_{11}$  and  $H_{21}$  is [26]

$$\Delta_{11,21} = E[H_{11}H_{21}^*] \quad , \quad (7.14)$$

where  $*$  is the complex conjugate. Assume that the number of scatterers around the transmitter and receiver equals  $N$ ;  $A_{in}$  is a zero mean unit variance normal random variable because of the central limit theorem for many scatterers;  $\theta_{ti}$  and  $\theta_{rn}$  are uniform random variables. All the above random variables are mutually independent. Then, we have

$$\Delta_{11,21} = \frac{J_0(\beta d) + \sqrt{K_{11}}\sqrt{K_{21}}}{\sqrt{1 + K_{11}}\sqrt{1 + K_{21}}} \quad . \quad (7.15)$$



The general form of the channel correlation between  $H_{ml}$  and  $H_{pq}$  should be expressed as

$$\Delta_{ml,pq} = \frac{J_0(\beta d(m-p))J_0(\beta d(l-q)) + \sqrt{K_{ml}}\sqrt{K_{pq}}}{\sqrt{1+K_{ml}}\sqrt{1+K_{pq}}}, \quad (7.16)$$

where  $J_0(\cdot)$  is the zeroth-order Bessel function of the first kind.

From (7.13), the average capacity of the MIMO channel can be expressed as

$$C_E = E \left[ \log_2 \left( \det \left( \mathbf{I}_M + \frac{\text{SNR}}{L} \cdot \mathbf{H}\mathbf{H}^\dagger \right) \right) \right]. \quad (7.17)$$

By using Jensen's inequality, we conclude that the average capacity is bounded by

$$C_E \leq \log_2 \left( \det \left( \mathbf{I}_M + \frac{\text{SNR}}{L} \cdot E[\mathbf{H}\mathbf{H}^\dagger] \right) \right). \quad (7.18)$$

Let  $\mathbf{R}$  denote the correlation channel matrix  $E[\mathbf{H}\mathbf{H}^\dagger]$ , where

$$R_{ij} = \sum_{v=1}^L E[H_{iv}H_{jv}^*] = \sum_{v=1}^L \frac{J_0(\beta d(i-j)) + \sqrt{K_{iv}}\sqrt{K_{jv}}}{\sqrt{1+K_{iv}}\sqrt{1+K_{jv}}}. \quad (7.19)$$

Thus, we can derive the entire correlation channel matrix  $\mathbf{R}$  and channel capacity from (7.19). Substituting  $\mathbf{R}$  into (7.18), we can find an upper bound for the mobile-to-mobile MIMO channel capacity.

## 7.4.2 Level Crossing Rate and Average Fade Duration

To examine the temporal behavior of the MIMO capacity, we first study the level crossing rate (LCR) and average fade duration (AFD). Denote  $L_\varepsilon$  and  $\tau_\varepsilon$  the LCR across a specified level  $\varepsilon$  of the instantaneous capacity  $c(t)$ , and the AFD below the level  $\varepsilon$ , respectively. Based on the definition of LCR [106], we have

$$L_\varepsilon = \int_0^\infty \dot{c} p_{c,\dot{c}}(\varepsilon, \dot{c}) d\dot{c} \quad (7.20)$$

where  $\dot{c} \triangleq \frac{dc(t)}{dt}$  is the derivative of the instantaneous channel capacity with respect to time  $t$ ;  $p_{c,\dot{c}}(c, \dot{c})$  is the joint probability density function (pdf) of the instantaneous channel capacity and its derivative. Obviously, how to obtain the joint pdf  $p_{c,\dot{c}}(c, \dot{c})$  is the key issue to calculate  $L_\varepsilon$ . From [27, 123, 124], we know that the instantaneous capacity distribution for MIMO systems in the independent Rayleigh fading channel can be estimated by Gaussian distribution. Whether the Gaussian approximation of the instantaneous MIMO capacity is accurate for the Rician fading channel is less well-known. Further, it is worthwhile examining if a Gaussian sequence can match the temporally correlated sequence of instantaneous MIMO capacity in a Rician fading channel. To this end, we first hypothesize that the instantaneous capacity distribution of the mobile-to-mobile MIMO Rician channel is Gaussian. In Section 7.5, we will perform simulations based on the proposed sum-of-sinusoids method to confirm this theory. If the instantaneous MIMO capacity  $c(t)$  in the mobile-to-mobile Rician fading channel is accurately estimated by a Gaussian process, the LCR problem can be solved by using Rice's formula of stochastic processes [23]. Specifically, we can have

$$L_\varepsilon = \frac{(-\ddot{\rho}_c(0))^{1/2}}{2\pi} \exp\left(-\frac{\varepsilon^2}{2}\right), \quad (7.21)$$

where  $\rho_c(\tau)$  is the autocorrelation function of  $c(t)$  and

$$-\ddot{\rho}_c(0) = \text{var}\left(\frac{dc(t)}{dt}\right)\Big|_{t=0}. \quad (7.22)$$

Since the analytical formula of  $\rho_c(\tau)$  is not available [125], we adopt a semi-analytical method. That is, we obtain  $-\ddot{\rho}_c(0)$  from simulation data and then substitute it into (7.21). Once  $L_\varepsilon$  is known, it follows that

$$\tau_\varepsilon = \frac{F_c(\varepsilon)}{L_\varepsilon}, \quad (7.23)$$

where  $F_c(\cdot)$  is the cumulative density function (cdf) of instantaneous channel capacity  $c(t)$ . Note that  $F_c(\cdot)$  can be obtained by pure simulation or the cdf

of a Gaussian random variable with a mean and variance from the simulation data.

## 7.5 Numerical Results

In our simulations, we randomly generate the mobile-to-mobile MIMO channel matrix  $\mathbf{H}$  and calculate the instantaneous and average channel capacity of  $\mathbf{H}$  according to (7.13) and (7.17), respectively. The purposes of simulations are the following. First, we want to prove the ergodicity of our MIMO channel capacity model by examining time and ensemble averages. Second, we evaluate the capacity of MIMO Rician fading channel with different Doppler frequencies. Third, we vary the antenna separations and the Rician factors to explore the relationship between spatial channel correlation and channel capacity. Then, we vary the numbers of scatterers to inspect the scattering effect to the MIMO channel capacity. Finally, we compare the pdf of the channel capacity with Gaussian distribution to verify the correctness of the hypothesis used in Section 7.4. We will present the LCR and AFD of MIMO capacity for various Rician factor and number of antennas.

### 7.5.1 Channel Correlation

To check the correctness of (7.16), we calculate the analytical and simulation values of the channel correlations of a  $3 \times 3$  MIMO channel with SNR = 20 dB,  $d = \frac{\lambda}{2}$ , and  $K = 4.77$  dB, which are listed in Table 7.1. We can see the analytical and simulation values are very close. Note that the analytical value for  $\Delta_{ml,pq}$  in (7.16) is a real number. In Table 7.1, the simulation values have a small or zero imaginary part, which agrees with (7.16).

Table 7.1: The simulation and analytical values of the channel correlation of a  $3 \times 3$  MIMO channel.

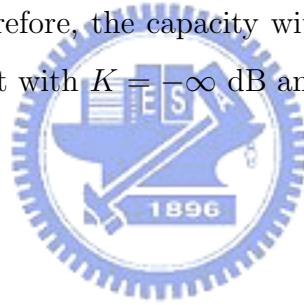
	$\Delta_{11,21}$	$\Delta_{11,22}$	$\Delta_{11,23}$
analysis	0.6739	0.7731	0.7332
simulation	$0.6751 + j0.0792$	$0.7676 - j0.0227$	$0.7360 - j0.0273$
		$\Delta_{11,13}$	$\Delta_{11,11}$
analysis		0.8051	1
simulation		$0.7966 - j0.0532$	1.0182

## 7.5.2 Impacts of Doppler Frequencies

Figure 7.4 shows the impact of various Doppler frequencies on the instantaneous capacity  $c(t)$  defined in (7.13) of a  $3 \times 3$  MIMO channel with SNR = 20 dB,  $d = \frac{\lambda}{2}$ , and  $K = 4.77$  dB. From the simulations, we note that the LCR of the capacity is proportional to the Doppler frequency. The mean of the capacity under  $f_1 = 10$  Hz, 50 Hz, and 100 Hz are 10.9876 bps/Hz, 11.7725 bps/Hz, and 10.8143 bps/Hz, respectively. The corresponding variances are 1.7242, 2.4615, and 2.3634, respectively. This result tells us that in a mobile-to-mobile MIMO communication environment the speed of the mobilities will not affect the average channel capacity but will influence the accuracy of channel estimation. This property has not been shown in [26] because  $\phi_{in}$  is assumed to be uniformly distributed over  $[-\pi, \pi)$  in (7.9). In our model, we relax this assumption and produce the time function  $\phi_{in}(t)$ . Thus, the temporal behaviors of the channel capacity based on the sum-of-sinusoids method can be observed.

### 7.5.3 Effect of Spatial Correlation

Figure 7.5 shows the capacity of a  $3 \times 3$  mobile-to-mobile MIMO channel for different Rician  $K$  factors and antenna separation  $d$ . The capacity obtained by the simulation is lower than its upper bound. In general, we find that the MIMO capacity grows with the increase of the antenna separations when  $d \geq \frac{\lambda}{10}$ , and it reaches the maximum when  $d \geq \frac{\lambda}{2}$ . We also find that the capacity vibrates when  $d$  becomes very large. This phenomenon results from the Bessel function in (7.16). Recall that the tail of the Bessel function is cosine vibration and its amplitude is exponentially decreased. For the fixed antenna separation, the other source of channel correlation is from the Rician factor. Based on (7.16), if the channel correlation arises, the capacity reduced at the same time. Therefore, the capacity with  $K = 4.77$  dB shown in the figure is lower than that with  $K = -\infty$  dB and  $K = 0$  dB.



### 7.5.4 Impact of Numbers of Antennas

Figure 7.6 shows the effect of various numbers of antennas on the channel capacity and the capacity per antenna of a MIMO channel, respectively, when  $d = \frac{\lambda}{2}$  and  $K = -\infty$  dB, 4.77 dB, 6.99 dB. It is well known that MIMO channel capacity is proportional to the number of antennas [120–122]. From the figure, however, we note that the capacity will no longer linearly increase as the number of antennas increases. The total channel capacity increases slowly when the number of antennas exceeds about 20. Thus, it is not a good idea to increase the number of antennas without limit.

### 7.5.5 Impact of Numbers of Scatterers

Figure 7.7 shows the effect of various numbers of scatterers on the total channel capacity of an MIMO system when  $d = \frac{\lambda}{2}$  and  $K = -\infty$  dB. We examine the effect of the number of scatterers on channel capacity with various number of scatterers (denoted by  $I$  and  $N$ ). One can see that the total capacity is linearly proportional to the number of antennas when  $I = N = 40$ . When  $I = N = 20$  and  $I = N = 8$ , due to less richness of the scatterers the total capacity of the MIMO channel is saturated as the number of antenna increases. Thus, if we want to obtain higher channel capacity by increasing the number of antennas, it is important to consider the scattering environment.

### 7.5.6 Capacity Distribution

Figure 7.8 shows the pdf of the  $2 \times 2$  MIMO capacity in mobile-to-mobile Rician fading channels. In the figure, we see that the pdf of the MIMO capacity in Rician fading channels can be approximated by Gaussian pdf. As the Rician factor  $K$  increases, the MIMO capacity decreases and varying capacity is also reduced. We also check the accuracy of Gaussian approximation for the MIMO capacity in a mobile-to-mobile Rician fading channel by changing different Doppler frequencies and reach the same conclusion.

### 7.5.7 LCR and AFD

Figures 7.9 and 7.10 show the LCR and AFD of the MIMO capacity in a mobile-to-mobile Rician fading channel. We confirm the accuracy of Gaussian approximation used in the proposed semi-analytical model by simulations. In Fig. 7.9, we find that the range of the capacity crossing level decreases when  $K$  increases. This is mainly because the capacity correla-

tion is proportional to the extent of the LOS component. Also, the extent of the capacity variation decreases when  $K$  increases. In Fig. 7.10, we find that the rate of rising of the AFD will rapidly increase when Rician factor increases. This phenomenon comes from that the variance of the channel capacity decreasing as  $K$  increasing, as we noted in Fig. 7.8.

## 7.6 Conclusions

In this chapter, we have developed a sum-of-sinusoids simulation method for the MIMO system in a mobile-to-mobile fading channel. Based on the “correlated double-ring” scattering model [114], we incorporate the effect of Doppler effects, antenna separation, and LOS components for the MIMO system in a mobile-to-mobile environment. We have also derived the capacity upper bound of the mobile-to-mobile MIMO Rician channel. The channel capacity has been confirmed through simulations. We find that for MIMO systems with constant number of scatterers, increasing number of antennas cannot linearly increase the capacity. The capacity per antenna is decreased as Rician factor increases. We also find that the total channel capacity is related to the richness of the scattering environment. We looked into the temporal behavior of the capacity of the mobile-to-mobile MIMO Rician channel. Besides, we proposed a “semi-analytical” model for computing the LCR and AFD of the MIMO channel capacity. From those simulation results, we noted the influence of the LOS component, Doppler frequency, and other parameters on the temporal behavior of the MIMO channel capacity.

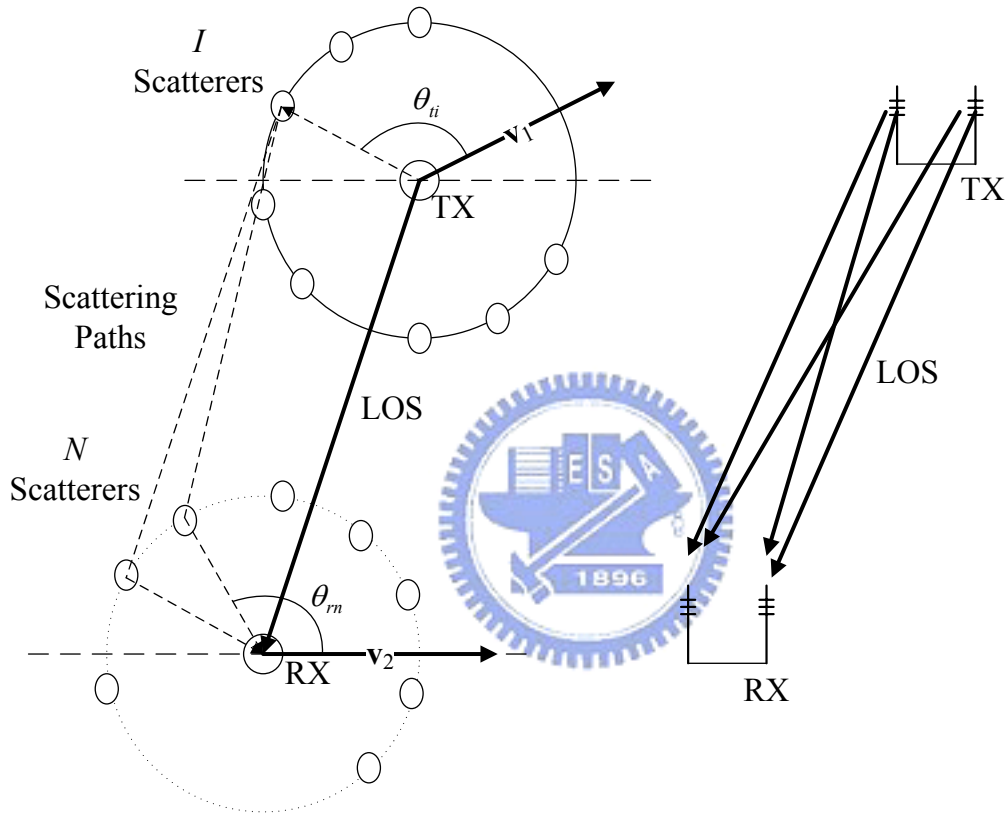


Figure 7.1: Correlated double-ring scattering model with LOS components.



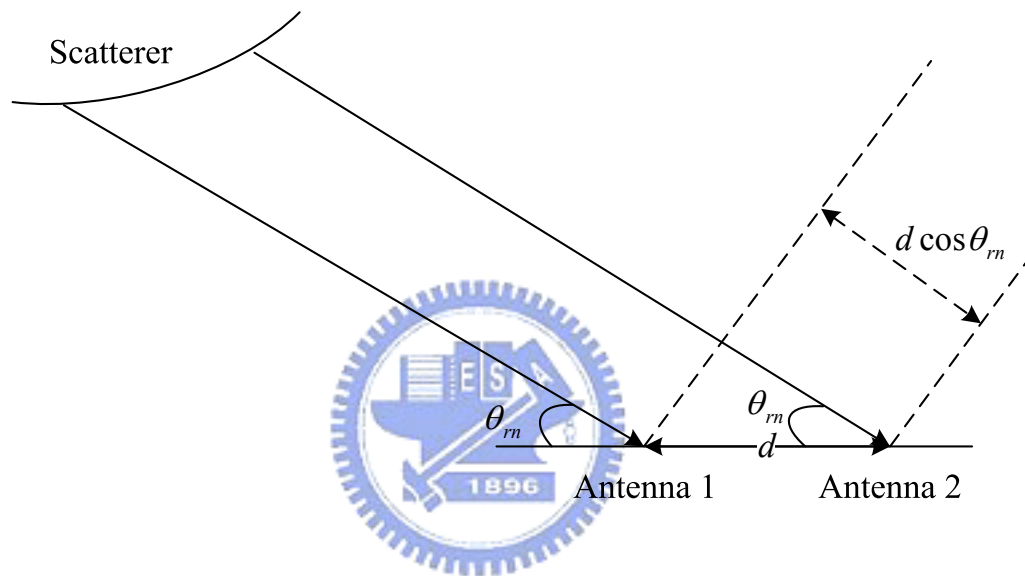


Figure 7.2: Received signals at multiple antennas with an AOA  $\theta_{rn}$  and separation distance  $d$  under the assumption that the transmission distance is much longer than  $d$ .

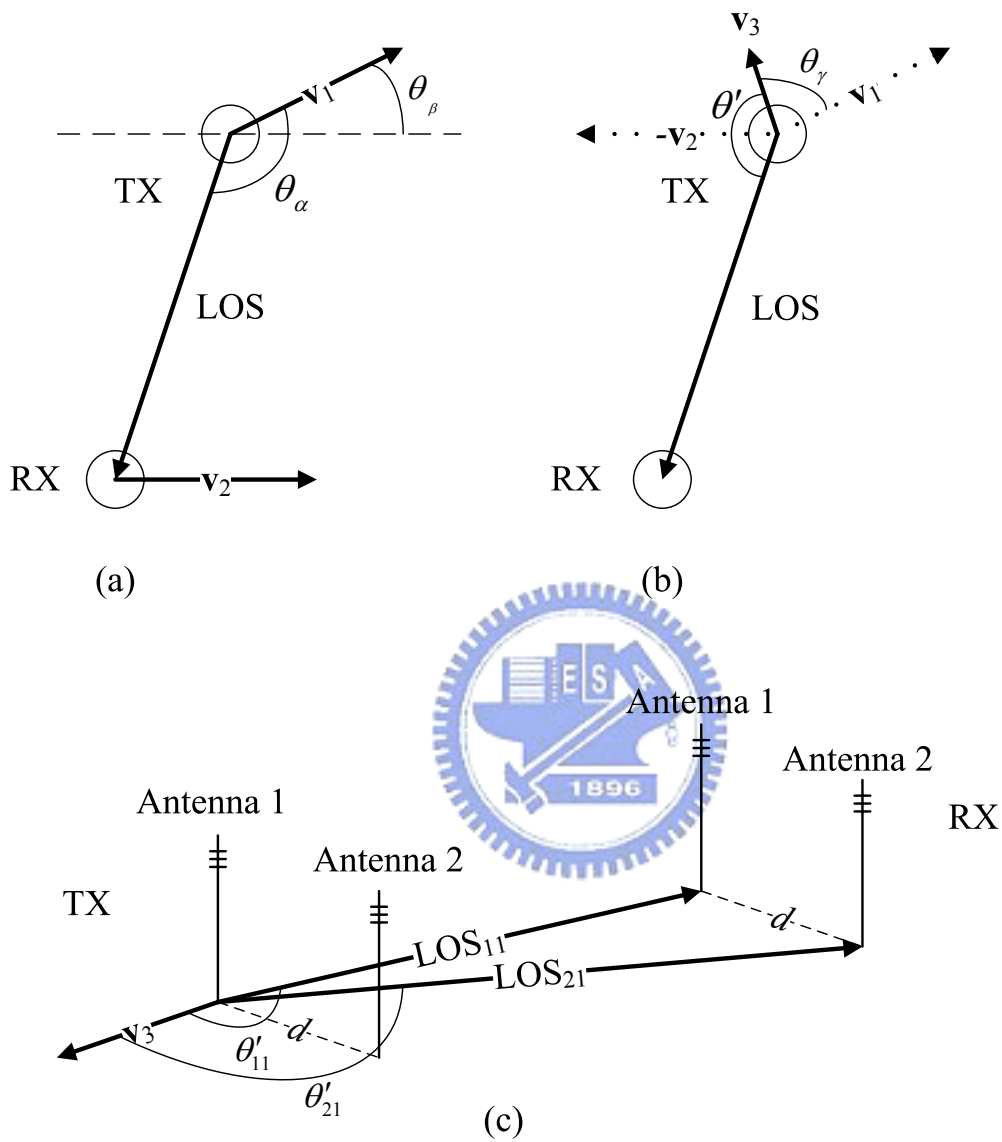


Figure 7.3: LOS component model for moving transmitter TX and receiver RX of which velocity vectors are  $\mathbf{v}_1$  and  $\mathbf{v}_2$  with a relative angle of  $\theta_\beta$ , respectively.

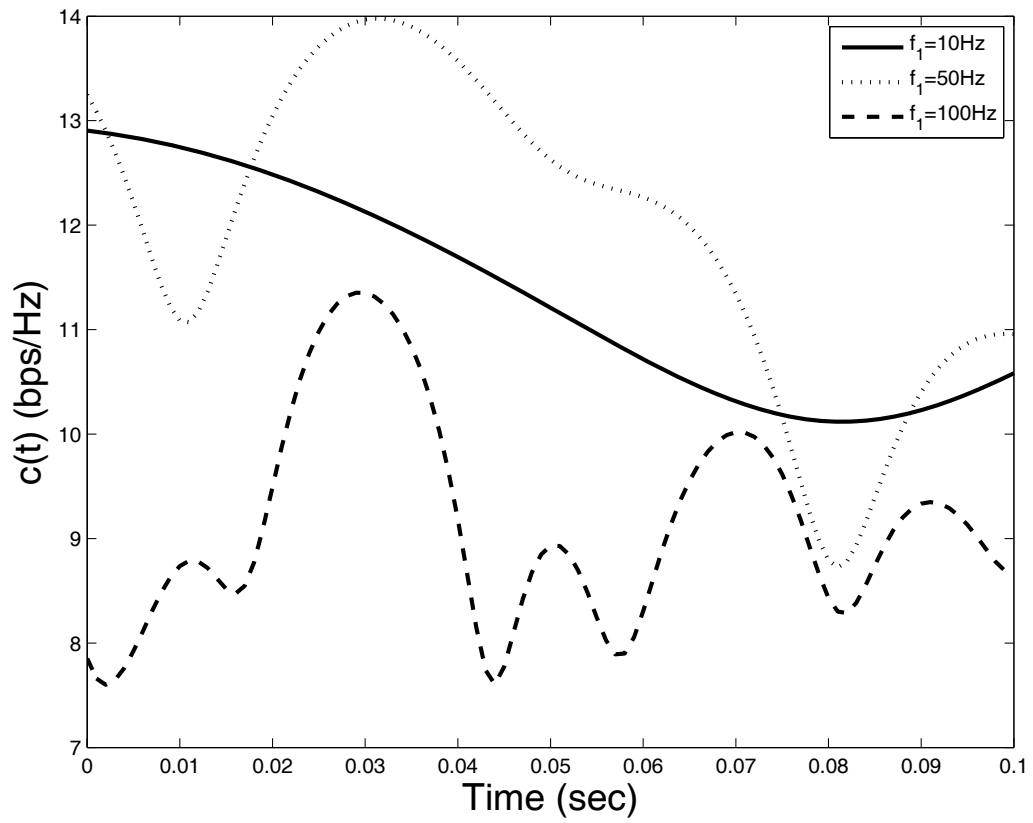


Figure 7.4: MIMO Rician capacity with different Doppler frequencies where  $\text{SNR} = 20 \text{ dB}$ ,  $d = \lambda/2$ ,  $K = 4.77 \text{ dB}$ .

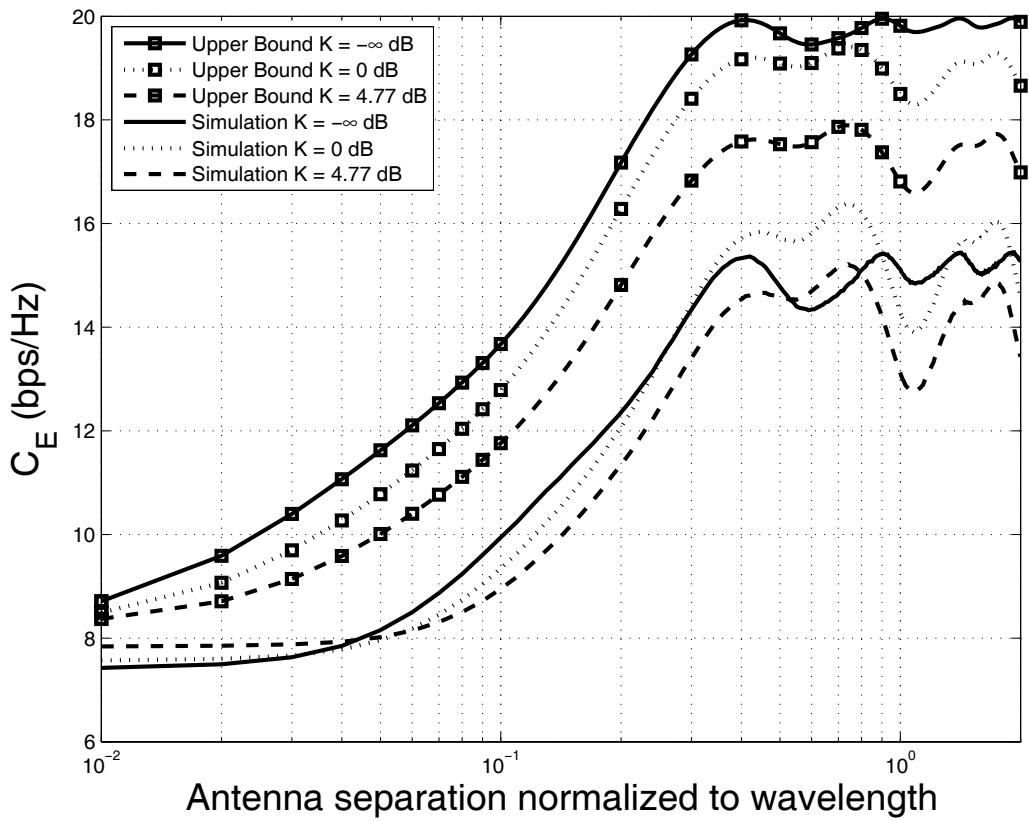


Figure 7.5: Effect of antenna separation on the ergodic capacity of a  $3 \times 3$  MIMO channel for SNR = 20 dB and various values of  $K$  factors.

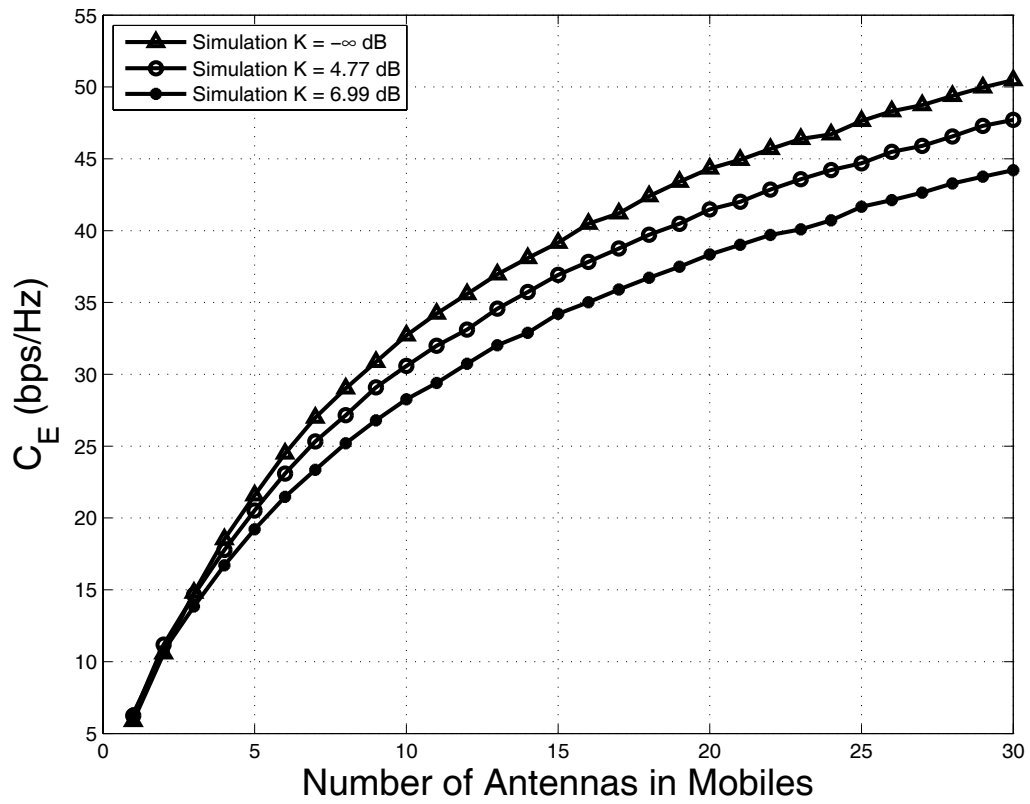


Figure 7.6: The ergodic capacity of MIMO channels against the number of antennas when  $\text{SNR} = 20$  dB,  $d = \lambda/2$  and  $I = N = 8$ .

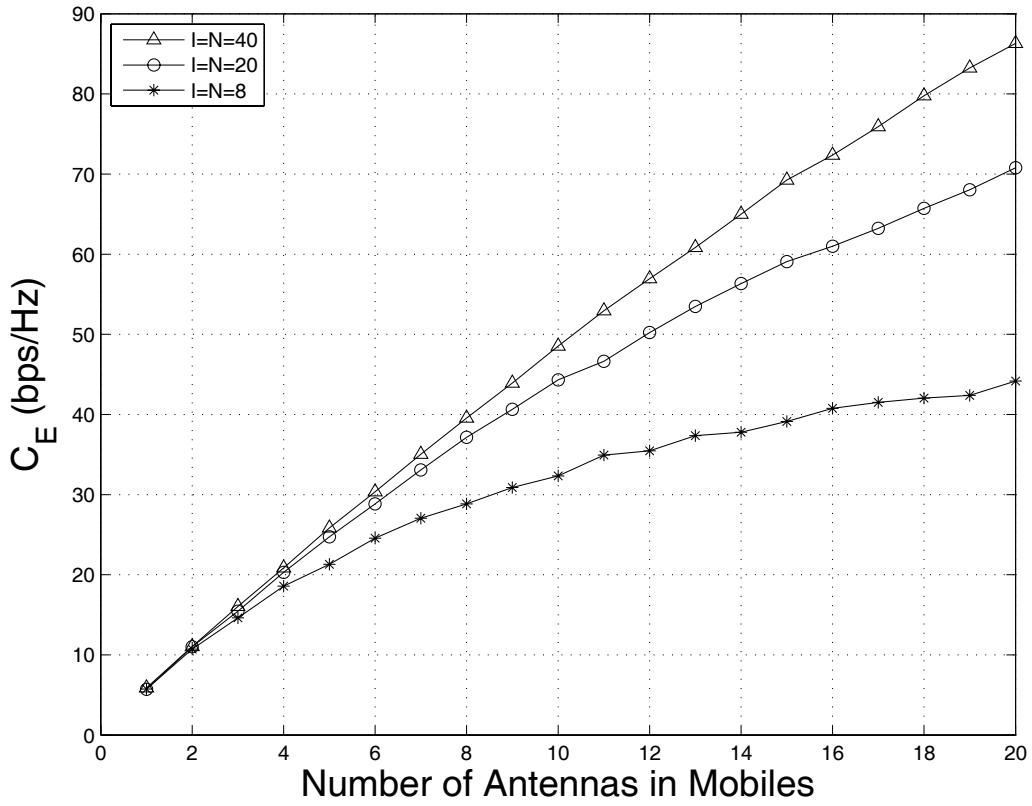


Figure 7.7: The ergodic capacity of MIMO channels against the number of antennas for various number of scatterers ( $I$  and  $N$ ) when  $\text{SNR} = 20$  dB,  $d = \lambda/2$  and  $K = -\infty$  dB.

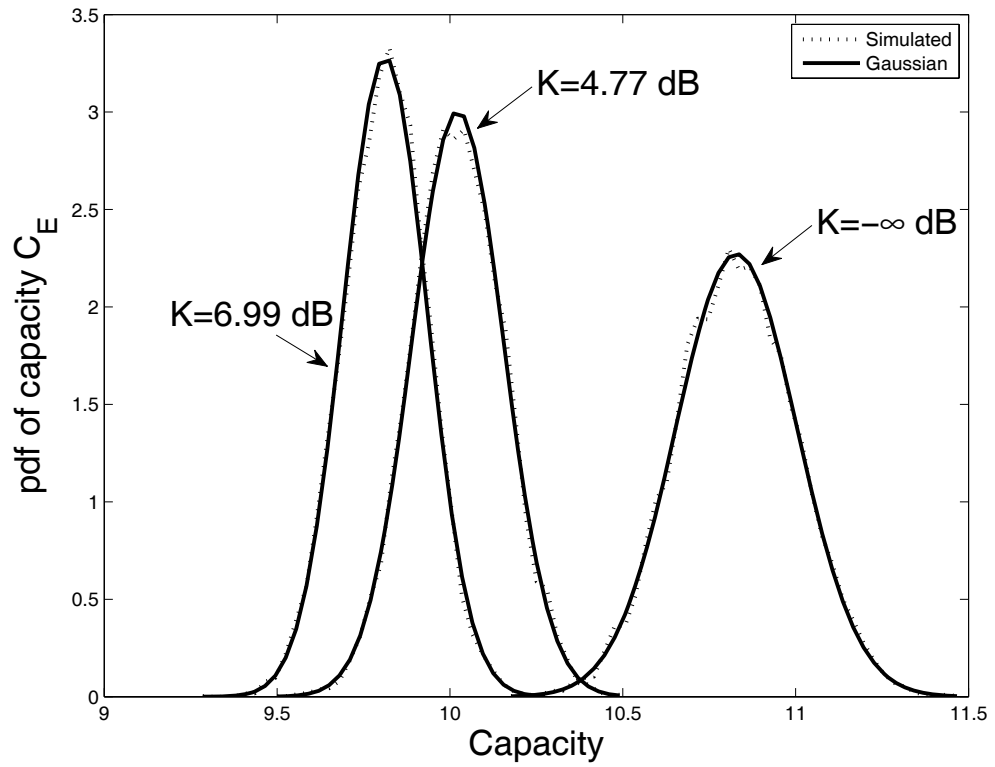


Figure 7.8: Probability density functions of MIMO capacity in a mobile-to-mobile Rician fading channel.

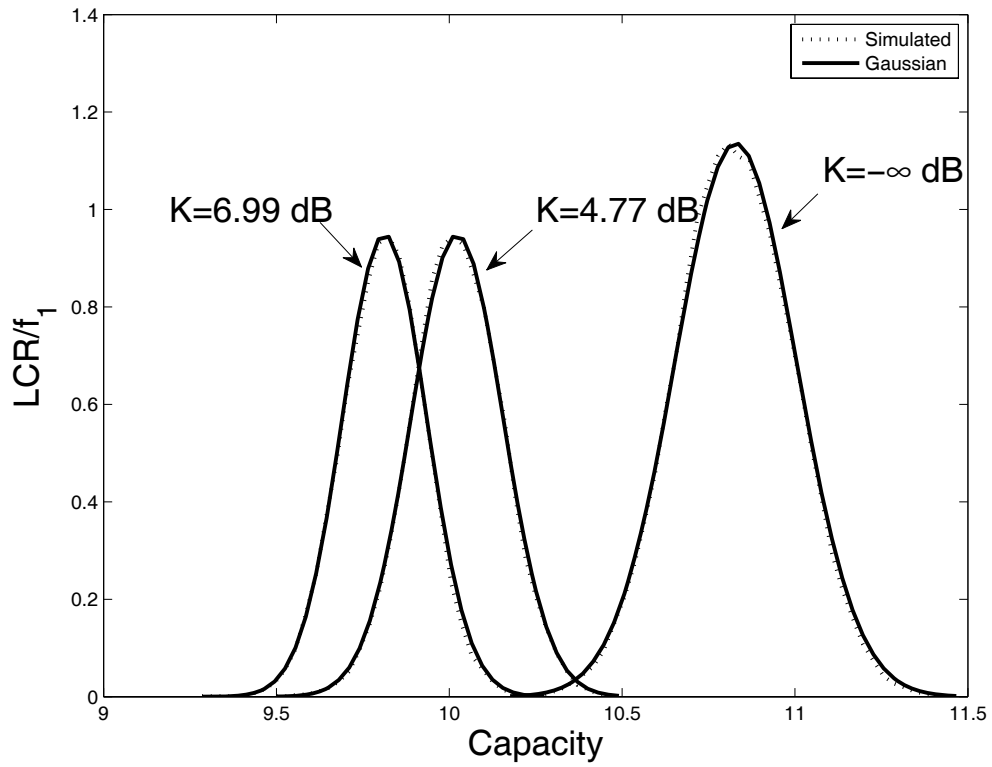


Figure 7.9: Level crossing rate of the MIMO capacity in a mobile-to-mobile Rician fading channel.



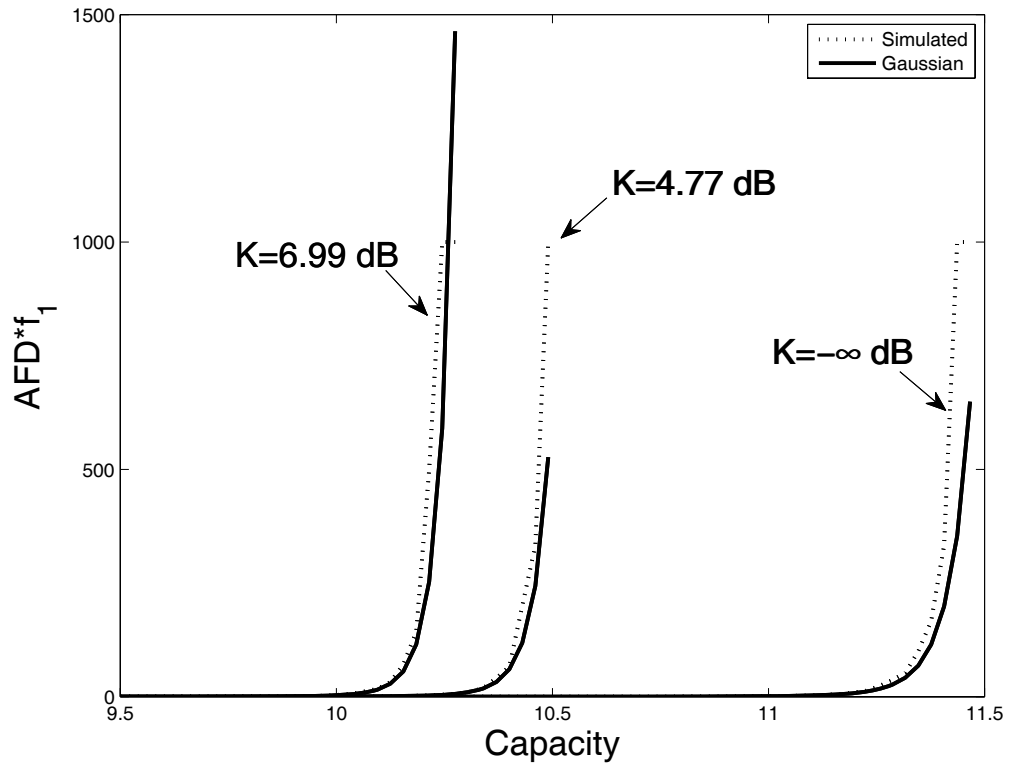



Figure 7.10: Average fade duration of the MIMO capacity in a mobile-to-mobile Rician fading channel.

# Chapter 8

## Network Coding for Cooperative Multiplexing in Relay Channels



In this chapter we consider a relay channel and decode-and-forward (DF) cooperative communications system combined with the network coding. We derive the outage probability and diversity-multiplexing tradeoff (DMT) for the proposed cooperative network coding (CNC) protocol. Our results show that the relay nodes not only can provide cooperative diversity gain, but also cooperative multiplexing gain.

### 8.1 Motivation

Cooperative communication attracts a great deal of interests recently. Relay terminals in a cooperative communication system can help the transmitter send information to the receiver. This is similar to a virtual multiple-input multiple-output (MIMO) system because the terminals in a cooperative net-

work form a virtual antenna array. Clearly, cooperative communication systems can provide diversity gains similar to the MIMO techniques.

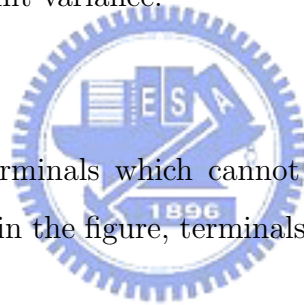
Many cooperative communication protocols were proposed to improve diversity gain, such as orthogonal amplify and forward (OAF) [67], nonorthogonal amplify and forward (NAF) [68], space-time coded (STC) cooperative diversity protocols [69–71], dynamic decode-and-forward (DDF) [68], enhanced static decode-and-forward (ESDF), and enhanced dynamic decode-and-forward (EDDF) [72].

However, how to provide multiplexing gain by taking advantage of relays has not received much attention so far. Combining the network coding with the cooperative communications, or called the cooperative network coding (CNC) [73–84], have a potential to exploit the multiplexing gain in many relay nodes (virtual antennas). The outage probability and the diversity-multiplexing tradeoff (DMT) are two common measures of the performance of cooperative protocols. The DMT analysis of CNC has not been seen in the literature. Through the analysis of DMT, we can observe that if exploiting the “XOR in the air” approach onto cooperative protocols could improve the multiplexing gain or diversity gain or both compared with the traditional cooperative protocols. Moreover, the DMT can give more insights than the capacity results because the capacity is only a quantity while DMT is a tradeoff curve. The capacity is the upper bound of the error-free transmission rate, but the DMT gives us the tradeoff between transmission rate and the error rate. Thus, it motivates us to derive the outage probability and diversity-multiplexing tradeoff of the cooperative network coding.

## 8.2 System Model and CNC Protocol

Figure 8.1 shows the system model for the cooperative network coding with one relay node. Terminals  $A$  and  $B$  transmit and receive users' data, and relay  $R$  forward data. Denote the channel gains between nodes  $X$  and  $Y$  as  $h_{XY}$ , where  $X, Y \in \{A, B, R\}$ . In addition to additive white Gaussian noise, the radio channel effect  $h_{XY}$  experienced at each terminal is assumed to be independent and identically distributed (i.i.d.) complex normal random variables with zero mean and unit variance.

Consider the half-duplex terminals which cannot transmit and receive data simultaneously. As shown in the figure, terminals  $A$  and  $B$  can directly communicate with each other.



In the figure the cooperative network coding protocols are illustrated for the case with one relay node. In phase (1) and (2),  $A$  and  $B$  transmit information  $a$  and  $b$ , respectively. Then  $R$  decodes out  $a$  and  $b$  in the binary form and compute  $a \oplus b$ , where  $\oplus$  is the bitwise exclusive or (XOR) operator. In phase (3), terminal  $R$  broadcasts the mixed information  $a \oplus b$  to  $A$  and  $B$ . Then  $A$  can obtain information  $b$  via the operation  $(a \oplus b) \oplus a = b$  and terminal  $B$  can obtain information  $a$  via the operation  $(a \oplus b) \oplus b = a$ . Thus the relay node here play a decode-and-forward (DF) [67] role.

## 8.3 Diversity-Multiplexing Tradeoff of CNC Protocol

### 8.3.1 Equivalent Signal Models

To begin with, the signals received by  $B$  and  $R$  in the first phase are modeled as

$$y_{B1}[n] = h_{AB}x_a[n] + z_{B1}[n] \quad (8.1)$$

and

$$y_{R1}[n] = h_{AR}x_a[n] + z_{R1}[n], \quad (8.2)$$

respectively, where  $x_a[n]$  is the transmitted signal which contains information  $a$  from  $A$ . Similarly, in the second phase, the received signals at  $A$  and  $R$  is represented as

$$y_{A2}[n] = h_{AB}x_b[n] + z_{A2}[n] \quad (8.3)$$

and

$$y_{R2}[n] = h_{BR}x_b[n] + z_{R2}[n] \quad (8.4)$$

respectively, where  $x_b[n]$  is the transmitted signal which contains information  $b$  from  $B$ . In the third phase, the received signals at  $A$  and  $B$  are

$$y_{A3}[n] = h_{AR}x_c[n] + z_{A3}[n] \quad (8.5)$$

and

$$y_{B3}[n] = h_{BR}x_c[n] + z_{B3}[n], \quad (8.6)$$

respectively, where  $x_c[n]$  is the signal which contains information  $c = a \oplus b$  from  $R$ . We model  $z_{Xi}[n]$  as zero-mean mutually independent, circularly symmetric, complex Gaussian random sequences with variance  $N_0$ , where  $X \in \{A, B, R\}$  and  $i \in \{1, 2, 3\}$ .

### 8.3.2 Parameterizations

In this subsection, we define signal to noise ratio (SNR), multiplexing gain  $r$ , and diversity gain  $d$  for the proposed cooperative network coding system.

The SNR is defined as

$$\text{SNR} := \frac{\mathbb{E}\{|x_k[n]|^2\}}{N_0}, \quad (8.7)$$

where  $k \in \{a, b, c\}$ .  $\mathbb{E}\{Z\}$  is the expectation of a random variable  $Z$ .

Denote  $\mathbf{R}$  as the data rate on each channel, where  $\mathbf{R}$  can be a function of SNR if the communication system applies the channel-driven rate adaptation scheme. The multiplexing gain  $r$  is defined as

$$r := \lim_{\text{SNR} \rightarrow \infty} \frac{\mathbf{R}(\text{SNR})}{\log \text{SNR}}. \quad (8.8)$$

Note that the base of the log function is  $e$  in this chapter.

Let  $P_{\text{out}}(\text{SNR})$  be the system outage probability as a function of SNR, which is defined as the probability of the maximum average mutual information  $I$  between input and output being less than the data rate  $\mathbf{R}$ , i.e.,

$$P_{\text{out}}(\text{SNR}) := \mathbb{P}[I < \mathbf{R}], \quad (8.9)$$

where  $\mathbb{P}[E]$  denotes the probability of an event  $E$ . The diversity gain  $d$  is then defined as

$$d := - \lim_{\text{SNR} \rightarrow \infty} \frac{\log[P_{\text{out}}(\text{SNR})]}{\log \text{SNR}}. \quad (8.10)$$

### 8.3.3 Diversity-Multiplexing Tradeoff Analysis

The analysis of the outage probability of the cooperative network coding protocol with one relay node at high SNR regime is given by the following theorem and proof:

**Theorem 6** *The outage probability of the CNC protocol with one relay node at high SNR regime is characterized by*

$$P_{out}^{CNC} = \frac{1}{2}\Gamma(0, s)s^2 - K_1(2s)s - \frac{1}{2}e^{-s}(s + 1) + 1, \quad (8.11)$$

where  $s = e^{3R/2}/\text{SNR}$ ,  $\Gamma(a, z) = \int_z^\infty t^{a-1}e^{-t}dt$  is the gamma function,  $K_1(z)$  is the modified Bessel function of the second kind and the first order.

*Proof:* First, the maximum average mutual information of the CNC protocol with one relay node can be seen as the sum of that of two different decode-and-forward protocols [67]:

$$I_{\text{CNC}} = \frac{1}{3} \min\{\log(1 + \text{SNR}|h_{BR}|^2), \log[1 + \text{SNR}(|h_{AR}|^2 + |h_{AB}|^2)]\} + \frac{1}{3} \min\{\log(1 + \text{SNR}|h_{AR}|^2), \log[1 + \text{SNR}(|h_{BR}|^2 + |h_{AB}|^2)]\}. \quad (8.12)$$

To ease the notation, let  $x = |h_{AR}|^2$ ,  $y = |h_{BR}|^2$ , and  $z = |h_{AB}|^2$ . Then  $x$ ,  $y$ , and  $z$  are i.i.d. exponential random variables with unit mean. The outage probability can be computed as

$$\begin{aligned} P_{out}^{CNC} &= \mathbb{P}[I_{\text{CNC}} < R] \\ &= \mathbb{P}[I_{\text{CNC}} < R | y \leq x + z, x \leq y + z] \mathbb{P}[y \leq x + z, x \leq y + z] \\ &\quad + \mathbb{P}[I_{\text{CNC}} < R | y > x + z, x \leq y + z] \mathbb{P}[y > x + z, x \leq y + z] \\ &\quad + \mathbb{P}[I_{\text{CNC}} < R | y \leq x + z, x > y + z] \mathbb{P}[y \leq x + z, x > y + z] \\ &\quad + \mathbb{P}[I_{\text{CNC}} < R | y > x + z, x > y + z] \mathbb{P}[y > x + z, x > y + z] \\ &=: \sum_{i=1}^4 p_i q_i. \end{aligned} \quad (8.13)$$

Then

$$\begin{aligned}
p_1 &= \text{P} \left[ \frac{1}{3} \log(1 + \text{SNR}_y) + \frac{1}{3} \log(1 + \text{SNR}_x) < \mathbf{R} \right] \\
&= \text{P}[\log[(1 + \text{SNR}_y)(1 + \text{SNR}_x)] < 3\mathbf{R}] \\
&= \text{P}[(1 + \text{SNR}_y)(1 + \text{SNR}_x) < e^{3\mathbf{R}}]. \tag{8.14}
\end{aligned}$$

When SNR is high,  $1 + \text{SNR}_y$  and  $1 + \text{SNR}_x$  can be approximated as  $\text{SNR}_y$  and  $\text{SNR}_x$ , respectively. Then

$$\begin{aligned}
p_1 &= \text{P}[\text{SNR}^2 xy < e^{3\mathbf{R}}] \\
&= \text{P}[xy < e^{3\mathbf{R}}/\text{SNR}^2] \\
&= \int_0^\infty \int_0^\infty 1_{xy < s^2} \cdot e^{-x-y} dx dy \\
&= 1 - 2sK_1(2s), \tag{8.15}
\end{aligned}$$

where

$$1_E = \begin{cases} 1, & \text{if the expression } E \text{ is true,} \\ 0, & \text{if the expression } E \text{ is false.} \end{cases} \tag{8.16}$$

On the other hand,

$$q_1 = \int_0^\infty \int_0^\infty \int_0^\infty 1_{y \leq x+z, x \leq y+z} \cdot e^{-x-y-z} dx dy dz = \frac{1}{2}. \tag{8.17}$$

Similarly, we have

$$p_2 = p_3 = 1 - (1 + s)e^{-s} + s^2\Gamma(0, s), \tag{8.18}$$

$$q_2 = q_3 = \frac{1}{4}, \tag{8.19}$$

and

$$q_4 = 0. \tag{8.20}$$

Combining the above equations into (8.13), we get the desired result.



According to the definition of the diversity gain in (8.10), we can find that the diversity-multiplexing tradeoff achieved by the cooperative network coding protocol with one relay node is characterized by

$$d_{\text{CNC}}(r) = 2 - 3r \quad (8.21)$$

for  $0 < r < \frac{2}{3}$ .

## 8.4 Numerical Results

Figure 8.2 illustrates the diversity-multiplexing tradeoff comparison of the upper bound (UB), the CNC protocol for one relay node, selection decode-and-forward (SDF) [67], and DF. The upper bound is for a  $2 \times 1$  MISO system, which is the best situation that an one-relay cooperative communications system could achieve.

From this figure, we can see that the CNC protocol improves both diversity gain and multiplexing gain compared with the DF protocol. The maximum diversity and multiplexing gain that the CNC protocol can achieve are 2 and  $2/3$ , respectively, while the maximum diversity and multiplexing gain of the DF protocol are 1 and  $1/2$ , respectively. Furthermore, the CNC protocol also outperforms the SDF protocol, which is an enhanced version of DF. Hence, we can conclude that using network coding at the relay node can improve not only diversity gain but also multiplexing gain.

## 8.5 Conclusions

In this chapter, we investigate the diversity-multiplexing tradeoff for the cooperative network coding protocol which integrates the concept of DF relay transmission of cooperative communications with the information mixing of

network coding in relay channels. The proposed CNC protocol is suitable for two users which can transmit information to each other. We give a theorem to show our outage probability analytical result with proof and DMT comparison for our CNC protocol with upper bound, SDF, and DF. We find that the CNC protocol improves both diversity and multiplexing gain compared with the DF protocol.

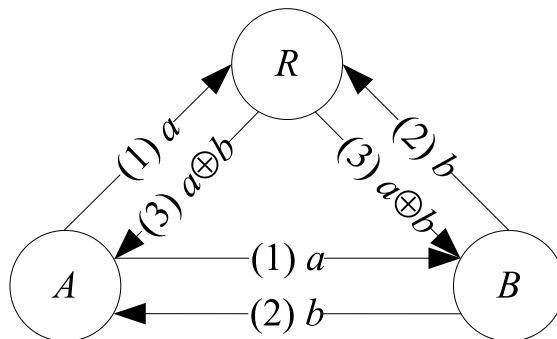


Figure 8.1: The system model and proposed CNC protocol, where phase (1):  $A$  sends  $a$  to  $B$  and  $R$ ; phase (2):  $B$  sends  $b$  to  $A$  and  $R$ ; phase (3):  $R$  broadcasts  $a \oplus b$  to  $A$  and  $B$ .

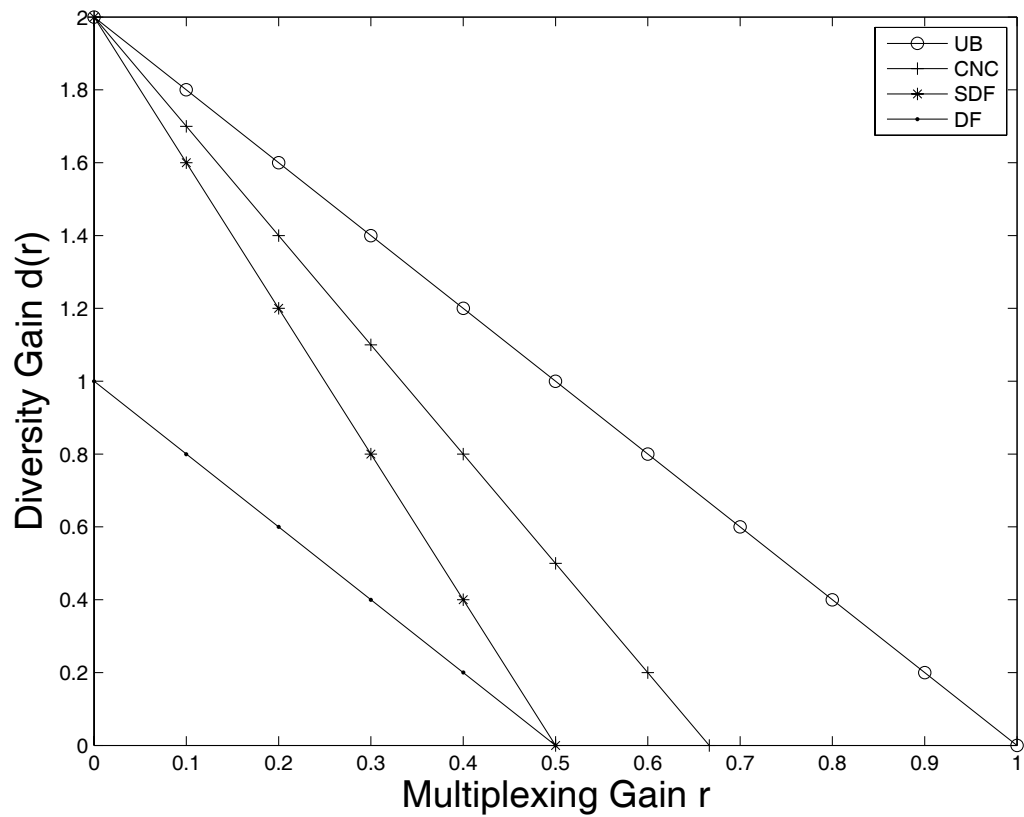


Figure 8.2: Diversity-multiplexing tradeoff comparison of the upper bound (UB), cooperative network coding (CNC), selection decode-and-forward (SDF), and decode-and-forward (DF).

# Chapter 9

## Conclusions

In this dissertation, we have investigated the analysis and design for the MIMO wireless systems under three kinds of channels: UWB channels, mobile-to-mobile channels, and relay channels. For the first issue, we analyzed the performance and designed BER-minimized STF codes for MIMO systems in UWB channels. Then, we analyzed some statistical characteristics for a MIMO mobile-to-mobile ad hoc channel. At last, we designed a cooperative network coding protocol and analyzed its performance in relay channels.

This dissertation includes the following research topics.

- Bit Error Rate Analysis in IEEE 802.15.3a and 802.15.4a UWB Channels
- On the Performance of Using Multiple Transmit and Receive Antennas in Pulse-Based Ultrawideband Systems
- BER-Minimized Space-Time-Frequency Codes for MIMO Highly Frequency-Selective Block-Fading Channels
- Statistical Analysis of A Mobile-to-Mobile Rician Fading Channel Model

- Modeling and Capacity Fades Analysis of MIMO Rician Channels in Mobile Ad Hoc Networks
- Network Coding for Cooperative Multiplexing in Relay Channels

The contribution from these research works are list as follows.

1. Provide analytical BER formula for RAKE receivers in IEEE 802.15.3a and 802.15.4a UWB channel with shadowing effect.
2. Present an analytical expression for the SNR of the PPM signal in an UWB channel with multiple transmit and receive antennas.
3. Design BER-minimized STF block codes for MIMO highly frequency-selective block-fading channels.
4. Suggest a sum-of-sinusoids MIMO mobile-to-mobile channel simulation method, which can characterize the spatial/temporal channel correlation and Rician fading effect.
5. Derive the autocorrelation function, level crossing rate, and average fade duration of the mobile-to-mobile Rician fading channel
6. Analyze the temporal behavior of the capacity of the mobile-to-mobile MIMO Rician channel and proposed a “semi-analytical” model for computing the LCR and AFD of the MIMO channel capacity.
7. Analyze the outage probability and diversity-multiplexing tradeoff for the cooperative network coding protocol in relay channels.

In the following, we summarize the results from the above contributions.

## 9.1 Bit Error Rate Analysis in IEEE 802.15.3a and 802.15.4a UWB Channels

First, we have derived the computable BER formula for a RAKE receiver in the complete IEEE 802.15.3a UWB channel models. In particular, we find that deriving a BER formula taking account of RAKE finger numbers and shadowing is quite challenging for the IEEE 802.15.3a UWB channel. This is mainly because the jointly two-dimension lognormal and doubly-stochastic Poisson random variables yield infinite number of rays. We propose an approximation technique for the collected energy at an  $L$ -finger RAKE receiver. We find that the proposed BER computation method can save a significant amount of computer simulation time. Furthermore, we propose a characteristic function based BER formula to overcome the convergence problem of MGF-based BER formula when shadowing is included. The accuracy of the proposed technique is verified by simulations. Our results quantitatively indicate the effect of shadowing and RAKE finger numbers on BER performance in the IEEE 802.15.3a UWB channel.

Second, we have derived the BER analytical formula for a coherent RAKE receiver under the IEEE 802.15.4a UWB channel model. Our proposed analytical method can accurately and quickly compute the BER values for the sophisticated IEEE 802.15.4a UWB channel, and evaluate the impact of various channel parameters. We find that of all the parameters in the IEEE 802.15.4a channel, the inter-cluster arrival rate  $\Lambda$  has the most significant impact on the BER performance. We also observe that the BER can be lowered due to the increase on the inter-cluster arrival rate  $\Lambda$ , the inter-cluster decay constant  $\Gamma$ , the ray arrival parameters  $\lambda_1$ ,  $\lambda_2$ , and  $\beta$ . We also find that increasing the intra-cluster decay constant  $\gamma_0$  causes the BER to first

increase and then remain the same or even decrease.

In general, the time-domain parameters in the IEEE 802.15.4a UWB channel affect BER performance quite significantly. This reflects the comment in [94], that time-of-arrival characteristics are more important than amplitude characteristics for MIMO-UWB systems. In the future, it would be worth extending the suggested analytical method to other multipath channel models with any given fading distribution, PDP, and cluster and ray inter-arrival time distributions.

## 9.2 On the Performance of Using Multiple Transmit and Receive Antennas in Pulse-Based Ultrawideband Systems

In this part, we have derived an analytical expression for the PPM signal in an UWB channel characterized by the cluster effect and highly dense frequency selective fading. Furthermore, we have demonstrated that the time-switched transmit diversity combined with the template-based pulse detection can improve the performance of the PPM based UWB system.

Through analysis and simulations, we have the following two major remarks:

- Although multiple transmit or receive antennas cannot deliver diversity gain for the UWB system in the strict sense (i.e., improving the slope of BER v.s. SNR), multiple transmit antennas can improve the system performance in the manner of reducing signal variations. Thus, transmit antennas can be used to reduce receiver complexity since the number of fingers of a Rake receiver in the UWB system can be very

high.

- Multiple receive antennas can provide higher antenna array combining gain. Because the transmitted power in the UWB system is extremely low, multiple receive antennas techniques can be an effective approach to improve the performance from the view point of coverage extension.

### 9.3 BER-Minimized Space-Time-Frequency Codes for MIMO Highly Frequency-Selective Block-Fading Channels

In this part, we study the BER-minimized STF block codes design for the MIMO highly frequency-selective block fading channels. We consider the IEEE 802.15.3a UWB channel model. Based on the BER analysis under the aforementioned environment in [19], we provide a BER-minimized design criterion, an efficient searching algorithm for the optimal STF block codes, and optimal BER performance curves. Among our proposed optimal STF block codes, we find that almost all of them need nonlinear operations in the encoder. Thus it is necessary to consider nonlinear codes when we design the optimal STF block codes for the MIMO-OFDM systems under the IEEE 802.15.3a UWB channel model. When the number of subcarriers  $M$  which are jointly encoded is equal to two and the number of transmit antennas  $N_t$  is  $2 \sim 4$  or  $M = 3, N_t = 4$ , the optimal STF block codes for all the IEEE 802.15.3a UWB channel models CM 1  $\sim$  4 can be found according to the proposed code search algorithm in the above considered cases. When 1)  $M = 3, N_t = 2 \sim 3$ , and 2)  $M = 4, N_t = 2 \sim 3$ , there does not exist optimal STF block codes for all the four UWB channel models. We also find that the



BER decreases as CM increases, i.e., our optimal STF block codes provide better BER performance when the channel fading is more severe. On the other hand, increasing the number of transmit antennas does NOT improve the BER performance for the MIMO-UWB systems when  $M = 2$ . This is similar to the case of the uncoded MIMO-UWB systems but opposite to the STBC case. However, increasing the number of received antennas improves the BER performance for the MIMO-UWB systems. This is similar to the STBC case. We also find that the diversity order is different for different CM in the  $M = 3 \sim 4$ ,  $N_t = 2 \sim 3$  cases. Compared with other space-frequency-time codes [1, 2] for multiband UWB-MIMO communication systems, our code has about 1 and 8 dB coding gain at  $\text{BER} = 10^{-4}$ , respectively.

## 9.4 Statistical Analysis of A Mobile-to-Mobile Rician Fading Channel Model

In this part, a sum-of-sinusoids-based mobile-to-mobile Rician fading simulator is developed. The double-ring scattering model is proposed for characterizing the mobile-to-mobile communication environment with LOS components. Furthermore, the theoretical correlation functions of the mobile-to-mobile Rician channel are derived and its accuracy is verified by simulations. The LCR and AFD of the mobile-to-mobile Rician fading channel are derived. Finally, it is proved that the proposed sum-of-sinusoids approximation developed from the double-ring with a LOS component model can approach the theoretical value more closely than the single-ring model at a slightly higher cost of computation loads.

## 9.5 Modeling and Capacity Fades Analysis of MIMO Rician Channels in Mobile Ad Hoc Networks

In this part, we have developed a sum-of-sinusoids simulation method for the MIMO system in a mobile-to-mobile fading channel. Based on the “correlated double-ring” scattering model [114], we incorporate the effect of Doppler effects, antenna separation, and LOS components for the MIMO system in a mobile-to-mobile environment. We have also derived the capacity upper bound of the mobile-to-mobile MIMO Rician channel. The channel capacity has been confirmed through simulations. We find that for MIMO systems with constant number of scatterers, increasing number of antennas cannot linearly increase the capacity. The capacity per antenna is decreased as Rician factor increases. We also find that the total channel capacity is related to the richness of the scattering environment. We looked into the temporal behavior of the capacity of the mobile-to-mobile MIMO Rician channel. Besides, we proposed a “semi-analytical” model for computing the LCR and AFD of the MIMO channel capacity. From those simulation results, we noted the influence of the LOS component, Doppler frequency, and other parameters on the temporal behavior of the MIMO channel capacity.

## 9.6 Network Coding for Cooperative Multiplexing in Relay Channels

In this part, we investigate the diversity-multiplexing tradeoff for the cooperative network coding protocol which integrates the concept of DF relay

transmission of cooperative communications with the information mixing of network coding in relay channels. The proposed CNC protocol is suitable for two users which can transmit information to each other. We give a theorem to show our outage probability analytical result with proof and DMT comparison for our CNC protocol with upper bound, SDF, and DF. We find that the CNC protocol improves both diversity and multiplexing gain compared with the DF protocol.

## 9.7 Suggestions for Future Research

In this dissertation, we have discussed some preliminary issues for cooperative MIMO wireless systems. Other possible interesting research topics that can be extended from this dissertation are listed as follows:

- MIMO systems in UWB channels:

1. Consider the frequency-dependent pathloss and M-ary modulation in the BER analysis for IEEE 802.15.3a and 802.15.4a channel.
2. Design a faster searching algorithm for the BER-minimized STF codes for MIMO-UWB channels.

- MIMO systems in mobile-to-mobile channels:

1. Take the interference of other mobile terminals into account in ad hoc networks.
2. Find a more accurate analytical capacity formula instead of the proposed upper bound.

- MIMO systems in relay channels:

1. Generalize the CNC protocol, e.g., more than two users, each user has multiple transmit and receive antennas, using advanced cooperation protocols and network coding techniques in relay channels.
2. Consider adding the dirty paper coding into the cooperative network coding in relay channels.

MIMO is a powerful technique, but its performance gains depend on channel characteristics. The insights obtained from this thesis can help exploit the MIMO's potentials in different wireless channels. A famous slogan by a worldwide communication company is said, "human technology." Through the MIMO wireless communications technique, we believe that the dream of freely connecting people anywhere anytime is no longer an impossible mission but will be come true in the near future. After all, the development of technology is to satisfy the need that people want.



# Bibliography

- [1] W. Zhang, X.-G. Xia, and P. C. Ching, “High-rate full-diversity space–time–frequency codes for broadband MIMO block-fading channels,” *IEEE Trans. Commun.*, vol. 55, no. 1, pp. 25–34, Jan. 2007.
- [2] J. Chusing, L. Wuttisittikulij, and S. Segkhoontod, “Achieving rate two space-time-frequency codes for multiband UWB-MIMO communication systems using rotated multidimensional modulation,” *IEEE Fifth Annual Conference on Communication Networks and Services Research (CNSR’07)*, pp. 294–301, May 14–17, 2007.
- [3] J. Foerster, et. al., “Channel modeling sub-committee report final,” *IEEE P802.15 Wireless Personal Area Networks, P802.15-02/490r1-SG3a*, Feb. 2003.
- [4] A. F. Molisch et al., “IEEE 802.15.4a channel model - final report,” IEEE 802.15 WPAN Low Rate Alternative PHY Task Group 4a (TG4a), Tech. Rep., Nov. 2004.
- [5] J. Foerster and Q. Li, “UWB channel modeling contribution from intel,” *IEEE P802.15-02/279-SG3a*, June 2002.

- [6] D. Cassioli, M. Z. Win, and A. F. Molisch, “The ultra-wide bandwidth indoor channel: From statistical model to simulations,” *IEEE J. Sel. Areas Commun.*, vol. 20, no. 6, pp. 1247–1257, Aug. 2002.
- [7] J. A. Gubner and K. Hao, “A computable formula for the average bit-error probability as a function of window size for the IEEE 802.15.3a UWB channel model,” *IEEE Trans. on Microwave Theory Tech.*, vol. 54, no. 4, pp. 1762–1777, Apr. 2006.
- [8] S. I. Resnick, *A Probability Path*. Birkhäuser, 1999.
- [9] F. Zhu, Z. Wu, and C. Nassar, “Generalized fading channel model with application to UWB,” in *IEEE Conf. on Ultra Wideband Syst. and Technol.*, 2002, pp. 13–17.
- [10] M. Z. Win and R. A. Scholtz, “Characterization of ultra-wide bandwidth wireless indoor channels: a communication-theoretic view,” *IEEE J. Sel. Areas Commun.*, vol. 20, pp. 1613–1627, Dec. 2002.
- [11] H. Hashemi, “Impulse response modeling of indoor radio propagation channels,” *IEEE J. Sel. Areas Commun.*, vol. 11, pp. 967–978, Sept. 1993.
- [12] M. Z. Win, F. Ramirez-Mireles, R. A. Scholtz, and M. A. Barnes, “Ultra-wide bandwidth (UWB) signal propagation for outdoor wireless communications,” in *IEEE Veh. Technol. Conf.*, vol. 1, May 1997, pp. 251–255.
- [13] M. Z. Win, R. A. Scholtz, and M. A. Barnes, “Ultra-wide bandwidth signal propagation for indoor wireless communications,” in *IEEE Inter. Conf. on Communi.*, vol. 1, June 1997, pp. 56–60.

- [14] D. Cassioli, M. Z. Win, and A. F. Molisch, "A statistical model for the UWB indoor channel," in *IEEE Veh. Technol. Conf., Spring*, vol. 2, 2001, pp. 1159–1163.
- [15] J. Keignart and N. Daniele, "Subnanosecond UWB channel sounding in frequency and temporal domain," in *IEEE Conf. on Ultra Wideband Syst. and Technol.*, 2002, pp. 25–30.
- [16] J. Foerster, et. al., "Channel modeling sub-committee report final," *IEEE P802.15 Wireless Personal Area Networks, P802.15-02/490r1-SG3a*, Feb. 2003.
- [17] R. T. Derryberry, S. D. Gray, D. M. Ionescu, G. Mandyam, and B. Raghothaman, "Transmit diversity in 3G CDMA systems," *IEEE Commun. Mag.*, vol. 40, pp. 68–75, Apr. 2002.
- [18] S. S. Tan, B. Kannan, and A. Nallanathan, "Ultra-wideband impulse radio systems with temporal and spatial diversities," in *IEEE Veh. Technol. Conf. Fall*, Orlando, Oct. 2003, pp. 607–611.
- [19] W. P. Siritwongpairat, W. Su, and K. J. R. Liu, "Performance characterization of multiband UWB communication systems using Poisson cluster arriving fading paths," *IEEE J. Sel. Areas Commun.*, vol. 24, no. 4, pp. 745–751, Apr. 2006.
- [20] C. S. Patel, G. L. Stüber, and T. G. Pratt, "Simulation of Rayleigh faded mobile-to-mobile communication channels," *IEEE Veh. Technol. Conf.*, vol. 1, pp. 163–167, Oct. 6–9, 2003.
- [21] T. Tank and J.-P. M. G. Linnartz, "Statistical characterization of Rician multipath effects in a mobile-to-mobile communication channel," *Inter. J. of Wireless Inf. Networks*, vol. 2, no. 1, pp. 17–26, Jan. 1995.

- [22] J.-P. M. Linnartz and R. F. Diesta, “Evaluation of radio links and networks,” University of California, Berkeley, PATH research program, Tech. Rep. UCB-ITS-PRR-96-16, 1996.
- [23] W. C. Jakes, *Microwave Mobile Communications*. Piscataway, NJ: Wiley-IEEE Press, 1994.
- [24] Y. R. Zheng and C. Xiao, “Improved models for the generation of multiple uncorrelated Rayleigh fading waveforms,” *IEEE Commun. Lett.*, vol. 6, pp. 256–258, June 2002.
- [25] C. Xiao and Y. R. Zheng, “A statistical simulation model for mobile radio fading channels,” *IEEE Wireless Commun. and Networking Conf.*, vol. 1, pp. 144–149, Mar. 16–20, 2003.
- [26] H. Kang, G. L. Stüber, T. G. Pratt, and M. A. Ingram, “Studies on the capacity of MIMO systems in mobile-to-mobile environment,” *IEEE Wireless Commun. and Networking Conf.*, vol. 1, pp. 21–25, March 2004.
- [27] A. Giorgetti, M. Chiani, M. Shafi, and P. J. Smith, “Level crossing rates and MIMO capacity fades: impacts of spatial/temporal channel correlation,” *IEEE Int. Conf. on Commun.*, vol. 5, pp. 3046–3050, May 2003.
- [28] P.-H. Kuo and P. J. Smith, “Temporal behavior of MIMO channel quality metrics,” *IEEE Wireless Commun. and Networking Conf.*, June 2005.
- [29] K. Eshima, Y. Hase, S. Oomori, F. Takahashi, and R. Kohno, “M-ary UWB system using Walsh codes,” in *IEEE Conf. Ultra Wideband*



*Syst. and Technologies*, Baltimore, Maryland, USA, May 21–23, 2002, pp. 37–40.

- [30] M. Hämäläinen, R. Tesi, and J. Iinatti, “On the UWB system performance studies in AWGN channel with interference in UMTS band,” in *IEEE Conf. Ultra Wideband Syst. and Technologies*, Baltimore, Maryland, USA, May 21–23, 2002, pp. 321–325.
- [31] İ. Güvenç and H. Arslan, “Performance evaluation of UWB systems in the presence of timing jitter,” in *IEEE Conf. Ultra Wideband Syst. and Technologies*, Virginia, USA, Nov. 16–19, 2003, pp. 136–141.
- [32] T. Q. S. Quek and M. Z. Win, “Ultrawide bandwidth transmitted-reference signaling,” *IEEE Int. Conf. on Commun.*, vol. 6, pp. 3409–3413, June 20–24, 2004.
- [33] K. Hao and J. A. Gubner, “Performance measures and statistical quantities of rake receivers using maximal-ratio combining on the IEEE 802.15.3a UWB channel model,” *IEEE Trans. on Wireless Commun.*, submitted for publication. [Online]. Available: <http://homepages.cae.wisc.edu/~gubner/HaoGubnerTWaf2col.pdf>
- [34] W. P. Siriwongpairat, W. Su, and K. J. R. Liu, “Characterizing performance of multiband UWB systems using Poisson cluster arriving fading paths,” in *IEEE Workshop on Signal Process. Advances in Wireless Commun. (SPAWC)*, July 2005, pp. 264–268.
- [35] L.-C. Wang, W.-C. Liu, and K.-J. Shieh, “On the performance of using multiple transmit and receive antennas in pulse-based ultrawideband systems,” *IEEE Trans. on Wireless Commun.*, vol. 4, no. 6, pp. 2738–2750, Nov. 2005.

- [36] H. Liu, R. C. Qiu, and Z. Tian, "Error performance of pulse-based ultra-wideband MIMO systems over indoor wireless channels," *IEEE Trans. on Wireless Commun.*, vol. 4, no. 6, pp. 2939–2944, Nov. 2005.
- [37] W.-D. Wu, C.-C. Lee, C.-H. Wang, and C.-C. Chao, "Signal-to-interference-plus-noise ratio analysis for direct-sequence ultra-wideband systems in generalized Saleh–Valenzuela channels," *IEEE J. Select. Topics in Signal Process.*, vol. 1, no. 3, pp. 483–497, Oct. 2007.
- [38] K. Siwiak and D. McKeown, *Ultra-Wideband Radio Technology*. John Wiley & Sons, 2004.
- [39] K. Siwiak, "Ultra-wide band radio: introducing a new technology," in *IEEE Veh. Technol. Conf. Spring*, vol. 2, 2001, pp. 1088–1093.
- [40] M. Z. Win and R. A. Scholtz, "Impulse radio: how it works," *IEEE Commun. Lett.*, vol. 2, pp. 36–38, Feb. 1998.
- [41] —, "Ultra-wide bandwidth time-hopping spread-spectrum impulse radio for wireless multiple-access communications," *IEEE Trans. Commun.*, vol. 48, pp. 679–689, Apr. 2000.
- [42] S. M. Alamouti, "A simple transmit diversity technique for wireless communications," *IEEE J. Sel. Areas Commun.*, vol. 16, pp. 1451–1458, Oct. 1998.
- [43] V. Tarokh, H. Jafarkhani, and A. R. Calderbank, "Space-time block codes from orthogonal designs," *IEEE Trans. Inf. Theory*, vol. 45, pp. 1456–1467, July 1999.
- [44] V. Tarokh, N. Seshadri, and A. R. Calderbank, "Space-time codes for high data rate wireless communication: performance criterion and code

- construction,” *IEEE Trans. Inf. Theory*, vol. 44, pp. 744–765, Mar. 1998.
- [45] A. F. Naguib, V. Tarokh, N. Seshadri, and A. R. Calderbank, “A space-time coding modem for high-data-rate wireless communications,” *IEEE J. Sel. Areas Commun.*, vol. 16, pp. 1459–1478, Oct. 1998.
- [46] H. E. Gamal, A. R. Hammons, Y. Liu, M. P. Fitz, and O. Y. Takeshita, “On the design of space-time and space-frequency codes for mimo frequency-selective fading channels,” *IEEE Trans. Inf. Theory*, vol. 49, no. 9, pp. 2277–2292, Sept. 2003.
- [47] A. Sibille and S. Bories, “Spatial diversity for UWB communications,” in *5th European Personal Mobile Communi. Conf. (EPMCC 2003)*, Apr. 2003.
- [48] M. Weisenhorn and W. Hirt, “Performance of binary antipodal signaling over the indoor UWB MIMO channel,” in *IEEE Inter. Conf. on Communi.*, May 2003, pp. 2872–2878.
- [49] L. Yang and G. B. Giannakis, “Analog space-time coding for multi-antenna ultra-wideband transmissions,” *IEEE Trans. Commun.*, vol. 52, pp. 507–517, Mar. 2004.
- [50] A. F. Molisch, M. Z. Win, and J. H. Winters, “Space-time-frequency (STF) coding for MIMO-OFDM systems,” *IEEE Commun. Lett.*, vol. 6, no. 9, pp. 370–372, Sept. 2002.
- [51] E. Bizzarri, A. S. Gallo, and G. M. Vitetta, “Adaptive space-time-frequency coding schemes for MIMO OFDM,” *IEEE GLOBECOM '04*, vol. 2, pp. 933–937, Nov. 2004.

- [52] M. Fozunbal, S. W. McLaughlin, and R. W. Schafer, "On space-time-frequency coding over MIMO-OFDM systems," *IEEE Trans. Wireless Commun.*, vol. 4, no. 1, pp. 320–331, Jan. 2005.
- [53] P. Dent, G. E. Bottomley, and T. Croft, "Jakes fading model revisited," *Electron. Lett.*, vol. 29, no. 13, pp. 1162–1163, June 1993.
- [54] M. F. Pop and N. C. Beaulieu, "Limitations of sum-of-sinusoids fading channel simulator," *IEEE Trans. on Commun.*, vol. 49, no. 4, pp. 699–708, Apr. 2001.
- [55] C. Xiao, Y. R. Zheng, and N. C. Beaulieu, "Second-order statistical properties of the WSS Jakes' fading channel simulator," *IEEE Trans. on Commun.*, vol. 50, no. 6, pp. 888–891, June 2002.
- [56] A. S. Akki and F. Haber, "A statistical model for mobile-to-mobile land communication channel," *IEEE Trans. on Veh. Technol.*, vol. VT-35, no. 1, pp. 2–7, Feb. 1986.
- [57] R. Wang and D. Cox, "Channel modeling for ad hoc mobile wireless networks," *IEEE Veh. Technol. Conf.*, vol. 1, pp. 21–25, May 6–9, 2002.
- [58] C. S. Patel, G. L. Stüber, and T. G. Pratt, "Simulation of Rayleigh-faded mobile-to-mobile communication channels," *IEEE Trans. Commun.*, vol. 53, no. 11, pp. 1876–1884, Nov. 2005.
- [59] D. J. Young and N. C. Beaulieu, "The generation of correlated Rayleigh random variates by inverse discrete Fourier transform," *IEEE Trans. on Commun.*, vol. 48, no. 7, pp. 1114–1127, July 2000.

- [60] I. Z. Kovács, P. C. F. Eggers, K. Olesen, and L. G. Petersen, “Investigations of outdoor-to-indoor mobile-to-mobile radio communication channels,” *IEEE Veh. Technol. Conf.*, pp. 430–434, Sept. 24–28, 2002.
- [61] D. Gesbert, H. Bolcskei, D. A. Gore, and A. J. Paulraj, “Outdoor MIMO wireless channels: Models and performance prediction,” *IEEE Trans. on Commun.*, vol. 50, pp. 1926–1934, Dec 2002.
- [62] A. F. Molisch, “A generic model for MIMO wireless propagation channels in macro- and microcells,” *IEEE Trans. on Signal Process.*, vol. 52, pp. 61–71, Jan 2004.
- [63] A. Giorgetti, P. J. Smith, M. Shafi, and M. Chiani, “MIMO capacity, level crossing rates and fades: The impact of spatial/temporal channel correlation,” *Int. J. of Commun. and Networks (special issue on coding and signal processing for MIMO systems)*, vol. 5, pp. 104–115, Jun 2003.
- [64] S. Wang, A. Abdi, J. Salo, H. M. El-Sallabi, J. W. Wallace, P. Vainikainen, and M. A. Jensen, “Time-varying MIMO channels: Parametric statistical modeling and experimental results,” *IEEE Trans. on Veh. Technol.*, vol. 56, no. 4, pp. 1949–1963, July 2007.
- [65] D.-S. Shiu, G. J. Foschini, M. J. Gans, and J. M. Kahn, “Fading correlation and its effect on the capacity of multielement antenna systems,” *IEEE Trans. on Commun.*, vol. 48, no. 3, pp. 502–513, Mar. 2000.
- [66] D.-S. Shiu, *Wireless Communication Using Dual Antenna Arrays*. Boston/Dordrecht/London: Kluwer Academic Publishers, 2000.

- [67] J. N. Laneman, D. N. C. Tse, and G. W. Wornell, “Cooperative diversity in wireless networks: efficient protocols and outage behavior,” *IEEE Trans. Inf. Theory*, vol. 50, no. 12, pp. 3062–3080, Dec. 2004.
- [68] K. Azarian, H. E. Gamal, and P. Schniter, “On the achievable diversity–multiplexing tradeoff in half-duplex cooperative channels,” *IEEE Trans. Inf. Theory*, vol. 51, no. 12, pp. 4152–4172, Dec. 2005.
- [69] J. N. Laneman and G. W. Wornell, “Distributed space–time-coded protocols for exploiting cooperative diversity in wireless networks,” *IEEE Trans. Inf. Theory*, vol. 49, no. 10, pp. 2415–2425, Oct. 2003.
- [70] R. Nabar, H. Bolcskei, and F. W. Kneubuhler, “Fading relay channels: performance limits and space-time signal design,” *IEEE J. Sel. Areas Commun.*, vol. 22, no. 6, pp. 1099–1109, Aug. 2004.
- [71] N. Prasad and M. K. Varanasi, “Diversity and multiplexing tradeoff bounds for cooperative diversity protocols,” in *Proc. IEEE Intl. Symposium on Inform. Theory*, Chicago, IL, USA, June 27–July 2, 2004, p. 271.
- [72] —, “High performance static and dynamic cooperative communication protocols for the half duplex fading relay channel,” in *Proc. of IEEE Global Telecommun. Conf.*, San Francisco, CA, USA, Nov. 27–Dec. 1, 2006, pp. 1–5.
- [73] R. Ahlswede, N. Cai, S.-Y. R. Li, and R. W. Yeung, “Network information flow,” *IEEE Trans. Inf. Theory*, vol. 46, no. 4, pp. 1204–1216, July 2000.
- [74] B. Rankov and A. Wittneben, “Spectral efficient protocols for nonregenerative half-duplex relaying,” in *Allerton Conf. on Commun.*,

*Control, and Comput.*, Sept. 2005. [Online]. Available: <http://www.nari.ee.ethz.ch/wireless/pubs/p/allerton2005>

- [75] X. Bao and J. Li, "On the outage properties of adaptive network coded cooperation (ANCC) in large wireless networks," in *Proc. of IEEE Int. Conf. on Acoustics, Speech and Signal Processing (ICASSP 2006)*, vol. 4, Toulouse, France, May 14–19, 2006, pp. 57–60.
- [76] Y. Chen, S. Kishore, and J. Li, "Wireless diversity through network coding," in *Proc. of IEEE Wireless Commun. and Networking Conf. (WCNC)*, vol. 3, Las Vegas, NV USA, Apr. 3–6, 2006, pp. 1681–1686.
- [77] C. Hausl and J. Hagenauer, "Iterative network and channel decoding for the two-way relay channel," in *Proc. of IEEE Int. Conf. on Commun. (ICC 2006)*, vol. 4, Istanbul, Turkey, June 11–15, 2006, pp. 1568–1573.
- [78] C. Hausl and P. Dupraz, "Joint network-channel coding for the multiple-access relay channel," in *Third Annual IEEE Commun. Society Conf. on Sensor, Mesh and Ad Hoc Commun. and Networks (SECON)*, vol. 3, Reston, VA, USA, Sept. 25–28, 2006, pp. 817–822.
- [79] S. Katti, H. Rahul, W. Hu, D. Katabi, M. Médard, and J. Crowcroft, "XORs in the air: Practical wireless network coding," in *Proc. of ACM SIGCOMM*, Pisa, Italy, Sept. 11–15, 2006, pp. 243–254.
- [80] P. Popovski and H. Yomo, "Bi-directional amplification of throughput in a wireless multi-hop network," in *IEEE 63rd Veh. Technol. Conf. (VTC) 2006 Spring*, Melbourne, Australia, May 7–10, 2006, pp. 588–593.

- [81] W. Chen, K. B. Letaief, and Z. Cao, “Opportunistic network coding for wireless networks,” in *IEEE Inter. Conf. on Commun. (ICC)*, Glasgow, Scotland, June 24–28, 2007, pp. 4634–4639.
- [82] S. Fu, K. Lu, Y. Qian, and M. Varanasi, “Cooperative network coding for wireless ad-hoc networks,” in *IEEE Global Telecommun. Conf. (GLOBECOM)*, Washington, D.C., USA, Nov. 26–30, 2007, pp. 812–816.
- [83] S. Katti, S. Gollakota, and D. Katabi, “Embracing wireless interference: Analog network coding,” in *Proc. of ACM SIGCOMM*, Kyoto, Japan, Aug. 27–31, 2007, pp. 397–408.
- [84] L. Lv, H. Yu, and J. Yang, “Opportunistic cooperative network-coding based on space-time coding for bi-directional traffic flows,” in *IEEE Fourth Workshop on Network Coding, Theory, and Applications (Net-Cod) 2008*, Hong Kong, China, Jan. 3–4, 2008, pp. 43–48.
- [85] E. M. Stein and R. Shakarchi, *Real Analysis : Measure Theory, Integration, and Hilbert Spaces*. Princeton University Press, 2005.
- [86] K. Hao and J. A. Gubner, “The distribution of sums of path gains in the IEEE 802.15.3a UWB channel model,” *IEEE Trans. on Wireless Commun.*, vol. 6, no. 3, pp. 811–816, Mar. 2007.
- [87] K. Witrisal, “Statistical analysis of the IEEE 802.15.4a UWB PHY over multipath channels,” in *IEEE Wireless Commun. and Networking Conf.*, Las Vegas, USA, Mar. 31–Apr. 3, 2008, pp. 130–135.
- [88] W.-C. Liu and L.-C. Wang, “Performance analysis of pulse based ultra-wideband systems in the highly frequency selective fading channel with



- cluster property,” in *IEEE Veh. Technol. Conf.*, vol. 3, Melbourne, Australia, May 7–10, 2006, pp. 1459–1463.
- [89] P. J. Davis and P. Rabinowitz, *Methods of Numerical Integration*, 2nd ed. San Diego, Academic Press, Inc., 1984.
- [90] [Online]. Available: [http://www.efunda.com/math/num\\_integration/num\\_int\\_gauss.cfm](http://www.efunda.com/math/num_integration/num_int_gauss.cfm)
- [91] J. G. Proakis, *Digital Communications*, 4th ed. Boston: McGraw-Hill, 2001.
- [92] M. C. Fu and X. Jin, “On the convergence rate of ordinal comparisons of random variables,” *IEEE Trans. on Automatic Control*, vol. 46, no. 12, pp. 1950–1954, Dec. 2001.
- [93] L.-C. Wang and W.-C. Liu, “Bit error rate analysis in IEEE 802.15.3a UWB channels,” submitted to *IEEE Trans. Wireless Commun.*
- [94] X. Hong and C. Wang, “A correlation based double directional stochastic model for MIMO-UWB propagation channels,” in *The IEE Seminar on Ultra Wideband Syst., Technol. and Applicat*, London, UK, Apr. 20, 2006, pp. 249–253.
- [95] R. C. Qiu, “A generalized time domain multipath channel and its application in ultra-wideband (GWU) wireless optimal receiver design: system performance analysis,” in *IEEE Wireless Communi. and Network Conf.*, Mar. 2004, pp. 901–907.
- [96] A. Leon-Garcia, *Probability and Random Processes for Electrical Engineering*, 2nd ed. Addison-Wesley Publishing Company, 1994.

- [97] H. Stark and J. W. Woods, *Probability and Random Processes with Application to Signal Processing*, 3rd ed. Prentice Hall, 2002.
- [98] J. Foerster, et. al., “Channel modeling sub-committee report final,” *IEEE P802.15 Wireless Personal Area Networks, P802.15-02/490r1-SG3a*, Feb. 2003.
- [99] R. A. Horn and C. R. Johnson, *Matrix Analysis*. Cambridge, U.K.: Cambridge Univ. Press, 1985.
- [100] B. Vucetic and J. Yuan, *Space-Time Coding*. Chichester, England: John Wiley and Sons Ltd, 2003.
- [101] D. B. West, *Introduction to Graph Theory*, 2nd ed. Upper Saddle River, NJ 07458: Prentice-Hall, Inc., 2001.
- [102] S. Alamouti, “A simple transmit diversity technique for wireless communications,” *IEEE J. Sel. Areas Commun.*, vol. 16, no. 8, pp. 1451–1458, Oct. 1998.
- [103] L.-C. Wang, W.-C. Liu, and K.-J. Shieh, “On the performance of using multiple transmit and receive antennas in pulse-based ultrawideband systems,” *IEEE Trans. Wireless Commun.*, vol. 4, no. 6, pp. 2738–2750, Nov. 2005.
- [104] C. Xiao, Y. R. Zheng, and N. C. Beaulieu, “Statistical simulation models for Rayleigh and Rician fading,” *IEEE Int. Conf. on Commun.*, pp. 3524–3529, May 16–20, 2003.
- [105] —, “Novel sum-of-sinusoids simulation models for Rayleigh and Rician fading channels,” *IEEE Trans. on Wireless Commun.*, vol. 5, no. 12, pp. 3667–3679, Dec. 2006.

- [106] A. Papoulis, *Probability, Random Variables, and Stochastic Process*, 3rd ed. McGraw-Hill, 2001.
- [107] S. O. Rice, "Statistical properties of sine wave plus random noise," *Bell Syst. Tech. J.*, pp. 109–157, Jan. 1948.
- [108] A. S. Akki, "Statistical properties of mobile-to-mobile land communication channels," *IEEE Trans. on Veh. Technol.*, vol. 43, no. 4, pp. 826–831, Nov. 1994.
- [109] G. L. Stüber, *Principles of Mobile Communication*, 2nd ed. 3300 AH Dordrecht, The Netherlands: Kluwer Academic, 2001.
- [110] J.-Z. Sun, J. Sauvola, and D. Howie, "Features in future: 4G visions from a technical perspective," *Proc. of IEEE Global Telecommun. Conf.*, vol. 6, pp. 25–29, Nov 2001.
- [111] IEEE TGN Sync working group. [Online]. Available: <http://www.tgnsync.org/techdocs/>
- [112] P. Beckman, S. Verma, and R. Rao, "Use of mobile mesh networks for inter-vehicular communication," *IEEE Veh. Technol. Conf.*, vol. 4, pp. 2712–2715, Oct 2003.
- [113] S. Haykin, "Cognitive radio: brain-empowered wireless communications," *IEEE J. on Sel. Areas in Commun.*, vol. 23, pp. 201–220, Feb 2005.
- [114] L.-C. Wang and Y.-H. Cheng, "A statistical mobile-to-mobile Rician fading channel model," in *IEEE Vehicular Technology Conference*, May 2005.

- [115] V. Erceg, L. Greenstein, S. Y. Tjandra, S. R. Parkoff, A. Gupta, B. Kulic, A. A. Julius, and R. Bianchi, “Theory, experiment, and statistical models,” *IEEE J. on Sel. Areas in Commun.*, vol. 7, pp. 1205–1211, Jul 1999.
- [116] D. Halliday and R. Resnick, *Fundamentals of Physics*, 3rd ed. New York: John Wiley & Sons, 1988.
- [117] C. Xiao, Y. R. Zheng, and N. C. Beaulieu, “Second-order statistical properties of the WSS Jakes fading simulator,” *IEEE Trans. on Commun.*, vol. 50, pp. 888–891, June 2002.
- [118] L.-C. Wang and Y.-H. Cheng, “Modelling and capacity analysis of MIMO Rician fading channels for mobile-to-mobile communications,” in *IEEE Vehicular Technology Conference*, Sep. 2005.
- [119] D. Tse and P. Viswanath, *Fundamentals of Wireless Communication*. Cambridge University Press, 2005.
- [120] A. Paulraj, R. Narbar, and D. Gore, *Introduction to Space-Time Wireless Communications*. Cambridge University Press, 2003.
- [121] G. J. Foschini and M. J. Gans, “On limits of wireless communications in a fading environment when using multiple antennas,” *Wireless Personal Communications*, no. 6, pp. 311–335, 1998.
- [122] I. E. Teletar, “Capacity of multi-antenna Gaussian channels,” *AT&T Bell Lab. Tech. Memo.*, June 1995.
- [123] P. J. Smith and M. Shafi, “On a Gaussian approximation to the capacity of wireless MIMO systems,” *IEEE Int. Conf. on Commun.*, vol. 1, pp. 406–410, April 2002.

- [124] M. Shafi and P. J. Smith, "An approximate capacity distribution for MIMO systems," *IEEE Trans. on Commun.*, vol. 52, pp. 887–890, June 2004.
- [125] C. Gao, M. Zhao, S. Zhou, and Y. Yao, "Capacity autocorrelation characteristic of MIMO systems over doppler spread channels," *IEEE Veh. Technol. Conf.*, vol. 1, pp. 44–46, April 2003.
- [126] S. Ross, *A First Course in Probability*, 7th ed. Prentice-Hall International, Inc., 2006.
- [127] H. Stark and J. W. Woods, *Probability, Random Processes, and Estimation Theory for Engineers*, 2nd ed. Englewood Cliffs: Prentice Hall International, Inc., 1994.
- [128] A. Andersson, "The intensity concept," *SICS Technical Report ISRN:SICS-T-2000/03-SE T2000:03 ISSN 1100-3154*, 2000. [Online]. Available: <http://www.sics.se/~aeg/report/node11.html>
- [129] J. F. C. Kingman, *Poisson Processes*. Oxford, UK: Clarendon, 1993.

# Appendix A

## Derivation of the PDF of $\mathcal{E}$

The objective in this part is to find the PDF of  $\mathcal{E}$ , where

$$\mathcal{E} = X^2 \sum_{m=1}^L A_m^2. \quad (\text{A.1})$$

With the characteristic function of  $A_m$  in (3.7), we can obtain the PDF of  $A_m$  as

$$f_{A_m}(y) = \frac{1}{2\pi} \int_{-\infty}^{\infty} e^{-juy} \Psi_{A_m}(u) du. \quad (\text{A.2})$$

Given  $f_{A_m}(y)$ , the PDF of  $A_m^2$  can be obtained as

$$f_{A_m^2}(y) = \frac{1}{2\sqrt{y}} [f_{A_m}(\sqrt{y}) + f_{A_m}(-\sqrt{y})]. \quad (\text{A.3})$$

The derivation of (A.3) can be referred to [126, Example 7b]. Then, the characteristic function of  $A_m^2$  can be computed as

$$\Psi_{A_m^2}(\nu) = \int_{-\infty}^{\infty} e^{j\nu x} f_{A_m^2}(x) dx. \quad (\text{A.4})$$

Recall that  $B = \sum_{m=1}^L A_m^2$ . Then, the characteristic function of the random variable  $B$  can be found via

$$\Psi_B(\nu) = \prod_{m=1}^L \Psi_{A_m^2}(\nu). \quad (\text{A.5})$$

Note that we have made an assumption that  $A_1, A_2, \dots, A_L$  are independent, since  $\Psi_B(\nu)$  is difficult to find for dependent  $A_1, A_2, \dots, A_L$ . Combining (A.2)–(A.5) and

$$f_B(x) = \frac{1}{2\pi} \int_{-\infty}^{\infty} e^{-j\nu x} \Psi_B(\nu) d\nu, \quad (\text{A.6})$$

we can get (3.10). The remaining task is to find the PDF of  $X^2$ . Since  $X$  is a lognormal random variable satisfying  $20 \log_{10} X \propto \text{Normal}(0, \sigma_x^2)$ , its PDF can be expressed as

$$f_X(x) = \begin{cases} \frac{10\sqrt{\frac{2}{\pi}} \exp\left[-200\left(\frac{\log_{10} x}{\sigma_x}\right)^2\right]}{x\sigma_x \ln 10}, & x > 0, \\ 0, & x \leq 0. \end{cases} \quad (\text{A.7})$$

Again using the result in [126, Example 7b], we can find that the PDF of  $X^2$  is as in (3.9).

Finally, from Example 3.3-1 in [127], we know that for two random variables  $X'$  and  $Y'$  with a joint PDF  $f_{X',Y'}(x, y)$ , the PDF of the new random variable  $Z = X'Y'$  is

$$f_Z(z) = \int_{-\infty}^{\infty} \frac{1}{|y|} f_{X',Y'}\left(\frac{z}{y}, y\right) dy. \quad (\text{A.8})$$

Since  $X^2$  and  $B$  are independent,  $f_{X^2,B}(x, y) = f_{X^2}(x)f_B(y)$ . Applying this relation to (A.8), we can obtain (3.8).

# Appendix B

## Proof of Theorem 1

Let  $f_{G|T,t}(x)$  be the PDF of the path gain  $G \triangleq \alpha_{k,l}$  arriving at time  $t$  with a cluster that starting at time  $T$ . According to [86], it follows that

$$f_{G|T,t}(x) = \frac{1}{2}[f_{|G||T,t}(x) + f_{|G||T,t}(-x)] \quad (\text{B.1})$$

because the path gain is positive or negative with equal probability of 0.5. Note that  $f_{|G||T,t}(x)$  is lognormally distributed, i.e.,

$$f_{|G||T,t}(x) = \begin{cases} \frac{20 \exp\left[-\frac{1}{2\sigma^2} (20 \log_{10} x - \mu_{T,t})^2\right]}{\sqrt{2\pi\sigma x \ln 10}}, & x > 0, \\ 0, & \text{otherwise,} \end{cases} \quad (\text{B.2})$$

where  $\mu_{T,t}$  given in (3.15) and  $\sigma = \sqrt{\sigma_1^2 + \sigma_2^2}$  are the mean and the standard deviation of the random variable  $20 \log_{10} |G|$ , respectively. Note that (3.15) is the continuous-time representation of (2.8) because the discrete indices  $k$  and  $l$  are changed to continuous arrival time  $t$  and  $T$ , respectively. Thus, it follows that

$$\begin{aligned} 20 \log_{10} G^2 &= 2(20 \log_{10} |G|) \\ &\propto \text{Normal}(2\mu_{T,t}, (2\sigma)^2) . \end{aligned} \quad (\text{B.3})$$



Then the PDF of the squared path gain arriving at time  $t$  in a cluster starting at time  $T$  can be written as

$$f_{T,t}(x) = \begin{cases} \frac{10 \exp\left[-\frac{1}{2\sigma^2}(10 \log_{10} x - \mu_{T,t})^2\right]}{\sqrt{2\pi\sigma x \ln 10}}, & x > 0, \\ 0, & \text{otherwise.} \end{cases} \quad (\text{B.4})$$

Denote  $\tilde{\mathcal{L}}_{T,t}(\nu)$  as the characteristic function of  $f_{T,t}(x)$ . We can obtain (3.14), i.e.,

$$\tilde{\mathcal{L}}_{T,t}(\nu) = \mathbb{E}_{T,t}[e^{j\nu G^2}] = \int_{-\infty}^{\infty} e^{j\nu x} f_{T,t}(x) dx. \quad (\text{B.5})$$



# Appendix C

## Proof of Theorem 2

In [86] the authors obtained the characteristic function of the sum of path gains in the time window  $[a, b]$ , but did not take the lognormal shadowing into account. The method in [86] can be modified and extended to determine the characteristic function of  $\tilde{\mathcal{E}}$ . Consider an  $L$ -finger RAKE receiver in the time window  $[0, LT_c]$ , where  $T_c$  is the chip duration between two fingers.

Defined

$$\tilde{\psi}_\nu(T, L) = \begin{cases} \int_{\max(a, T)}^b [1 - \tilde{\mathcal{L}}_{T,t}(\nu)] dt, & T \leq b, \\ 0, & T > b, \end{cases} \quad (\text{C.1})$$

and

$$\tilde{J}(\nu, L) = \int_0^a [1 - e^{-\lambda \tilde{\psi}_\nu(T, L)}] dT + \int_a^b [1 - \tilde{\mathcal{L}}_{T,T}(\nu) e^{-\lambda \tilde{\psi}_\nu(T, L)}] dT. \quad (\text{C.2})$$

By setting  $a = 0$  and  $b = LT_c$ , we can transform the above equations to (3.18) and (3.20), respectively.

# Appendix D

## Proof of Lemma 1

According to [4, (18)], the PDF of interarrival time of ray is

$$f(\tau) = \begin{cases} \beta\lambda_1 e^{-\lambda_1\tau} + (1-\beta)\lambda_2 e^{-\lambda_2\tau}, & \tau \geq 0, \\ 0, & \tau < 0. \end{cases} \quad (\text{D.1})$$

The cumulative distribution function (CDF) is

$$\begin{aligned} F(\tau) &= \int_{-\infty}^{\tau} f(x) dx \\ &= \begin{cases} 1 - \beta e^{-\lambda_1\tau} - (1-\beta)e^{-\lambda_2\tau}, & \tau \geq 0, \\ 0, & \tau < 0. \end{cases} \end{aligned} \quad (\text{D.2})$$

The ray arrival rate  $\lambda$  is the intensity function [128] of the interarrival time of rays:

$$\begin{aligned} \lambda(\tau) &= \frac{f(\tau)}{1 - F(\tau)} \\ &= \begin{cases} \frac{\beta\lambda_1 e^{-\lambda_1\tau} + (1-\beta)\lambda_2 e^{-\lambda_2\tau}}{\beta e^{-\lambda_1\tau} + (1-\beta)e^{-\lambda_2\tau}}, & \tau \geq 0, \\ 0, & \tau < 0. \end{cases} \end{aligned} \quad (\text{D.3})$$

The ray arrival is indeed a nonhomogeneous Poisson process. The ray arrival rate is a function of time  $\tau$ . Note that when  $\beta = 1$ , the PDF in (D.1) reduces

to the exponential PDF and the intensity function reduces to the constant  $\lambda_1$ . This case corresponds to a homogeneous Poisson process.



# Appendix E

## Proof of Theorem 4

Denote  $f_{Y|T,t}(y)$  as the PDF of squared amplitude  $Y$  corresponding to the cluster arrival time  $T$  and ray arrival time  $t$ . Because  $\Phi_{r0}$  is a shot-noise random variable driven by a two-dimensional Poisson process with intensity function  $\lambda(t)f_{Y|0,t}(y)$ , the function  $R(\nu, L)$  can be calculated as [129]

$$\begin{aligned}
 R(\nu, L) &= E [e^{j\nu\Phi_{r0}}] \\
 &= \exp \left\{ \int_0^\infty \int_{-\infty}^\infty [e^{j\nu y I_{[0,LT_c]}(t)} - 1] \lambda(t) f_{Y|0,t}(y) dy dt \right\} \\
 &= \exp \left\{ - \int_0^\infty \int_{-\infty}^\infty [1 - e^{j\nu y I_{[0,LT_c]}(t)}] f_{Y|0,t}(y) dy \lambda(t) dt \right\} \\
 &= \exp \left\{ - \int_0^{LT_c} [1 - \mathcal{L}_{0,t}(\nu)] \lambda(t) dt \right\} \\
 &= \exp [-\psi_\nu(0, L)]. \tag{E.1}
 \end{aligned}$$

The derivation of the function  $J(\nu, L)$  is similar to the derivation of the function  $\tilde{J}(\nu, L)$  in [93]. The only difference is that we have to delete the term  $\lambda$  in (66) in [93] because the ray arrival rate is already considered in the function  $\psi_\nu(T, L)$  here. Thus,

$$J(\nu, L) = \int_0^{LT_c} [1 - \mathcal{L}_{T,T}(\nu) e^{-\psi_\nu(T, L)}] dT. \tag{E.2}$$

# Appendix F

## Proof of Theorem 5

From [93], we know that the PDF of  $X^2$  is

$$f_{X^2}(x) = \begin{cases} \frac{5\sqrt{\frac{2}{\pi}} \exp\left[-50\left(\frac{\log_{10} x}{\sigma_x}\right)^2\right]}{x\sigma_x \ln 10}, & x > 0, \\ 0, & x \leq 0. \end{cases} \quad (\text{F.1})$$

From Example 3.3-1 in [127], we know that for two random variables  $X'$  and  $Y'$  with the known joint PDF  $f_{X',Y'}(x, y)$ , the PDF of the new random variable  $Z = X'Y'$  is

$$f_Z(z) = \int_{-\infty}^{\infty} \frac{1}{|y|} f_{X',Y'}\left(\frac{z}{y}, y\right) dy. \quad (\text{F.2})$$

Because  $X^2$  and  $\tilde{\mathcal{E}}$  are independent,  $f_{X^2, \tilde{\mathcal{E}}}(x, y) = f_{X^2}(x)f_{\tilde{\mathcal{E}}}(y)$ . Applying this relation to (F.2), we have, for  $z \geq 0$ ,

$$\begin{aligned} f_{\tilde{\mathcal{E}}_X}(z) &= \int_{-\infty}^{\infty} \frac{1}{|y|} f_{X^2}\left(\frac{z}{y}\right) f_{\tilde{\mathcal{E}}}(y) dy \\ &\approx \int_{-\infty}^{\infty} \frac{1}{|y|} f_{X^2}\left(\frac{z}{y}\right) \frac{1}{2\pi} \sum_{k=1}^{N^{(\text{H})}} w_k^{(\text{H})} \Psi(\nu) e^{-jy\nu} e^{\nu^2} \Big|_{\nu=x_k^{(\text{H})}} dy \\ &= \frac{1}{2\pi} \sum_{k=1}^{N^{(\text{H})}} w_k^{(\text{H})} \Psi(\nu) \int_{-\infty}^{\infty} \frac{1}{|y|} f_{X^2}\left(\frac{z}{y}\right) e^{-jy\nu} dy e^{\nu^2} \Big|_{\nu=x_k^{(\text{H})}}. \end{aligned} \quad (\text{F.3})$$

Since  $\tilde{\mathcal{E}} \geq 0$ ,  $f_{\tilde{\mathcal{E}}}(y) = 0$  for  $y < 0$  and

$$\begin{aligned}
& \int_{-\infty}^{\infty} \frac{1}{|y|} f_{X^2} \left( \frac{z}{y} \right) e^{-jy\nu} dy \\
&= \int_0^{\infty} \frac{1}{y} \cdot 5 \sqrt{\frac{2}{\pi}} \frac{\exp \left[ -50 \left( \frac{\log_{10}(z/y)}{\sigma_x} \right)^2 \right]}{(z/y) \sigma_x \ln 10} e^{-jy\nu} dy \\
&= \sqrt{\frac{2}{\pi}} \frac{5}{z \sigma_x \ln 10} \int_0^{\infty} \exp \left[ -50 \left( \frac{\log_{10} z - \log_{10} y}{\sigma_x} \right)^2 \right] e^{-jy\nu} dy. \quad (\text{F.4})
\end{aligned}$$

Let

$$w = \frac{\sqrt{50}(\log_{10} z - \log_{10} y)}{\sigma_x}, \quad (\text{F.5})$$

then

$$y = z \cdot 10^{-\frac{\sigma_x w}{\sqrt{50}}} \quad (\text{F.6})$$

and

$$\frac{dy}{dw} = -\frac{1}{5\sqrt{2}} 10^{-\frac{\sigma_x w}{5\sqrt{2}}} \sigma_x z \ln 10. \quad (\text{F.7})$$

The above equation (F.4) becomes

$$\begin{aligned}
& \frac{1}{\sqrt{\pi}} \int_{-\infty}^{\infty} \exp \left( -w^2 - jz\nu 10^{-\frac{\sigma_x w}{\sqrt{50}}} \right) 10^{-\frac{\sigma_x w}{\sqrt{50}}} dw \\
& \approx \frac{1}{\sqrt{\pi}} \sum_{l=1}^{N^{(H)}} w_l^{(H)} \exp \left( -jz\nu 10^{-\frac{\sigma_x w}{\sqrt{50}}} \right) 10^{-\frac{\sigma_x w}{\sqrt{50}}} \Big|_{w=x_l^{(H)}}. \quad (\text{F.8})
\end{aligned}$$

Hence, the PDF  $f_{\tilde{\mathcal{E}}_X}(x)$  can be approximated as

$$\begin{aligned}
f_{\tilde{\mathcal{E}}_X}(x) & \approx \frac{1}{2\pi\sqrt{\pi}} \sum_{k=1}^{N^{(H)}} w_k^{(H)} \Psi(\nu) \\
& \quad \sum_{l=1}^{N^{(H)}} w_l^{(H)} \exp \left( -jx\nu 10^{-\frac{\sigma_x w}{\sqrt{50}}} \right) 10^{-\frac{\sigma_x w}{\sqrt{50}}} \Big|_{w=x_l^{(H)}} e^{\nu^2} \Big|_{\nu=x_k^{(H)}} \\
& = \frac{1}{2\pi\sqrt{\pi}} \sum_{k=1}^{N^{(H)}} w_k^{(H)} \Psi(x_k^{(H)}) e^{[x_k^{(H)}]^2} \\
& \quad \sum_{l=1}^{N^{(H)}} w_l^{(H)} \exp \left( -jxx_k^{(H)} 10^{-\frac{\sigma_x x_l^{(H)}}{\sqrt{50}}} \right) 10^{-\frac{\sigma_x x_l^{(H)}}{\sqrt{50}}}. \quad (\text{F.9})
\end{aligned}$$

# Appendix G

## Proof of Proposition 1

From (4.13) and (4.2), we can express the mean of the processed data  $z_{p1}$  as

$$\mathbb{E}[z_{p1}] = \mathbb{E}[s_{p1}] + \mathbb{E}[r_{p1}] + \mathbb{E}[n_{p1}] + \mathbb{E}[n_{p0}], \quad (\text{G.1})$$

where the signal part  $\mathbb{E}[s_{p1}]$

$$\mathbb{E}[s_{p1}] = \mathbb{E}\left[\sum_{l=0}^{L-1} x_l x_l\right] = \sum_{l=0}^{L-1} \mathbb{E}[\xi_l^2]. \quad (\text{G.2})$$

From (4.5) and (4.16), we can have

$$\sum_{l=0}^{L-1} \mathbb{E}[\xi_l^2] = A + B, \quad (\text{G.3})$$

where  $A$  is defined in (4.18) and

$$\begin{aligned} B &= \sum_{l=4}^{L-1} (\pi_H(1 - \alpha) + \pi_L\beta) \mathbb{E}[a_l^2] \\ &= \sum_{l=4}^{L-1} \left( \frac{\beta}{\alpha + \beta}(1 - \alpha) + \frac{\alpha}{\alpha + \beta}\beta \right) \mathbb{E}[a_l^2] \\ &= \left( \frac{\beta}{\alpha + \beta} \right) \frac{\gamma e^{-3\eta} - \gamma e^{-(L-1)\eta}}{1 - e^{-\eta}}. \end{aligned} \quad (\text{G.4})$$



Recalling that  $b_l$  in (4.2) is  $+/- 1$  equiprobable, we can calculate the redundancy part  $\mathbb{E}[r_{p1}]$  of the processed data mean  $\mathbb{E}[z_{p1}]$  from (4.13) as follows:

$$\begin{aligned}\mathbb{E}[r_{p1}] &= -\mathbb{E}\left[\sum_{l=0}^{L-\delta-1} x_l x_{l+\delta}\right] = -\mathbb{E}\left[\sum_{l=0}^{L-\delta-1} a_l b_l a_{l+\delta} b_{l+\delta}\right] \\ &= -\sum_{l=0}^{L-\delta-1} \mathbb{E}[a_l a_{l+\delta}] \cdot \mathbb{E}[b_l b_{l+\delta}] = 0.\end{aligned}\tag{G.5}$$

Note that  $n_l$  is a Gaussian random variable with zero mean, and  $x_l$  and  $n_l$  are mutually independent. Thus from (4.13), we can express the  $\mathbf{p}_1$  noise part  $\mathbb{E}[n_{p1}]$  of the processed data mean  $\mathbb{E}[z_{p1}]$  as follows:

$$\mathbb{E}[n_{p1}] = \mathbb{E}\left[\sum_{l=0}^{L-1} n_{l+\delta} x_l\right] = \sum_{l=0}^{L-1} \mathbb{E}[n_{l+\delta}] \cdot \mathbb{E}[x_l] = 0,\tag{G.6}$$

Similar to (G.6), the  $\mathbf{p}_0$  noise part  $\mathbb{E}[n_{p0}]$  of the processed data mean  $\mathbb{E}[z_{p1}]$  can be calculated as

$$\mathbb{E}[n_{p0}] = \mathbb{E}\left[\sum_{l=0}^{L-1} n_l x_l\right] = \sum_{l=0}^{L-1} \mathbb{E}[n_l] \mathbb{E}[x_l] = 0.\tag{G.7}$$

Form (G.1), we prove Proposition 1.

# Appendix H



## Proof of Proposition 2

In this appendix, we derive the remaining terms of the right hand side of (4.19) except  $\text{var}[s_{p1}]$ . For the redundancy part  $\text{var}[r_{p1}]$  of the processed data, we first consider the ideal pulse in the worst case of  $\delta = 1$ . Since  $b_l$  is equiprobable to take on the value  $+/- 1$ , it is obvious that  $E[b_l] = 0$ .

Recalling (4.2), (4.9), and (4.13), we can obtain

$$\begin{aligned}
& \text{var}[r_{p1}] \\
&= \text{var}\left[-\sum_{l=0}^{L-2} x_l x_{l+1}\right] \\
&= \text{var}\left[-\sum_{l=0}^{L-2} \xi_l \xi_{l+1}\right] \\
&= \sum_{l=0}^{L-2} \text{var}[a_l b_l a_{l+1} b_{l+1}] \\
&\quad + 2 \sum_{m=0}^{L-2} \sum_{n=m+1}^{L-2} \text{cov}[a_m b_m a_{m+1} b_{m+1}, a_n b_n a_{n+1} b_{n+1}] \\
&= \sum_{l=0}^{L-2} \text{var}[a_l b_l a_{l+1} b_{l+1}] \\
&= \sum_{l=0}^{L-2} \mathbb{E}[a_l^2 a_{l+1}^2 b_l^2 b_{l+1}^2] - \mathbb{E}[a_l a_{l+1} b_l b_{l+1}]^2 \\
&= \sum_{l=0}^{L-2} \mathbb{E}[a_l^2 a_{l+1}^2] \mathbb{E}[b_l^2 b_{l+1}^2] \\
&= \sum_{l=0}^{L-2} \pi_H(l) \pi_H(2) \mathbb{E}[a_l^2] \mathbb{E}[a_{l+1}^2]. \tag{H.1}
\end{aligned}$$

For the more general case  $\delta \neq 1$ , one can derive

$$\text{var}[r_{p1}] = \sum_{l=0}^{L-\delta-1} \pi_H(l) \pi_H(\delta + 1) \mathbb{E}[a_l^2] \mathbb{E}[a_{l+\delta}^2]. \tag{H.2}$$

Next, we derive the noise part  $\text{var}[n_{p1}]$  of the processed data variance

$\text{var}[z_{p1}]$ . For the Gaussian noise with zero mean and the variance of  $\sigma_n^2/2$ ,

$$\begin{aligned}
& \text{var}[n_{p1}] \\
&= \text{var}\left[\sum_{l=0}^{L-1} n_{l+1}x_l\right] \\
&= \sum_{l=0}^{L-1} \text{var}[n_{l+1}x_l] + 2 \sum_{m=0}^{L-2} \sum_{n=m+1}^{L-1} \text{cov}[n_{m+1}x_m, n_{n+1}x_n] \\
&= \sum_{l=0}^{L-1} \frac{\pi_H(l)\sigma_n^2}{2} \mathbb{E}[a_l^2].
\end{aligned} \tag{H.3}$$

Similar to derive (H.3), we can obtain

$$\text{var}[n_{p0}] = \sum_{l=0}^{L-1} \frac{\pi_H(l)\sigma_n^2}{2} \mathbb{E}[a_l^2], \tag{H.4}$$

and

$$\begin{aligned}
& \text{cov}[s_{p1}, r_{p1}] \\
&= \mathbb{E}[s_1 r_{p1}] - \mathbb{E}[s_1] \mathbb{E}[r_1] \\
&= \sum_{l=0}^{L-2} \pi_H(l) \pi_H(2) \mathbb{E}[a_l | n_l \neq 0] \mathbb{E}[a_l^2] \mathbb{E}[a_{l+1}^2] \\
&= 0.
\end{aligned} \tag{H.5}$$

Last, it is easy to show that

$$\begin{aligned}
& \text{cov}[s_{p1}, r_{p1}] = \text{cov}[s_{p1}, n_{p1}] = \text{cov}[s_{p1}, n_{p0}] \\
&= \text{cov}[r_{p1}, n_{p1}] = \text{cov}[r_{p1}, n_{p0}] = \text{cov}[n_{p1}, n_{p0}] \\
&= 0.
\end{aligned} \tag{H.6}$$

Hence, from (4.22) to (4.25) and (H.1) to (H.6), we proved Proposition 2.

# Vita

**Wei-Cheng Liu** (S'04) received the B.S. and M.S. degrees from National Tsing Hua University, Hsinchu, Taiwan, in 1999 and 2001, respectively, both in electrical engineering. He is currently working toward the Ph.D. degree in Department of Communication Engineering of National Chiao Tung University, Hsinchu, Taiwan.

After he got the M.S. degree, he served the military service in Cheng Gong Ling, Taichung, Taiwan. In 2002, he was a GSM Layer 1 Software Engineer at Compal Communications, Inc., Taipei, Taiwan. His current research interests are in the areas of MIMO Rician channels in mobile ad-hoc networks, cross-layer rate and power adaptation for wireless LANs, performance analysis for UWB systems, space-time-frequency codes design, and cooperative network coding.

# Publication List

## Journal Paper (published or accepted)

1. Li-Chun Wang, Wei-Cheng Liu, and Kuan-Jiin Shieh, “On the Performance of Using Multiple Transmit and Receive Antennas in Pulse Based Ultra-Wideband Systems,” *IEEE Transactions on Wireless Communications*, vol. 4, no. 6, pp. 2738-2750, Nov. 2005.
2. Li-Chun Wang, Wei-Cheng Liu and Yun-Huai Cheng, “Statistical Analysis of A Mobile-to-Mobile Rician Fading Channel Model,” accepted by *IEEE Transactions on Vehicular Technology*.
3. Li-Chun Wang, Wei-Cheng Liu, Anderson Chen, and Kuang-Nan Yen, “Joint Rate and Power Adaptation for Wireless Local Area Networks in Generalized Nakagami Fading Channels,” accepted by *IEEE Transactions on Vehicular Technology*.

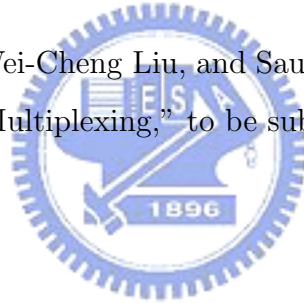
## Journal Paper (revision)

1. Li-Chun Wang and Wei-Cheng Liu, “Bit Error Rate Analysis in IEEE 802.15.3a UWB Channels,” submitted to *IEEE Transactions on Wireless Communications*, Apr. 2008.

2. Li-Chun Wang, Wei-Cheng Liu, and Yun-Huai Cheng, “Modeling and Capacity Fades Analysis of MIMO Rician Channels in Mobile Ad Hoc Networks,” submitted to *EURASIP Journal on Wireless Communications and Networking*, May 2008.

## Journal Paper (to be submitted)

1. Li-Chun Wang, Wei-Cheng Liu, and Andreas F. Molisch, “BER Analysis in IEEE 802.15.4a UWB Channels,” to be submitted.
2. Li-Chun Wang and Wei-Cheng Liu, “BER-Minimized Space-Time-Frequency Codes for MIMO Highly Frequency-Selective Block-Fading Channels,” to be submitted.
3. Li-Chun Wang, Wei-Cheng Liu, and Sau-Hsuan Wu, “Network Coding for Cooperative Multiplexing,” to be submitted.



## Patent

1. Li-Chun Wang (NCTU), Wei-Cheng Liu (NCTU), “A Searching Algorithm for Optimal Space-Time-Frequency Block Codes for Multiband MIMO-UWB Systems,” filed for Taiwan patent on Dec. 23, 2007.
2. Li-Chun Wang (NCTU), Kuang-Nan Yen (NCTU), Ming-Bing Chen (NCTU), Wei-Cheng Liu (NCTU), Yu-Ren Yang (ITRI), Ping-Jung Huang (ITRI), “Cross-Layer Rate Adaptation Mechanism for WLAN,” Taiwan patent (No. I-257220), issued on June 21, 2006.
3. Li-Chun Wang (NCTU), Kuang-Nan Yen (NCTU), Ming-Bing Chen (NCTU), Wei-Cheng Liu (NCTU), Yu-Ren Yang (ITRI), Ping-Jung

Huang (ITRI), Cross-Layer Rate Adaptation Mechanism for WLAN, filed for the US patent with ITRI, Application No. 20060215561, Sep. 28, 2006.

## Conference Paper

1. Wei-Cheng Liu and Li-Chun Wang, "BER-Minimized Space-Time-Frequency Codes for MIMO Highly Frequency-Selective Block-Fading Channels," in *IEEE International Conference on Communications (ICC) 2008*, Beijing, China, pp. 5113-5117, May 19-23, 2008.
2. Wei-Cheng Liu and Li-Chun Wang, "BER Analysis in A Generalized UWB Frequency Selective Fading Channel With Randomly Arriving Clusters and Rays," in *IEEE International Conference on Communications (ICC) 2007*, Glasgow, Scotland, pp. 4281-4286, Jun. 24-28, 2007.
3. Wei-Cheng Liu and Li-Chun Wang, "Universal Space-Time-Frequency Block Codes Design for the Multiband MIMO-OFDM Systems," in *IEEE AP-S International Symposium on Antennas and Propagation*, Honolulu, Hawaii, USA, pp. 2435-2438, Jun. 10-15, 2007.
4. Wei-Cheng Liu and Li-Chun Wang, "BER Analysis of the IEEE 802.15.4a Channel Model with RAKE Receiver," *IEEE Vehicular Technology Conference (VTC) 2006 Fall*, Montreal, Canada, pp. 1-5, Sep. 25-28, 2006.
5. Wei-Cheng Liu and Li-Chun Wang, "Performance Analysis of Pulse Based Ultra-Wideband Systems in the Highly Frequency Selective Fading Channel with Cluster Property," *IEEE Vehicular Technology Con-*



- ference (VTC) 2006 Spring*, Melbourne, Australia, vol. 3, pp. 1459-1463, May 7-10, 2006.
6. Li-Chun Wang, Kuang-Nan Yen, Anderson Chen, and Wei-Cheng Liu, "Joint Rate and Power Adaptation for Wireless Local Area Networks in Nakagami Fading Channels," *The 11-th Mobile Computing Workshop*, Taoyuan, Taiwan, pp. 80-84, Mar. 31, 2005.
  7. Li-Chun Wang and Wei-Cheng Liu, "Performance of Pulse Position Modulated Signals over the Ultra-Wideband Channel with Multiple Transmit and Receive Antennas," *IEEE Vehicular Technology Conference (VTC) 2004 Fall*, Los Angeles, USA, vol. 2, pp. 822-826, Sep. 26-29, 2004.
  8. Li-Chun Wang, Ya-Wen Lin, and Wei-Cheng Liu, "Cross-layer Goodput Analysis for Rate Adaptive IEEE 802.11a WLAN in the Generalized Nakagami Fading Channels," *IEEE International Conference on Communications (ICC)*, Paris, France, vol. 4, pp. 2312-2316, Jun. 20-24, 2004.
  9. Wei-Cheng Liu, Li-Chun Wang, and Ya-Wen Lin, "Physical Layer Effects on the MAC Goodput Performance for the Rate Adaptive IEEE 802.11a/g WLAN," *IEEE Wireless Communications and Networking Conference (WCNC)*, Atlanta, USA, vol. 3, pp. 1873-1878, Mar. 21-25, 2004.